CHARACTERISATION OF THE DIELECTRIC PROPERTIES OF RHINOCEROS TISSUE USING COMPUTER SIMULATION AND PHYSICAL TISSUE PHANTOM MODELS

by

Floris Johannes van Zyl

Thesis presented in partial fulfilment
of the requirements for the Degree

of

MASTER OF ENGINEERING
(ELECTRICAL AND ELECTRONIC ENGINEERING)
or
(BIOMEDICAL ENGINEERING)

in the Faculty of Engineering
at Stellenbosch University

Supervisor
(Prof. T. Niesler)

Co-Supervisor/s
(Prof. M. Nieuwoudt)

December 2017

DECLARATION

By submitting this thesis electronically, I declare that the entirety of the work contained therein is my own, original work, that I am the sole author thereof (save to the extent explicitly otherwise stated), that reproduction and publication thereof by Stellenbosch University will not infringe any third party rights and that I have not previously in its entirety or in part submitted it for obtaining any qualification.

Name: ……..Floris Johannes van Zyl.....

Date: ……..…December 2017 .....

Abstract

Introduction:

Understanding the electromagnetic behaviour of in-vivo devices within rhinoceros tissue will aid existing tracking and anti-poaching endeavours and provide new insights into rhinoceros physiology and environment. The simulation and agar models proposed in this project allow the investigation of electromagnetic propagation by in-vivo and ex-vivo devices without the need for surgery. Computer simulation and agar phantom models of rhinoceros tissue based on approximated dielectric properties are designed and evaluated.

Methods:

Since the dielectric properties of rhinoceros tissue have not been documented, the conductivity and permittivity of the skin, fat, muscle, blood and other organs were approximated by means of a meta-analysis that includes animals with similar physical properties. Alternative dielectric properties of the skin (epidermis, dermis and fat) were calculated based on previously reported mechanical measurements and chemical composition. Recipes using salt, sugar and agar were designed to match the dielectric properties of each tissue within the Industrial, Scientific and Medical (ISM) frequency band by applying previously reported mathematical models. Various phantom models were designed and produced to measure the power efficiency of an in-vivo transmitter to an ex-vivo receiver for two types of antenna.

Results:

The average error between the measured and theoretically predicted dielectric values was 6.22% when measured over all recipes and 4.49% for the 2.4 GHz group specifically. The specific absorption rate (SAR) within the various tissues complied with international standards. The findings indicate that the planar inverted-F antenna (PIFA) implanted in the chest of the rhinoceros is the optimal combination in terms of power efficiency, when communication with an ex-vivo receiver attached to the hind leg of the rhinoceros is considered. The power efficiency of the PIFA was seen to improve by 16 dbm when a 10 mm air gap between the antenna and phantom was introduced. Signal penetration through the hide of the rhinoceros is possible, but communication from an in-vivo transmitter located in the back, chest or neck to an ex-vivo receiver on the hind leg is not ideal for the specified antenna size and power constraints. All practical results were compared with corresponding simulation models and found to agree to an acceptable degree. The comparability between the agar and simulated rhinoceros flank models was 67.38% when regarding the efficiency between the transmitting and receiving antennas.

Discussion:

The simulation and agar models have been demonstrated to be in substantial agreement with respects to the power efficiency of in-vivo and ex-vivo antennas. It is therefore concluded that both models represent a good basis for the design of in-vivo and ex-vivo sensors for the rhinoceros. The comparability between the simulation and agar models might be improved by including more real-world mitigation factors to the computer models. Further validation can be performed in future by analysis of the dielectric properties of actual rhinoceros tissue.

Opsomming

Inleiding:

`n Begrip van die elektromagnetiese gedrag van in-vivo toestelle binne renoster weefsel, kan bestaande opsporings en anti-stropery ondernemings bevorder en terselfdetyd nuwe insig in die biologiese funksionaliteit en omgewing van renosters verskaf. Die simulasie en agar modelle wat in hierdie projek voorgestel word, kan opsporings en monitor projekte bevoordeel deur `n middel te verskaf om in-vivo en ex-vivo toestelle te toets, sonder die noodsaaklikheid vir chirurgie. Hierdie projek stel rekenaar simulasies en agar modelle van renoster weefsel voor, wat op benaderde diëlektriese eienskappe gebaseer is.

Metodes:

Aangesien die diëlektriese eienskappe van renoster weefsel nog nie gemeet of gedokumenteer is nie, is die permitiwiteit en geleidingsvermoë van die vel, vet, spier, bloed en ander organe deur middel van `n meta-analise van diere met soortgelyke fisiese eienskappe aan renosters, benader. Alternatiewe diëlektriese eienskappe van die vel (epidermis, dermis en vet) is bereken met behulp van meganiese metings en chemiese samestellings wat alreeds in die literatuur bekend gestel is. Resepte van sout, suiker en agar is bereken om met die diëlektriese eienskappe van elke tipe weefsel in die industriële, wetenskaplike en mediese frekwensie band ooreen te stem, deur die wiskundige modelle wat alreeds in die literatuur voorgestel is, toe te pas. Verskeie modelle is ontwerp om die doeltreffendheid van die kragoordarg tussen `n in-vivo transmitter en `n ex-vivo ontvanger van twee tipes antenna pare te meet.

Resultate:

Die gemiddelde fout tussen die gemete en teoretiese waardes was 6.22% vir al die resepte en 4.49% vir die 2.4 GHz groep. Die spesifieke absorpsie koers binne die verskeie weefsel tipes, het aan internasionale standaarde voldoen. Die bevindinge het aangedui dat `n planêre omgekeerde-F antenna wat in die bors van die renoster geïmplanteer is, die optimale ontwerp is om met `n ex-vivo ontvanger op die agterpoot van die renoster te kommunikeer in terme van die doeltreffendheid van kragoordrag. Die kragoordrag van die PIFA het met 16 dbm verbeter met die byvoeging van `n 10 mm lug gaping tussen die antenna en die agar model. Alhoewel die sein die vel van die renoster kan penetreer, is kommunikasie van `n in-vivo sender in die rug, bors of nek na `n ex-vivo ontvanger op die agterpoot, nie ideaal vir die gespesifiseerde antenna grootte en kragverbruik nie. Alle praktiese resultate was met hul ooreenstemmende simulasie modelle vergelyk en die ooreenkoms was bevredigend. Die vergelykbaarheid van die agar en simulasie renoster sy ("flank") modelle, was 67.38% met betrekking tot die doeltreffendheid van die kragoordrag tussen die sender en ontvanger antennas.

Bespreking:

Die simulasie en agar modelle bied voldoende benaderings van renoster weefsel, gebaseer op die evaluering van die doeltreffendheid van in-vivo en ex-vivo antennas se kragoordrag. Daarom word daar aanvaar dat beide modelle `n goeie basis vir die ontwerp van in-vivo en ex-vivo sensors vir renosters verteenwoordig. Die vergelykbaarheid van die simulasie en agar modelle kan egter verder verbeter word deur addisionele regte-wêreldse verswakkingsfaktore tot die rekenaar simulasies by te voeg. Verdere bevestiging kan toekomstig ondersoek word deur die analise van die diëlektriese eienskappe van werklike renoster weefsel.

Acknowledgements

I would like to express my gratitude towards the following people, whose help and support made this work possible:

- Prof. Thomas Niesler, for going far beyond what is expected from him as supervisor for all his students. His experience and guidance was of tremendous value.

- Prof. Martin Nieuwoudt, who delivered ample insight into the medical aspects of this project and provided much appreciated advice as co-supervisor.

- My dad, mom, brothers and sisters, whose love and support are unfailing.

- Prof. Anna-Maria Botha-Oberholzer and the Postgraduate Department of Genetics (University of Stellenbosch) for providing access to their facilities.

- Dr. J. Marais for delivering great insight into the anatomy of the rhinoceros and for making himself available to be interviewed.

- All the members of the RhinoNET group and the DSP lab, for the Monday morning coffee meetings and necessary silliness and distractions.

- The South African Centre for Epidemiological Modelling and Analysis (SACEMA) for additional funding and for providing a platform to showcase this work.

- The Centre for High Performance Computing (CHPC) for providing access to their facilities and resources.

- "Peace I leave with you: My peace I give you. I do not give to you as the world gives. Do not let your hearts be troubled and do not be afraid." *John 14:27*

Table of Contents

DECLARATION ii
Abstract iii
Acknowledgements v
Glossary x
List of Figures xiv
List of Tables xxi
Layout of Thesis xxiii

Chapter 1. 1
1. Introduction 1

1.1 Background 1

1.2 Overall Aims 1

1.3 Specific Aims 2

1.4 Objectives 2

1.5 Contributions 3

Chapter 2. 4
2. Literature Review: Background 4

2.1 Tissue Characteristics of a White Rhinoceros 4

2.2 Availability of Frequency Spectrum for Wireless Communication 7
2.2.1 Implant Antenna Frequency Band Candidates 9

2.3 Wave Propagation: Matter 10
2.3.1 Fundamental Definitions 10
2.3.2 Dielectric Properties: Human Tissue 11

2.4 Phantom Body Simulations and Procedures 12
2.4.1 MICS Standard for Human Physical Phantom Simulations 13
2.4.2 Recipes for the Simulation of Human Tissue 14
2.4.3 Identification of Phantom Parameter Preferences 15

2.5 Types of Phantom Materials 16
2.5.1 Phantom Material Selection 17
2.5.2 Phantom Recipe Calculation Methods 18
2.5.3 The Effect of Temperature on Permittivity Measurements 20

2.6 Implantation Antenna Design 23
2.6.1 Antenna Design Selection 23
2.6.2 Practical Antenna Measurements 28

2.7 Conclusion 30

Chapter 3. 31
3. Computer Simulation Models 31

3.1 Computer Simulation Configuration....31

3.2 Rhinoceros Simulation Models....32
3.2.1 Model Size and Layering....32
3.2.2 Potential Points for Implantation....34

3.3 Summary....36

Chapter 4....37
4. Approximation of Rhinoceros Tissue Permittivity and Conductivity....37

4.1 Approximation of Dielectric Properties....37

4.2 Summary....39

Chapter 5....40
5. Agar Samples of Rhinoceros Tissue....40

5.1 Agar Preparation....40

5.2 Permittivity Measurement....43

5.3 Dielectric Property Error Analysis....52
5.3.1 Phantom Material Characteristics and Trends....58

5.4 Practical Viability of a Rhinoceros Agar Model....65

5.5 Conclusion....66

Chapter 6....68
6. Computer Simulation Results....68

6.1 Rhinoceros Flank (Slab) Phantom Model....68
6.1.1 MFPEMA Transmitting and Receiving Pair....69
6.1.2 PIFA Transmitting and Receiving Pair....71
6.1.3 Summary and Conclusion....72

6.2 Rhinoceros Cylindrical Phantom Model....73
6.2.1 MFPEMA Transmitting and Receiving Pair....74
6.2.2 PIFA Transmitting and Receiving Pair....75

6.2.3 Summary and Conclusion....76

6.3 Anatomical Rhinoceros Phantom Model....76
6.3.1 Anatomical Layered Model....76
6.3.2 Anatomical Skeleton and Organ Models....89
6.3.3 Summary and Conclusion....91

6.4 Conclusion....91

Chapter 7....92
7. Rhinoceros Flank Agar Model Results....92

7.1 The 403 MHz and 2.4 GHz Agar Rhinoceros Flank Models....92

7.2 The 2.4 GHz Rhinoceros Flank Power Measurements 93

7.3 Conclusion 97

Chapter 8. 98
8. Summary and Conclusion 98

8.1 Achievement of Aims and Objectives 99

8.2 Recommendations 100
8.2.1 Internal Organs and Skeletal Structure 100
8.2.2 Wireless Charging 100
8.2.3 Measure Real Rhinoceros Tissue 100
8.2.4 Develop an Implant Device 100

Bibliography 101
APPENDICES 110

A. Outcomes Compliance of Project Objectives 111
A.1 Specific Aims Chapter Analysis 111
A.2 Additional Objective Completion 112

B. Location and Orientation of the Antenna Designs in the Rhinoceros and Cylindrical Simulation Models 114

C. Cylindrical Model Volume Calculations 116

D. Interview with Dr Johan Marais 117

E. Phantom Material Discussion 120
E.1 TX-150 Phantoms 120
E.2 Agar Phantoms 120
E.3 Acrylamide Phantoms 121
E.4 Hydroxyethyl Cellulose Phantoms 121
E.5 Gelatin Phantoms 122
E.6 Gellan Gum Phantoms 122
E.7 Carrageenan Phantoms 123
E.8 Alginate Phantoms 123

F. Additional Phantom Material Characteristics and Trends 124

G. Simulation Model Radiation Patterns 127
G.1 Rhinoceros Flank Model Radiation Patterns 127
G.2 Cylindrical Phantom Model Radiation Patterns 128

H. Directional Realised Gain of the Rhinoceros Model 131
H.1 Back Implantation 131
H.2 Chest Implantation 132
H.3 Neck Implantation 132

I. List of External Media 133

J. Permittivity Measurements of the 403 MHz, 910 MHz and 4.5 GHz Recipes 134

K. Decision Matrix and Similarity Criteria 142

L. Constituents of the Dielectric Properties of Specific Tissues 144
L.1 Constituents of 403 MHz Permittivity and Conductivity Approximations 144
L.2 Constituents of 910 MHz Permittivity and Conductivity Approximations 146
L.3 Constituents of 2.4 GHz Permittivity and Conductivity Approximations 148
L.4 Constituents of 4.5 GHz Permittivity and Conductivity Approximations 150

M. Characteristics of the Considered Generic Antenna Designs 152

N. Rhinoceros Phantom Material Recipes 154

O. Full List of Sample Measurements 156

Glossary

Units

V	*Volt, unit of voltage*
A	*Ampère, unit of current*
Ω	*Ohm, unit of resistance*
F	*Farad, unit of capacitance*
W	*Watt, unit of power*
S	*Siemens, unit of conductance*
Hz	*Hertz, unit of frequency*
J	*Joule, unit of energy*
T	*Tesla, unit of magnetic flux density*
g	*Grams, metric unit of mass*
Rad	*Radians, unit of angle*
dB	*Decibel, unit of power of electrical signals on a logarithmic scale*
l	*Litre, metric unit of capacity*
°C	*Celsius, scale of temperature*
m	*Milli,* 10^{-3}
µ	*Micro,* 10^{-6}
n	*Nano,* 10^{-9}
p	*Pico,* 10^{-12}
k	*Kilo,* 10^{3}
M	*Mega,* 10^{6}
G	*Giga,* 10^{9}

Abbreviations

ECC	*Electronic Communications Committee*
EIRP/ERP	*Effective Isotropic Radiated Power/ Effective Radiated Power*
EMI	*Electromagnetic Interference*
ERC	*European Research Council*
ETSI	*European Telecommunications Standards Institute*
FCC	*Federal Communications Commission*
FHSS	*Frequency Hopping Spread Spectrum*
GND	*Ground*
HEC	*Hydroxyethyl-cellulose*
ICASA	*Independent Communications Authority of South Africa*
IEEE	*Institute of Electrical and Electronic Engineers*
ISM	*Industrial, Scientific and Medical*
MICS	*Medical Implants and Communications Service*
MoM	*Method of Moments*
PCB	*Printed Circuit Board*
RFID	*Radio Frequency Identification*
SAR	*Specific Absorption Rate*
SRD	*Short Ranged Devices*
UTS	*Ultimate Tensile Strength*

Symbols

f	*Frequency, rate of occurrence within a specific period of time*
G	*Gain, an increase in the amount or rate*
R	*Resistance*
ρ	*Density*
e	*Thickness*
ε	*Permittivity, the ability to store electrical energy in an electric field*
σ	*Conductivity, degree to which a material conducts electricity*
p	*Polarization mismatch*
q	*Impedance mismatch*
α	*Attenuation constant, a value indicating the reduction in the strength of a signal*
γ	*Propagation constant, a value indicating the reproduction or spreading of a signal*
δ	*Skin depth, a measure of how closely electric currents flow along the surface of a material*
v	*Velocity*
V	*Volume*
$\underline{D}$	*Electric flux density, a measure of the strength of an electric field generated by a free electric charge*
$\overline{B}$	*Magnetic flux density, the amount of magnetic flux in an area perpendicular to the direction of the magnetic flux*
$\overline{E}$	*Electric field, a region around a charged particle or object within which a force would be exerted on other charged particles or objects*
$\overline{H}$	*Magnetic field, a region around a magnetic material or a moving electric charge within which the force of magnetism acts*
$\overline{J}$	*Current density, the amount of electric current flowing per unit cross-sectional area of a material*
$\overline{I}$	*Identity operator*
τ	*Mean relaxation time*

λ	*Wavelength, the distance between successive crests of a wave*
A	*Area*
P	*Power*
η	*Efficiency*
V	*Voltage*
I	*Current*

List of Figures

Figure 1: Examples of ETSI's saline human phantom models [10]. 13

Figure 2: Relative permittivity of 100 ml gelatine and agar solutions within the frequency range of 1 GHz to 6 GHz [16]. 21

Figure 3: Relative permittivity of 100 ml gelatine and sugar solutions within the frequency range of 1 GHz to 6 GHz [16]. 21

Figure 4: Relative permittivity of 100 ml gelatine and sugar (31 g) solution within the temperature range of 19°C to 26°C [16]. 22

Figure 5: Permittivity of salt (NaCl) as a function of ionic concentration for various temperatures [20]. 22

Figure 6: Permittivity of saline solution with various concentrations at 25°C from 0 GHz to 8 GHz [22]. 23

Figure 7: The specifications of the microstrip-fed planar elliptical monopole antenna (2.4 GHz). 25

Figure 8: The specifications of the printed inverted-F antenna (PIFA) (2.4 GHz)..... 26

Figure 9: The specifications of the planar trapezoidal monopole antenna (2.4 GHz). 27

Figure 10: The top view (Left) and side view (Right) of the circular pin-fed linearly polarised patch antenna (2.4 GHz). 28

Figure 11: Transmitting and receiving PCB antenna pairs. 29

Figure 12: E-field Comparison between the practical and simulated MFPEMA antenna..... 29

Figure 13: Example of the surface equivalence principle mesh [24]..... 31

Figure 14: Example of the MLFMM discretization of an electrically large model [25]. 32

Figure 15: Dimensions of the anatomically accurate rhinoceros computer simulation model. 33

Figure 16: Layered cylindrical rhinoceros computer simulation model. 33

Figure 17: Layered anatomically accurate rhinoceros computer simulation model. 33

Figure 18: Dimensions of the layered cylindrical phantom computer simulation model. 34

Figure 19: Individual layers of the anatomically accurate rhinoceros computer simulation model..... 34

Figure 20: Individual layers of the cylindrical rhinoceros computer simulation model. 34

Figure 21: Position of the back and chest implantation in the cylindrical phantom model. 35

Figure 22: Position of the neck implantation in the cylindrical phantom model. 35

Figure 23: Position of the back implantation in the anatomical model. 35

Figure 24: Position of the neck implantation in the anatomical model. 35

Figure 25: Position of the chest implantation in the anatomical model. 36

Figure 26: Weighting factors of animals contributing to rhinoceros tissue approximations. 37

Figure 27: Weighing of the dry ingredients. 41

Figure 28: Addition of the distilled water. 42

Figure 29: (a) Magnetic stirrer and (b) sterilisation of the sample materials within an autoclave. 42

Figure 30: Laminar flow machine with sterilized petri dishes. 43

Figure 31: Sterilized sample materials. 43

Figure 32: Completed agar plates of phantom material recipes. 43

Figure 33: Equivalent circuit of the broadband measurement probe [34]. 44

Figure 34: Room temperature during phantom material permittivity measurements. 48

Figure 35: Dielectric phantom recipe generator permittivity error. 50

Figure 36: Polynomial regression function recipe permittivity error. 50

Figure 37: Closest point incrementation recipe permittivity error. 51

Figure 38: Closest point polynomial regression recipe permittivity error. 51

Figure 39: Permittivity values of the 2.4 GHz recipes. 52

Figure 40: Permittivity values of the 2.4 GHz recipes Br. 53

Figure 41: Permittivity error of the 2.4 GHz recipes with recipe error margins. 54

Figure 42: Permittivity values of the 2.4 GHz closest point polynomial regression recipes with recipe error margins. 54

Figure 43: Measured permittivity values of the 403 MHz heart and lung recipes. 57

Figure 44: Permittivity error of the 403 MHz heart and lung recipes with aggregate error margins. 57

Figure 45: Permittivity error of the 403 MHz heart and lung recipes with recipe error margins. 58

Figure 46: The estimated density of the rhinoceros phantom materials at the specified frequencies. 59

Figure 47: Salt requirements for the 100 ml recipes for the specified frequencies. 60

Figure 48: The estimated thermal properties of the phantom materials for the 100 ml recipes across the specified frequencies. 61

Figure 49: The permittivity of the sample materials for the 100 ml recipes across the specified frequencies. 62

Figure 50: Loss tangent measurements of the 100 ml 4.5 GHz blood recipe samples. 63

Figure 51: Permittivity measurements of the 100 ml 4.5 GHz blood recipe samples. 63

Figure 52: Average loss tangent of the 100 ml 4.5 GHz blood recipe samples. 64

Figure 53: Average permittivity of the 100 ml 4.5 GHz blood recipe samples. 64

Figure 54: Phantom leg concept model. 65

Figure 55: Rhinoceros flank (slab) phantom model. 66

Figure 56: The transparency and consistency of the agar samples. 67

Figure 57: Configuration of the rhinoceros flank phantom model. 68

Figure 58: SAR values of the MFPEMA Shadwick and weighted average flank models. 69

Figure 59: SAR values of the PIFA Shadwick and weighted average flank models. 71

Figure 60: Configuration of the cylindrical phantom back implantation model. 73

Figure 61: Configuration of the cylindrical phantom neck implantation model. 73

Figure 62: Configuration of the anatomical phantom back implantation model. 76

Figure 63: Configuration of the anatomical phantom chest implantation model. 77

Figure 64: Configuration of the anatomical phantom neck implantation model 77

Figure 65: Realised gain of the Shadwick (left) and weighted average (right) anatomical rhinoceros back model [MFPEMA pair]. 78

Figure 66: Realised gain of the Shadwick (left) and weighted average (right) anatomical rhinoceros neck model [MFPEMA pair]. 78

Figure 67: Electric field of the MFPEMA in the back location for the Shadwick approximation. 79

Figure 68: Electric field of the MFPEMA in the back location for the weighted average approximation. 79

Figure 69: Electric field of the MFPEMA in the neck location for the Shadwick approximation. 79

Figure 70: Electric field of the MFPEMA in the neck location for the weighted average approximation. 80

Figure 71: Electric field of the MFPEMA in the back location for the Shadwick [left] and weighted average [right] approximations. 80

Figure 72: Electric field of the MFPEMA in the neck location for the Shadwick [left] and weighted average [right] approximations. 80

Figure 73: SAR of the MFPEMA propagating through the back, chest and neck of the Shadwick and weighted average models in the y-direction. 81

Figure 74: Realised gain of the Shadwick (left) and weighted average (right) anatomical rhinoceros back model [PIFA pair] 83

Figure 75: Realised gain of the Shadwick (left) and weighted average (right) anatomical rhinoceros chest model [PIFA pair]. 83

Figure 76: Realised gain of the Shadwick (left) and weighted average (right) anatomical rhinoceros neck model [PIFA pair] 83

Figure 77: Electric field of the PIFA located in the back location for the Shadwick approximation. 84

Figure 78: Electric field of the PIFA located in the back location for the weighted average approximation. 84

Figure 79: Electric field of the PIFA in the chest location for the Shadwick approximation 85

Figure 80: Electric field of the PIFA in the chest location for the weighted average approximation. 85

Figure 81: Electric field of the PIFA in the neck location for the Shadwick approximation. 85

Figure 82: Electric field of the PIFA in the neck location for the weighted average approximation. 86

Figure 83: Electric field of the PIFA pair through the back of the Shadwick [left] and weighted average [right] approximation models. 86

Figure 84: Electric field of the PIFA pair through the chest of the Shadwick [left] and weighted average [right] approximation models. 86

Figure 85: Electric field of the PIFA pair through the neck of the Shadwick [left] and weighted average [right] approximation models. 87

Figure 86: SAR of the PIFA propagating through the back, chest and neck of the Shadwick and weighted average models in the y-direction. 87

Figure 87: Rhinoceros skeletal model. 89

Figure 88: Combination of the skeletal and anatomical rhinoceros models. 89

Figure 89: Rhinoceros organ models. 90

Figure 90: Combination of the organ and anatomical rhinoceros models. 90

Figure 91: The deconstructed slabs of the 403 MHz rhinoceros flank model. 92

Figure 92: The mould used to cast the 2.4 GHz rhinoceros flank model. 93

Figure 93: The partially filled container of the 2.4 GHz rhinoceros flank model. 93

Figure 94: The practical configuration of the 2.4 GHz cable loss measurements. 94

Figure 95: The air gap (foam) power loss measurements of the 2.4 GHz MFPEMA pair. 94

Figure 96: The T-incision on the side of the 2.4 GHz rhinoceros flank model with the connector cable and implanted antenna. 95

Figure 97: The configuration of the power loss measurement of the 2.4 GHz rhinoceros flank model [Left: 10 mm foam air gap above; Right: 10 mm foam air gap above and below]. . 96

Figure 98: Coordinates and angle of the back implantation in the anatomical phantom model. 114

Figure 99: Coordinates and angle of the chest implantation in the anatomical phantom model. 114

Figure 100: Coordinates and angle of the neck implantation in the anatomical phantom model. 114

Figure 101: Coordinates and angle of the back implantation in the cylindrical model. 114

Figure 102: Coordinates and angle of the neck implantation in the cylindrical model. 115

Figure 103: Coordinates and angle of the chest implantation in the cylindrical model. 115

Figure 104: The estimated density of the rhinoceros phantom materials at the specified frequencies. 124

Figure 105: Salt requirements for the 100 ml alternative recipes for the specified frequencies. 124

Figure 106: Sugar requirements for the 100 ml alternative recipes for the specified frequencies. 125

Figure 107: The estimated thermal properties of the phantom materials for the alternative 100 ml recipes across the specified frequencies. 125

Figure 108: The permittivity of the sample materials for the alternative 100 ml recipes across the specified frequencies. 126

Figure 109: Sugar requirements for the 100 ml recipes for the specified frequencies. 126

Figure 110: Realised gain of the embedded MFPEMA: Shadwick model (left) and weighted average model (right). 127

Figure 111: Realised gain of the embedded PIFA: Shadwick model (left) and weighted average model (right). 127

Figure 112: Realised gain of the embedded CPFLPPA: Shadwick model (left) and weighted average model (right). 128

Figure 113: Realised gain of the embedded MFPEMA [Back]: Shadwick model (left) and weighted average model (right). 128

Figure 114: Realised gain of the embedded MFPEMA [Neck]: Shadwick model (left) and weighted average model (right). 129

Figure 115: Realised gain of the embedded PIFA [Back]: Shadwick model (left) and weighted average model (right). 129

Figure 116: Realised gain of the embedded PIFA [Neck]: Shadwick model (left) and weighted average model (right). 130

Figure 117: Back implantation of MFPEMA: Shadwick model (Left) and weighted average model (Right). 131

Figure 118: Back implantation of PIFA: Shadwick model (Left) and weighted average model (Right). 131

Figure 119: Chest implantation of PIFA: Shadwick model (Left) and weighted average model (Right). 132

Figure 120: Neck implantation of MFPEMA: Shadwick model (Left) and weighted average model (Right). 132

Figure 121: Neck implantation of PIFA: Shadwick model (Left) and weighted average model (Right). 132

Figure 122: Measured permittivity values of the 403 MHz recipes. 134

Figure 123: Measured permittivity values of the 910 MHz recipes. 134

Figure 124: Permittivity values of the 4.5 GHz recipes..... 135

Figure 125: Permittivity values of the 910 MHz closest point polynomial regression recipes. . 135

Figure 126: Permittivity values of the 4.5 GHz closest point polynomial regression recipes.... 136

Figure 127: Permittivity error of the 403 MHz recipes with aggregate error margins. 136

Figure 128: Permittivity error of the 910 MHz recipes with aggregate error margins. 137

Figure 129: Permittivity error of the 4.5 GHz recipes with aggregate error margins. 137

Figure 130: Permittivity error of the 910 MHz closest point polynomial regression recipes with aggregate error margins. 138

Figure 131: Permittivity values of the 4.5 GHz closest point polynomial regression recipes with aggregate error margins. 138

Figure 132: Permittivity error of the 403 MHz recipes with recipe error margins. 139

Figure 133: Permittivity error of the 910 MHz recipes with recipe error margins. 139

Figure 134: Permittivity error of the 4.5 GHz recipes with recipe error margins. 140

Figure 135: Permittivity values of the 910 MHz closest point polynomial regression recipes with recipe error margins. 140

Figure 136: Permittivity values of the 4.5 GHz closest point polynomial regression recipes with recipe error margins. 141

List of Tables

Table 1: Mechanical properties of white rhinoceros skin [1]. 4

Table 2: Specific mechanical test results for white rhinoceros skin samples [1]. 5

Table 3: Mechanical properties of porcine skin [2]. 5

Table 4: Rhinoceros skin histology [1]. 7

Table 5: Dielectric and electrical properties of collagen-chitosan films [4] [3]. 7

Table 6: The dielectric properties of 0.1M NaCl [7]. 12

Table 7: Recipes for muscle and brain simulating liquids [6]. 14

Table 8: Tissue simulating liquid dielectric properties (403.5 MHz) [6]. 14

Table 9: Actual human tissue dielectric properties [11]. 14

Table 10: Critical parameters of phantoms in different radio frequency thermal modalities [13]. 15

Table 11: The advantages and limitations of popular and suggested phantom material gelling agents [13]. 17

Table 12: Characteristics of the selected antenna designs. 24

Table 13: Detailed design specifications of the microstrip-fed planar elliptical monopole antenna (2.4 GHz). 25

Table 14: Detailed design specifications of the printed inverted-F antenna (PIFA) (2.4 GHz). 26

Table 15: Detailed design specifications of the planar trapezoidal monopole antenna (2.4 GHz). 27

Table 16: Detailed design specifications of the circular pin-fed linearly polarised patch antenna (2.4 GHz). 28

Table 17: S11 Measurements of the practical PCB antenna pairs. 29

Table 18: Rhinoceros tissue permittivity and conductivity approximations. 38

Table 19: Sigma-Aldrich cost of ingredients (As seen on 14 September 2016). 40

Table 20: Measured permittivity of the agar samples prepared according to the 403 MHz phantom material recipes. 45

Table 21: Measured permittivity of the agar samples prepared according to the 910 MHz phantom material recipes. 45

Table 22: Measured permittivity of the agar samples prepared according to the 2.4 GHz phantom material recipes. 46

Table 23: Measured permittivity of the agar samples prepared according to the 4.5 GHz phantom material recipes. 46

Table 24: Measured permittivity of the agar samples prepared according to the closest point polynomial regression method recipes. 47

Table 25: Extract - Measured dielectric properties of phantom materials. 56

Table 26: Measured permittivity of the 403 MHz heart and lung phantom material recipes. 58

Table 27: Ingredient requirements for phantom leg model. 65

Table 28: Ingredient requirements for rhinoceros flank model. 66

Table 29: Specific absorption rate of the individual phantom layers (Flank - MFPEMA). 70

Table 30: The IEEE and ICNIRP SAR limitations for human tissue exposure [36]. 70

Table 31: Specific absorption rate of the individual phantom layers (Flank - PIFA). 72

Table 32: Specific absorption rate of the individual phantom layers (Cylinder - MFPEMA). 74

Table 33: Specific absorption rate of the individual phantom layers (Cylinder - PIFA). 75

Table 34: Specific absorption rate and power loss of the individual phantom layers (Rhinoceros back – MFPEMA). 82

Table 35: Specific absorption rate and power loss of the individual phantom layers (Rhinoceros back - PIFA). 88

Table 36: Received power through the 2.4 GHz rhinoceros flank phantom (output = 0 dBm). 95

Table 37: Received power through the 2.4 GHz rhinoceros flank phantom (output = +12 dBm). 96

Table 38: Decision matrix for dielectric property weighting factors. 143

Table 39: Prototype antenna considerations. 152

Table 40: Phantom recipes for biological tissue A. 154

Table 41: Phantom recipes for biological tissue B. 155

Table 42: Measured dielectric properties of rhinoceros phantom recipes (24 degC, 100 ml) A. 156

Table 43: Measured dielectric properties of rhinoceros phantom recipes (24 degC, 100 ml) B. 158

Layout of Thesis

Chapter 1: Introduction

This chapter clearly identifies the aims of the project and the objectives required to accomplish said aims, whilst also providing the necessary background information regarding rhinoceros poaching.

Chapter 2: Literature Review

This chapter encapsulates the information regarding the mechanical properties of rhinoceros skin, the availability of the frequency spectrum, tissue simulating materials and common phantom recipes. It also elaborates on viable implantable antenna designs, including a comparison between their measured and simulated characteristics.

Chapter 3: Computer Simulation Models

This chapter elaborates on the configuration of the computer simulations and the proposed models, including a cylindrical phantom model and an anatomically accurate rhinoceros model. Three viable locations for implantation are identified.

Chapter 4: Approximation of Rhinoceros Tissue Permittivity and Conductivity

This chapter illustrates the calculated permittivity and conductivity approximations of the rhinoceros tissues for various frequencies and elaborates on two methods used to approximate the dielectric properties of rhinoceros tissue.

Chapter 5: Agar Samples of Rhinoceros Tissue

This chapter elaborates on the phantom recipe calculation methods and the phantom material samples, including the cost of fabrication and their measured dielectric properties. The repeatability of samples are indicated in the form of average error rates between the measured and theoretical permittivity values. The general phantom material characteristics and trends are compared to those found in literature. New phantom models are proposed based on the findings of the project thus far.

Chapter 6: Computer Simulation Results

This chapter illustrates the findings of the computer simulations in terms of the realised gain, power efficiency and specific absorption rate of the radiation of the implantable antennas used within the various simulation models.

Chapter 7: Rhinoceros Flank Agar Model Results

This chapter elaborates on the practical measurements conducted on a 2.4 GHz rhinoceros flank agar model and compares the results to those of the corresponding computer simulation.

Chapter 9: Conclusion

This chapter summarizes the findings of the project and confirms the accomplishment of all specific aims and objectives. Further recommendations are made for future endeavours.

Chapter 1.

1. Introduction

1.1 Background

Although rhinoceroses have few natural predators, the African black rhinoceros (*Diceros bicornis*) and the African white rhinoceros (*Ceratotherium simum*) are nearing extinction in the wild due to active poaching by humans. The prevention of this illegal practice is impeded by the vastness of the rhinoceroses' habitat. It is often the case that the mutilated corpses of rhinoceroses are only discovered several days after their horns have been removed. Many attempts have been made to monitor and study these animals using ex-vivo attached devices. These are often unsuccessful due to the anatomical structure of the rhinoceros, their regular exposure to confrontational impact during intraspecific territorial combat and the difficulty of achieving wireless communication with such devices. Furthermore, little is known about the physiological, social and migratory behaviour of rhinoceroses. This inhibits the optimization of devices specifically designed for monitoring these animals in the wild.

To design better ex-vivo wireless sensors, as well as new in-vivo sensors, the electromagnetic properties of the rhinoceros body must be, at least approximately, known. Active radio frequency implantation and animal telemetry devices utilize frequencies ranging from the low kilohertz region (30 kHz) to the higher megahertz region (915 MHz). Typically, the lower frequencies are preferred in wildlife telemetry devices due to the advantage of longer range. However, due to the abnormally thick skin of rhinoceroses, higher frequencies need to be utilized owing to their superior penetrative ability. Currently, the only direct means of comparing frequencies and testing devices are live field tests, using either external attachments or implantation by means of surgery. This is practically difficult and potentially dangerous for both the researchers and animals.

1.2 Overall Aims

It is the aim of this project to develop both a computational and a phantom model that replicates the dielectric properties of the body of a rhinoceros. These models will be used to aid the design and development of new animal-attached and implanted sensors to support anti-poaching initiatives. They will provide a test environment for experimental in-vivo and ex-vivo devices used for tracking and monitoring rhinoceros movement, as well as physiology (such as heartrate). The intended purpose of such implantation devices is to transmit data through the thick hide of a rhinoceros. Thus, the models should sufficiently portray the radiation attenuation of rhinoceros tissue. Models for various frequencies within the Industrial, Scientific and Medical (ISM) bands must be investigated to accommodate a broad range of in-vivo and ex-vivo antenna designs.

1.3 Specific Aims

The specific aims of this project are as follows:

i) Determine the approximate dielectric properties of rhinoceros tissue.
ii) Identify viable and common frequency ranges of operation for implantable sensors.
iii) Identify viable antenna designs for implantable sensors.
iv) Identify viable points of implantation within a rhinoceros.
v) Identify the limitations or parameters of a rhinoceros implantation device.
vi) Deliver a computer simulation model.
vii) Deliver a means of creating a phantom model for practical experimentation.
viii) Practically measure the dielectric characteristics of the phantom models.
ix) Compare results of the computational and physical phantom models.
x) Apply the models to the analysis of an implantable sensor.

1.4 Objectives

The specific aims (numbered correspondingly) will be addressed by achieving the following objectives:

i) Research the mechanical properties of rhinoceros skin and determine its composition. Calculate the overall permittivity of the skin based on the permittivity of its individual constituents. Create a second model for comparison by means of a meta-analysis based on animals with similar physical characteristics to rhinoceroses. The permittivity of the second model is to be calculated from the permittivity of the constituent animals' contribution to a specific organ or tissue by applying a weighted average, favouring animals with greatest similarity to rhinoceroses.

ii) Research the standards for local (South Africa) and international use of radio frequency devices as stipulated by the governing regulatory authorities. Investigate viable frequency bands and select frequencies of operation based on their availability and those commonly used within the Industrial, Scientific and Medical (ISM) band in active tracking and monitoring devices.

iii) Research active implanted antenna designs used for animal monitoring and tracking. Identify candidates that comply with the specifications advised by a practicing veterinary surgeon specializing in large, thick-skinned mammals, particularly rhinoceroses. Apply a process of elimination based on antenna characteristics such as gain, radiation pattern and return loss. Confirm the theoretical selection of viable antenna designs by means of simulation and practical measurement.

iv) Research the anatomy of the rhinoceros with respect to the thickness of the skin, fat and muscle, as well as the size of the internal organs. Consult a practicing veterinary surgeon specializing in large, thick-skinned mammals, particularly rhinoceroses.

v) Research active implantation devices used for tracking and monitoring wildlife and identify commonly used materials, as well as limitations pertaining to size. Consult a practicing veterinary surgeon specializing in large, thick-skinned mammals, particularly rhinoceroses.

vi) Research active phantom body simulations and procedures. Research the anatomy of the rhinoceros pertaining to the thickness of the skin, fat and muscle, as well as the size of the internal organs. Consult a practicing veterinary surgeon specializing in large, thick-skinned mammals, particularly rhinoceroses. Use computer aided design software to sculpt both simplified and anatomically accurate phantom models that are compatible with electromagnetic computational software such as FEKO and apply the dielectric properties calculated in objective (i).

vii) Apply objective (v) to identify commonly used phantom model material. Select materials based on the suitability of their mechanical properties in conjunction with attributes such as their availability, cost, ease of use and safety. Establish recipes for individual phantom tissues for various frequencies within the selected range and create samples to empirically validate their respective dielectric properties.

viii) Apply the selected antenna designs of objective (vii) to the simulation models and investigate the model characteristics with regards to propagation, power loss and the specific absorption rate (SAR) of the various tissues.

ix) Evaluate the agreement of the models based on their measured and simulated results with regards to characteristics such as power efficiency.

x) Evaluate different model configurations to identify most viable solution.

1.5 Contributions

The work presented in this thesis makes the following scientific contributions.

1. EM Rhinoceros Simulation Model:

   A numerical model of the rhinoceros body including the epidermis, dermis, fat, muscle, blood, organs and skeleton, is developed. No such model was available at the time of writing.

2. Agar Rhinoceros Phantom:

   Phantom recipes that can be used to approximate real rhinoceros tissue in practical experiments are designed. No such model was available at the time of writing.

3. Analysis of the Numerical and Agar Models:

   The above two models are validated by means of comparative assessment.

4. Evaluation of In-vivo to Ex-vivo Communication:

   An analysis is performed to determine the best implantation location and antenna type for communicating between in-vivo and an ex-vivo sensor located on the back leg of a rhinoceros.

Additional smaller contributions and objectives are presented in Appendix A (page 111).

Chapter 2.

2. Literature Review: Background

This chapter identifies and elaborates on the mechanical properties of rhinoceros skin, the available frequency spectrum, tissue simulating materials and common phantom recipes. The selection of the implantation antenna design, along with some initial comparisons between the simulated and practically measured antennas are discussed.

2.1 Tissue Characteristics of a White Rhinoceros

Shadwick et al [1] investigated the structure and mechanical design of rhinoceros dermal armour, which "is three times thicker than predicted allometrically, and it contains a dense and highly ordered three-dimensional array of relatively straight and highly cross-linked collagen fibres". This investigation yielded a description of the mechanical strengths of rhinoceros skin with specific reference to the dorsolateral areas and indicated that the hide of a rhinoceros is well adapted to cushion forceful blows from conspecific horn attacks. Table 1 indicates the results of the mechanical stress tests conducted by these authors on skin samples from the back and flanks (referred to as dorsolateral skin), and belly of a deceased adult white rhinoceros known as Duncan (at least 28 years of age, weighing 1600 kg). At the time of Duncan's death at Calgary Zoo (Alberta, Canada), he was lighter than the average field mass for adult bulls, which is usually in the range of 1800 kg to 2500 kg.

Table 1: Mechanical properties of white rhinoceros skin **[1]**.

Dorsolateral Skin	
Properties	**Value**
Elastic Modulus	240 MPa (High)
Tensile Strength	30 MPa (High)
Breaking Strain	0.24 (Low)
Breaking Energy	3 MJm^{-3} (High)
Work of Fracture	78 kJm^{-2}
Average Skin Breaking Point	
Stress	170 MPa
Strain	0.7

Standard dumbbell shapes were used during skin tensile tests to ensure that failure or rupture occurred in the central sections of the samples. The samples were measured with vernier calipers prior to testing to establish the initial thickness, width and distance between parallel markings on the central sections of the dumbbell shape. A tensometer was used to stretch the samples at rates of 5 mm/min and 10 mm/min respectively. Numerous stable force-extension cycles consisting of extensions to strains of approximately 0.10 were recorded, prior to stretching the samples to their rupturing point. Controlled tear tests and compressive tests were also conducted to establish the work of fracture, compressive strength, stiffness and mode of compressive failure of the skin samples. Table 2 indicates the results of these mechanical tests.

Table 2: Specific mechanical test results for white rhinoceros skin samples **[1]**.

Collagen Fibre Morphology in Rhinoceros Skin				
Property	**Dorsolateral**		**Belly**	
	Mean	**+/- Standard Error of Mean**	**Mean**	**+/- Standard Error of Mean**
Fibre Diameter/mm				
Superficial	0.07	0.01	0.06	0.01
Deep	0.10	0.02	0.20	0.02
Crimp Period/mm	-	-	0.82	0.01
Mechanical Properties of Skin: Uniaxial Tensile Tests				
Property	**Dorsolateral**		**Belly**	
	Mean	**+/- Standard Error of Mean**	**Mean**	**+/- Standard Error of Mean**
Breaking Stress/MPa	30.5	1.08	14.5	1.59
Breaking Strain	0.24	0.01	0.33	0.02
Breaking Energy/MJm^{-3}	2.89	0.16	3.28	0.43
Elastic Modulus/MPa	237.3	9.75	107.8	+/- 13.9
Work of Fracture/kJm^{-2}				
Superficial	77.6	4.35	-	-
Deep	43.0	2.3	-	-
Compressive Properties of Rhinoceros Skin				
Property	**Dorsolateral**		**Belly**	
	Mean	**+/- Standard Error of Mean**	**Mean**	**+/- Standard Error of Mean**
Failure Stress/MPa	172.7	7.5	169.1	9.4
Failure Strain	0.68	0.01	0.73	0.02
Failure Mode	Explosive		Non-Explosive	
Compressive Stiffness/MPa	700	5.3	667	9.6

Table 3: Mechanical properties of porcine skin **[2]**.

Skin Location	**Strain Rate**	**Ultimate Tensile Strength (UTS) [MPa]**	**Failure Strain (%)**	**Elastic Modulus [MPa]**
Back and Abdomen	Quasistatic: 50 mm/min	7 - 30	31 - 53	-
Abdomen	Quasistatic: 0.25 - 10%/s	0.25 - 1.0	123 - 126	0.9 - 4.2
Back	Dynamic: 1700 - 3500/s	0.1 - 0.8	16 - 30	-
Rump	Dynamic: 40 - 4000/s	25 - 57	40 - 60	-
Jowl	Dynamic: 1000 - 5700/s	1.9 - 3	24 - 35	-

Porcine and human skin are very similar in terms of their mechanical properties and are often used as a frame of reference for the comparison of skin properties. According to mechanical tests performed by Gallagher et al [2] on human skin, the mean ultimate tensile strength (UTS) was 27.2 ± 9.3 MPa, the mean strain energy was 4.9 ± 1.5 MJ/m^3, the mean elastic modulus was 98.97 ± 97 MPa and the mean failure strain was 25.45 ± 5.07%. Gallagher compared these results to those of porcine skin, which had the mechanical properties indicated in Table 3. By comparing the results from Shadwick to those of Gallagher, it is evident that rhinoceros dermis is much more durable than human or porcine skin. Specifically, the elastic modulus of rhinoceros dermis is 2.7 MPa higher than human skin and can withstand up to 12.1 MPa more pressure with regards to its tensile strength. Shadwick suggests that the superior strength of the

rhinoceros dermis is caused by its dense collagen content, which could explain the inaccurate predictions of allometric calculations pertaining to the thickness of rhinoceros skin. Allometric equations for calculating total skin mass (M_S), surface area (A) and average skin thickness (t) were used to theoretically estimate rhinoceros skin properties, which were then compared to the practically measured values. The allometric equations are as follows [1]:

Total skin mass:	M_S	$= 0.106*M^{0.94}$ [kg]
Surface area:	A	$= 0.111*M^{0.62}$ [m^2]
Average skin thickness:	t	$= 0.868*M^{0.29}$ [mm] (Assuming a density of 1.1 ton/m^3)

M represents the body mass of the animal. The average skin thickness (Volume/Area) was calculated as follows:

$$t = 0.868(1600)^{0.29} = 7.374 \text{ mm}$$

The theoretically predicted value indicated above did not portray an accurate estimation of the practically measured thickness of the rhinoceros skin (indicated below):

Actual thickness:	Back and Flanks	= 25 mm
	Belly	= 15 mm

Shadwick et al [1] investigated the collagenous properties of the white rhinoceros' skin by means of histological processes, in order to establish why the theoretical values differ so drastically from the practically measured results. These investigations indicated the presence of thick collagen fibres with variations in orientation and dimensions in correlation to different positions and depths. The preparations involved fixing the tissue samples in 10% formalin (by volume) and sectioning them on a freezing microtome for observational purposes. Other freeze-dried samples were weighed and hydrolysed in 6N HCL for 24 hours, prior to be being subjected to colorimetric hydroxyproline assay to determine the collagen content of the rhinoceros dermis.

Collagen, which is a stiff protein constituting approximately 70 – 80% of dry mammalian dermis, is the basic material found in various organs and tissues that provide structural integrity. Shadwick et al [1] qualitatively assessed intermolecular collagen cross-linking by digesting the skin collagen in cyanogen bromide of which the resulting peptides were separated with a sodium dodecyl-sulphate polyacrylamide gel, by a process known as electrophoresis. The results of these experiments are illustrated in Table 4 and the dielectric properties of collagen are illustrated in Table 5. The complex dielectric functions of the collagen, chitosan and collagen-chitosan blend films indicated in Table 5 were acquired by Lima et al [3] with the aid of a HP 4291A Material Impedance Analyzer and a HP 4194 Impedance Analyzer (jointly covering the 100 Hz to 1.8 GHz region).

Table 4: Rhinoceros skin histology **[1]**.

Collagen Fibre Diameter Averages	
Section of Rhinoceros Dermis	**Average Diameter (um)**
Dorsum and Flanks (Superficial fibres)	70
Dorsum and Flanks (Deep fibres)	100
Belly (Superficial fibres)	60
Belly (Deep fibres)	200
Collagen Characteristics of Dermis	
Component	**Quantity (%)**
Water	60.9 (+/- 1.2 %)
Collagen of dry fraction	85
Collagen of tissue wet mass	33.2
Remarks	
· Collagen present in dermis is primarily Type I. · Peptide α1-CB6 is greatly involved in extracellular cross-linking between collagen models. · α1-CB6 is incorporated into large molecular mass of polymers of CB6 (and other peptides) during maturation. · Post maturation, the collagen of in the rhinoceros dermis has an abundance of high molecular peptides and essentially no monomeric α1-CB6.	

Table 5: Dielectric and electrical properties of collagen-chitosan films **[4] [3]**.

Dielectric Properties of Collagen						
Dielectric constant (Ambient temperature)			4.5 (Approx.)			
Dielectric constant (After desorption)			2.3 (Approx.)			
Collagen and Chitosan Characteristics						
Samples	**Density (ρ) [Kg/m^3]**	**Thickness (*e*) [um]**	**1 MHz ($\varepsilon/\varepsilon_0$)**	**1 GHz ($\varepsilon/\varepsilon_0$)**	**DC Conductivity (σ_{DC}) @ 300 K [$(\Omega m)^{-1}$]**	**Temperature (T_D) [°C]**
CH100	1078.45	40.8	3.94	2.71	3.4×10^{-17}	60.75
CH90CO10	1192.4	68	3.35	2.29	1.3×10^{-17}	50.31
CH50CO50	977.71	83.4	2.68	2.05	9.2×10^{-18}	75.59
CH10CO90	936.53	86.4	2.96	2.41	5.2×10^{-18}	58.73
CO100	670.76	55.9	2.60	2.3	2.4×10^{-19}	73.75

As concluded by Shadwick et al [1], the results indicate that the superior strength of rhinoceros skin is not solely due to its greater thickness, but also due to its dense and cross-linked collagen fibre content. The result is that it is a much harder material to penetrate, both in terms of physical incisions and signal propagation, which influences the characteristics and dielectric properties of the implantation environment. Later in this work, the mechanical properties of rhinoceros skin and the dielectric characteristics of collagen are utilized in computer simulations to determine the effect of these materials on the propagation of radio waves. These characteristics also contributed to the design of a physical rhinoceros phantom with properties estimated to be similar to those of an actual rhinoceros. The computer simulation and phantom experiments are discussed in Chapter 3 (page 31) and in Chapter 5 (page 40) of this report respectively.

2.2 Availability of Frequency Spectrum for Wireless Communication

The use of wireless technology has become so widespread, that the availability of unused, beneficial or practical frequency bands has become increasingly limited. Thus, the use of frequency bands in the frequency spectrum is regulated by authorities around the world, such as the Independent Communications Authority of South Africa (ICASA), as well as regulatory organizations in Europe and the United States. These regulations ensure that interference

between wireless communications systems is kept to a minimum and it also identifies suitable frequency bands for various applications, including suggestions for implantable antenna designs.

Regulatory organizations often harmonise frequencies used at global, national and regional levels in order to constrain spectrum allocations for specific purposes. These agreements are beneficial to manufacturers and antenna designers, since the frequency of operation is a fundamental design aspect which can greatly influence the characteristics of an antenna. Although regulatory organizations often differ with regards to their assignment of frequency bands for specific applications, the use of wireless medical implanted devices in a license exempt environment is permitted, if it satisfies one of the following conditions [5]:

i) The wireless medical device operates within a spectrum specifically identified for medical implant devices, or

ii) The wireless medical device operates within a spectrum identified for exempt use more generally, thus the spectrum would be shared between the medical devices and other applications/users.

European regulatory systems implement the Short Ranged Devices (SRD) regime, which allocates specific frequency bands to devices that communicate only over a few hundreds of meters, on condition that they do not interfere with other devices using the same spectrum or claim protection from interference from these other devices. Thus low power radiation and other specified mitigation measures need to be incorporated to allow co-existence between spectrum users. The European Research Council (ERC) and the Electronic Communications Committee (ECC) have identified the following two bands for the use of applications in implanted devices [5]:

1. "Active Medical Implants and Their Associated Peripherals."

This option allows for a relatively predictable interference environment, although the number of operational frequency bands is limited. The only requirements for co-existence are between the medical devices and the primary users of the bands. Thus exempted devices are not subjected to any other forms of interference.

2. "Non-Specific Short Range Devices."

This option allows medical devices to operate within a wider selection of frequency bands, although these bands would be shared with numerous other license exempt implementations such as RFID tags, WiFi networks (802.11 standards) and Bluetooth. If this option is selected, special precautions must be implemented to ensure sufficient protection and isolation from the interferences generated from other propagation sources. Due to the frequency of new developments in this market, the environment is unpredictable in terms of the interference that may be expected within these frequency bands.

Other available frequencies are those specified in the Industrial, Scientific and Medical (ISM) bands, which is similar to the European SRD bands in the sense that users do not cause interference to other users or claim protection from the interference caused by other users. The long-term interference consequences of this environment are therefore unpredictable and thus the Federal Communications Commission (FCC) of the United States has established the "Medical Device Radio Communications Service" or "MedRadio", which ranges from 401 MHz to 457 MHz and is used for medical communications devices. The full list of the various frequency bands that are available in Europe and in the United States respectively, can be

viewed in the external media as referred to in Appendix I (page 133). The frequency bands regulated by ICASA are also presented here.

2.2.1 Implant Antenna Frequency Band Candidates

Candidate frequency bands for the development of implant medical devices are constrained by various factors, including economic and social influences from other countries. Since the proposed antenna design only has to satisfy requirements for use in countries where the rhinoceros natively roams, the antenna design does not have to be optimised for the frequency bands that are available in Europe or in the United States. However, this could be taken into consideration in order to expose potential economic benefits and to allow the tracking of animals indigenous to other countries. Other practical factors such as skin penetration losses and body tissue losses also need to be considered. According to research conducted by C. Conran into antenna designs for wireless medical implants [5], the use of frequencies above 2.4 GHz (which is one of the ISM band frequencies) should be avoided to mitigate these losses. Taking the above-mentioned aspects into account, the following frequency bands were considered viable candidates for medical implant devices:

- 401 - 406 MHz:

Although the centre frequencies of this band (402 - 405 MHz) are allocated to medical implants with channels up to 300 kHz wide, the use of frequencies closer to the boundaries of the band are only permitted under restrictive conditions. The entire 5 MHz band must be shared with meteorological devices, but due to their scarcity the likelihood of interference is quite low. This band is unavailable to other exempted devices, which contributes to the level of protection from interference. The United States and Europe share harmonised frequency bands for this region of operation, making this band a more appealing option.

- 863 - 915 MHz:

This frequency band is a compromise between the non-specific SRD band in Europe (between 863 - 870 MHz, which has a high likelihood of interference) and the ISM band used in the United States (between 902 - 928 MHz). Although the band is quite broad, a single antenna could be designed to cover both spectra, as long as mitigation techniques such as Direct Sequence Spread Spectrum (DSSS), Listen Before Talk (LBT) and Adaptive Frequency Agility (AFA) are applied. However, medical implant devices will not be protected from interference and the available bandwidth is quite low.

- 2.4 - 2.5 GHz:

This frequency band incorporates non-specific SRD bands (such as the 2400 - 2483.5 MHz spectrum) and bands utilised by active wireless medical implants (such as the 2483.5 - 2500 MHz spectrum). Due to the lower section of the band (below 2483.5 MHz) coinciding with the frequencies used in the SRD band, the likelihood of interference is high. In Europe and the United States, medical implants are permitted to use the entire band on the condition that LBT and AFA mitigation procedures are implemented, along with a transmit duty cycle of at most 10%. Medical devices implemented in this band will not be protected from interference, due to the band being available to high power users and other exempt devices. Battery power can be conserved by utilising a 2.4 GHz signal, even if this frequency is not selected as the frequency of operation. A multi-band antenna can be designed to utilise more than one frequency band and switch off parts of the circuitry when they are not in use [5].

Although the 2.4 GHz ISM band can potentially be used for communication with medical implants, there are many other devices utilising this part of the spectrum, including household microwave ovens, telephones, WiFi devices and Bluetooth systems. The maximum effective isotropic radiated power (EIRP) should not exceed -10 dBW (100 mW) and if this band is utilised, mitigation techniques such as FHSS or DSSS must be implemented. A minimum of 15 separate and non-overlapping channels must be used for a Frequency-Hopping Spread Spectrum (FHSS) and an EIRP of -20dBW/MHz should be used as the maximum power density for DSSS [5]. The candidate frequency bands and the conditions of their use are illustrated in the external media, as referred to in Appendix I (page 133).

2.3 Wave Propagation: Matter

The radiation efficiency of an antenna cannot be considered in isolation from the influence of its surrounding materials. These objects, including those to which the antenna is attached and its casing/housing, affect the performance of propagation and attenuation. The impact of the materials in close proximity to the antenna become even more important in the case of implantations, not only because of the effect the biological materials have on the device, but also due to the effects of the device on these tissues which should be regulated with regards to possible health risks. Only when the wavelength of the frequency of operation is substantially shorter than the size of the surrounding objects, can the effects of distant parts of the object be ignored and only the parts closer to the antenna be taken into consideration [6].

Thus, in the case of implantable antennas, the housing of the implant and the body of the host must be taken into consideration when the far-field radiation of the antenna is evaluated. The body can be interpreted as a non-stationary, lossy encapsulation, which extends from the antenna's near-field to its far-field. In order to investigate the influence of the antenna on the body or those of the body on the antenna, the electromagnetic properties of the body must be known and evaluated in accordance with the specific properties of an antenna. Both aspects must be considered. The effect of a plane wave incident on the body of a rhinoceros will be investigated to establish available magnetic and electric fields within its body. Dielectric properties are often frequency and temperature dependent [7] and the amplitude and phase are dependent on the frequency and the structure of the body [6].

2.3.1 Fundamental Definitions

Typically, antennas are assumed to operate in a vacuum or in air when theoretical modelling is performed. Permittivity is defined as the ability to store electrical energy in an electrical field. The permittivity of free space (ε_0) is an ideal physical constant with a value of $\varepsilon_0 = 8.854188 \times 10^{-12}$ [F/m] and refers to a non-conducting environment. For biological implants, the environment of the antenna will have a higher permittivity (ε) and non-zero conductivity (σ) [S/m]. These are complex quantities consisting of real and imaginary parts ($j = \sqrt{-1}$):

$$\varepsilon = \varepsilon' - j\varepsilon'' \tag{1.0}$$

$$\sigma = \sigma' - j\sigma'' \quad \text{or} \quad \sigma = \sigma_d + \sigma_i \tag{1.1}$$

where

ε' = *The relative permittivity* - a measure of the charge displacement and consequent energy stored in the material [7].

ε'' = *The out-of-phase loss factor* - a measure of the dissipated electrical energy [7].

σ_d = *The displacement electrical conductivity.*

σ_i = *The ionic conductivity.*

Because the complex relative permittivity of a material is a relative quantity, it has no units. The conductivity σ of the material is related to the loss factor as follows:

$$\varepsilon'' = \sigma/(\varepsilon_0\omega) \tag{1.2}$$

where ω is the angular frequency of the field (rad/s). Thus, the complex permittivity ε_c of a medium can be written as [6]:

$$\varepsilon_c = \varepsilon_e - j(\sigma_e/\omega) \tag{1.3}$$

and the effective permittivity ε_e and effective conductivity σ_e can be written as:

$$\varepsilon_e = \varepsilon' - j\sigma''/\omega \tag{1.4}$$

$$\sigma_e = \sigma' + \omega\varepsilon'' \tag{1.5}$$

The permittivity of free space ε_o can be used to scale the effective permittivity ε_e of the medium, which is then defined as the relative permittivity ε_r [6]:

$$\varepsilon_r = \varepsilon_e/\varepsilon_o \tag{1.6}$$

The dissipation factor, which is the loss due to the conductivity of the matter, is defined as:

$$\begin{aligned} \text{Diss} = \tan\delta &= -\text{Im}[\varepsilon_c]/\text{Re}[\varepsilon_c] \\ &= \sigma_e/\omega\varepsilon_e \end{aligned} \tag{1.7}$$

These equations will be useful in the following analyses for defining the propagation characteristics of biological tissue and for illustrating the relation between the permittivity and conductivity of a material relative to frequency.

2.3.2 Dielectric Properties: Human Tissue

The permissible frequency spectrum of tissue covers the range from hertz to gigahertz, due to the risk of higher frequencies causing radiation damage that can be attributed to thermal interactions. It is categorised into three regions: the α (low frequencies), β (intermediate frequencies) and γ-dispersions (γ representing the dispersion observed at high frequencies). The implantation device described in this project will function in the mega- and gigahertz range and thus only the γ-dispersion will be considered. This dispersion primarily results from the polarisation and relaxation of water molecules [7]. Tissue, with its high water content, will exhibit similar γ-dispersion characteristics to pure water. As mentioned earlier, the complex permittivity is dependent on the frequency and the relation thereof in the γ-dispersion can be expressed by the Cole-Cole expression [7]:

$$\hat{\varepsilon}(\omega) = \varepsilon_\infty + \frac{\varepsilon_s - \varepsilon_\infty}{1+(j\omega\tau)^{1-\alpha}} + \frac{\sigma_l}{j\omega\varepsilon_0} \tag{2.0}$$

where

ε_∞ = The permittivity at field frequencies where $\omega\tau >> 1$.
ε_s = The permittivity at field frequencies where $\omega\tau << 1$.
α = The dispersion broadening parameter.
σ_l = The conductivity due to ionic shift and lower frequency polarisation mechanisms.
τ = The mean relaxation time.

The dispersion broadening parameter can be further described as follows:

Pure Water: $\alpha = 0$
Most Tissues: $\alpha \geq 0$
Body Fluids: α = Negligible

Peyman et al [7] conducted experiments to determine the dielectric properties of 0.1M NaCl, which has conductivity values close to those of tissue. The tolerance values for the permittivity and conductivity were calculated using the following expressions [7]:

$$\varepsilon'_{\text{tolerance}}[\%] = 100 \times \left|\frac{\varepsilon'_{\text{measured}} - \varepsilon'_{\text{reference}}}{\varepsilon'_{\text{reference}}}\right| \quad (2.1)$$

$$\sigma'_{\text{tolerance}}[\%] = 100 \times \left|\frac{\sigma_{\text{measured}} - \sigma_{\text{reference}}}{\sigma_{\text{reference}}}\right| \quad (2.2)$$

where $\varepsilon'_{\text{reference}}$ and $\sigma_{\text{reference}}$ refer to the dielectric properties of human tissue stated in literature. Peyman obtained the dielectric properties by applying the experimental results to Cole-Cole and Debye models, which are illustrated and compared to similar experiments conducted by Stogryn [8] and Buchner [9] (respectively) in Table 6.

Table 6: The dielectric properties of 0.1M NaCl **[7]**.

0.15 NaCl	**Temp [°C]**	**Model**	ε_s	+/- ε_s	ε_∞	+/- ε_∞	τ_{relax} [ps]	+/- τ_{relax}	σ [S/m]	+/- σ	α	+/- α
Peyman	20	Debye	78.8	0.3	5	-	9.2	0.3	0.96	0.005	-	-
Stogryn	20	Debye	77.1	-	4.9	-	9.24	-	1.36	-	0.012	0.01
Peyman	20	Cole-Cole	79.0	0.4	5	-	9.13	0.3	0.96	0.005	-	-
Buchner	20	Cole-Cole	79.1	-	5.6	-	9.4	-	0.96	-	0.017	-

These findings provide an indication of the tolerance of the dielectric properties that can be expected from biological tissue measurements and will be useful in future analyses, particularly with regards to the permittivity and conductivity in relation to temperature, to determine the accuracy of the phantom model dielectric measurements.

2.4 Phantom Body Simulations and Procedures

It is considered unethical and potentially dangerous to test developmental systems and medical devices on living animals and humans. Computer simulations are helpful for initial testing purposes with regards to new designs, but are often not able to model some of the real-world constraints and scenarios which might drastically influence the results. A phantom is a liquid or gelatinous substance simulating muscle, fat and skin with the same physical properties as those

of a specific animal in terms of conductivity and permittivity. Phantoms are often used by regulatory organizations to test implantable devices regarding adherence to a proposed standard [6]. As described in the next section, the MICS standard of the European Telecommunications Standards Institute (ETSI), defines the procedure for using a human physical phantom.

2.4.1 MICS Standard for Human Physical Phantom Simulations

The physical phantom defined by the MICS standard consists of an acrylic plastic cylinder with a radius of 15 cm and a wall thickness of 0.635 cm and is filled to a height of 76 cm with the tissue simulating liquid. A plastic grid/grating should be placed at a height of 38 cm and a distance of 6 cm from the inside wall. This is used to hold the medical implantation device in place during the testing procedures. Wires protruding from the implantation should be coiled and placed adjacent to the device. Flexible antennas should be placed at the same distance and height as the implant, along the wall of the phantom model. Although the orientation of the implanted device is not specified in the MICS standard, it should resemble the orientation that would be maintained during operation. Examples of ETSI artificial saline human phantoms, referred to as "Salty-Man" and "Salty-Lite", are illustrated in Figure 1 below.

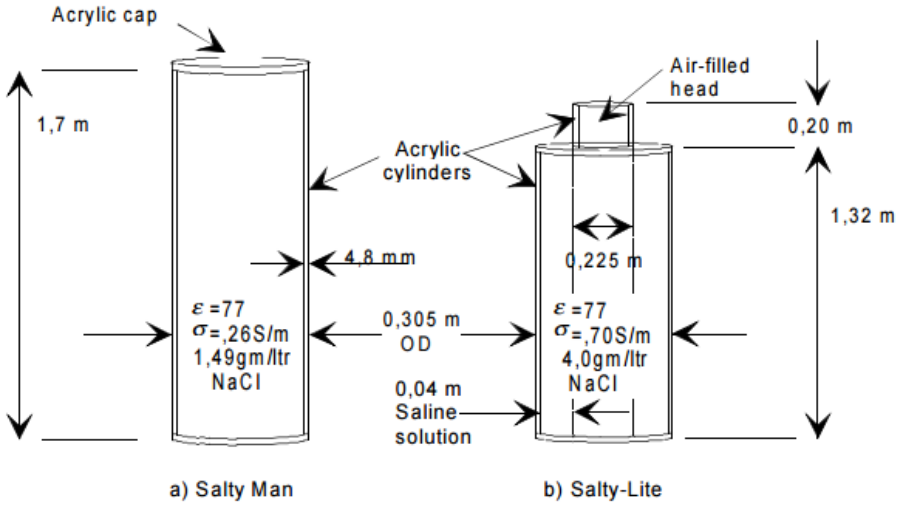

Figure 1: Examples of ETSI's saline human phantom models **[10]**.

Although simple phantoms such as the one proposed by the MICS Standard are fairly easy to build and use, they are not particularly anthropomorphic due their constant curvature, which is in contrast to the shape of an animal's body or in this particular case, the human body. In the case of a flat implant or antenna, this would cause certain parts of the device to be closer to the skin and thus affect the attenuation of the signal. Also, the specifications regarding the placement of the implant within the phantom, do not necessarily match the location at which it would reside in the host. For example, pacemakers are placed subcutaneously beneath the collarbone between the fat and the pectoral muscle. A deeper placement of the device would result in larger propagation losses due to the body's and tissue simulating liquid's lossy nature.

Thus, the MICS phantom does not provide an accurate model for specific points of implantation. It also does not model fat and skin layers, which could provide erroneous EIRP results. The electromagnetic properties of fat are substantially different to those of muscle and skin [6] and could influence the propagation properties of an implanted antenna. Thus a suitable substitute material must be included to account for this deficiency. In experiments conducted by Johannson [6], micro-spheres (small gas-filled spheres) made of plastic were filled with hydrocarbon (such as isobutane and isopentane) and used to simulate lung tissue and fat tissue. The suggested ratio with regards to volume is 47% muscle simulating liquid and 53% micro-spheres, with the diameter of the spheres ranging from 30 - 180 μm.

Due to the obscurity surrounding the dielectric properties of fat tissue, interchangeable fat layers with varying thickness were suggested to evaluate the effect of layered substances on antenna propagation. The following chapter elaborates on such recipes for simulating fat, brain, muscle, lung and bone tissue for humans. These recipes were used by Johannson, who also suggests the implementation of a more anatomically correct phantom by adding additional layers to the model. The suggested procedure consists of filling a container (50 cm x 50 cm x 40 cm) with muscle simulating tissue to a height of 40 cm and then adding two surrounding layers: first a dielectric material simulating the fat layer and second a dielectric layer simulating the skin. This model allows the implant to be placed in or between any of the layers of tissue, making it better suited for the observation of the effects of the different tissue types. For example, Johannson discovered that the wavelength of a 400 MHz radio signal is 74 cm in air, but approximately 9 cm in the muscle tissue of the human body.

2.4.2 Recipes for the Simulation of Human Tissue

The recipes for the muscle simulating tissue used in Johannson's experiments are indicated in Table 7. The measured effective permittivity (ε_{er}) and conductivity (σ_e) of the propagation of a 403.5 MHz and a 2.45 GHz signal through this tissue simulating phantom, are indicated in Table 8. Table 9 lists the measured conductivity and permittivity of various types of human tissues and supplies a model for comparison for the similarity between the simulated and actual human tissue.

Table 7: Recipes for muscle and brain simulating liquids **[6]**.

Tissue	Water (%)	Sugar (%)	Salt (NaCl) (%)	Hydroxyethyl-cellulose (HEC) (%)
Muscle	52.4	45.0	1.4	1.0
Brain	40.4	56.0	2.5	1.0

Table 8: Tissue simulating liquid dielectric properties (403.5 MHz) **[6]**.

Tissue	Effective Permittivity (ε_{er})	Conductivity (σ_e) [S/m]
Muscle	62.5	0.9
Brain	50.3	0.75
Lung	32.6	0.43
Bone Cast	9.3	0.11
Bone Liquid	9.1	0.066

Table 9: Actual human tissue dielectric properties **[11]**.

Tissue	Frequency = 403.5 MHz		Frequency = 2.45 GHz	
	Effective Permittivity (ε_{er})	Conductivity (σ_e) [S/m]	Effective Permittivity (ε_{er})	Conductivity (σ_e) [S/m]
Muscle	57.1	0.797	52.7	1.7
Fat (non-infiltrated)	5.6	0.041	5.3	0.1
Lung	23.8	0.375	-	-
Skin (Dry)	46.7	0.690	38.0	1.5
Skin (Wet)	49.8	0.670	42.8	1.6
Bone Cancellous	22.4	0.235	18.5	0.8
Brain Grey Matter	57.4	0.739	48.9	1.8
Brain White Matter	42.0	0.445	36.2	1.2

These results indicate a large discrepancy between the dielectric properties of existing phantom models and actual human tissue. This suggests that large error rates between the theoretical and measured dielectric properties of biological tissue are to be expected. In this work we performed

similar experiments for rhinoceros phantoms (Chapter 5, page 40). Since the recipes for biological tissue found in the literature are primarily limited to human tissue, physical similarities between human tissue and those of other animals were investigated to establish whether these recipes could be altered to create phantoms for other species.

The skin thickness of various parts of the human body ranges from 0.5 mm to 4 mm. A study conducted on the dielectric properties of Steller sea lions, pigs and sheep [12], yielded results comparable to those for humans as indicated in Table 8 and Table 9. The skin thicknesses and dielectric properties of these animals can be viewed in the external media, as referred to in Appendix I (page 133). The dielectric properties of sea lions, which are conceivably comparable to those of the rhinoceros due to their large fat layer and thick skin, range between 20 to 40 for frequencies varying between 0.1 GHz and 10 GHz. The conductivity of sea lion skin increased from less than 1 to 5 S/m as the frequency increased in this range. These results can be used for comparative purposes between skin thickness and its resulting effect on propagation, which could contribute to estimations regarding the dielectric properties of rhinoceros skin.

2.4.3 Identification of Phantom Parameter Preferences

There are many properties to take into consideration when developing a phantom which accurately replicates biological tissue. The acoustic, thermal, electric and optical characteristics of a medium are all examples of the parameters that define a particular biological tissue. Not all of the parameters need to be replicated, however, since phantoms are usually fabricated to resemble specific physical and geometrical properties, which are used for well-defined applications and experimentation. These properties are particular to the objective at hand. Therefore, the parameters that are of importance and those that will have a negligible effect on the outcome of the application of this project, must be identified. Some of the most significant parameters to consider for microwave and radio frequency applications are listed in Table 10.

Table 10: Critical parameters of phantoms in different radio frequency thermal modalities **[13]**.

Common Thermal Parameters	**Symbol**	**Unit**	**Definition**
Density	ρ	kg/m^3	-
Specific Heat Capacity	C	J/kg/K	-
Thermal Conductivity	k (or λ, κ)	W/m/K	-
Thermal Diffusivity	D (or a, k)	m^2/s	-
Radio frequency and Microwave Parameters	**Symbol**	**Unit**	**Definition**
Specific Absorption Rate	SAR	W/kg	Time rate of electromagnetic energy deposition per unit mass.
Electrical Conductivity	σ or κ	S/m	-
Complex Permittivity	ε	F/m	The resistance against formation of an electric field in the medium.
Real Part of Permittivity	ε'	F/m	The ability of the medium to store electric field energy.
Imaginary Part of Permittivity (Loss Factor)	ε''	F/m	A measure of the dissipated energy in the material.
Loss Tangent (tanδ)	$\varepsilon'/\varepsilon''$	-	A measure of loss-rate of electrical energy in the system.
Relative Permittivity	ε_r (or $\varepsilon/\varepsilon_0$)	-	The normalized permittivity of the medium according to vacuum
Dielectric Constant	ε'_r (or $\varepsilon'/\varepsilon_0$)	-	Ratio of the stored electrical energy in the material by a given voltage, relative to that in vacuum.

Other physical parameters not listed in Table 10, such as the nonlinearity parameter, the backscattering coefficient and the optical penetration depth are specific to high intensity focused ultrasound (HIFU) and laser-induced thermal ablation (LIT) applications. These factors are not influential in the outcome of this project and only affect specific thermal modalities, such as the effect of the relaxation time on microwave experimentation. These parameters are seldom listed in the literature, due to the difficulties associated with obtaining accurate measurements. The properties of biological tissues are highly dependent on the external temperature and the applied frequency – the magnitude of the dependency varies regarding the characteristics of the tissue [13]. Ideally, the phantom should replicate the selected tissue properties over wide frequency and temperature ranges, whilst also replicating the acoustic, thermal, optical and electric characteristics. Such phantoms are difficult to create and thus the focus parameters selected for this project are those listed in the radio frequency and microwave section of Table 10. Section 5.3.1 (page 58) elaborates on some of these aspects regarding the proposed phantom materials.

2.5 Types of Phantom Materials

Although this project eventually advocates the use of agar based phantoms, many other gel phantoms have been considered for the design and development of temperature sensitive experiments. Throughout the medical industry, the simulation of biological tissue by means of the experimental development and application of specialised solid, liquid and gel phantoms has led to many procedures (referred to as recipes) for the production of phantoms. Gel phantoms are often favoured above liquid and solid phantoms, due to their ability to replicate realistic irradiation geometries and their ability to represent a wide range of electrical, optical, thermal and acoustic properties [13]. The advantages and disadvantages of various types of phantom materials are discussed in Appendix E (page 120), whereas popular and suggested recipes for each type of gel phantom can be viewed in the external media (Appendix I, page 133).

Currently, numerous phantoms are available that mimic human tissue for biomedical investigations and applications. These however do not possess the properties required to simulate rhinoceros tissue. The dielectric properties of human tissue are different to those of rhinoceros tissue. Furthermore, these phantoms do not consist of multiple layers modelling the thickness and dielectric properties of the various subcutaneous tissues. Therefore, the design and fabrication of customized dielectric phantoms was necessary in order to obtain models with dielectric properties similar to those determined and specified in Chapter 4 (page 37). Many types of material can be utilized to achieve this depending on the specifications of the model. These range from liquid, gel and solid states to not only simulate electric properties, but also those relating to acoustic, thermal and optical properties. Although a gel state phantom was selected for the purposes of this project, the various materials and techniques used to create other types of phantom are briefly discussed in this section, along with some of their benefits and disadvantages.

When a new medical device is introduced, the effectiveness and restrictions of phantom models need to be evaluated and verified in accordance with regulated standards prior to their application in a clinical environment. Ideally, the phantom should perfectly replicate the conditions of the actual tissue. However, due to the strict laws governing the acquisition of rhinoceros tissue samples, as well as other factors such as the handling, preparation, storage and standardization of the results of real tissue samples, the acquisition of the empirical rhinoceros tissue data proved to be difficult. Although samples could not be obtained, a veterinary surgeon specialising in large mammals, including rhinoceros, at the Faculty of Veterinary Science at University of Pretoria was consulted regarding the anatomy of these animals. Much essential information was gathered this way for designing simulations that accurately replicate the in-vivo environment.

2.5.1 Phantom Material Selection

Electromagnetic propagation testing could be harmful to organic tissue even after careful calculation. Thus, substitute materials which exhibit similar characteristics to those of the organic materials are required. The parameters of the device and the effects of the radiation can then safely be explored without fear of contamination or illness. It is often the case that materials with similar densities exist, but that the dielectric properties of the materials are vastly different. This is the motivation for the fabrication of phantom tissue materials of which the permittivity and conductivity can be manipulated. Many methods and materials are used for such purposes, with varying degrees of success, as discussed in Appendix E (page 120). The advantages and disadvantages of these phantom materials are summarised in Table 11, which were used to gauge the applicability and benefits that each of the gelling mediums could deliver.

Table 11: The advantages and limitations of popular and suggested phantom material gelling agents **[13]**.

Gelling Agent	Advantages	Limitations	Suggested Use
TX-150	Simulation of high water content tissues over a wide frequency range. Controllable physical properties. Facile construction.	Inability to simulate low water content tissues. Variable gelation parameters. Limited shelf life. Unavailability of acoustic and optical values.	1. RF 2. MW
Agar	Thermal stability. Mechanical strength. Applicable in a wide frequency range. Adjustable physical properties. Capability of producing heterogeneous structures. Useful in construction of perfused phantoms.	High opacity. Low permittivity. Low cavitation threshold.	1. RF 2. MW 3. HIFU 4. LIT
PAA	Optical transparency. Thermal stability. Mechanical strength. High formability. Applicable for construction of heat sensitive phantoms. Adjustable physical properties. Appropriate cavitation threshold range.	Toxic ingredients. High cost of preparation. Complicated construction process. Limited shelf life.	1. HIFU 2. RF 3. MW 4. LIT
HEC	Desirable dielectric properties. Facile preparation. High durability.	Unavailability of acoustic and optical values.	1. MW 2. RF
Gelatin	Ease of construction. Low-cost ingredients. Long-term stability. Applicable in fabrication of heterogeneous structures.	Low melting point. Insufficient mechanical strength. High opacity level.	1. LIT 2. MW 3. RF
GGM	Sufficient transparency. Thermal stability. Low ratio of gelling agent needed for gelation. Formation of highly homogeneous structure.	Difficulties in reproducibility of acoustic and thermal values. Fragility. Unavailable optical and acoustic properties.	1. RF 2. MW 3. HIFU
CAG	Desirable mechanical properties.	Low opacity. Low melting point. Limited shelf life.	1. RF 2. MW
ALG	Mechanical stiffness. High melting point. Desirable optical properties.	Unavailability of thermal, electrical, and acoustic properties.	1. LIT

RF = radiofrequency; MW = microwave; HIFU = High Intensity Focused Ultrasound; LIT = Laser-induced thermal ablation; PAA = polyacrylamide; HEC = hydroxyethyl cellulose; GGM = gellan gum; CAG = carrageenan; ALG = alginate phantom.

Due to the ongoing nature of the research into most of the discussed materials, many of their acoustic, optical, electrical and thermal properties have not yet been characterized. Thus, the recalculation or replication of the presented values may be difficult to achieve, especially due to the lack of standardization for the proposed techniques and varying laboratory conditions. Despite the mentioned limitations, three phantom model types were selected for

experimentation: agar phantoms, hydroxyethyl cellulose phantoms and gelatin phantoms. These phantoms were selected based on their respective benefits and disadvantages as discussed in the external media and depicted in Table 11 as originally presented by Dabbagh et al [13]. Specifically, each of the identified mediums are easy to mould, have good mechanical strength and are non-toxic.

One of the ways to fabricate phantom tissue is the use of agar. This substance has the advantage of being very malleable, which is quite useful for creating geometrically intricate layers. Various concentrations of salt and sugar can be added to the substance in order to adjust its permittivity and conductivity. All of its ingredients are non-toxic, easily acquired and relatively inexpensive. The disadvantage of using a gelatinous substance is the limited time for which it maintains its structural integrity, which is also influenced by heat, and its dielectric properties, although certain chemicals can be added to increase its longevity. Without antibacterial additives such as benzoic acid and outside of cold storage (4°C), the expected time of use ranges from a few days to approximately one week. Considering these aspects and the advantages and limitations listed in Table 11, agar was selected as the gelling agent for the rhinoceros tissue phantom models. Specifically, agar has adjustable physical and dielectric properties and has a greater application across a wider frequency range than the other two candidates.

Initial recipes for creating agar plates with specific permittivity and conductivity were obtained from a study conducted by Duan et al [14] in which a dielectric phantom was characterized for high-field magnetic resonance imaging (MRI) applications. This phantom consisted of inexpensive and non-toxic materials, which had a biologically relevant range of dielectric properties between 150 MHz and 4.5 GHz. The ingredients used in the recipes are as follows:

Deionized water	: Used as the solvent.
NaCl	: Used to manipulate the conductivity.
Sucrose	: Used to manipulate the permittivity.
Agar	: Used to solidify the substance and reduce heat diffusivity.
Benzoic Acid	: Used to preserve the gelatinous substance.

The dielectric properties of 217 samples with various concentrations of NaCl and sucrose were measured with a dielectric probe by Duan et al [14]. These measurements were then fitted to a multivariate polynomial to model the frequency, NaCl concentration and sucrose concentration required to achieve those dielectric properties [14]. A polynomial equation was used due to the non-linear and dependent relationship between the concentration of the sucrose and the permittivity, as well as the conductivity and the NaCl. The concentrations that were obtained from the polynomial equation resulted in agar with measured permittivity and conductivity values within 2% of the predicted values for brain and muscle tissue. These measured values attained by Duan et al [14] were used in conjunction with the permittivity and conductivity values estimated in Chapter 4 (page 37) to compile phantom recipes for various tissues, as explained in Chapter 5 (page 40).

2.5.2 Phantom Recipe Calculation Methods

Phantom recipes were compiled by means of four methods, which are illustrated in Appendix N (page 154). The first method is the recipe generator designed by Duan et al [14]. The generator requests certain parameters such as the permittivity, conductivity and frequency and supplies the concentration of sucrose and NaCl to achieve those parameters. Although this method was quite useful, it did not cover all the dielectric values associated with certain frequencies, for example, the conductivity of skin rhinoceros at 2.4 GHz. Thus, it was necessary to use alternative methods for establishing the phantom recipes.

The three remaining methods were derived from the values obtained by Duan et al [14]. These methods were applied when the recipe generator was unable to deliver meaningful results. The first approach was a formula derived by means of polynomial regression from the results presented by Duan et al [14]. Two formulas were derived for each of the four frequencies, 403 MHz, 910 MHz, 2.4 GHz and 4.5 GHz, used in the simulations - one for determining the concentration of NaCl required to achieve the specific permittivity and conductivity values and another for determining the concentration of sucrose required to achieve the specific permittivity and conductivity values. A minimum of ten conductivity and permittivity pairings were used to derive each formula and a MATLAB script was written to calculate the concentration of NaCl and sucrose required, based on the permittivity and conductivity which were received as inputs.

The polynomial regression method proved quite useful, although it would occasionally deliver meaningless results by suggesting NaCl and sucrose that could not be achieved given the volumetric size of the simulation models. Thus, two other methods were applied to attain better estimates of NaCl and sucrose concentrations in these cases – a closest point approximation to the polynomial curve and an incremental approach in which the permittivity was kept constant whilst adjusting the conductivity in small increments until a suitable value was obtained. In the latter approach the permittivity was held constant as the permittivity estimations were already within the parameter ranges used by Duan et al [14]. The estimated permittivity and conductivity were used to signify a point (conductivity; permittivity) in the closest point approximation method. The shortest distance to the polynomial regression curve equation was calculated for each conductivity and permittivity pairing, yielding recipes for all tissue samples over all four frequencies. A MATLAB script was designed for this purpose, which utilized the mathematical optimization procedure illustrated in the following example.

Example

The estimation of the closest point (x = conductivity, y = permittivity) within the 2.4 GHz polynomial regression equation to the estimated dielectric properties of grey matter.

(conductivity; permittivity) = (2.286211699, 43.85216802)

2.4 GHz polynomial regression equation:
$x = 0.00005442851413y^3 - 0.009289785818y^2 + 0.4822356134y - 5.091784973$

Calculation:

The distance between the actual point and closest point within the polynomial is defined as:

$$d = \sqrt{(x - x\_p)^2 + (y - y\_p)^2}$$
$$= \sqrt{(x - 2.286211699)^2 + (y - 43.85216802)^2}$$
$$= \sqrt{(0.00005443y^3 - 0.00928979y^2 + 0.48223561y - 7.37799667)^2 + (y - 43.85216802)^2}$$

The partial derivative of the distance with regards to y:

$$\frac{dd}{dy} = \frac{(1.7775 \times 10^{-8})y^5 - (5.0563 \times 10^{-6})y^4 + (5.5518 \times 10^{-4})y^3 - 0.0293y^2 + 2.7393y - 94.8202}{2\sqrt{(0.00005443y^3 - 0.00928979y^2 + 0.48223561y - 7.37799667)^2 + (y - 43.85216802)^2}}$$

The permittivity (y) reaches a minimum when $\frac{dd}{dy} = 0$:

$0 = (1.7775 \times 10^{-8})y^5 - (5.0563 \times 10^{-6})y^4 + (5.5518 \times 10^{-4})y^3 - 0.0293y^2 + 2.7393y - 94.8202$
$= 0.02928863375y^2 - 2.739262409y + 94.82020154$

Of which the roots can be calculated:

$$y = \frac{-b \pm \sqrt{b^2 - 4ac}}{2a}$$
$= 46.76323301$

Thus, the closest y-coordinate = R{y} = 46.76323301.

By substituting the closest y-coordinate into the 2.4 GHz polynomial regression equation we obtain the closest x-coordinate as x = 2.7810167906. This is the closest feasible conductivity value within the polynomial regression equation that can be achieved by a solution of agar, NaCl and sucrose, given the selected permittivity. Due to the approximation of the polynomial regression curve, it was possible to obtain recipes for conductivity and permittivity values which were not within the original parameters used by Duan et al [14]. Some solutions found in this way remained practically infeasible, such as incredibly high quantities of salt or sugar which would not dissolve within the required solution volume. In this case the incremental method was used to obtain values within the experimental parameters by using the closest point approximation coordinate as a starting point.

The methods used to calculate the recipes for the concentrations of NaCl and sucrose for the various tissues proved very effective, although fat, bone cancellous and bone cortical delivered results with greater error margins compared to the other tissues within their specific frequency ranges. Thus, alternative materials were investigated to approximate these types of tissue. The parameters for defining the ratios of the recipes (the total amount of salt, sugar, agar and water that can be combined to create phantom materials) as used by Duan et al [14] are illustrated in the external media (Appendix I, page 133).

The phantom recipe generator used by Duan et al [14] also supplies estimated values for the density [g/l], the heat capacity [(J/g)/K] and the thermal conductivity (W/(m*K)) based on the selected water volume, agarose concentration, benzoic acid concentration and the temperature. A temperature of 24°C was selected for all calculations, seeing as this is commonly regarded as room temperature [15]. If it is assumed that the phantom recipe generator delivers the most accurate NaCl and sucrose concentrations for the phantom recipes, the method of substituting the approximated permittivity and conductivity values into the polynomial regression equation would be the second most accurate, since it is the closest approximation of the phantom recipe generator. The third most accurate method would thus be the closest point approximation method, followed by the incremental method. Although the second and third methods may be more accurate in their estimations, they also have a larger risk of delivering values outside of the practically realisable ranges and thus the incremental method would be preferred in terms of delivering values within a range that has predictable outcomes.

2.5.3 The Effect of Temperature on Permittivity Measurements

Four ingredients were used to create the rhinoceros phantom materials: agar, salt, sugar and water. These are substances commonly used in dielectric property experiments and the effect of temperature on the respective permittivity values of these constituents could deliver insight on

the effect of temperature on the permittivity of the combined phantom material. Figures 2 to 4 are illustrations from the experiments done by Chew et al [16] to establish the effect of ingredient concentration and temperature on the relative permittivity of agar and gelatine solutions. Figure 2 indicates the similarity between the permittivity of gelatine and agar mixtures with identical concentrations within the frequency range of 1 GHz to 6 GHz, which suggests that these two materials behave similarly in terms of their dielectric properties and are thus interchangeable with respect to their influence on the solution.

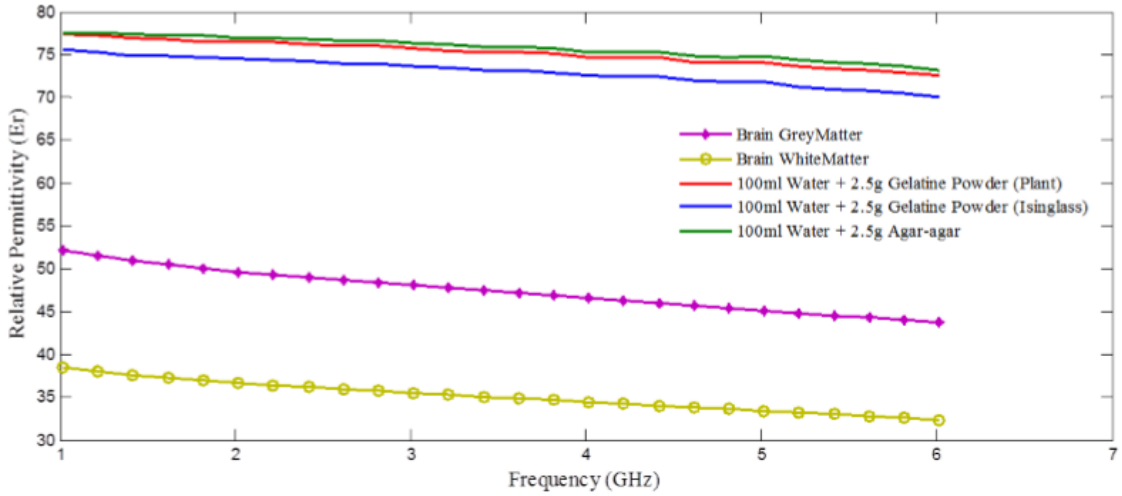

Figure 2: Relative permittivity of 100 ml gelatine and agar solutions within the frequency range of 1 GHz to 6 GHz **[16]**.

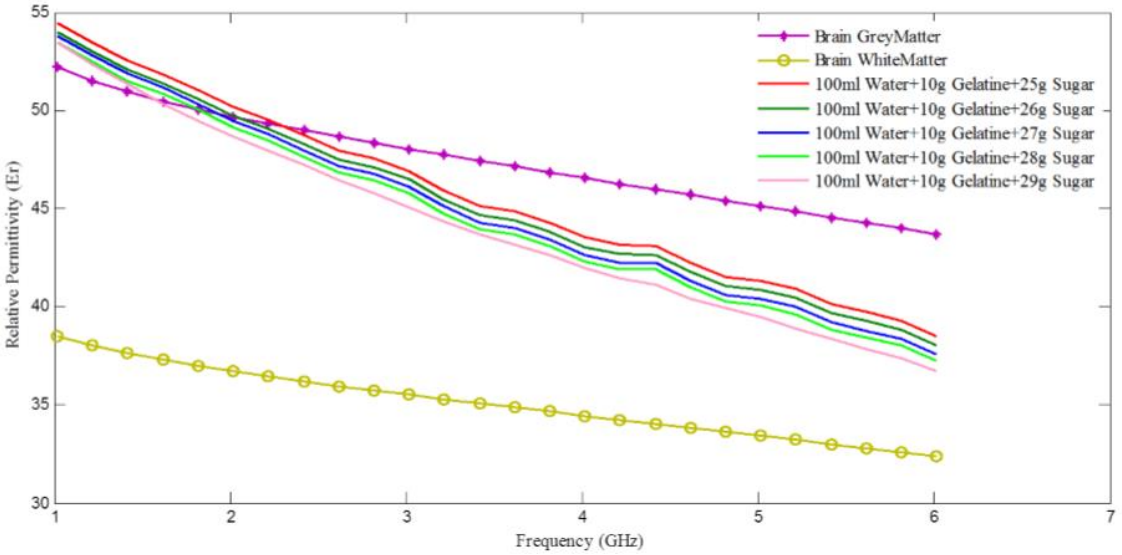

Figure 3: Relative permittivity of 100 ml gelatine and sugar solutions within the frequency range of 1 GHz to 6 GHz **[16]**.

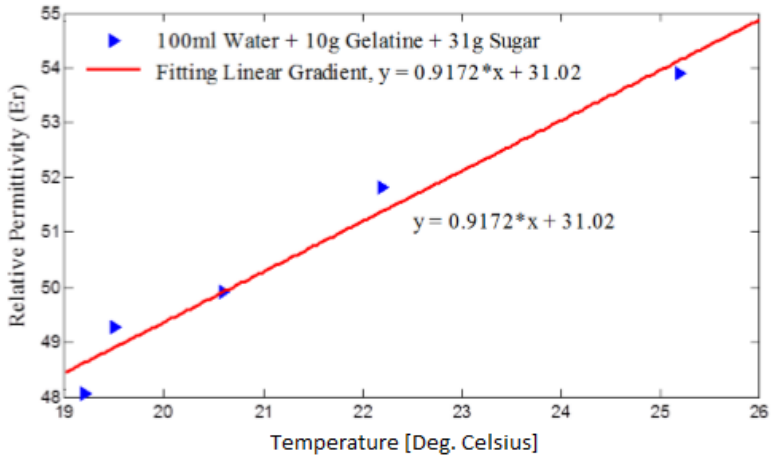

Figure 4: Relative permittivity of 100 ml gelatine and sugar (31 g) solution within the temperature range of 19°C to 26°C **[16]**.

Both solutions indicate a decrease in permittivity as frequency increases, with the downward slope being amplified by the addition of sugar as illustrated in Figure 3. The larger the amount of sugar, the lower the overall permittivity. The relationship between the permittivity and sugar quantity is confirmed by Figure 4, which also indicates the positive correlation between the permittivity and the temperature of the solution – as the temperature rises, the relative permittivity of the solution is increased. These trends are supported by other sources such as Singh et al [17], Tulasidas et al [18], Olmi et al [19] and Duan et al [14] as illustrated in the external media (Appendix I, page 133) and correspond to the findings of this project. Similar trends are exhibited in Figure 5, which illustrate a reduction in permittivity with an increase in salt concentration. Not only is the downward slope lessened by an increase in temperature, but the overall permittivity is also reduced. This figure is an extract from the results gathered by Gavish and Promislow [20], as part of a study to establish the dependence of the orientational polarization of water in aqueous electrolyte solutions with respect to the concentration of salt and the temperature [20].

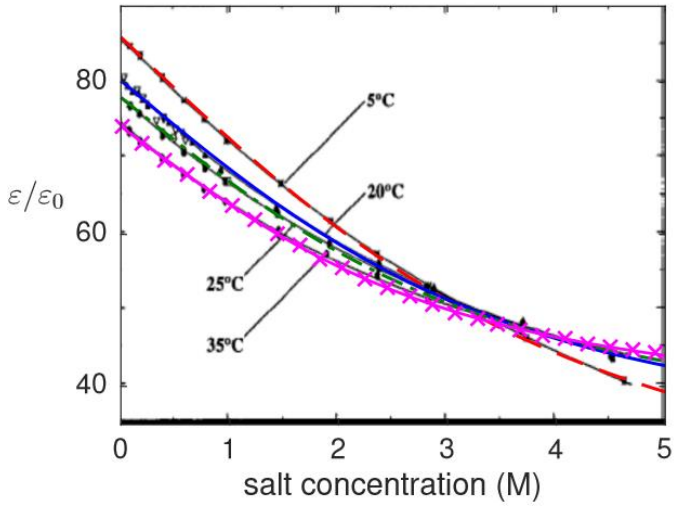

Figure 5: Permittivity of salt (NaCl) as a function of ionic concentration for various temperatures **[20]**.

The results are supported by other sources such as Ellison et al [21], which also documented an increase in conductivity with an elevation in temperature. Somaraju and Trumpf [22] conducted experiments to understand the properties of electromagnetic wave transmission in seawater, which delivered results indicating a negative relation between the permittivity of saline solutions

at various temperatures and frequency (up to 8 GHz). Some of their findings are illustrated in Figure 6, which also agree with the findings of this project.

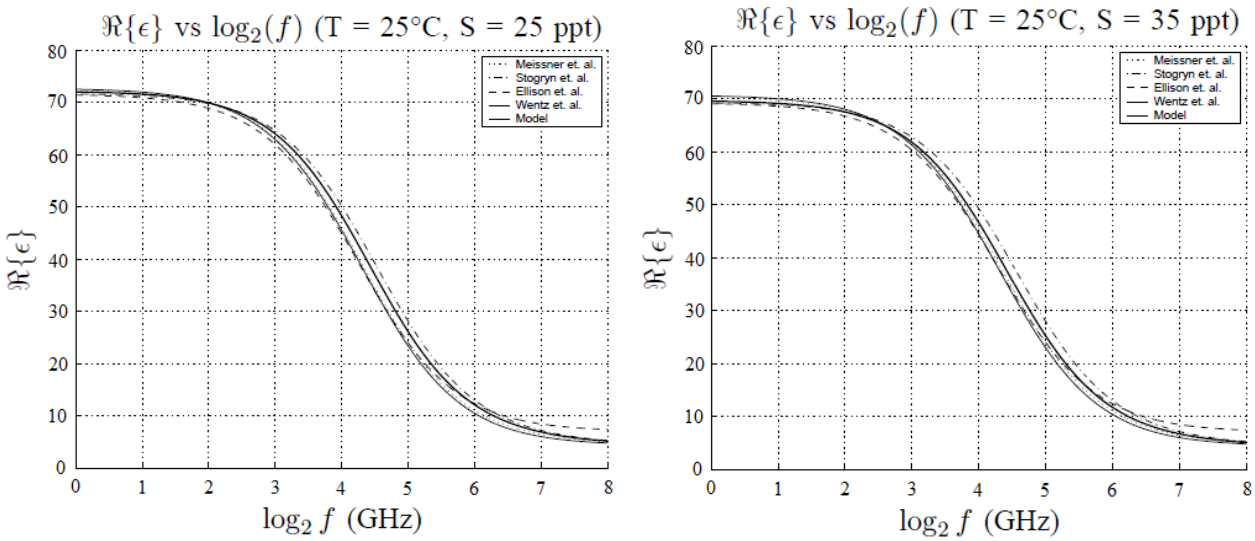

Figure 6: Permittivity of saline solution with various concentrations at 25°C from 0 GHz to 8 GHz **[22]**.

The dielectric constant of water is known to decrease with an increase in temperature. The above stated results indicate that the permittivity of salt and sugar tend to decline as the frequency increases. However, the relative permittivity of sugar solutions tend to increase with an elevation in temperature, whereas the relative permittivity of salt tends to decrease with an elevation in temperature. The overall effect of having a slightly higher room temperature of 24.91°C rather than the specified room temperature of 24°C (Section 5.2, page 43), would be that the measured permittivity would be slightly lower than expected. This deviation would be quite small considering the closeness of these two temperatures. The sugar permittivity trend line is illustrated in Figure 4 and the salt permittivity trend lines for 20°C and 25°C are depicted in Figure 5. These illustrations support the notion that the slight difference in temperature would have a negligible effect on the dielectric properties of the samples.

2.6 Implantation Antenna Design

Implanted devices are commonplace in the medical industry. However, this would not have been the case without the ability to wirelessly transmit data. Thus, the design of an implantable antenna is a significant factor for any implantation device and should be carefully considered. A number of antenna designs were examined and analysed in an attempt to establish the type of antenna best suited for the requirements of this project, such as small size and omnidirectional propagation. These antennas were designed from generic models to operate at the specific frequencies of 403 MHz, 910 MHz and 2.4 GHz. Of course, the selected frequency effects the shape and size of the antenna and thus most of the antennas had more than one physical design. In total, 67 generic antenna designs were simulated with the aid of software packages such as CADFEKO and Antenna Magus. All antenna designs were simulated under the same computational and analytical conditions, in order to make direct comparisons for selecting the optimal design. The detailed results of the generic antenna design simulations can be viewed in the external media (Appendix I, page 133).

2.6.1 Antenna Design Selection

The sixty-seven generic antenna designs were identified by reviewing the literature, which suggested that PCB antennas are preferred for medical implantation devices. A process of

elimination was followed to determine which antennas would deliver the most favourable results with regards to the computed gain, the radiation pattern, the reflection coefficient/return loss (S_{11}), the approximate bandwidth, the frequency to allow maximum penetration of the tissue and the smallest physical size. The most severe limiting factor was the size constraint of 7x5x2 cm [23], which only seven antenna designs were able to meet. The second most severe constraint was the return loss, seeing as only six of the eight remaining designs had a return loss of less than -10 dB. A points system was chosen to rank the remaining designs. The four antennas with the highest rank were selected for further consideration as described in Chapter 6 (page 68). Table 12 summarises the characteristics of the selected four best antenna designs.

Table 12: Characteristics of the selected antenna designs.

Criteria	**Antenna Design**			
	Microstrip-Fed Planar Elliptical Monopole Antenna	**Printed Inverted-F Antenna**	**Planar Trapezoidal Monopole Antenna**	**Circular Pin-Fed Linearly Polarised Patch Antenna**
Ranking	1	2	3	4
Design Frequency	2.4 GHz	2.4 GHz	2.4 GHz	2.4 GHz
Approximate Gain [dB]	2.11	2.461	1.37	7.49
Radiation Pattern	Toroidal	Toroidal Directional	Toroidal	Semi-Toroidal
Reflection Coefficient (At Design Frequency)	0.1226	0.128	0.139	0.557
S_{11} [dB] (Return Loss for Refl. Coef. at Design Frequency)	-18.23	-17.86	-17.14	-5.08
Minimum Reflection Coefficient	0.1057	0.0517	0.1265	0.221
S_{11} [dB] (Return Loss for Minimum Refl. Coef.)	-19.52	-25.73	-17.96	-13.11
Frequency At Minimum Reflection Coefficient	2.512 GHz	2.3565 GHz	2.305 GHz	2.358 GHz
Approximate Bandwidth Range (Refl. Coef. ≤ 0.316)	2.072 - 3.894 GHz	2.2318 - 2.4818 GHz	1.918 - 2.862 GHz	2.341 - 2.373 GHz
Approximate Bandwidth (Refl. Coef. ≤ 0.316)	1.82603 GHz	250.008 MHz	944.871 MHz	32.7124 MHz
Physical Size (Length x Width x Height) [mm]	49.97 x 50.7 x 1.104	53.66 x 35.77 x 1.767	52.32 x 69.7 x 2.208	49.75 x 49.75 x 2.65
Antenna Volume [mm^3]	2796.96	3391.61	8051.92	6558.92

The four selected antenna designs were simulated with an infinite substrate medium propagating in free space. This configuration was common to all simulations in order to establish a comparative environment for selecting the best design. The design specifications of the four selected antennas are illustrated in Figure 7 to Figure 10, whereas the detailed simulation results can be viewed in the external media (Appendix I, page 133). Table 13 and Figure 7 elaborate on the design specifications of the Microstrip-Fed Planar Elliptical Monopole Antenna (MFPEMA), which was designed to operate at 2.4 GHz. As can be seen in the specifications, the maximum dimensions of all antennas are within the requirements indicated by the veterinary expert (7cm x 5cm x 2cm).

Table 13: Detailed design specifications of the microstrip-fed planar elliptical monopole antenna (2.4 GHz).

Name	Description	Value
Le	Ellipse Length	24.98 mm
We	Ellipse Width	24.98 mm
Sf	Feed Gap	732.6 µm
Wf	Feed-Line Width	3.612 mm
H	Substrate Height	1.104 mm
ε_r	Substrate Relative Permittivity	2
Lg	Ground-Plane Length	24.98 mm
Wg	Ground-Plane Width	49.97 mm
X	Width (Maximum dimension in plane of substrate perpendicular to feed line axis)	49.97 mm
Y	Length (Maximum dimension along axis of feed line)	50.70 mm
Z	Height of substrate	1.104 mm

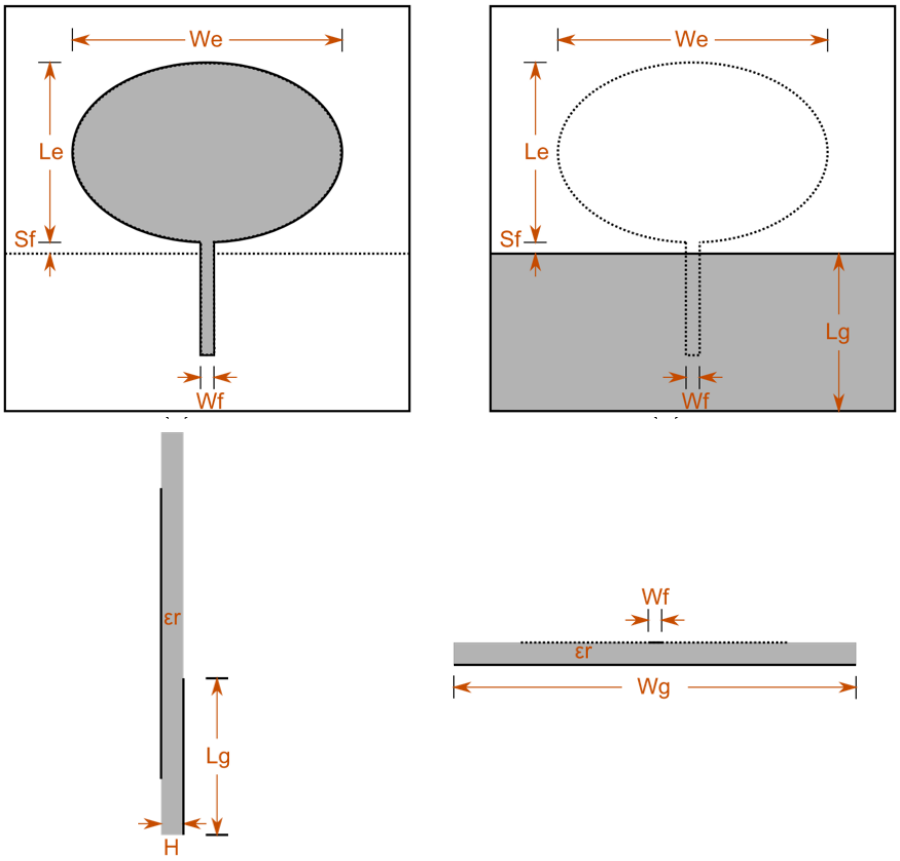

(c) (d)

Figure 7: The specifications of the microstrip-fed planar elliptical monopole antenna (2.4 GHz).

Table 14 and Figure 8 elaborate on the design specifications of the Printed Inverted-F Antenna (PIFA), which was designed to operate at 2.4 GHz. As can be seen in the specifications, the maximum dimensions of all antennas are within the requirements indicated by the veterinary expert.

Table 14: Detailed design specifications of the printed inverted-F antenna (PIFA) (2.4 GHz).

Name	Description	Value
Le	Element Length	25.06 mm
We	Element Width	1.114 mm
He	Element Height	4.566 mm
Sf	Short to Feed Spacing	4.455 mm
Wg	Ground-Plane Width	53.66 mm
Lg	Ground-Plane Length	23.85 mm
Lde	Dielectric Extension Above Ground plane edge	11.92 mm
H	Substrate Height	1.767 mm
ε_r	Relative Permittivity	2
X	Antenna Length	53.66 mm
Y	Antenna Height	35.77 mm
Z	Antenna Thickness	1.767 mm

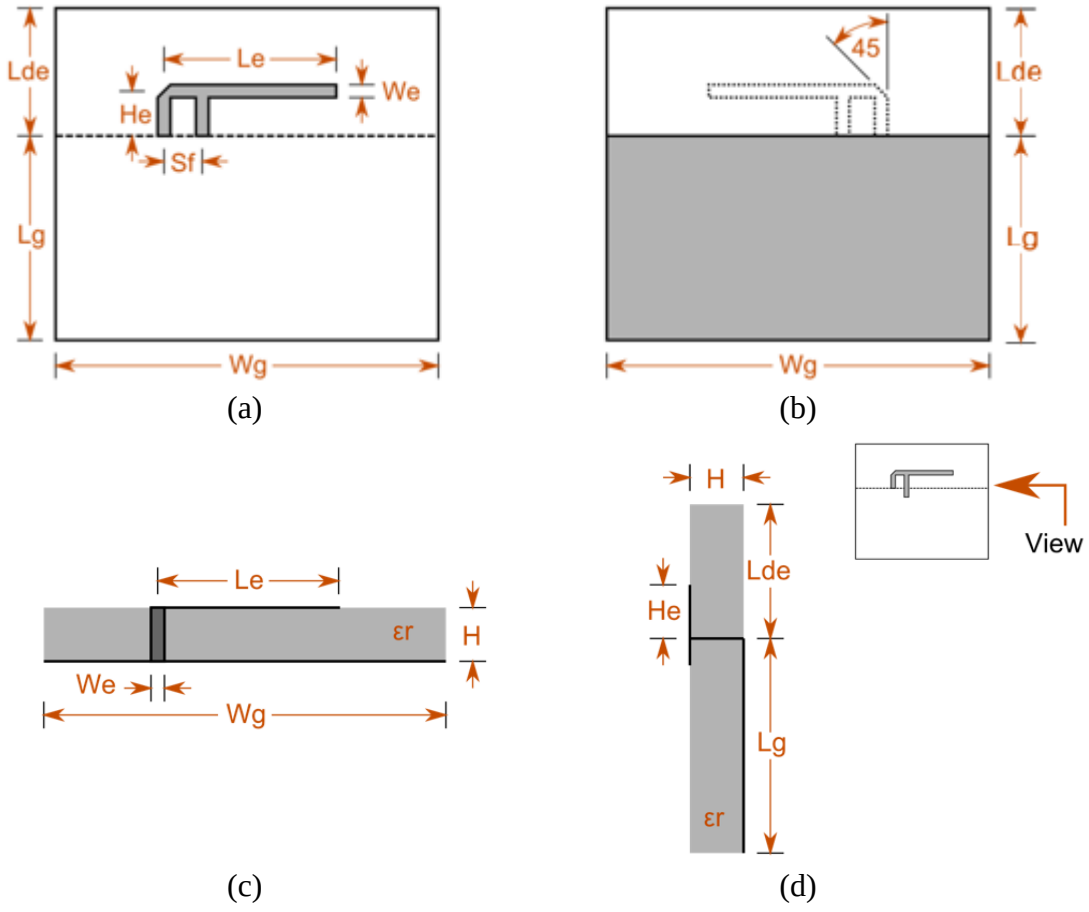

Figure 8: The specifications of the printed inverted-F antenna (PIFA) (2.4 GHz).

Table 15 and Figure 9 elaborate on the design specifications of the Planar Trapezoidal Monopole Antenna (PTMA), which was designed to operate at 2.4 GHz. As can be seen in the specifications, the maximum dimensions of all antennas are within the requirements indicated by the veterinary expert, even though this antenna is slightly larger than the previous two antennas.

Table 15: Detailed design specifications of the planar trapezoidal monopole antenna (2.4 GHz).

Name	Description	Value
Hs	Substrate Height	2.208 mm
ε_r	Relative Permittivity of the Dielectric	2
tanδ	Loss Tangent of the Dielectric	0
Le	Distance from the Base of the Trapezoidal Element to Top of Element	16.65 mm
Wb	Width of the Base of the Trapezoidal Element	7.224 mm
Wt	Width of the Top of the Trapezoidal Element	34.85 mm
Sf	Feed Gap	2.365 mm
Lf	Length of Feed Line	19.02 mm
Wf	Width of Feed Line	7.224 mm
Wg	Width of the Ground Plane	69.70 mm
Lg	Length of the Ground Plane	33.30 mm
X	Total Length of the Antenna	52.32 mm
Y	Width of the Ground Plane or Monopole Element, depending on which Layer is Larger	69.70 mm
Z	Substrate Height	2.208 mm

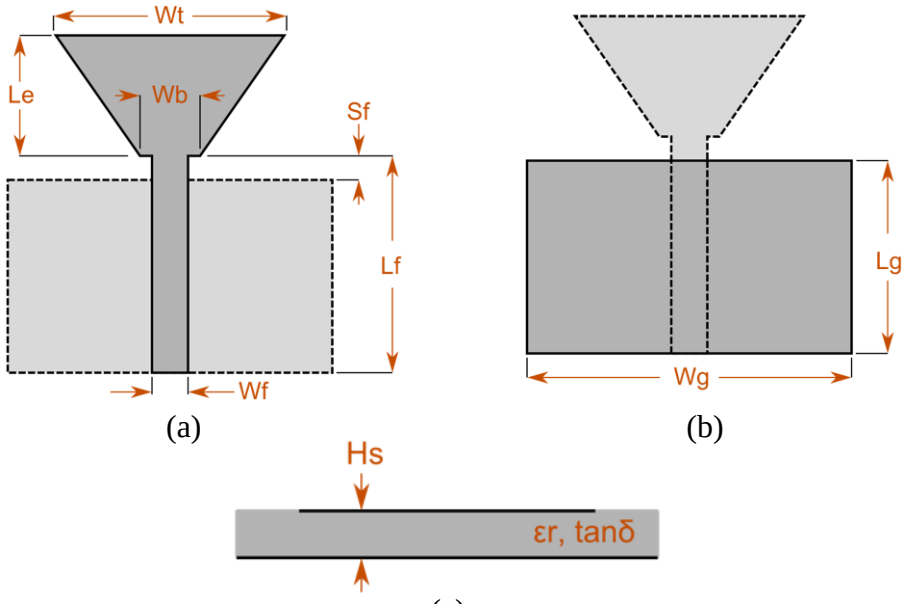

(a) (b)

(c)

Figure 9: The specifications of the planar trapezoidal monopole antenna (2.4 GHz).

Table 16 and Figure 10 elaborate on the design specifications of the Circular Pin-Fed Linearly Polarised Patch Antenna, which was designed to operate at 2.4 GHz. As can be seen in the specifications, the maximum dimensions of all antennas are within the requirements indicated by the veterinary expert.

Table 16: Detailed design specifications of the circular pin-fed linearly polarised patch antenna (2.4 GHz).

Name	Description	Value
D	Patch Diameter	49.75 mm
Sf	Feed Offset	5.566 mm
R	Feed Pin Radius	331.2 µm
H	Substrate Height	2.650 mm
ε_r	Relative Permittivity	2
tanδ	Loss Tangent of the Substrate Medium	0
X	Patch Diameter	49.75 mm
Y	Patch Diameter	49.75 mm
Z	Substrate Height	2.650 mm

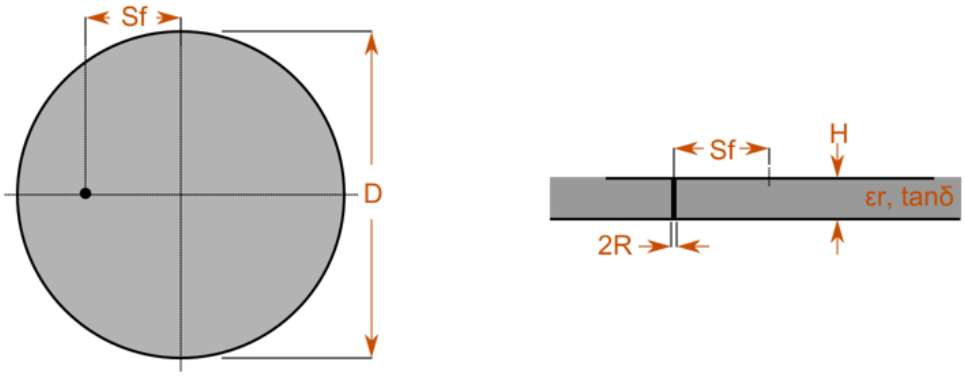

Figure 10: The top view (Left) and side view (Right) of the circular pin-fed linearly polarised patch antenna (2.4 GHz).

The MFPEMA and PIFA designs are quite similar in their simulated characteristics and are the recommended antennas for implantation. Many literature sources support using antennas such as the inverted-F antenna or variations thereof for implantation purposes. The PTMA and CPFLPPA designs were also quite similar with regards to their simulated characteristics. Although these designs are far less efficient than the previously mentioned antennas, they were still created and tested as a final validation of their characteristics.

2.6.2 Practical Antenna Measurements

The four antenna designs previously mentioned in this chapter, were created and tested within an anechoic chamber. Each design was constructed twice to deliver one transmitting antenna and one receiving antenna. Figure 11 illustrates the PCB antenna transmitting and receiving pairs.

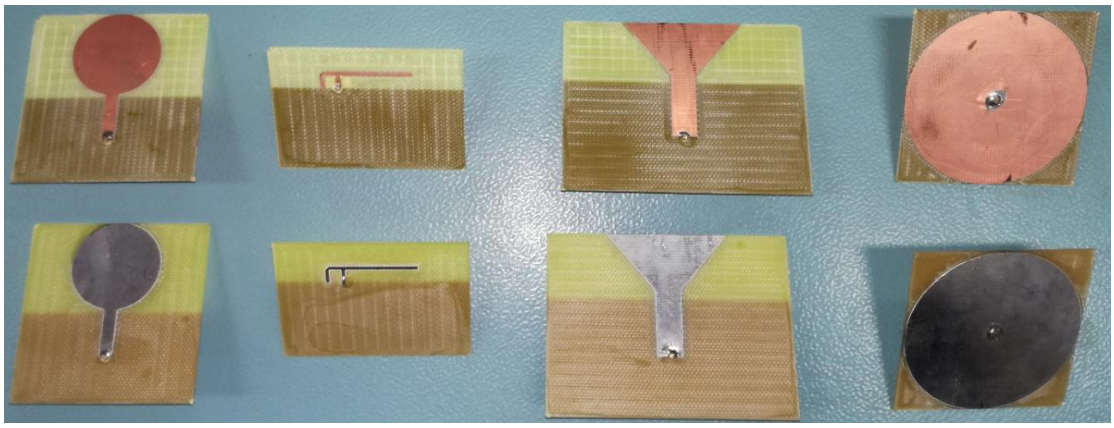

Figure 11: Transmitting and receiving PCB antenna pairs.

The practical measurements and the simulated results were compared in order to establish whether or not the practical antennas are in agreement with what is expected from the simulations and to create a basis for comparison in other experiments. The transmitting antennas (the antennas used for implantation) were printed on a 1.5 mm substrate with an aluminium finish. The receiving antennas (the antennas secured outside of the phantom material) were printed on a 1 mm substrate with a copper finish. Although this caused differences in the s11 measurements of the antennas as depicted in Table 17, the propagation characteristics in terms of the E-field of the antennas remained almost identical as illustrated by Figure 12. The same figure illustrates the agreement between the simulated and practical results of the E-Field magnitudes of the MFPEMA antenna design.

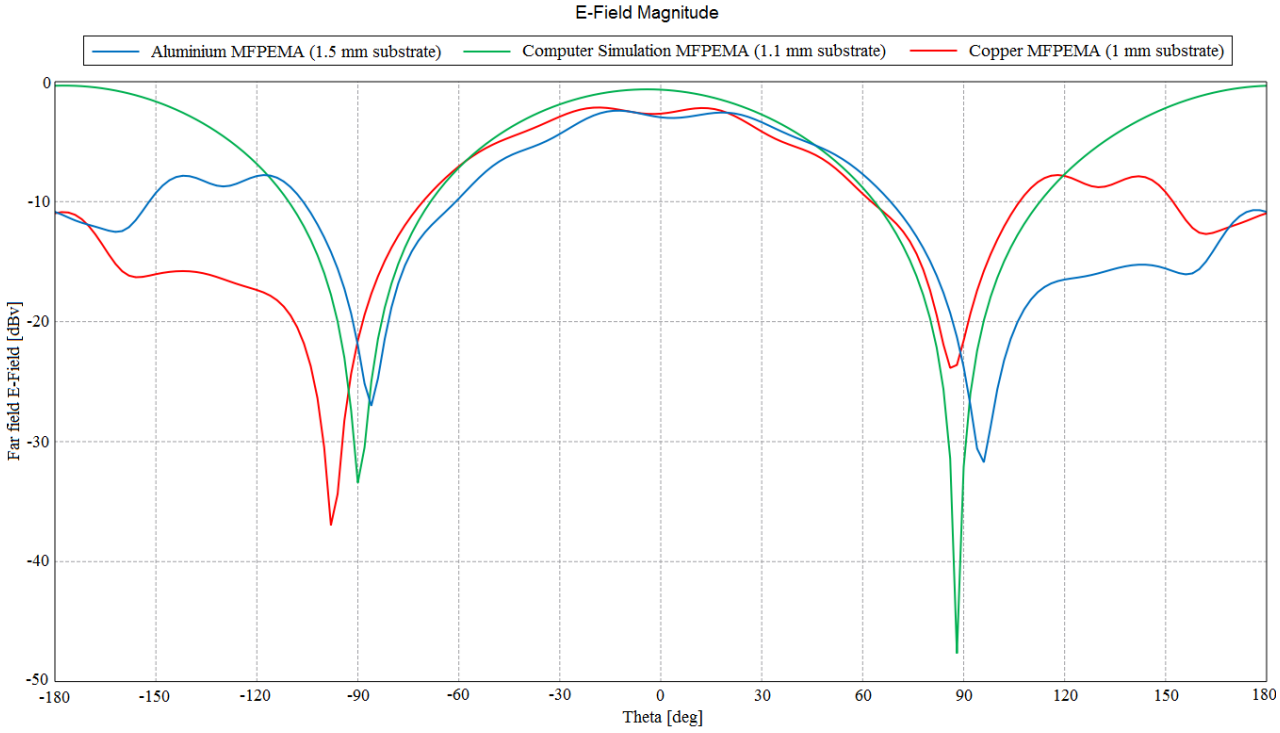

Figure 12: E-field Comparison between the practical and simulated MFPEMA antenna

Table 17: S_{11} Measurements of the practical PCB antenna pairs.

Antenna	Aluminium (1.5 mm substrate)	Copper (1 mm substrate)
MFPEMA	-26.10 dB	-6.64 dB
PIFA	-4.68 dB	-2.72 dB
PTMA	-4.83 dB	-1.73 dB

The practically measured E-field in the range -90° to -180° and in the range 90° to 180° differs from the simulated E-field values at those angles, due to the base station to which the antenna was connected within the anechoic chamber. The face of the antenna is orientated at 0° degrees (perpendicular to the substrate) and thus the lowest E-field values are attained at ±90° angles, which are aligned with the substrate. The small variation in angle of these points are caused by the slight miss-alignment of the antennas within the anechoic chamber and can therefore be dismissed. Although the base station clearly absorbed some of the energy radiating from the antenna as seen at the ±180° angles, the remainder of the radiation pattern is in good agreement with the simulated results for both constructed antennas. Thus, these antennas are good representations of the simulation models and are used from here on, to compare further practical measurements to the simulated results.

2.7 Conclusion

The literature identified 403 MHz, 910 MHz and 2.4 GHz as viable frequencies of operation, along with restrictions regarding their usage. Various gelling mediums were discussed and agar was selected as the phantom material for this project. Agar recipes were investigated and methods for calculating the specific permittivity and conductivity values of the approximated rhinoceros dielectric properties were established. Numerous implantable antenna designs were identified and practical measurements validated their comparability to the simulation models. The MFPEMA and PIFA were chosen as the antenna designs to be used in numerical simulations and practical experimentation.

Chapter 3.

3. Computer Simulation Models

Computer software was used to calculate the effects of electromagnetic propagation prior to conducting any practical experiments. These computer simulations were not only helpful in verifying the safety of the implantation device, but also in providing estimations regarding the functionality and limitations of the device prior to construction. These results were then used to improve the design of the device and to establish a benchmark for comparison with the physical model parameters. The software applications used for creating and testing dielectric mediums and antenna propagation were CADFEKO [24] and Antenna Magus [25], which were used in conjunction with auxiliary software programs such as 123D CAD [26] and Blender [27] to sculpt and create the phantom and anatomical rhinoceros computer simulation models. This chapter elaborates on the model designs and methods used in the computer simulations.

3.1 Computer Simulation Configuration

Method of Moments (MoM) techniques such as the Surface Equivalent Principle (SEP) were utilized to simulate the electric and magnetic properties of the various dielectric materials used in the simulations. The method of moments bounds arbitrarily-shaped planar multilayered media into finite sized dielectric objects, whose surfaces are discretised as triangles. Thus, the surface of such an object is approximated by a SEP triangle mesh, whilst the internal layers are approximated using the multilayered dielectric media method [28]. Dielectric media with specific dielectric properties were designed to simulate the tissue properties as discussed in Chapter 4 (page 37), whilst object meshes simulating the shape and size of rhinoceros organs were designed to contain the various dielectric mediums. Figure 13 illustrates an example of a mesh used in the surface equivalence principle for calculating the magnetic and electric currents on the surface of a spherical dielectric body. Adjacent mesh elements form surface boundaries and the spaces between these boundaries define volumes with specific dielectric properties.

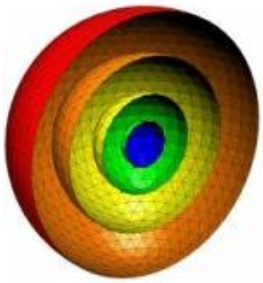

Figure 13: Example of the surface equivalence principle mesh **[28]**.

The number of triangle mesh elements used to approximate the true surface affects the computation time required to evaluate the behaviour of objects, such as antennas and tissue materials. A finer mesh results in more accurate estimations due to smaller increments in the surface approximations used for the electromagnetic calculations. One of the methods to reduce computation time is to assume symmetry of the objects under study. This can halve the time required to calculate the propagation through those specific objects. Other methods include adjusting the size of the mesh elements of the simulation model to a tenth of the minimum wavelength of the appropriate antenna, where the minimum wavelength of the antenna is defined as the speed of light divided by the maximum frequency of the antenna. Furthermore, the Multilevel Fast Multipole Method (MLFMM) was applied, which represents an alternative MoM formulation applicable to electrically large objects [29]. Figure 14 illustrates an example of how

the MLFMM discretizes an electrically large model into smaller cubes (or variables), which are more easily solved and combined to interpret the full model.

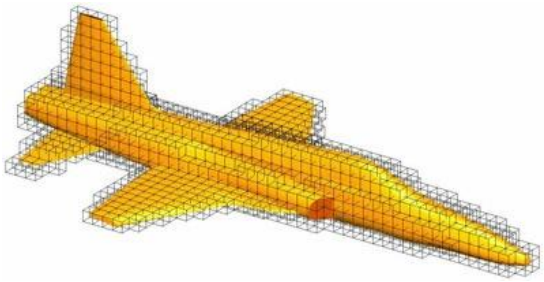

Figure 14: Example of the MLFMM discretization of an electrically large model **[29]**.

The chosen methods to reduce the model complexity with regards to mesh elements proved successful. The use of a super computer was still required to execute the more intricate (large and layered) simulations, however. Simpler models such as the propagation of antenna designs in free space and infinite mediums were possible without the use of enhanced hardware, in order to efficiently manage the available resources.

3.2 Rhinoceros Simulation Models

To investigate the characteristics of candidate antenna designs and their propagation properties through rhinoceros tissue, computer simulation models were designed. Two models were used, firstly an anatomically accurate rhinoceros model and secondly a cylindrical phantom model. Both these models consist of various layers with specific thicknesses and dielectric properties to simulate the skin, fat, muscle and blood (organs) of a rhinoceros. A skeletal and organ model were created with specific dielectric properties for the various frequencies. These models were not included in the anatomical rhinoceros model, due to their high computational requirements and unknown volumes and shape, which have yet to be measured from actual rhinoceros. The skeletal and organ models can be viewed in Section 6.3.2 (page 89).

Both models have numerous configurations to simulate various scenarios. For instance, three positions were considered for the location of the implanted antenna – one behind the head (in the neck), one below the head (in the neck) and one in the chest. These positions were also approximated for the cylindrical models, although the position of the chest implantation and the back of the neck implantation were simplified to one model due to the symmetry of the cylinder. There are also two configurations for the permittivity of the rhinoceros dermis, one according to a weighted average and one approximated from various literature studies as described in Chapter 4 (page 37). All of the above-mentioned configurations were simulated at the frequencies of 403 MHz, 910 MHz, 2.4 GHz and 4.5 GHz with specific dielectric properties for each tissue and organ with regards to the specific frequency.

3.2.1 Model Size and Layering

The approximations for the size of the anatomical and cylindrical simulation models were based on the fact sheet published by the International Rhino Foundation [30]. These sizes were compared to those indicated by other sources such as Bearcraft and Jamieson [31], Jun Huang [32] and Shadwick et al [1] in order to establish a computer model based on realistic sizes. The final dimensions of the anatomical model are indicated in Figure 15 and the layered cylindrical model is illustrated in Figure 16.

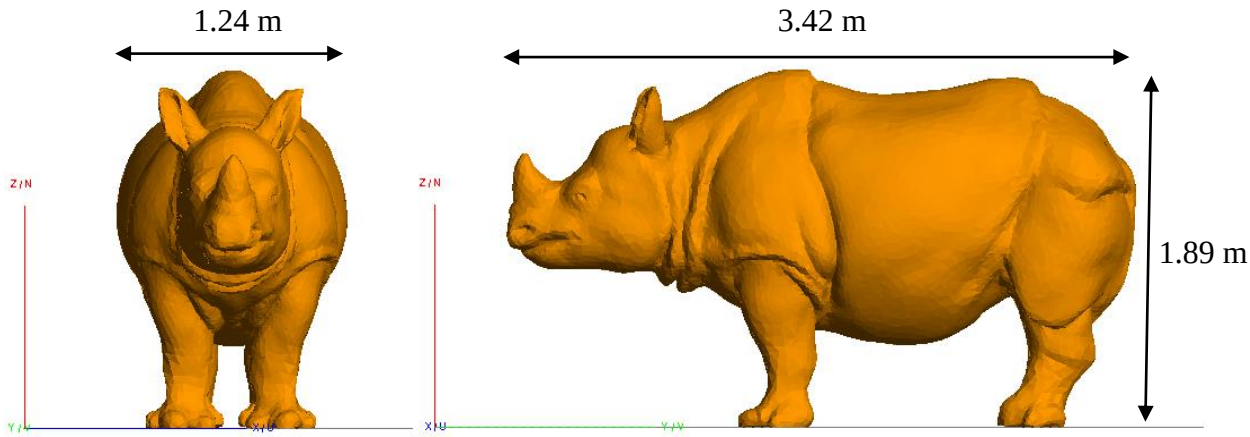

Figure 15: Dimensions of the anatomically accurate rhinoceros computer simulation model.

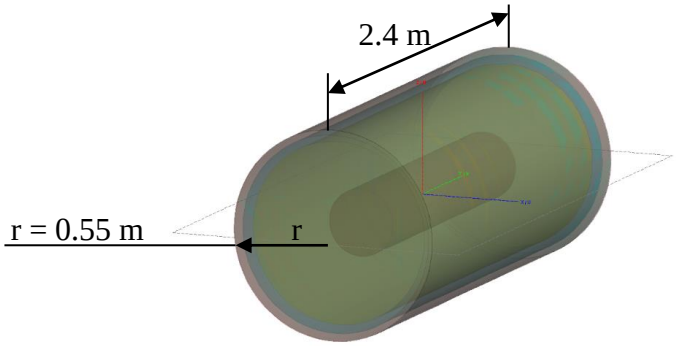

Figure 16: Layered cylindrical rhinoceros computer simulation model.

The cylindrical model approximates the torso of a rhinoceros and therefore does not include the head or legs. It consists of five cylinders located within one another, and modelling the epidermis, dermis, fat layer, muscle layer and blood respectively. The exterior cylinder has a length of 2400 mm and a radius of 550 mm. The layers of both models are spaced identically with thicknesses as illustrated in Figure 17 and Figure 18. Each surface encapsulates a volume to which a specific permittivity and conductivity value is assigned – the innermost volume is referred to as the "blood" layer and represents the organs of the rhinoceros to simplify the model.

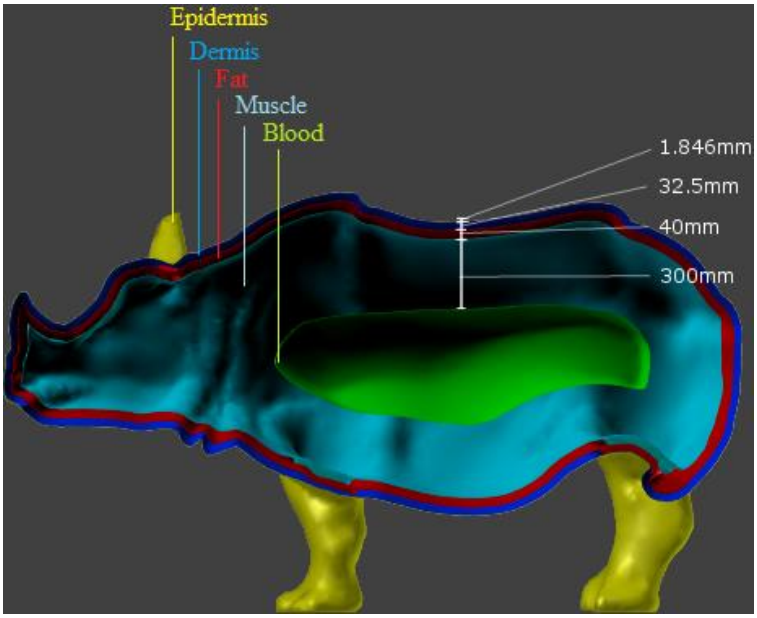

Figure 17: Layered anatomically accurate rhinoceros computer simulation model.

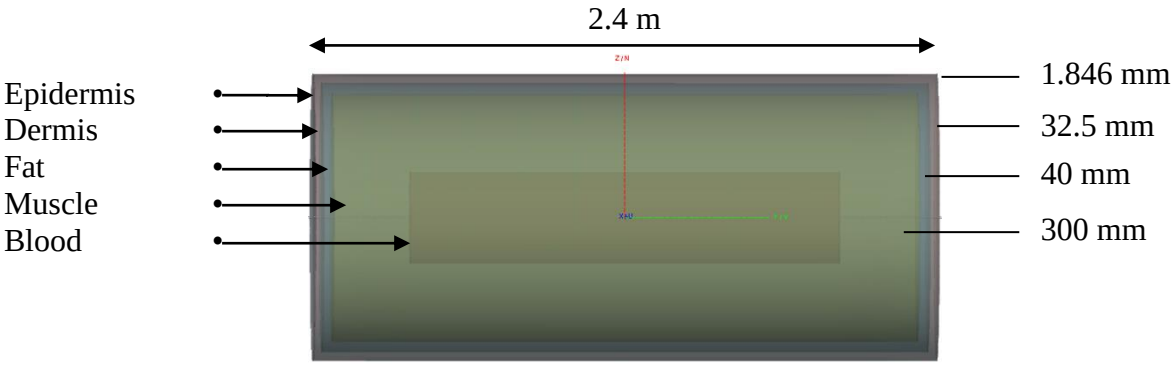

Figure 18: Dimensions of the layered cylindrical phantom computer simulation model.

The thicknesses of the layers were approximated by averaging measured values of actual rhinoceros tissue [1] [31] [23] and typical values for field rhinoceroses [33]. Figure 19 illustrates the individual layers of the anatomical model and Figure 20 illustrates the individual layers of the cylindrical model.

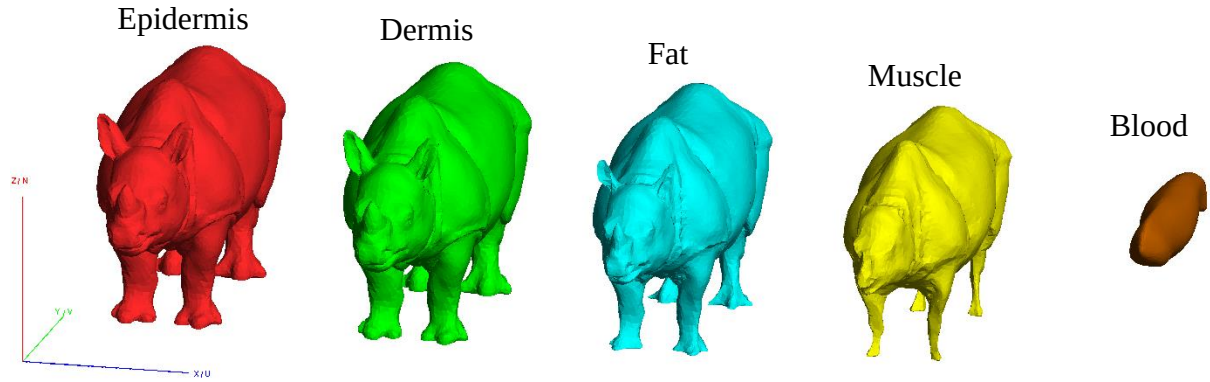

Figure 19: Individual layers of the anatomically accurate rhinoceros computer simulation model.

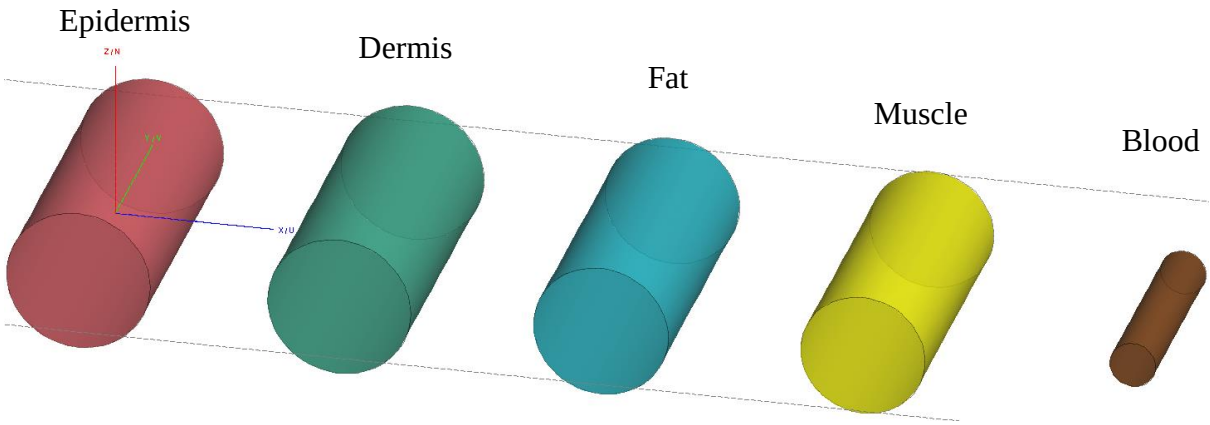

Figure 20: Individual layers of the cylindrical rhinoceros computer simulation model.

3.2.2 Potential Points for Implantation

Consultation with a wildlife veterinary specialist identified three locations within the body of the rhinoceros as possible points of implantation - the back of the neck (behind the head), the front of the neck (below the head) and the chest (between the front legs). In each case the implantation device could be situated within the subcutaneous fat layer, as illustrated in Figures 21 to 25.

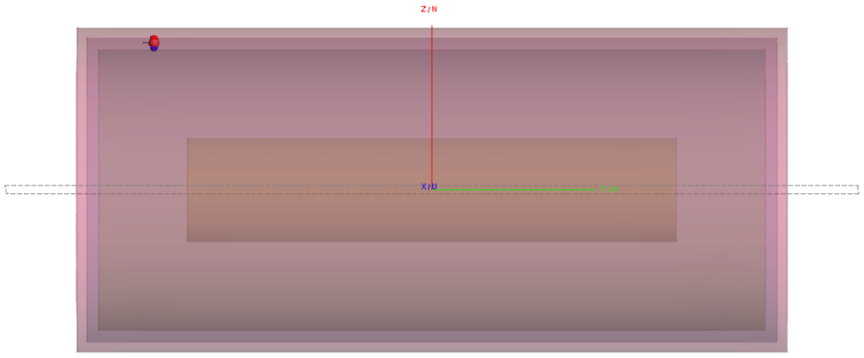

Figure 21: Position of the back and chest implantation in the cylindrical phantom model.

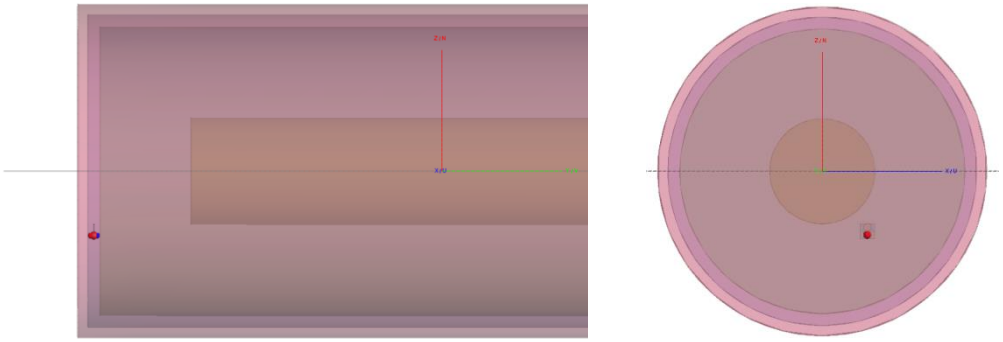

Figure 22: Position of the neck implantation in the cylindrical phantom model.

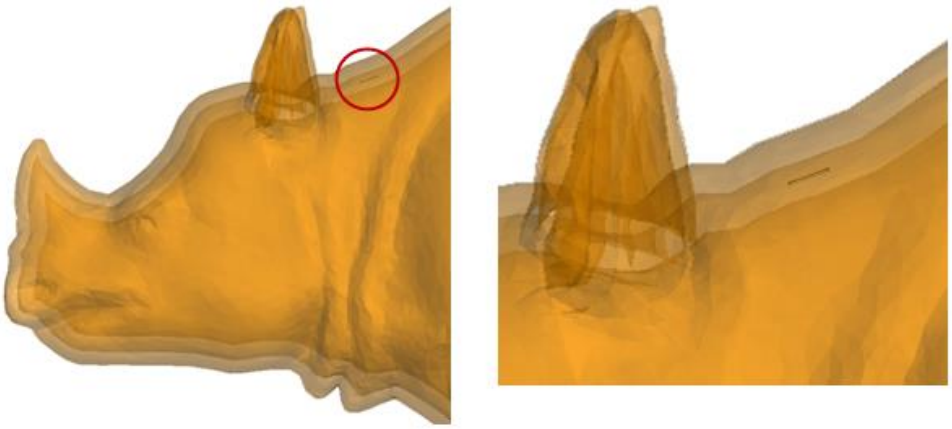

Figure 23: Position of the back implantation in the anatomical model.

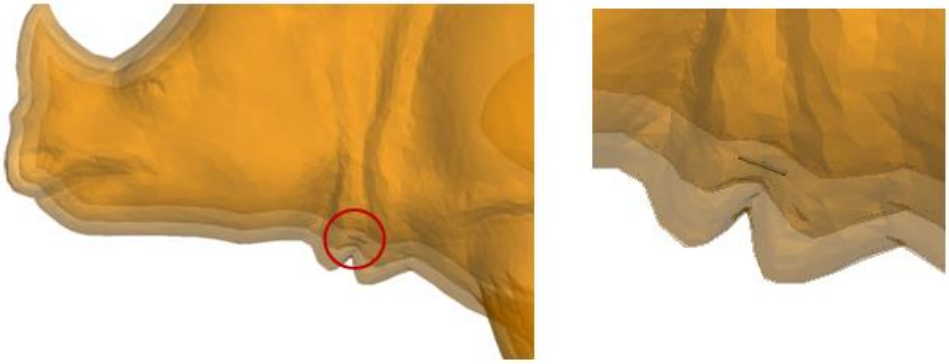

Figure 24: Position of the neck implantation in the anatomical model.

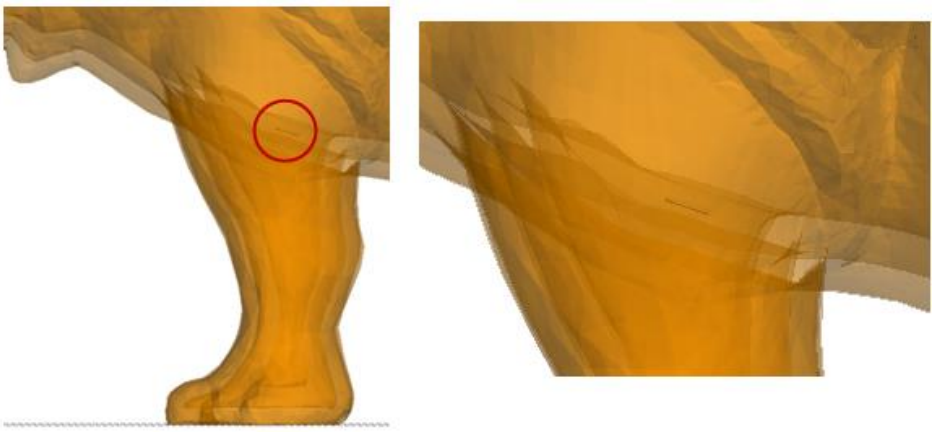

Figure 25: Position of the chest implantation in the anatomical model.

Figures 21 to 25 show that the implantation devices within the cylindrical phantom models and the anatomical models in all cases have their antennas flush (angle of 0 degrees) to the outside surface of the animal and facing outward to allow maximum radiation. The device is placed at an off-centre position in the cylindrical neck implantation model to minimize the distance from the potential heart sensor to the antenna.

The technical details regarding the execution of one rhinoceros simulation, are as follows:

Computer:

PC LINUX EM64T MKL IMPI -- fat03
Linux x86_64 3.10.0-514.6.1.el7.x86_64
Intel(R) Xeon(R) CPU E7-4850 v3 @ 2.20GHz; GenuineIntel family 6 model 63 stepping 4 brand id 0
4 physical CPUs with a total of 56 processors found (multi-core CPUs with max. 14 cores per physical CPU)

Maximum number of triangles for the layered rhinoceros model = 864984 triangles

Summary of memory requirement for MLFMM (in total for all parallel processes)

Near field matrix:	37638.68	MByte
Far field matrix	388244.35	MByte

Total:	425883.03	MByte
For comparison classical to MoM:	51369881.50	MByte

Per process, 34.621 GByte of memory was allocated dynamically, which corresponds to 1.014 TByte in total for all processes together. A total runtime of 24.657 hours was required.

3.3 Summary

Three-dimensional models of the body of a rhinoceros were developed for use in numerical EM simulations. Anatomically accurate as well as cylindrically approximated three-dimensional models with associated permittivity values were defined to account for the epidermis, dermis, fat, muscle and blood layers of the animal's body. Strategies for reducing the computational requirements of the simulation models, such as the Multilevel Fast Multipole Method (MLFMM) and the Sparse Approximate Inverse (SPAI) technique, proved successful and allowed the models to maintain complex geometries.

Chapter 4.

4. Approximation of Rhinoceros Tissue Permittivity and Conductivity

The dielectric properties of rhinoceros tissue have yet to be measured in practice. Here, these values are approximated using the permittivity and conductivity of animals with similar characteristics.

4.1 Approximation of Dielectric Properties

Gabriel et al [34] obtained the dielectric properties of various animal tissues by considering this data from published papers extending back five decades before the time of their study conducted in 1996. The compilation of data was illustrated in a graphic format which presented the permittivity and conductivity values for the blood, bone cancellous, bone cortical, fat, grey matter, white matter, kidney, spleen, heart, liver, lungs, muscle and skin of various animals. The temperature of the tissue samples during measurements ranged between 20°C and 37°C. Data in the frequency range between 1 MHz and 10 GHz was used to approximate rhinoceros tissue, although the frequencies used in the initial study had a wider range. This data, combined with data from similar studies conducted by Hall and Hao [11], Azad [35], Johansson [6], Conran [5], Olewale [12] and Rauf [36] constituted to the basis for our rhinoceros approximations.

The animals used among these studies for approximating rhinoceros tissue were canine, bovine, equine, feline, frog, human, mouse, ovine, pinniped, porcine, rabbit and rat. Of course, certain animals are more similar to rhinoceroses than others. Specifically, bovine (cattle) have similar skeletal characteristics to rhinoceroses while equine have similar intestinal and organ characteristics to rhinoceroses [23]. Weighted averages of the permittivity and conductivity values for each organ or tissue at each of the four frequencies used in this study, were calculated to estimate the corresponding values for rhinoceros tissue. The contribution of each animal for each specific tissue sample was selected by means of a decision matrix, which determined the similarity of the animal to a rhinoceroses by comparing various physical characteristics. Each characteristic was assigned a level of importance to distinguish between essential and auxiliary identifiers for approximating the model. A multiplier system was used to ascribe greater weight to characteristics of higher importance.

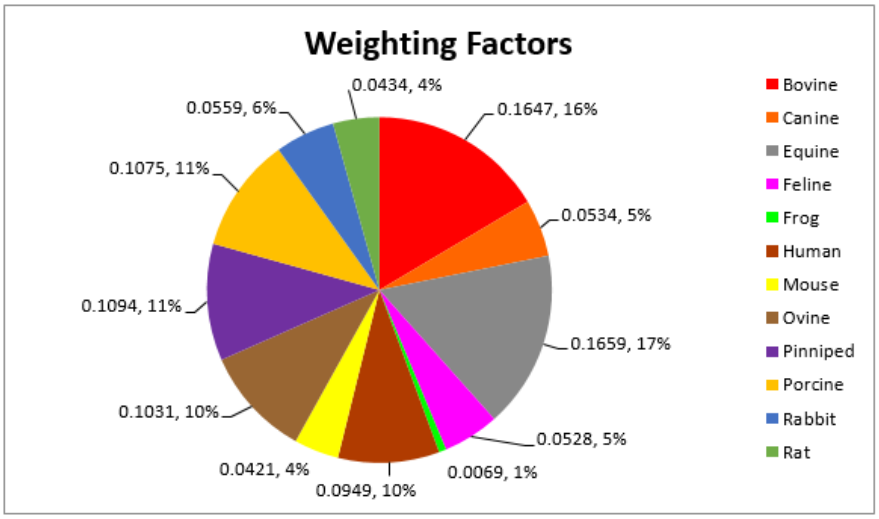

Figure 26: Weighting factors of animals contributing to rhinoceros tissue approximations.

The decision matrix and similarity criteria can be viewed in Appendix K (page 142) and the calculations regarding all the animal's contributions to specific tissue types can be viewed in Appendix L (page 144). The weighting factors representing each of the animals' contribution were calculated by comparing each animal's subtotal to a global total number of points. Figure 26 illustrates the final contributions the dielectric properties of each considered animal should have on the rhinoceros model. These results indicate that equine, bovine, pinniped and porcine are most similar to rhinoceroses and will consequently have a greater influence on the dielectric properties of the various tissues. The weighting factors were used to calculate a weighted average for the permittivity and conductivity of each tissue and organ type at each of the specified frequencies. These results are indicated in Table 18 by the values within the "Approx." column. The permittivity and conductivity values indicated within the "Avg." column are the calculated averages without applying the weighting factors.

Table 18: Rhinoceros tissue permittivity and conductivity approximations.

Lower Frequency Spectrum								
Biological Tissue	**403 MHz**				**910 MHz**			
	Permittivity		**Conductivity**		**Permittivity**		**Conductivity**	
	Approx.	**Avg.**	**Approx.**	**Avg.**	**Approx.**	**Avg.**	**Approx.**	**Avg.**
Blood	63.98	70.00	1.27	1.26	59.14	63.75	1.49	1.46
Bone Cancellous	19.21	19.00	0.19	0.22	17.50	17.33	0.34	0.39
Bone Cortical	10.89	11.75	0.10	0.10	9.78	10.50	0.15	0.14
Fat	11.36	11.60	0.09	0.11	10.07	10.10	0.11	0.14
Grey Matter	63.03	60.73	0.87	0.92	54.35	53.42	1.17	1.26
White Matter	47.80	47.80	0.51	0.52	36.44	39.00	0.82	0.88
Kidney	48.58	51.00	1.12	1.08	45.32	47.80	1.69	1.76
Spleen	55.01	57.00	1.08	1.13	49.49	50.60	1.50	1.47
Heart	45.17	52.50	1.14	1.04	41.26	47.00	1.61	1.49
Liver	49.49	50.83	0.90	0.94	43.46	44.67	1.14	1.16
Lung	35.65	37.33	0.55	0.57	31.91	33.33	0.75	0.77
Muscle	65.94	64.43	1.12	1.06	59.23	58.29	1.36	1.31
Skin	41.24	41.69	0.48	0.48	39.79	40.00	0.74	0.73
Upper Frequency Spectrum								
Biological Tissue	**2.4 GHz**				**1 MHz - 10 GHz (Avg)**			
	Permittivity		**Conductivity**		**Permittivity**		**Conductivity**	
	Approx.	**Avg.**	**Approx.**	**Avg.**	**Approx.**	**Avg.**	**Approx.**	**Avg.**
Blood	54.14	58.75	2.56	2.46	57.26	57.50	1.30	1.34
Bone Cancellous	15.78	15.67	0.68	0.80	59.01	53.33	0.18	0.20
Bone Cortical	8.78	9.50	0.29	0.27	29.28	32.38	0.11	0.13
Fat	8.29	8.50	0.18	0.24	20.71	21.10	0.07	0.08
Grey Matter	43.85	43.48	2.29	2.30	52.91	56.36	0.99	1.12
White Matter	32.53	35.04	1.44	1.50	46.21	43.82	0.58	0.73
Kidney	40.56	43.40	2.68	2.58	64.46	63.00	1.06	1.02
Spleen	45.83	47.20	2.12	2.12	113.93	99.00	0.86	0.99
Heart	34.47	39.50	2.47	2.35	52.21	53.75	0.78	0.94
Liver	39.14	39.67	1.75	1.82	59.20	55.83	0.46	0.45
Lung	27.57	27.67	1.05	1.07	63.26	61.67	0.67	0.65
Muscle	53.40	53.29	2.06	2.04	65.47	62.86	1.16	1.00
Skin	36.41	36.36	1.43	1.38	39.65	39.34	0.80	0.76

As can be seen in Table 18, the permittivity of the tissue materials tends to decrease with a rise in frequency and the conductivity of the materials tends to increase with a rise in frequency. It is also worth noting that the permittivity and conductivity values of bone cancellous, bone cortical and fat are vastly different from the other tissue types for each of the frequencies. Due to the uncertainty of the dielectric properties of these materials in the literature, they were identified as irregular values regarding the phantom recipe approximations.

Another method that can be used to determine the permittivity of rhinoceros dermis, was to identify the components present in the dermis and to use their corresponding dielectric properties to estimate the collective permittivity of the skin. According to Shadwick et al [1], the dorsolateral and belly skin of the rhinoceros which they examined had a water content of approximately 60.9% (+/- 1.2%), the collagen content of the dry faction was 85% and the collagen of the tissue wet mass was 33.2%. The dielectric constant of water was selected as 80 [37], the dielectric constant of wet collagen was selected as 4.5 [4] and the dielectric constant of dry collagen was selected as 2.3 [4]. The remaining tissue was approximated as 0.1MNaCl, which has dielectric properties similar to human tissue and is often used in phantom tissue simulations [7]. Peyman et al [7] determined the dielectric of this material as 78.8 with a Debye-model at 20°C, which is similar to the value (77.1) given by the Debye-model (at 20°C) used by Stogryn (1971). All of the above values were used to calculate the permittivity of the rhinoceros dermis:

$$
\begin{aligned}
\text{Alternative permittivity estimate (Dermis)} &= (\%\ \text{water} \times \varepsilon_{water}) \\
&\quad + (\%\ \text{wet collagen} \times \varepsilon_{wet\_collagen}) \\
&\quad + (\%\ \text{dry collagen} \times \varepsilon_{dry\_collagen}) \\
&\quad + (\%\ 0.1\text{MNaCl} \times \varepsilon_{0.1MNaCl}) \\
&= (60.9\% \times 80) + (33.2\% \times 4.5) + (5.015\% \times 2.3) \\
&\quad + (0.885\% \times 78.8) \\
&= 51.026725 \\
&\approx 51.03
\end{aligned}
$$

The dermis weighted average approximations in Table 18 of 41.24, 39.79, 36.41 and 39.65 for their respective frequencies of 403 MHz, 910 MHz, 2.4 GHz and 1 MHz to 10 GHz are all lower than the alternative approximation of 51.03. Following the same trend with regards to the change in permittivity values relative to frequency as mentioned earlier, the alternative approximation resembles a permittivity measurement taken at a frequency lower than 403 MHz, although the exact frequency is unknown which could explain the difference between this permittivity value and the value suggested by the weighted average approximation. Both the weighted average dermis permittivity approximation and the “Shadwick” dermis permittivity approximation illustrated above, were used in computer simulation models to represent the thick skin of a rhinoceros, seeing as the true permittivity value of rhinoceros skin is unknown. The conductivity of the dermis model was kept the same for these two configurations in order to observe the effect of the adjustment in permittivity, so that the results of these simulations may be compared to each other.

4.2 Summary

The dielectric properties of rhinoceros tissue were approximated for frequencies within the ISM band, using the permittivity and conductivity of animals with similar characteristics. A second approximation for the rhinoceros dermis was made by considering the dielectric properties of the individual components of the skin to estimate its collective permittivity. These approximations were used in numerical simulation and practical models as described in Chapter 5 (page 40) and Chapter 6 (page 68).

Chapter 5.

5. Agar Samples of Rhinoceros Tissue

The procedure for creating the rhinoceros organic tissue simulating agar plates for the frequencies of 403 MHz, 910 MHz, 2.4 GHz and 4.5 GHz, as used for this project, are described in this chapter. Recipes for developing rhinoceros tissue can be viewed in Appendix N (page 154).

5.1 Agar Preparation

The recipes for developing rhinoceros tissue simulating materials were carefully realised in accordance with standard genetics and biochemistry lab sterilization procedures. Safety requirements, such as the use of a lab coat and latex gloves, were adhered to at all times and samples were clearly labelled and kept under constant supervision until such a time that the samples were put into refrigeration. All work surfaces and utensils were sterilised with 70% ETOH prior to use, between methodological proceedings and once again after specific task completion. Flasks and similar apparatus were also cleansed with distilled water prior to and after usage. In total, 75 recipes were used to create 300 agar plates - 100 ml of each material was used to create four agar plates in order to allow an average permittivity to be calculated. The total amount of required ingredients are as follows:

Total Amount of NaCl	=	355.63	g
Total Amount of Sucrose	=	6375.61	g
Total Amount of Agar	=	187.5	g
Total Amount of Benzoic Acid	=	75	g
Total Amount of Water	=	7500	ml

Sigma-Aldrich is a well-known supplier of chemicals and lab equipment in the biology, genetics and chemistry industries. The quantities and cost price of the specialized ingredients that could be used to fabricate the recipes are illustrated in Table 19.

Table 19: Sigma-Aldrich cost of ingredients (As seen on 14 September 2016).

Substance/Material	Quantity	Price
Sodium Chloride (BioXtra)	1 kg	R498.00
Sucrose (BioXtra) >= 99.5 % (GC)	5 kg	R5,820.00
Agar Powder (For Microbiology)	250 g	R1,034.00
Water (Double-Processed Cell Culture)	6 litre	R2,720.00
Petri Dish (100 mm x 15 mm)	500	R1,602.00
Total Cost		**R11,674.00**

The use of benzoic acid was omitted, seeing as the sterilization process of the autoclave was sufficient to deliver plates that would survive long enough for accurate measurement. If the cost of benzoic acid were to be added, the total cost would accumulate to R11 894.00. The calculations for the actual total cost of the used ingredients and materials, are as follows:

Cost of Petri Dishes:
R1,602.00/500 = R3.20/petri dish
Thus, 65 recipes x 4 petri dishes x R3.10 = R832.00

Cost of NaCl:
(Total NaCl/Order Quantity) x Cost Price = (355.63 g/1000 g) x R498.00
= R177.10

Cost of Pure Sucrose:
(Total Sucrose/Order Quantity) x Cost Price = (500 g/5000 g) x R5,820.00
= R582.00

Cost of Commercial Sugar:
5 kg bags x Cost Price = 2 x R34.99
= R69.98

Cost of Agar:
(Total Agar/Order Quantity) x Cost Price = (187.5 g/250 g) x R1,034.00
= R775.00

Total Cost of Used Ingredients = R2,436.08

As can be seen from the cost calculations, two types of sugar were used for mixing the agar plates – a household variety purchased from a supermarket and a purified form purchased from Sigma-Aldrich. The less expensive or impure sugar was included in an attempt to reduce the total cost of the agar plates. Although the effect of the impure sugar is severely mitigated by the sterilization process of the autoclave, duplicates of specific recipes were made with one batch using purified sugar and one batch using impure sugar, in order to establish whether or not the type of sugar has a significant impact on the results. The comparison between the results achieved with the two types of sugar are given in Section 5.3 (page 56). The distilled water and equipment used to fabricate the agar plates were provided by the JC Smuts Post-Graduate Genetics Laboratory at the University of Stellenbosch, which included safety gear, sterilization equipment and general utensils such as flasks, weighing scales, thermometers and magnetic stirrers.

The fabrication of an agar plate starts with labelling the flasks with the appropriate tissue description and frequency, before adding the dry ingredients of agar powder, NaCl and sucrose to the flask. 500 ml flasks were used to compensate for the water volume to be added and for the expansion which occurs during heating. Each dry ingredient was weighed separately to an accuracy of two decimal points before being added to the flask. A measuring flask was used to add exactly 100 ml of distilled water to each of the recipe mixtures. Figure 27 shows the scale and weigh boats used to weigh the dry ingredients and Figure 28 shows the measuring flask used to add the distilled water to the dry ingredients.

Figure 27: Weighing of the dry ingredients.

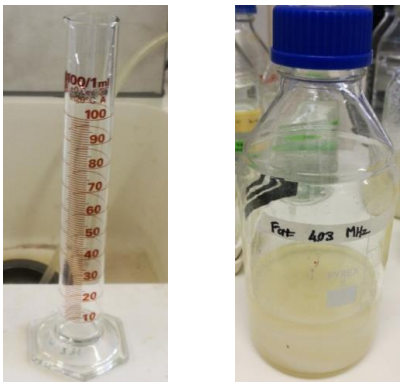

Figure 28: Addition of the distilled water.

Usually, such mixtures are placed directly into the autoclave for heating and sterilization. However, due to the large quantities of sugar required by the recipes, the mixtures were dissolved prior to autoclavation using a magnetic stirrer as illustrated in Figure 29. Figure 29 also shows the properly sealed autoclave used to sterilise the samples. This is a high-temperature, pressurized system and thus care must be exercised whilst operating this equipment, especially when steam is released when opening the locking mechanism. The agar powder melts at approximately 100°C, but stalls at approximately 50°C. Thus, the still warm flasks were removed from the autoclave and placed in a warm water bath at 55°C (just above the stalling threshold) to keep the samples in a fluid state until use. The petri dishes can now be appropriately labelled within a laminar flow machine to minimize contamination. The remaining recipe steps were conducted within the laminar flow, which filters the air at a microbial scale and blows cleansed air over the working station. Care was taken to always use 70% ETOH to clean the working station, the latex gloves and all other utensils prior to use and to refrain from exhaling over the samples or empty petri dishes. Figure 30 shows the petri dishes within the laminar flow.

(a) (b)

Figure 29: (a) Magnetic stirrer and (b) sterilisation of the sample materials within an autoclave.

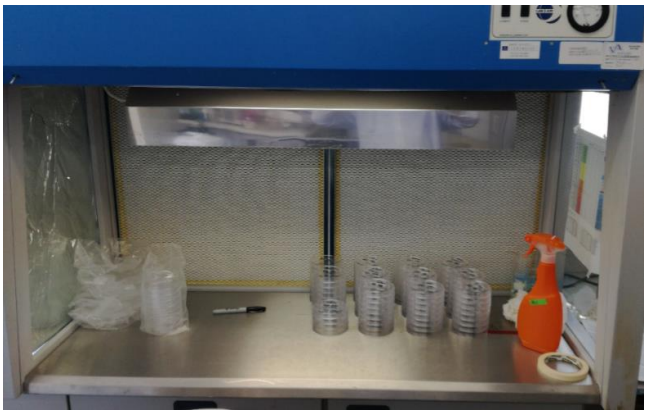

Figure 30: Laminar flow machine with sterilized petri dishes.

The sample mixtures can be poured into the petri dishes under the protection of the laminar flow and left to cool with the lids placed ajar to allow heat to escape and minimise the formulation of moisture droplets on the inside of the lid. Air bubbles can be moved to the side of the petri dish while the content is still warm by using a sterilised probe tip. Once the dish has sufficiently cooled and set, the lid can be closed and sealed. The sterilized and finished samples, as shown in Figures 31 and 32, were arranged in stacks, wrapped, placed in plastic sleeves and resealed again before being refrigerated at 4°C until used for measurements.

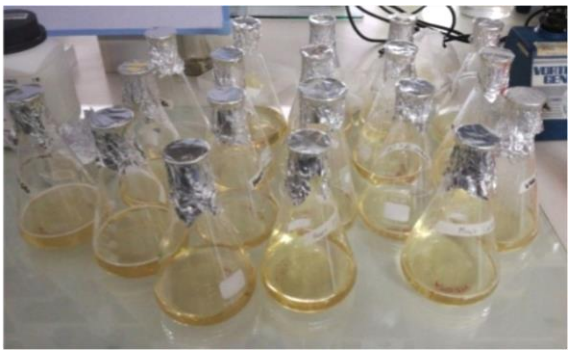

Figure 31: Sterilized sample materials.

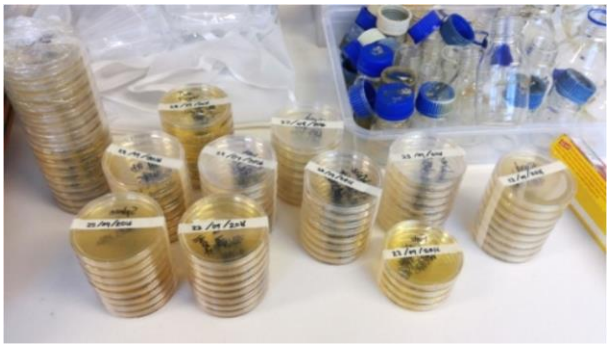

Figure 32: Completed agar plates of phantom material recipes.

5.2 Permittivity Measurement

A broadband measurement system, developed and presented by J.I.F. Marais [38], was utilised in conjunction with a network analyzer to measure the dielectric properties of the fabricated phantom material agar samples. The system consists of open-ended coaxial SMA-, N- and 7/16-type probes, which are suited for measurements of both solids and liquids. All three types of probes were calibrated and used to measure the dielectric properties of known materials such as Teflon and Perspex, of which the results indicated that the N-Type probe had the greatest

accuracy. Thus, the need for more than one probe was eliminated and the calibration process was simplified. Once the system was calibrated as specified by Marais, it was tested by measuring the S_{11}-parameters of well-known materials such as Teflon (PTFE), Nylon and Perspex. These S_{11} measurements were then converted to their respective dielectric constants by means of the MATLAB script illustrated in the external media (Appendix I, page 133). Marais derived an equivalent circuit from the physical topology of the probe as illustrated in Figure 33(a), which he approximated as illustrated in Figure 33(b).

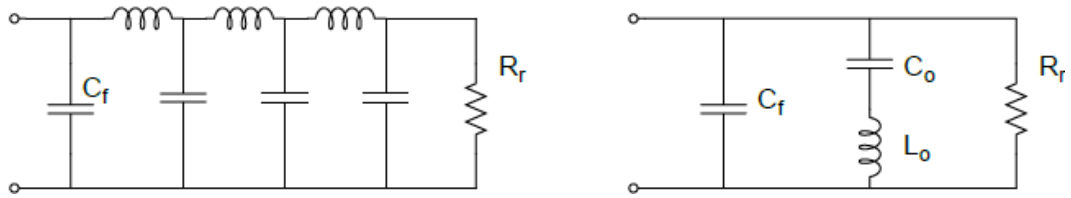

(a) (b)

Figure 33: Equivalent circuit of the broadband measurement probe **[38]**.

Due to the fringing fields outside the probe being much greater than those inside the coaxial line, the effect of C_f on the total capacitance is negligible. The radiation losses are also negligible at the low frequencies for which the probe was designed. Thus, the admittance of the probe in air is given by (1.1) [38] and the admittance of the probe in a sample material with permittivity ε_m is given by (1.2) [38]:

$$\gamma(\omega) = \frac{j\omega C_0}{1-\omega^2 L_0 C_0} \tag{3.0}$$

$$\gamma(\omega, \varepsilon_m^*) = \frac{j\varepsilon_m^* \omega C_0}{1-\omega^2 L_0 C_0 \varepsilon_m^*} \tag{3.1}$$

The formula used to calculate the permittivity from the reflection coefficient was [38]:

$$\varepsilon_m^* = \frac{\gamma_m}{j\omega C_0 + \gamma_m \omega^2 L_0 C_0} \tag{3.2}$$

Equation 2 includes the simple equivalent circuit of the probe, where C_0 = 0.44663 pF, L_0 = 1.6337 nH, Y_m is the measured admittance and ω is the angular frequency. Since this equation represents the measured permittivity relative to air, the permittivity of air should also be measured after calibration of the probe so that the data may be used to normalise the sample permittivity values. Marais had documented that the device delivered measured dielectric constants within 3% of the expected values quoted in literature. However, our measurements consistently found this error to be closer to 4.986% below the expected permittivity values.

The probe error percentage was calculated as the average error over two samples of PTFE with the same thickness, each measured a minimum of ten times and in each case recalibrating the probe before each measurement. Once the configuration of the system was confirmed to be correct, the dielectric properties of the phantom material samples were measured. A full list of the sample measurements can be viewed in Table 42 (Appendix O, page 156) from which extracts are illustrated in Table 20 to Table 24. The "Average Measured Permittivity of Samples" column refers to the permittivity measurements using the broadband measurement system and the "Recipe Estimated Permittivity" column refers to the approximated permittivity values as depicted in Table 18 (Chapter 4, page 37).

Table 20: Measured permittivity of the agar samples prepared according to the 403 MHz phantom material recipes.

Biological Tissue	Average Measured Permittivity of Samples	Recipe Estimated Permittivity	Error [%] (From Avg)	Average Error [%]	Average Permittivity (Probe Error of 4.986% Compensated)	Error [%] (Probe Error of 4.986% Compensated)	Avg Error [%] (Probe Error of 4.986% Compensated)
Blood	57.713	63.980	9.795	11.181	60.591	5.297	6.752
Bone Cancellous	-	19.215	-		-	-	
Bone Cortical	-	10.890	-		-	-	
Fat	-	11.358	-		-	-	
Grey Matter	56.705	63.029	10.033		59.533	5.547	
White Matter	42.297	47.802	11.516		44.406	7.104	
Kidney	43.946	48.580	9.539		46.138	5.028	
Spleen	-	55.014	-		-	-	
Heart	41.062	45.167	9.090		43.109	4.557	
Liver	45.079	49.491	8.915		47.327	4.374	
Lung	31.719	38.225	17.022		33.300	12.884	
Muscle	58.761	65.941	10.888		61.691	6.445	
Skin	35.536	41.240	13.829		37.308	9.533	

Table 21: Measured permittivity of the agar samples prepared according to the 910 MHz phantom material recipes.

Biological Tissue	Average Measured Permittivity of Samples	Recipe Estimated Permittivity	Error [%] (From Avg)	Average Error [%]	Average Permittivity (Probe Error of 4.986% Compensated)	Error [%] (Probe Error of 4.986% Compensated)	Avg Error [%] (Probe Error of 4.986% Compensated)
Blood	56.531	59.142	4.415	8.762	59.349	0.351	4.283
Bone Cancellous	-	17.499	-		-	-	
Bone Cortical	-	9.783	-		-	-	
Fat	-	10.071	-		-	-	
Grey Matter	50.748	54.350	6.628		53.278	1.972	
White Matter	33.430	36.437	8.253		35.096	3.678	
Kidney	41.695	45.316	7.991		43.774	3.403	
Spleen	45.759	49.486	7.531		48.040	2.921	
Heart	37.033	41.263	10.251		38.880	5.776	
Liver	39.180	43.459	9.844		41.134	5.349	
Lung	28.933	32.942	12.170		30.376	7.790	
Muscle	53.557	59.233	9.582		56.227	5.074	
Skin	35.434	39.792	10.952		37.201	6.512	

Table 22: Measured permittivity of the agar samples prepared according to the 2.4 GHz phantom material recipes.

Biological Tissue	Average Measured Permittivity of Samples	Recipe Estimated Permittivity	Error [%] (From Avg)	Average Error [%]	Average Permittivity (Probe Error of 4.986% Compensated)	Error [%] (Probe Error of 4.986% Compensated)	Avg Error [%] (Probe Error of 4.986% Compensated)
Blood	53.950	54.142	0.355	7.194	56.639	4.613	4.487
Bone Cancellous	-	15.783	-		-	-	
Bone Cortical	-	8.783	-		-	-	
Fat	-	8.293	-		-	-	
Grey Matter	40.257	43.852	8.198		42.264	3.621	
White Matter	29.695	32.531	8.717		31.176	4.166	
Kidney	37.743	40.557	6.939		39.625	2.299	
Spleen	42.354	45.829	7.583		44.466	2.975	
Heart	31.104	34.469	9.763		32.654	5.264	
Liver	35.396	39.139	9.562		37.161	5.052	
Lung	24.720	27.567	10.326		25.952	5.855	
Muscle	53.700	53.396	0.569		56.377	5.584	
Skin	32.791	36.405	9.928		34.426	5.437	

Table 23: Measured permittivity of the agar samples prepared according to the 4.5 GHz phantom material recipes.

Biological Tissue	Average Measured Permittivity of Samples	Recipe Estimated Permittivity	Error [%] (From Avg)	Average Error [%]	Average Permittivity (Probe Error of 4.986% Compensated)	Error [%] (Probe Error of 4.986% Compensated)	Avg Error [%] (Probe Error of 4.986% Compensated)
Blood	55.362	57.264	3.321	10.591	58.122	1.500	9.127
Bone Cancellous	59.745	59.012	1.243		62.724	6.291	
Bone Cortical	22.563	29.285	22.954		23.688	19.112	
Fat	14.139	18.638	24.136		14.844	20.353	
Grey Matter	44.608	52.914	15.697		46.832	11.494	
White Matter	39.442	46.213	14.653		41.408	10.398	
Kidney	62.241	64.455	3.436		65.344	1.378	
Spleen	-	113.928	-		-	-	
Heart	44.458	52.213	14.852		46.675	10.607	
Liver	60.353	59.197	1.952		63.362	7.035	
Lung	60.334	63.264	4.631		63.342	0.124	
Muscle	70.724	65.469	8.025		74.250	13.412	
Skin	34.811	39.647	12.197		36.547	7.820	

Table 24: Measured permittivity of the agar samples prepared according to the closest point polynomial regression method recipes.

Biological Tissue	Resonance Frequency	Average Measured Permittivity of Samples	Recipe Estimated Permittivity	Error [%] (From Avg)	Average Error [%]	Average Permittivity (Probe Error of 4.986% Compensated)	Error [%] (Probe Error of 4.986% Compensated)	Avg Error [%] (Probe Error of 4.986% Compensated)
Skin	910 MHz	35.680	39.791	10.333	10.333	37.453	5.878	5.878
Grey Matter	2.4 GHz	40.775	43.861	7.037	7.796	42.808	2.402	4.314
White Matter		28.794	32.470	11.319		30.225	6.913	
Kidney		36.613	40.558	9.725		38.439	5.224	
Spleen		42.448	45.845	7.410		44.565	2.793	
Heart		31.757	34.460	7.884		33.334	3.266	
Liver		36.246	39.133	7.378		38.047	2.776	
Lung		24.772	27.450	9.756		26.003	5.273	
Muscle		53.982	53.414	1.065		56.674	6.104	
Skin		33.234	36.375	8.634		34.891	4.078	
Blood	4.5 GHz	53.448	57.447	6.961	9.789	56.113	2.322	7.666
Bone Cancellous		56.035	59.282	5.477		58.819	0.782	
Bone Cortical		-	29.285	-		-	-	
Fat		-	20.706	-		-	-	
Grey Matter		44.200	52.610	15.986		46.396	11.812	
White Matter		40.804	46.080	11.450		42.831	7.051	
Kidney		65.632	64.735	1.385		68.892	6.422	
Spleen		-	113.928	-		-	-	
Heart		37.942	52.793	28.131		39.826	24.562	
Liver		57.696	59.456	2.960		60.572	1.878	
Lung		58.901	63.562	7.334		61.827	2.730	
Muscle		66.630	65.747	1.344		69.940	6.378	
Skin		32.647	39.267	16.858		34.269	12.728	

Table 20 to 24 indicate the theoretically estimated rhinoceros permittivity and measured permittivity of each of the biological materials for each of the selected frequencies and recipe determination methods. Table 24 indicates these values specifically for all frequencies within the polynomial regression recipe determination method, which served as an alternative to some of the other recipes when the ratio of salt and sucrose concentrations were impractical. Two sets of error are shown in the data tables. The first set indicates the error between the average measured permittivity and the estimated permittivity, which is a combination of the recipe error and the error introduced by the measuring probe. This error will henceforth be referred to as the "Aggregate Error". The second set indicates the error between the average measured permittivity and the estimated permittivity, with the probe error compensated. This error will henceforth be referred to as the "Recipe Error" and is based on the true value of the phantom material permittivity. The probe error was compensated for by averaging the permittivity measurements over all samples after adding 4.986% to each of the individual measured permittivities. We recall that 4.986% is our estimate of the probe error. The permittivity error of the samples was calculated as follows:

$$\%\, Error = 100 - \left(\frac{measured}{theoretical} \times 100\right) \tag{4.0}$$

It can be seen that, for each considered frequency, the aggregate error is approximately 11% or less, whereas the recipe error is approximately 9% or less, with the lowest being close to 4%. Due to the difficulty in replicating results and the risk factors (such as contamination) involved in preparing phantom materials, an error margin of 10% was deemed acceptable for the measured permittivity values. Thus, the measured results of the recipe error margins are within acceptable boundaries. The following factors are probable causes for the small error that remained:

1. Temperature

It is commonly known that dielectric properties are influenced by temperature. The recipes for the rhinoceros phantom materials were designed based upon an average room temperature of 24°C, which proved to be a fairly accurate assumption as indicated by Figure 34.

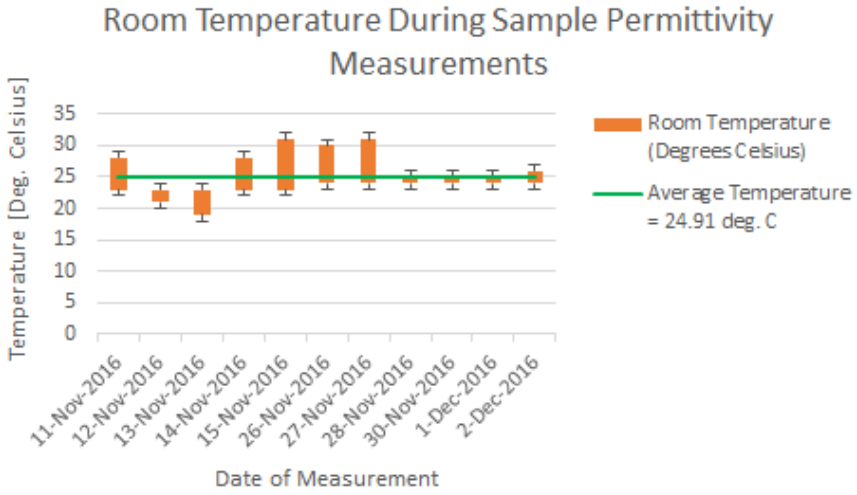

Figure 34: Room temperature during phantom material permittivity measurements.

The measurements were conducted over eleven days with each session lasting a few hours. This accounts for the fluctuation in temperature for each day depicted in Figure 34. Samples were kept in storage at 4°C until they were measured on the dates listed in Figure 34.

2. Calibration of the Probe

The broadband probe calibration was repeated a number of times over the span of the eleven days. This was done to ensure that the system was configured to the specifications documented by Marais, who had experienced an error of 3% during his own measurements of known samples. Nonetheless, the observed error could indicate a loss in precision within the specified calibration values.

3. Sample Thickness

The thickness of a sample is known to influence dielectric measurements due to its influence on the reflection coefficient of the material under test (MUT). This occurs due to the thickness altering the distance of the transition point from one material to the other (for example the transition from Teflon to air). The error introduced by sample thickness is illustrated by the difference in the estimated dielectric constant between a Teflon sample with thickness of 11 mm and a Teflon sample with thickness of 23 mm, which were both measured a minimum of ten times (each measurement occurring after the recalibration of the probe). Literature documents a dielectric constant of 2.1 at 3 GHz for Teflon (PTFE). However, the 11 mm sample delivered an average permittivity of 2.004 (which corresponds to an error of 4.56 %) and the 23 mm sample delivered an average permittivity of 1.817 (which corresponds to an error of 13.46 %).

Recommended sample thicknesses for measuring of rhinoceros phantom materials are as follows:

403 MHz Recipes = 8 mm.
910 MHz Recipes = 7 mm.
2.4 GHz Recipes = 5 mm.
4.5 GHz Recipes = 2 mm.

These recommendations are based on the wavelength of the corresponding signals in air (which decreases as the frequency increases) as well the experiments conducted by Banerjee et al [39], which indicated that at higher frequencies thinner samples deliver greater accuracy with regards to their measured dielectric properties.

4. Measurement Frequency

As previously described, a vector network analyser (VNA) was used in conjunction with the broadband measurement system to determine the dielectric properties of the known and phantom materials. Reflection coefficient measurements were made within the range from 300 kHz to 8 GHz, which accommodates all of the selected measurement frequencies and allows the investigation of various parts of the spectrum. However, the VNA records a number of discrete measurements, which in this case were chosen to correspond to 1001 data points across the frequency range. This corresponds to an interval of 7.992 MHz between data points. The measurement frequencies (403 MHz, 910 MHz, 2.4 GHz, 4.5 GHz) are situated between these measured discrete points and hence the closest measured frequency values were used. This deviation could introduce an error in the permittivity measurement value. However, this error must be small, because the recorded frequencies and the selected measurement frequencies are always within 2% of each other.

5. Impurity of Samples

Although great care was taken to prevent the contamination of samples during preparation, this is to some extent inevitable as soon as the samples are exposed to air in order to take measurements. Not only can particles in the air interfere with the measurements, but contamination from the probe itself is possible.

6. Method of Recipe Determination

The methods used to determine the recipes used to fabricate the rhinoceros phantom materials were based on the experiments performed by Duan et al [14]. As previously mentioned, methods such as the incremental, polynomial regression and closest point polynomial regression methods were used to determine recipes for regions outside the boundaries specified by Duan et al [14]. Some of the recipes delivered liquid phantom materials, due to their high sugar content, which could not fully dissolve within the specified water volume. These phantom materials, along with the phantom tissue values that did not deliver feasible recipes, are indicated by a dash (‘-‘) in Table 20 to Table 24.

The error between the theoretical and measured permittivity of each phantom material with regards to the recipe used to make the sample, is illustrated in Figure 35 to Figure 38. Empty columns refer to liquid state phantom materials or unfeasible solutions that could not be characterised and do not contribute to the averages displayed in these figures. As can be seen in Figure 35 (column labelled “Blood (2.4 GHz)”), it is possible for the recipe error to overflow and to exceed the aggregate error. This means that the error has switched directions across the estimated permittivity value, in which case the measured permittivity initially had a value lower than the estimated permittivity, but has a higher value than the estimated permittivity once the probe error was removed.

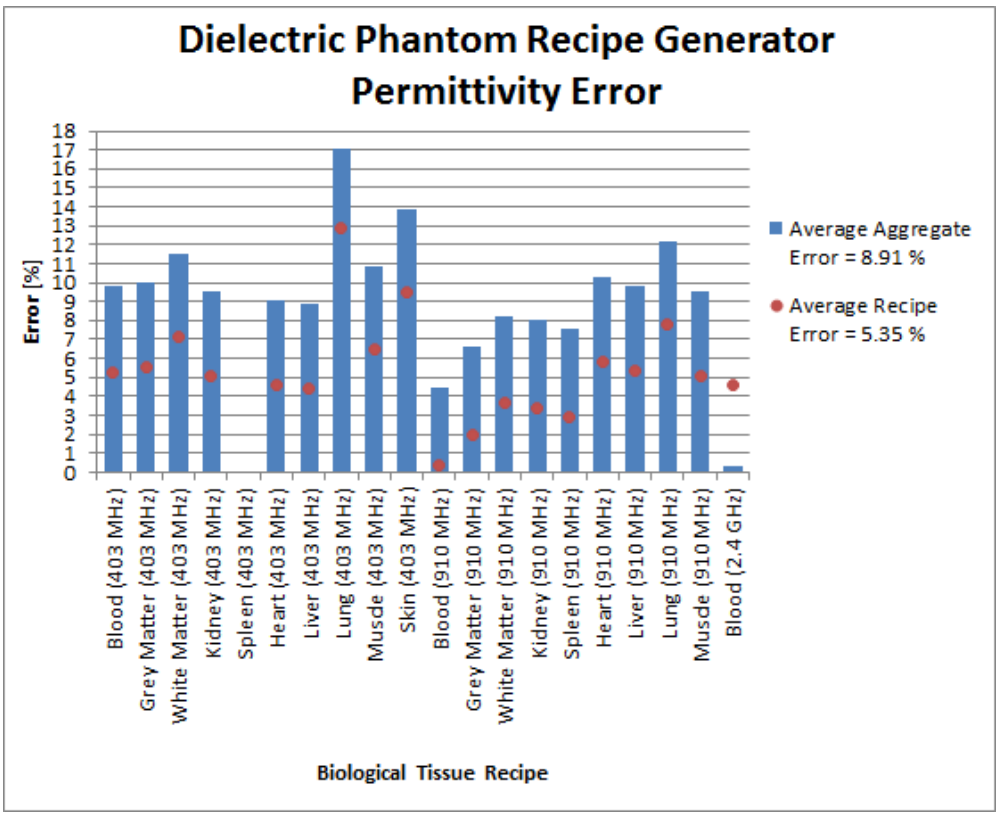

Figure 35: Dielectric phantom recipe generator permittivity error.

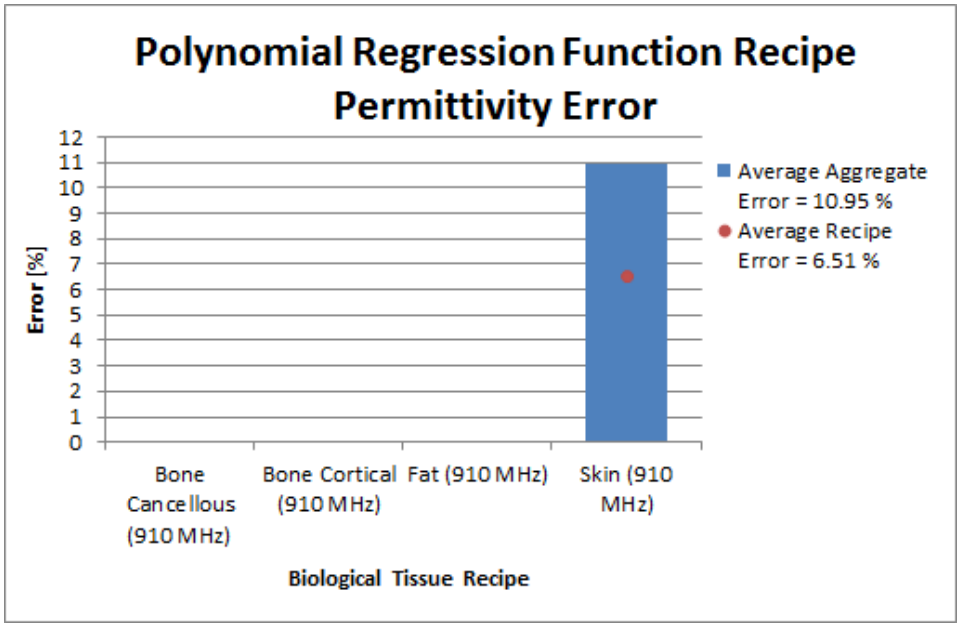

Figure 36: Polynomial regression function recipe permittivity error.

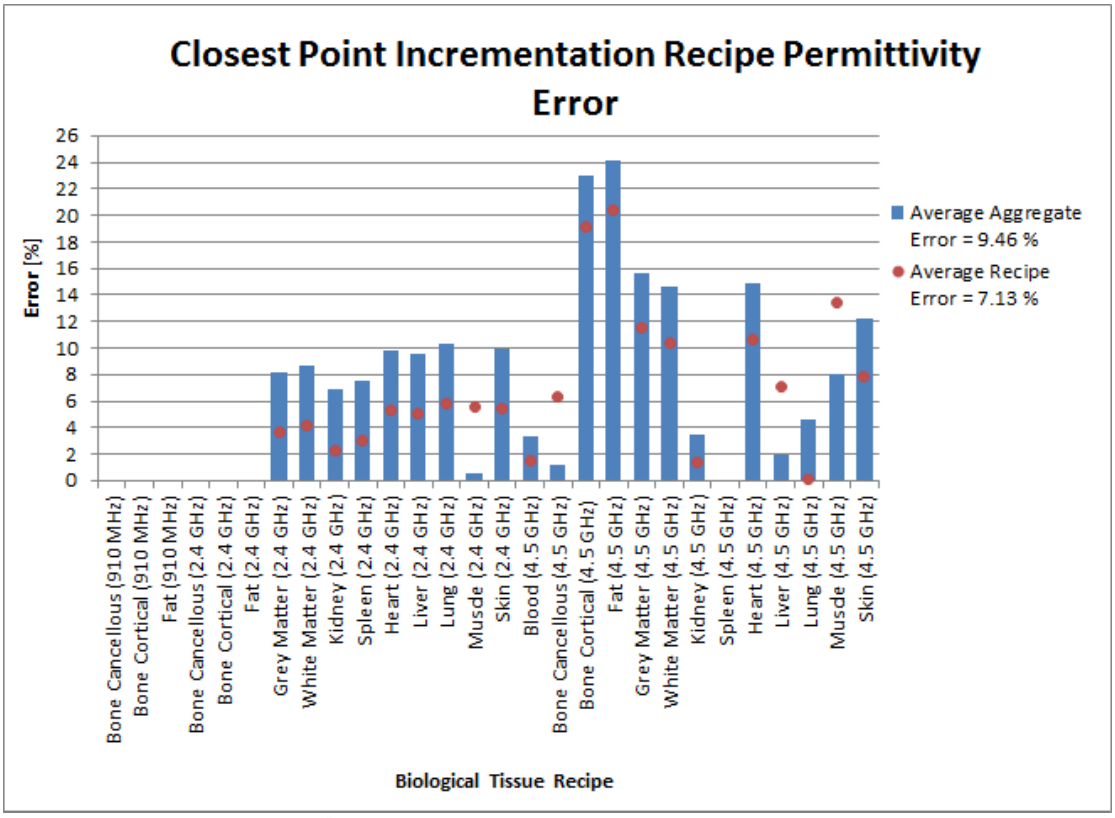

Figure 37: Closest point incrementation recipe permittivity error.

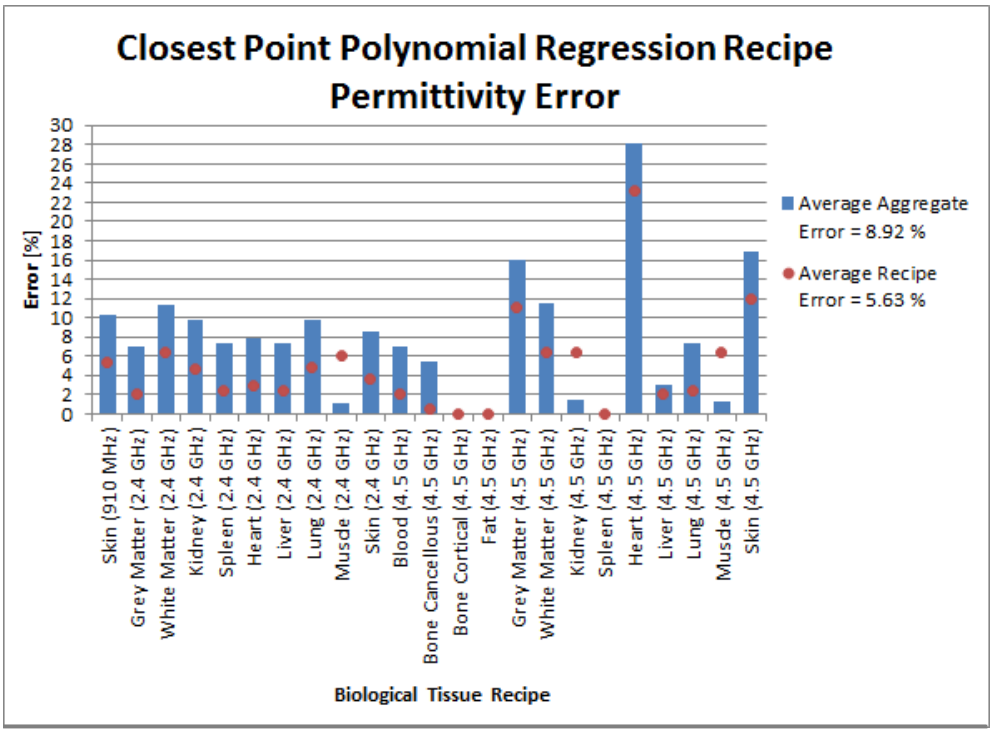

Figure 38: Closest point polynomial regression recipe permittivity error.

Figures 35 to 38 indicate similar error rates that are within acceptable boundaries. Thus, by using the additional methods for determining the recipes of materials with dielectric properties that were originally infeasible or impractical, recipes were developed that delivered these materials with minimal dielectric error.

5.3 Dielectric Property Error Analysis

As previously stated, a degree of error is to be expected between two preparations of the same phantom material. This chapter elaborates on the error margins for each of the phantom material recipes. Figures 39 and 40 depict four sets of data, namely the theoretical permittivity values of the phantom materials, the estimated permittivity values of the phantom materials, the measured permittivity values of the 2.4 GHz phantom materials with the probe error included (Aggregate Error) and the measured permittivity values of the 2.4 GHz phantom materials with the probe error excluded (Recipe Error). Omitted bars indicate recipes that delivered liquid state phantom materials or recipes with unfeasible solutions. Illustrations denoted with "Br" (indicated by the colour brown in Appendix N, page 154) refer to the alternative recipes for the phantom materials that were developed by using the closest point polynomial regression method. The results for the frequencies other than the 2.4 GHz group can be viewed in Appendix J (page 134).

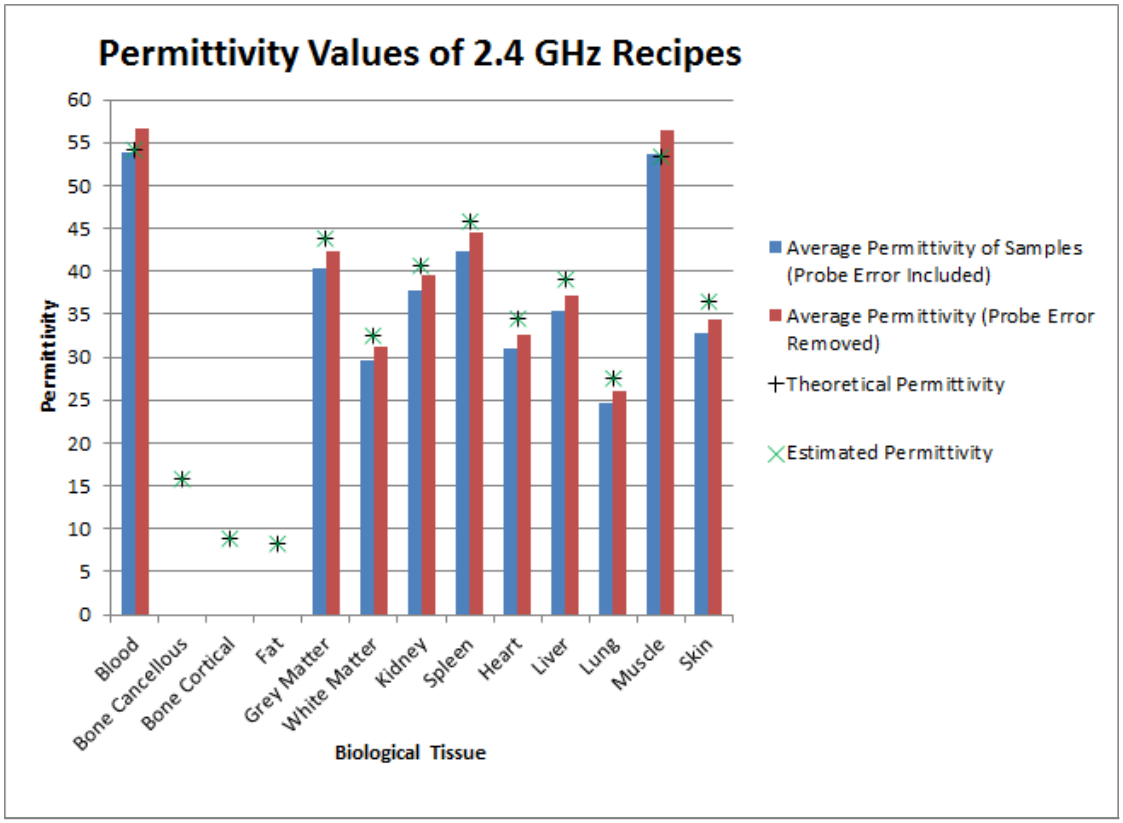

Figure 39: Permittivity values of the 2.4 GHz recipes.

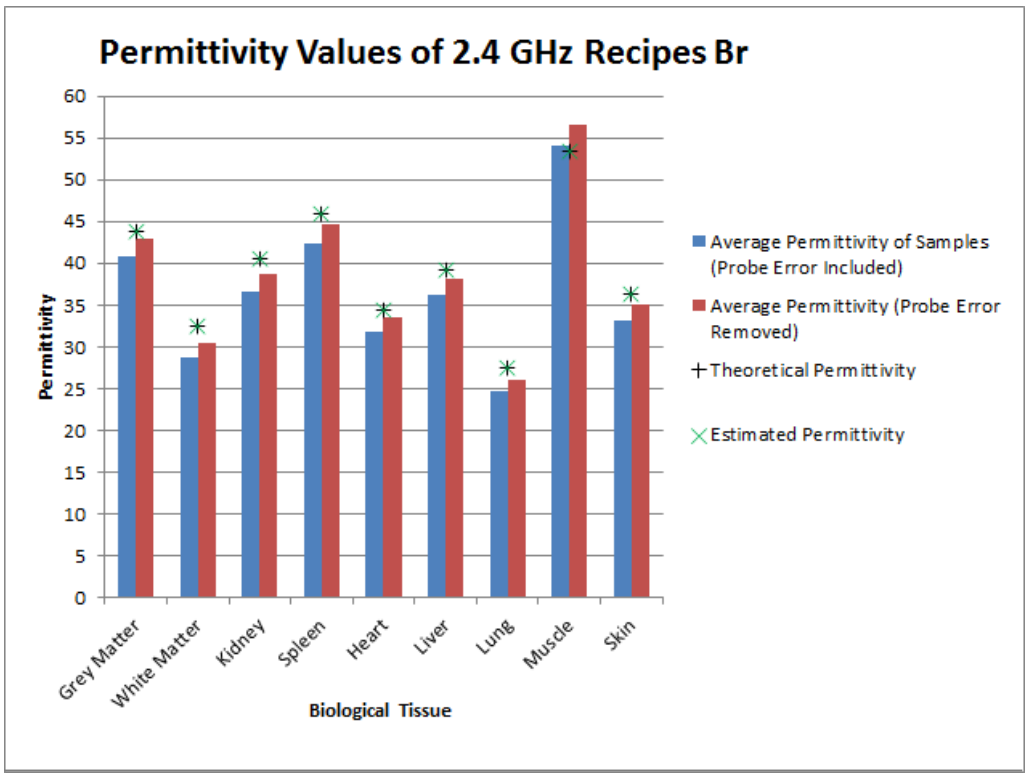

Figure 40: Permittivity values of the 2.4 GHz recipes Br.

These figures indicate the closeness of the measured dielectric properties of the two sets of recipes, although two different methods were used to develop the recipes. It also emphasizes the importance of considering individual recipes, rather than selecting recipes based on the average error of the group. Particular recipes may be more accurate at achieving the desired dielectric properties of a specific material, although the error of the group might be higher. For example, the average permittivity error of the recipes illustrated in Figure 39 (4.487%) is higher than the average permittivity of the recipes illustrated in Figure 40 (4.314%). However, the permittivity error for the kidney recipe depicted in Figure 39 is 2.299%, which is lower than the permittivity error for the kidney recipe (5.224%) depicted in Figure 40.

Figures 41 and 42 indicate the measured permittivity values of the 2.4 GHz phantom materials when compensating for the probe. The upper and lower boundaries indicated in these illustrations could be implemented as ranges within which the measured permittivity values of the rhinoceros phantom materials are expected to be. Each recipe was executed at least twice and in each case produced four or more samples from which the average error was calculated after the permittivity had been measured. Hence we obtained at least two sets of permittivity measurements each consisting of four samples, resulting from a single application of a recipe. These sets of at least eight individual permittivity measurements can be used to assess the repeatability of the agar preparation process. Omitted bars indicate recipes that delivered liquid state phantom materials or recipes with unfeasible solutions. Illustrations denoted with "Br" (indicated by a brown colour in Appendix N, page 154) refer to the alternative recipes that were developed by using the closest point polynomial regression method. The results for frequencies other than the 2.4 GHz group can be viewed in Appendix J (page 134).

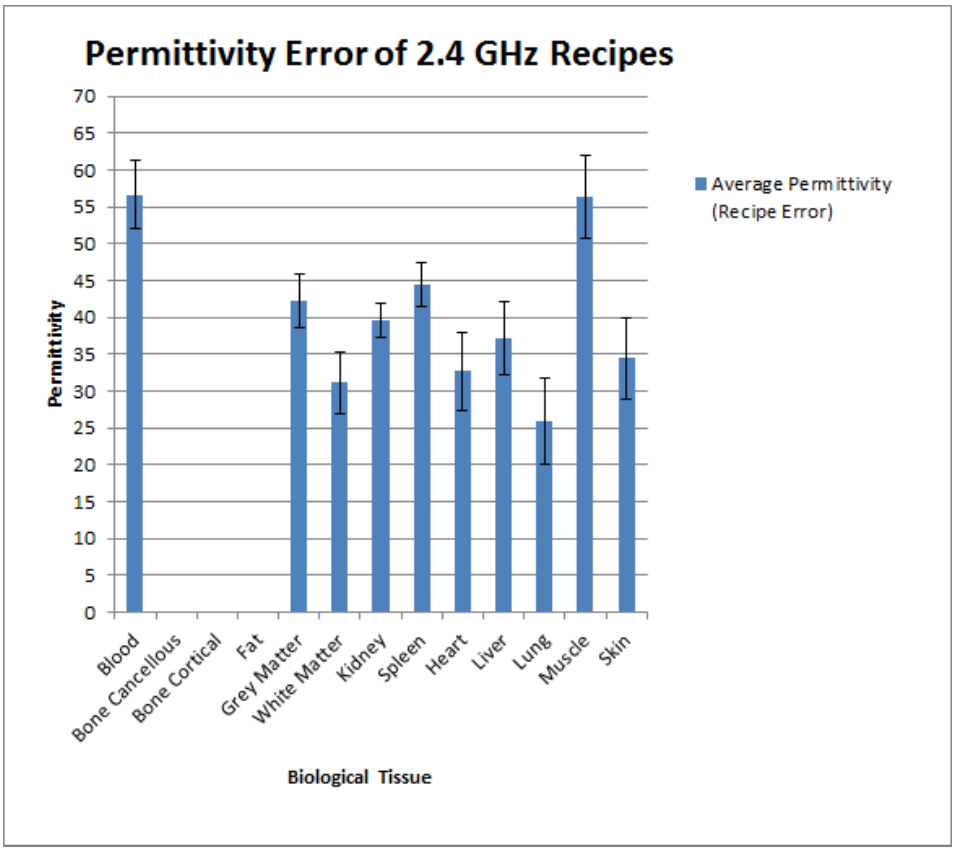

Figure 41: Permittivity error of the 2.4 GHz recipes with recipe error margins.

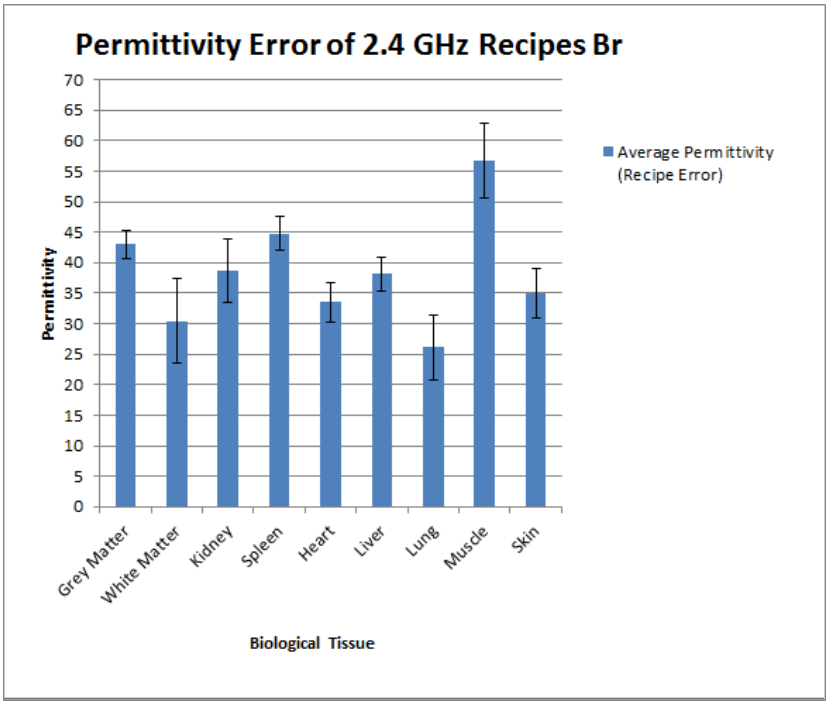

Figure 42: Permittivity values of the 2.4 GHz closest point polynomial regression recipes with recipe error margins.

Both figures indicate variability in the permittivity of the agar samples, but also that most permittivity values are lower than their theoretical and estimated permittivity counterparts. Practical measurements were possible for 61 of the proposed 75 recipes with the majority of the recipes delivering permittivity values below the estimated permittivity. The recipes that delivered permittivity values higher than the estimated values all delivered an error of less than

13.42% (all but one were below 7.04%). Repeated applications of these recipes suggest that the agar samples would not have permittivity values far outside the estimated ranges. The following list contains the recipes that delivered a recipe error greater than 10%:

Lung	403	MHz		(12.88 %)
Bone Cortical	4.5	GHz		(19.11 %)
Fat	4.5	GHz		(20.35 %)
Grey Matter	4.5	GHz		(11.49 %)
White Matter	4.5	GHz		(10.40 %)
Heart	4.5	GHz		(10.61 %)
Muscle	4.5	GHz		(13.41 %)
Grey Matter	4.5	GHz	Br	(11.81 %)
Heart	4.5	GHz	Br	(24.56 %)
Skin	4.5	GHz	Br	(12.73 %)

Thus, 51 out of the measured 61 recipes (83.61 %) were within 10% of the specified error margin and even with the recipes listed above included, the average error over all recipes amounted to 6.22%. The ten most variable recipes are similar in the sense that most of them are situated within the 4.5 GHz group and most of them required large amounts of sugar relative to the other recipes. The large error of the bone and fat recipes was expected, since the literature reports that these materials are difficult to replicate and that they have large variance with regards to their permittivity. A possible explanation for the greater variability for these particular recipes is that the estimated permittivities are generally lower. This requires larger quantities of ingredients to achieve the desired dielectric properties and thus causes the solution to be closer to its saturation point. Otherwise stated, some of these values might be unfeasible within the specified volume, temperature or phantom material type (in this case agar) seeing as the saturation point of the solution would be reached prior to achieving the desired dielectric properties of the material. Another explanation could be the shorter wavelength associated with the higher frequency, which could yield greater sensitivity to the contributive error factors described in Section 5.2 (page 48).

As mentioned earlier, some of the samples were not measured due to unfeasible recipes (no method of determination delivered a viable recipe) or because they delivered liquid state phantom material samples. The following list depicts these recipes:

Bone Cancellous	403	MHz		(Liquid State)
Bone Cortical	403	MHz		(Liquid State)
Fat	403	MHz		(Liquid State)
Spleen	403	MHz		(Liquid State)
Bone Cancellous	910	MHz		(Outside Recipe Parameters)
Bone Cortical	910	MHz		(Outside Recipe Parameters)
Fat	910	MHz		(Outside Recipe Parameters)
Bone Cancellous	2.4	GHz		(Outside Recipe Parameters)
Bone Cortical	2.4	GHz		(Outside Recipe Parameters)
Fat	2.4	GHz		(Outside Recipe Parameters)
Spleen	4.5	GHz		(Outside Recipe Parameters)
Bone Cortical	4.5	GHz	Br	(Outside Recipe Parameters)
Fat	4.5	GHz	Br	(Outside Recipe Parameters)
Spleen	4.5	GHz	Br	(Outside Recipe Parameters)

The trend among the recipes indicates that low (403 MHz) and high (4.5 GHz) frequencies generally require more salt and sugar to achieve the desired permittivity and conductivity of the phantom materials. For example, as the frequency increases the required amount of ingredients decreases, which could pose a possible explanation for the infeasible recipes within the higher frequency intervals – the necessary ratio of salt to sugar to water and coinciding necessary quantities cannot be attained. It is also important to note that the dielectric characteristics of materials vary with frequency [16] [22] [39]. This variation may make a certain recipe infeasible at certain frequencies.

The 2.4 GHz recipe group delivered the second best results since it showed the second smallest error between the measured and estimated permittivity. The average recipe error for this group was 4.49% and 4.31% for the alternative method recipes of the same frequency. As previously mentioned, 2.4 GHz antenna designs were selected as the most suitable candidates for implantation because their physical dimensions are realistic according to veterinary opinion. The analysis of the errors recipes presented in the preceding text has therefore indicated that, at 2.4 GHz, it is very likely that the phantoms produced will be a good approximation of the rhinoceros tissue in terms of desired permittivity values. It is important to remember that, although the average recipe error of a group of recipes may be small, the individual recipe error should be considered when selecting phantom material recipes for development.

The effect of using ordinary sugar instead of pure sugar was tested in two recipes, namely the heart 403 MHz recipe and the Lung 403 MHz recipe. As can be seen from the results listed in Tables 20 to 24 (page 45) good results with regards to desired permittivity values were achieved in both cases. However, it was observed that the samples made with pure sugar did not set properly, resulting in liquid phantom materials. Table 25 illustrates the amount of salt and sugar required to create phantom materials for white matter, the heart, the lung and skin for rhinoceroses specifically at 403 MHz and at 910 MHz. From this list, only the heart 403 MHz and Lung 403 MHz samples were created with pure sugar. Although the ingredient requirements between the listed recipes are quite similar, the specified heart and lung samples were the only two recipes that delivered unusable liquid state phantom materials. In some cases, recipes with greater ingredient requirements still delivered usable phantom materials and thus, with all other constituents kept constant, the only difference would be the use of pure sugar over ordinary sugar and less salt.

Table 25: Extract - Measured dielectric properties of phantom materials.

Biological Tissue	Frequency	Estimated Conductivity	Estimated Permittivity	Salt (NaCl) [g]	Sugar [g]
White Matter	403 MHz	0.508	47.802	3.631	145.304
Heart		1.137	45.167	13.505	144.866
Lung		0.552	35.645	14.195	201.452
Skin		0.477	41.240	4.912	185.169
White Matter	910 MHz	0.819	36.437	1.708	169.528
Heart		1.606	41.263	10.493	125.583
Lung		0.753	31.909	0.413	199.593
Skin		0.736	39.792	0.561	156.671

By comparing the total ingredient volume alone, it is clear to see that this does not necessarily cause the saturation of the heart and lung phantom solutions or cause them to deliver liquid state samples. For example, the total number of grams required to create the skin recipe at 403 MHz is 190.08 grams, whereas the heart recipe at 403 MHz only amounts to 158.37 grams in total – yet the skin recipe delivered usable samples and the heart recipe did not. In order to establish the

cause of the erroneous heart and lung samples, these samples were reproduced using regular sugar. Since the recipes were unaltered, all the ingredients remained the same apart from the type of sugar that was used. As illustrated by Figures 43 to 45, the regular sugar recipes delivered measurable results, which are also depicted in Table 26. This would suggest that the use of pure sugar is the cause of the erroneous samples and delivers phantom materials in liquid state.[1]

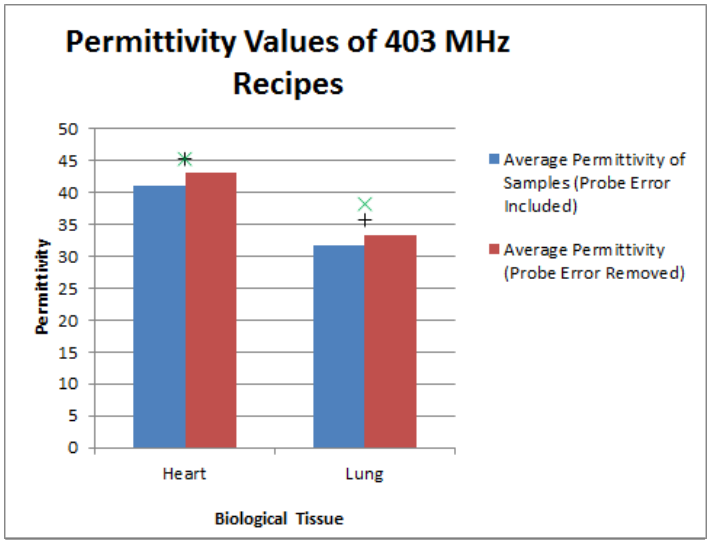

Figure 43: Measured permittivity values of the 403 MHz heart and lung recipes.

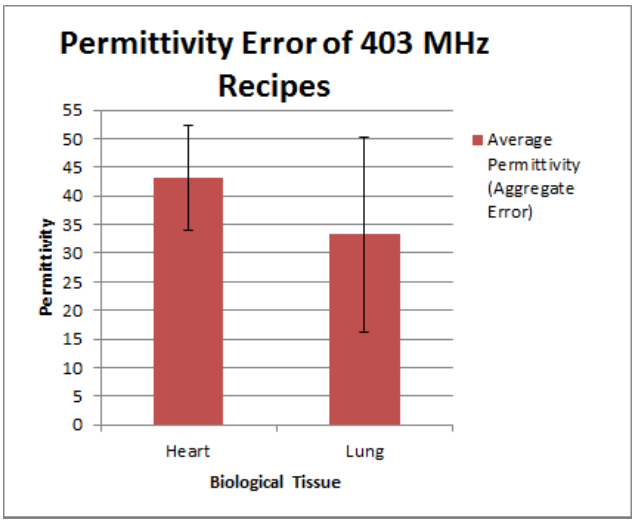

Figure 44: Permittivity error of the 403 MHz heart and lung recipes with aggregate error margins.

[1] A possible explanation for this effect could be the homogeneity produced by the pure sugar within the samples, which reflects on the amount of sugar which can be dissolved in the solution before saturation occurs. The pure sugar is likely to be better absorbed into the solution, causing it to saturate and deliver a texture resembling that of syrup. Of course, it is possible that a reduction in temperature could cause the material to set, but this would also alter the properties of the material.

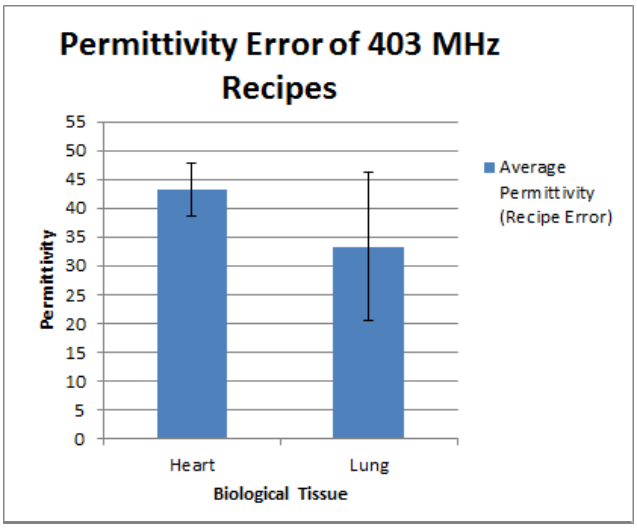

Figure 45: Permittivity error of the 403 MHz heart and lung recipes with recipe error margins.

The measured permittivity error of the 403 MHz heart recipe is within acceptable boundaries, however, the measured permittivity error for the 403 MHz lung recipe is slightly higher than expected. This is due to the error being calculated from the estimated permittivity (i.e. the permittivity value approximated from the recipe polynomial function) rather than the theoretical permittivity, which is the actual approximation of the rhinoceros tissue. If calculated from the theoretical permittivity, the aggregate error would be closer to 11.02% and the recipe error would be closer to 6.04% and deliver an average measured permittivity of 33.50. During the time of measurements, the room temperature fluctuated between 23°C and 26°C, with an average of 24.5°C.

Table 26: Measured permittivity of the 403 MHz heart and lung phantom material recipes.

Biological Tissue	Average Measured Permittivity of Samples	Recipe Estimated Permittivity	Theoretical Permittivity	Error [%] (From Avg)	Average Permittivity (Probe Error of 4.986% Compensated)	Error [%] (Probe Error of 4.986% Compensated)
Heart	41.06	45.17	45.17	9.09	43.11	4.56
Lung	31.72	38.23	35.65	17.02	33.30	12.88

5.3.1 Phantom Material Characteristics and Trends

The suggested phantom materials for rhinoceros tissue had diverse physical properties, due to their varying compositions. All samples could be handled with relative ease without causing them to rupture and most were quite flexible. The consistency of the samples varied from soft to semi-rigid or firm, which can be explained by their respective estimated sample densities as depicted in Figure 46. The density of each sample is determined by the amount of water, agar, salt and sugar used during fabrication. Since the amount of agar (2.5 g) and water (100 ml) were kept constant, the only two varying ingredients were salt and sugar. It can be seen from Figure 46 that the density of the lower frequency samples are higher than the density of the higher frequency samples. This is in accordance with the amount of each ingredient required at the specific frequency. The salt requirements for the 100 ml recipes across the specified frequencies are illustrated by Figure 47, whereas the sugar requirements for the 100 ml recipes across the specified frequencies can be viewed in Appendix F (page 124). Additional illustrations of the density and salt and sugar requirements for the alternative recipes of the samples, can also be viewed in Appendix F (page 124).

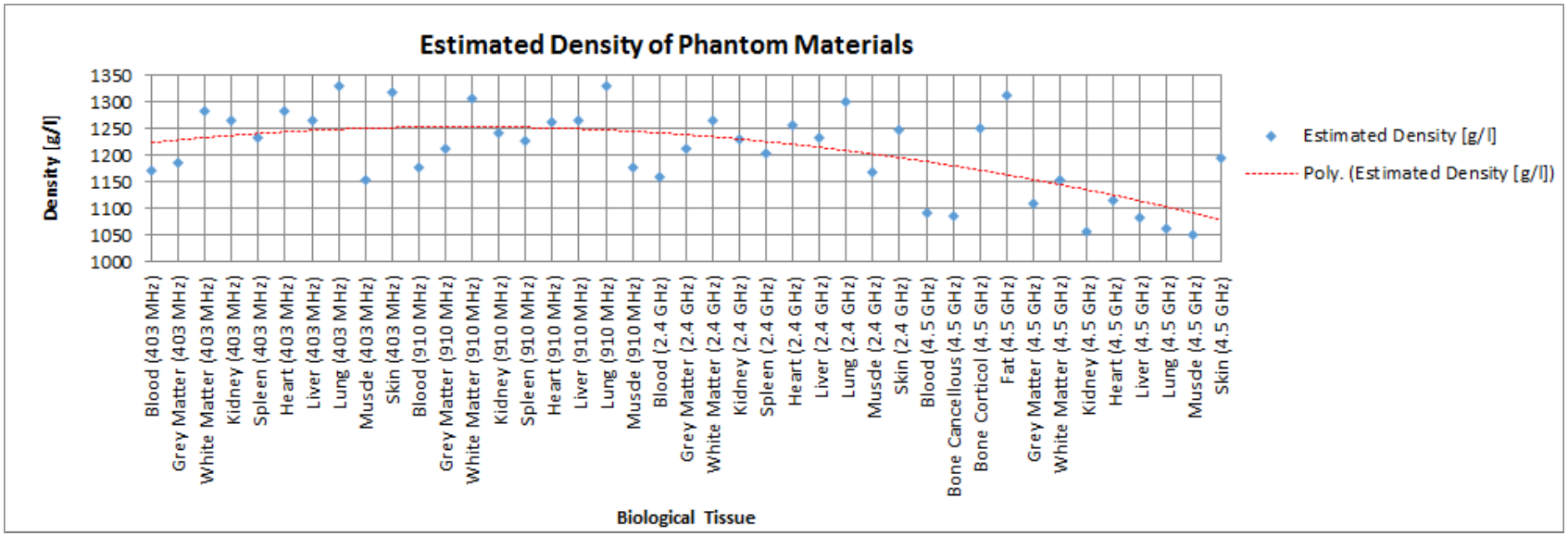

Figure 46: The estimated density of the rhinoceros phantom materials at the specified frequencies.

It is important to individually consider and compare the density and ingredient requirements for each material across all frequencies. Figure 46 illustrates a decrease in sample density at low (403 MHz) and high (4.5 GHz) frequencies, which is in agreement with the salt and sugar requirements. This corresponds to the findings of the previous section, which suggested that sample materials at higher and lower frequencies delivered a slightly greater difference between the estimated and measured permittivity values. Some of the recipes developed for these frequencies also delivered liquid state sample materials or infeasible recipes due to the unobtainable ratio of the ingredients within the specified solution volume.

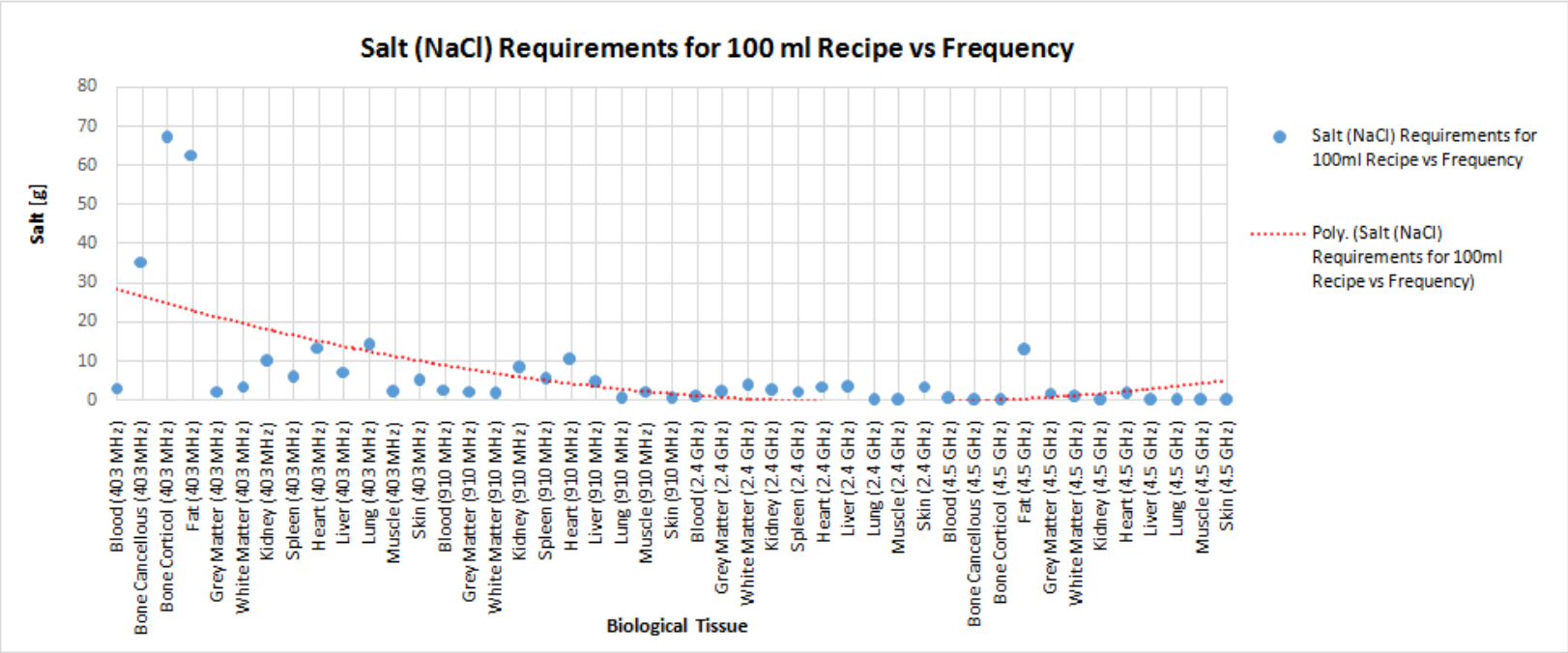

Figure 47: Salt requirements for the 100 ml recipes for the specified frequencies.

The sample material salt requirement for each recipe is illustrated in Figure 47, which indicates larger quantities of salt for the 403 MHz and 4.5 GHz recipes. Similar trends were depicted by the sample material sugar requirements (Appendix F, page 124). It is clear that the ingredients for the bone cancellous, bone cortical and fat recipes are much more variable than those of the other recipes. This is especially evident when comparing the salt and sugar requirements of the 403 MHz bone cortical recipe to the corresponding 910 MHz recipe, which indicates a large difference between the required ingredient quantities within a small difference in frequency.

The estimated thermal properties of the phantom materials for 100 ml recipes are illustrated by Figure 48. This illustrates that as the frequency increases and the amounts of ingredients decreases, the heat capacity and thermal conductivity tend to increase. Although the overall difference between the heat capacity and thermal conductivity at the lower frequencies are quite small compared to those at the higher frequencies, these estimations suggest that greater care should be taken whilst working with the higher frequency phantom models to control their temperature. Specifically, temperature control would support the structural integrity of the models and postpone the deterioration of their dielectric properties caused by spore growth.

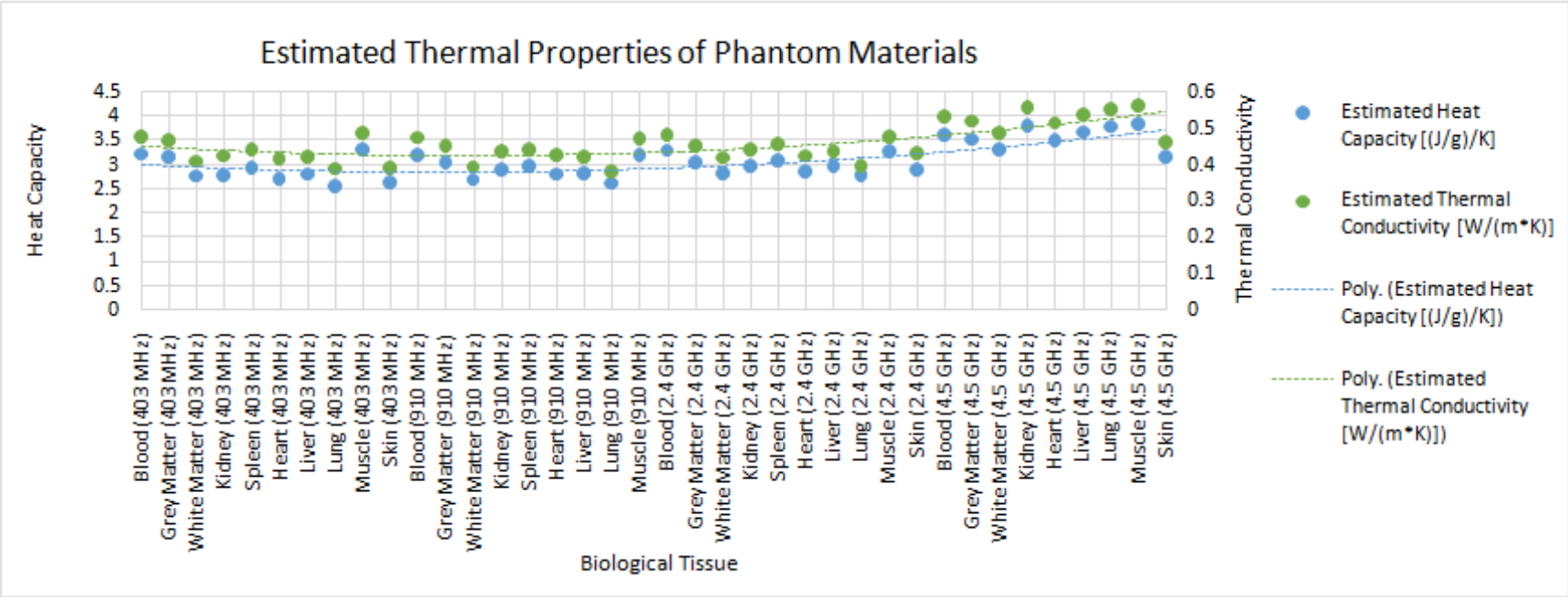

Figure 48: The estimated thermal properties of the phantom materials for the 100 ml recipes across the specified frequencies.

The permittivity of the phantom materials are lowest at the middle frequencies (910 MHz and 2.4 GHz) and higher at the lower and upper extremes (403 MHz and 4.5 GHz). Permittivity and conductivity behave differently at various frequencies and are also dependent on the material under test. However, generally permittivity tends to decrease as frequency increases, which is in contrast to conductivity which tends to increase as frequency increases. These trends are better illustrated by a logarithmic scale plotting permittivity against frequency, as illustrated by Gabriel et al [34] in Section 2.5.3 (page 20). However, due to the frequency of interest of this project only extending to 4.5 GHz, this trend is not depicted in Figure 49.

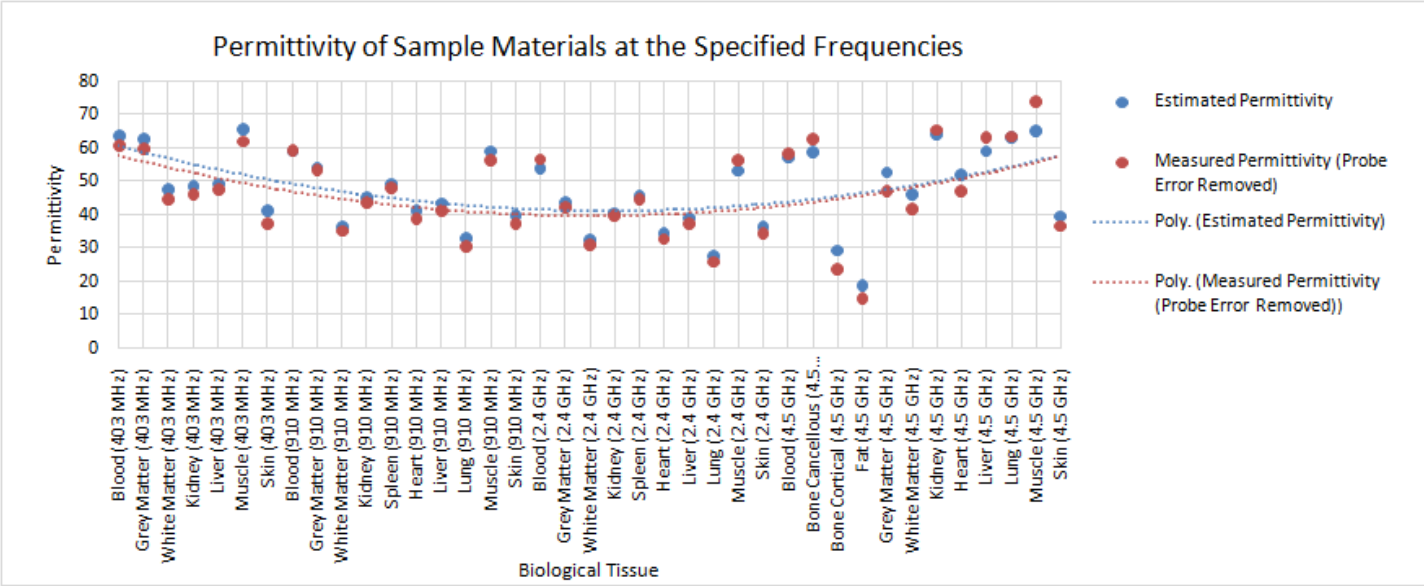

Figure 49: The permittivity of the sample materials for the 100 ml recipes across the specified frequencies.

Another trend that was investigated was the behaviour of phantom tissue permittivity measurements in terms of their loss tangent, which is a measure of the loss-rate of electrical energy in a system proportional to frequency. These were obtained by converting the reflection coefficients to dielectric constants over the frequency range of 300 kHz to 8 GHz. Figures 50 and 51 illustrate the measured loss tangent and permittivity of the respective samples of the 100 ml 4.5 GHz blood recipe, whereas Figure 52 and Figure 53 illustrate the average values of these measurements and their aggregate and recipe error margins. Due to the large number of sample measurements, the rest of the direct permittivity trend lines were attached electronically in the external media (Appendix I, page 133).

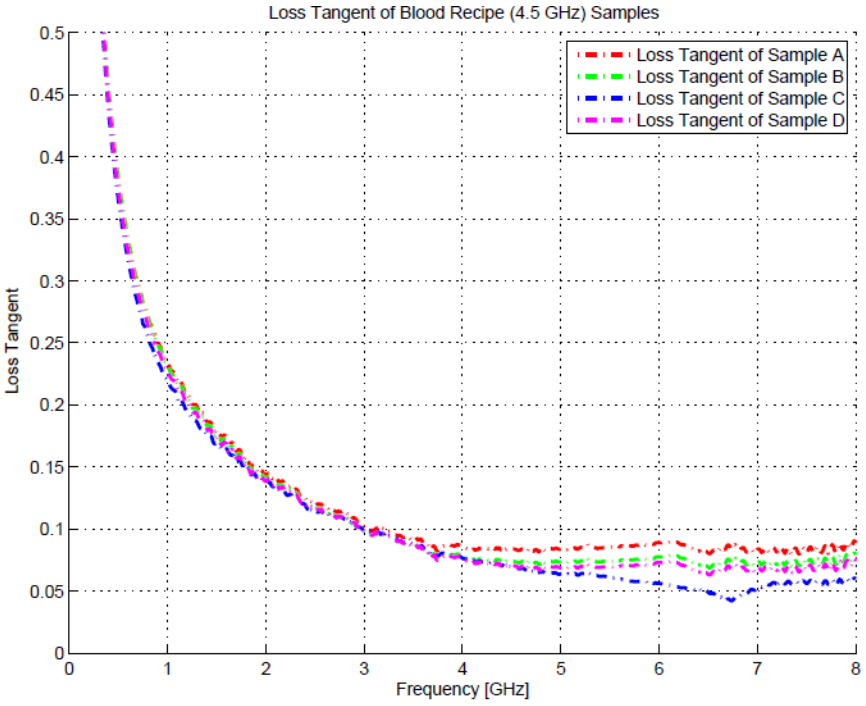

Figure 50: Loss tangent measurements of the 100 ml 4.5 GHz blood recipe samples.

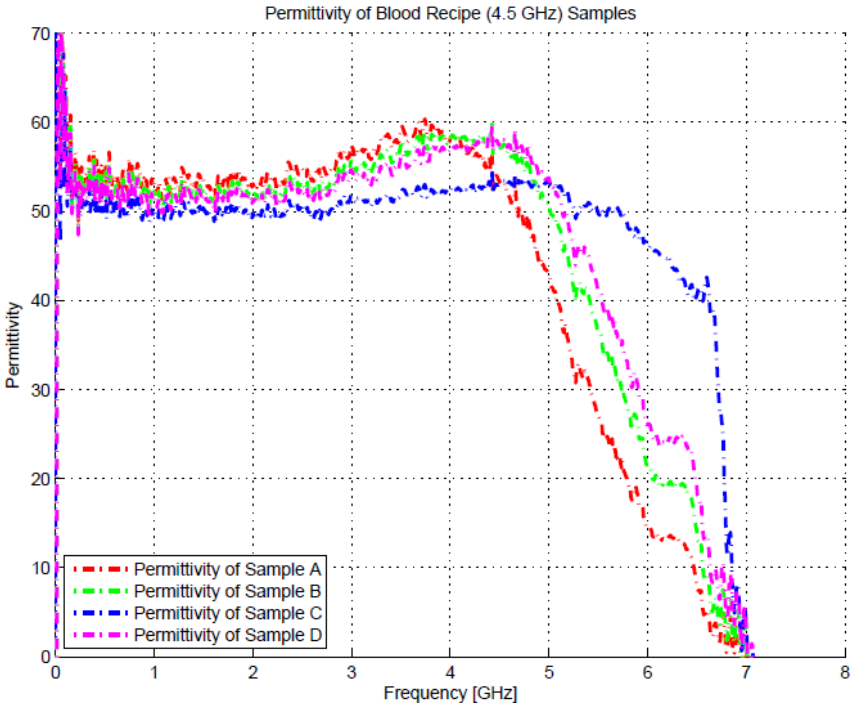

Figure 51: Permittivity measurements of the 100 ml 4.5 GHz blood recipe samples.

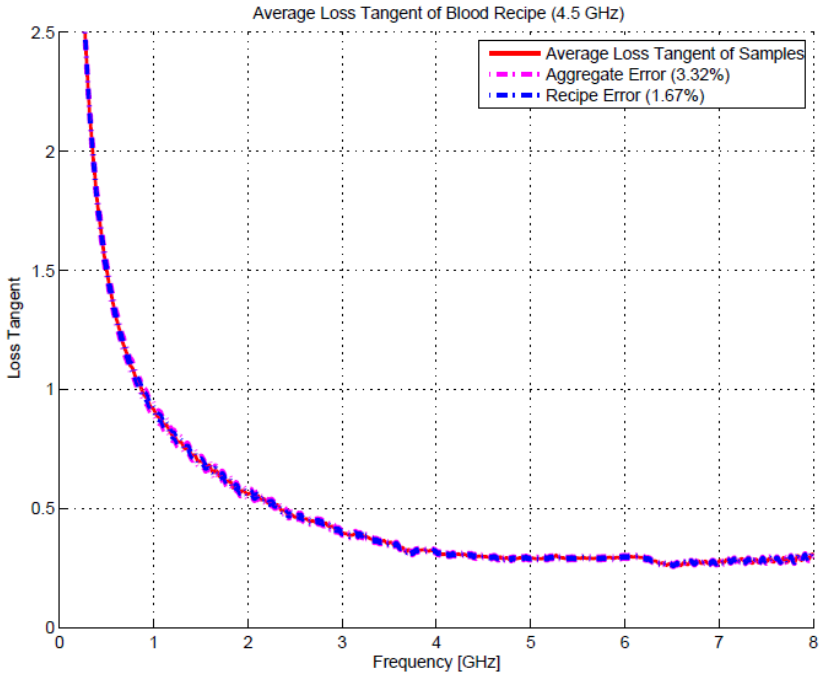

Figure 52: Average loss tangent of the 100 ml 4.5 GHz blood recipe samples.

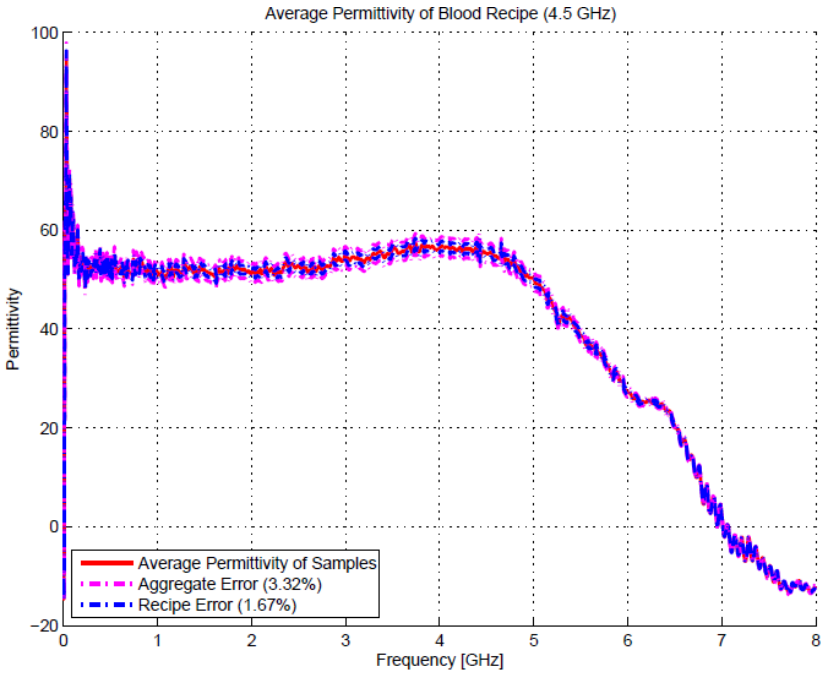

Figure 53: Average permittivity of the 100 ml 4.5 GHz blood recipe samples.

Figures 50 to 53 indicate a good agreement between the dielectric properties of the various samples, both in terms of loss tangent and permittivity. The error margins are also quite small with an average permittivity very close to the estimated value. Figure 53 clearly illustrates a heavy decline in the measured permittivity between 4 and 5 GHz. The same behaviour is evident for many other samples. This phenomenon is caused by the N-type measurement probe, which is defined as a middle ranged frequency device and could thus only accurately measure the reflection coefficient up to a frequency of approximately 5 GHz. Other types of probe such as the SMA or 7/16 probe are also restricted to operate in defined frequency ranges, which might overlap with some of the measurable frequencies of the N-Type probe. However, the N-Type probe was selected due its capability of measuring all of the frequencies considered in this project.

5.4 Practical Viability of a Rhinoceros Agar Model

Even though a less expensive form of sucrose could be used, the cost and practical difficulty of creating a full-scale phantom model remained prohibitive due to the amount of agar required and the weight of such a model (approximately 3 tons). Thus, two alternatives were investigated to further reduce the cost and ensure practical viability. The first approach is the representation of the rhinoceros leg from its foot to its hip, including all of the layers of the full-scale phantom model. The dimensions of the leg phantom model are illustrated in Figure 54.

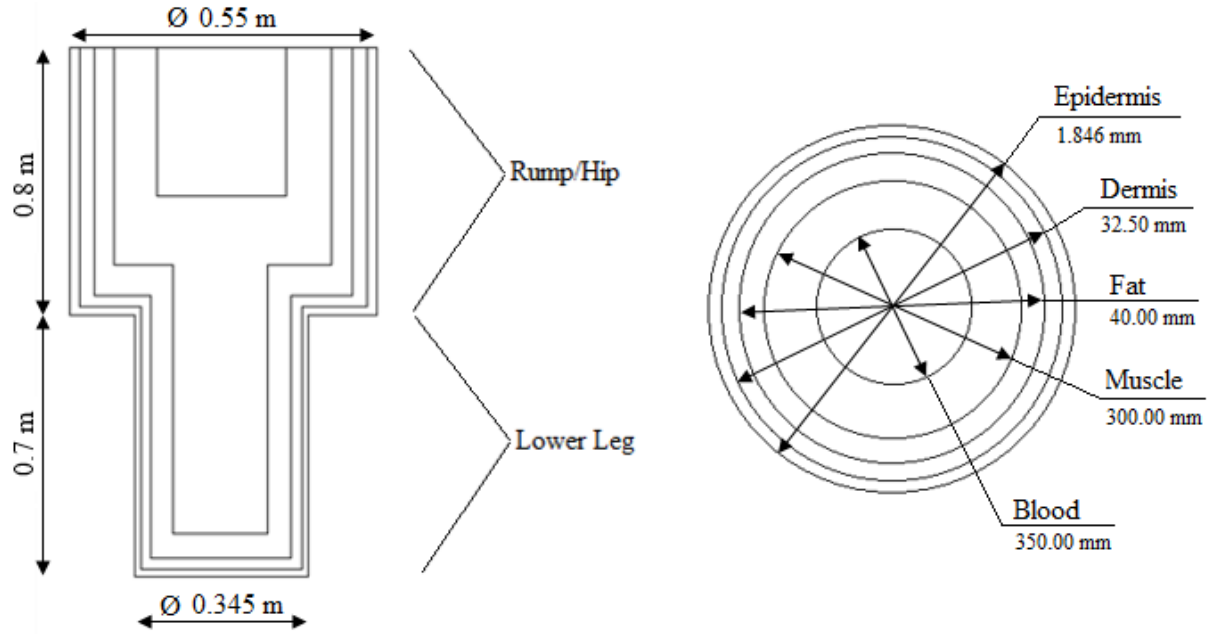

Figure 54: Phantom leg concept model.

The volume of each layer was calculated in order to establish the amount of gel required to create this phantom model. The 403 MHz recipes were selected, seeing as this frequency generally required the largest quantities of ingredients during previous experiments. The volumes were calculated as follows:

Table 27: Ingredient requirements for phantom leg model.

Biological Tissue	Volume [m^3]	Agar [g]	Salt [kg]	Sugar [kg]	Water [litre]	Final Estimated Volume [litre]
Epidermis	0.0044	55.00	0.999	4.369	2.20	4.9472
Dermis	0.0699	825.00	1.621	61.106	33.00	71.3860
Fat	0.0683	775.00	13.683	60.842	31.00	69.2477
Muscle	0.0697	1325.00	1.190	28.678	53.00	70.7862
Blood	0.0433	800.00	0.994	19.966	32.00	44.3971
Total	**0.2556**	**3780.00**	**18.488**	**174.961**	**151.20**	**260.7641**

The cost of the phantom leg model amounts to R16 866.21. Although this is much less than the full-scale model, it remains quite an expensive undertaking seeing as the agar phantom would only survive a few days outside of storage. This model would weigh approximately 283.8 kg (if a uniform density of 1100 kg/m^3 is used), which is a significant improvement over the full-scale model, but it would still be difficult to manoeuvre without the help of heavy machinery. Thus, a second approach was proposed, in which only the flank of a rhinoceros is considered and includes all of the layers of the full-scale phantom model. Figure 55 illustrates the dimensions of the rhinoceros flank phantom model.

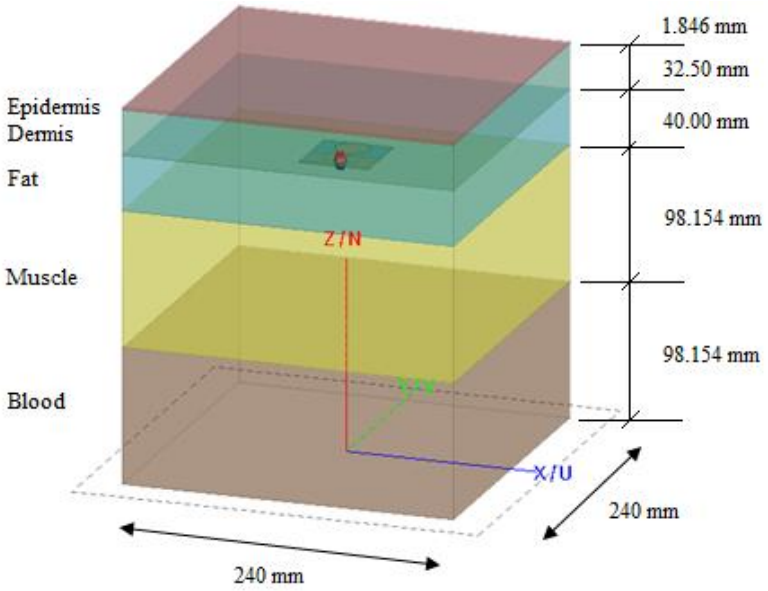

Figure 55: Rhinoceros flank (slab) phantom model.

As can be seen from Figure 55, the slab model is much smaller than the previous phantom models and therefore much more inexpensive. The overall volume of the slab amounts to 0.0156 m^3, which would require the following quantities of ingredients:

Table 28: Ingredient requirements for rhinoceros flank model.

Frequency	Agar [g]	Salt [kg]	Sugar [kg]	Water [litre]
403 MHz	295.50	1.567	13.383	11.820
2.4 GHz	270.50	0.114	8.696	10.820
Total	**566.00**	**1.680**	**22.078**	**22.640**

The cost of the flank model is R3430.83, which is significantly lower than both the previous candidates. This model provides a means of testing at more than one frequency due to its low cost. It is also much more practical due to its small size. Using a density of 1100 kg/m^3, the approximated weight of the model is 17.16 kg. As before, the antenna would be placed in the fat layer and propagation as well as transmission through the model would be investigated. The flank model was selected to establish whether or not it is a sufficient approximation to the full rhinoceros model to allow its use in the design of implanted sensors, which will be explored by numerical simulation.

5.5 Conclusion

In this chapter we have demonstrated a strong agreement between the theoretical and practical dielectric properties of the agar phantoms. An overall average error of 6.22% was achieved, even when including tissues with a large variance in permittivity such as bone and fat. The average error for the 2.4 GHz recipe group, which is the focus for this project, was even lower at 4.49%. The dielectric properties, along with other physical parameters such as the relationship between permittivity and temperature, permittivity and frequency, the salt and sugar requirements, the density and thermal characteristics were also in agreement with what can be found in the literature. Furthermore, the cost of the rhinoceros phantom was greatly reduced by using household sugar rather than the more expensive purified sucrose. This was shown to have a minimal effect on the accuracy of the resulting permittivities, affecting only the useable lifetime of the prepared samples.

The findings of this chapter support the use of agar as a gelling agent. Not only did it deliver accurate results, but it was easy to cast, safe to work with and had the additional benefit of transparency, which allowed faulty samples to be detected and sample end-of-life to be determined. The samples had a firm, yet soft consistency, which contributes to the physical similarities between the agar plates and biological tissues such as skin, muscle and fat. Figure 56 illustrates the transparency and texture of these samples.

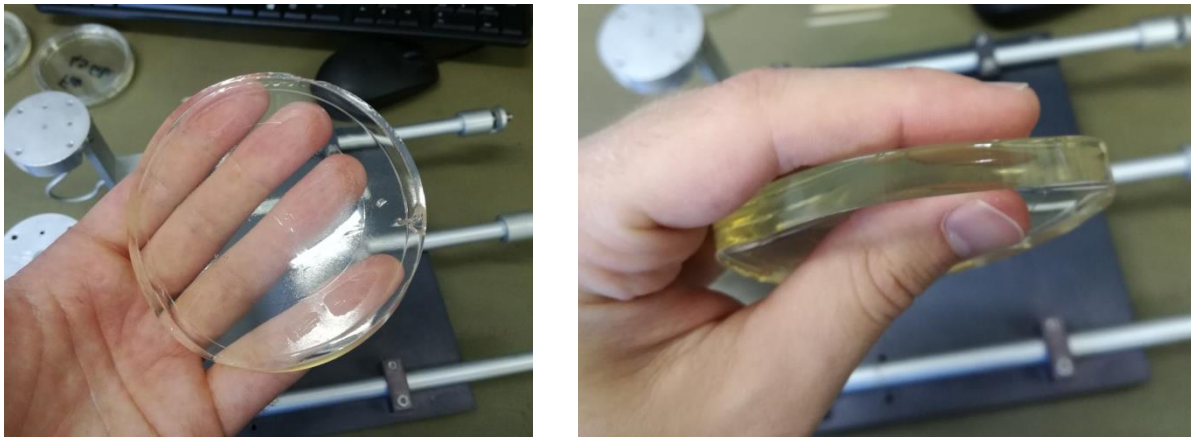

Figure 56: The transparency and consistency of the agar samples.

Full-body and leg phantom models were considered, but both were found to be impractical based on cost and weight estimations. Thus, a model of the rhinoceros flank was designed as a practical and economical phantom for further experimentation.

Chapter 6.

6. Computer Simulation Results

The Centre for High Performance Computing (CHPC) in Cape Town, South Africa, recently unveiled the Lengau high performance computer (HPC), with over 24 000 cores and an approximate speed of 1000 teraflops. This makes it the fastest computer on the African continent. The CHPC forms part of the Council for Scientific and Industrial Research (CSIR) group. The antenna and EM propagation simulations in this thesis, which were highly computationally expensive, were carried out on the Lengau cluster. The results of the computer simulations are illustrated and discussed in this chapter.

6.1 Rhinoceros Flank (Slab) Phantom Model

This model serves as an inexpensive lightweight phantom for observing the propagation and attenuation effects of an antenna through various layers of rhinoceros tissue. As for the other phantom models, this model can be configured in many ways, such as the option of using the weighted average or alternative dermis approximation which was calculated by using the permittivity values of individual rhinoceros skin constituents (Chapter 4, page 37). The alternative dermis approximation will henceforth be referred to as the "Shadwick approximation". Both these dermis properties were simulated and compared with respect to each type of suggested implant antenna at a frequency of 2.4 GHz. A transmitting antenna was placed facing upward 0.212308 m within the slab model. This places the antenna in the centre of the fat layer. A receiving antenna was placed facing downward at a height of 0.275 m, which is just outside and above the slab model. The distance between the antennas is 6.2692 cm, which is within the farfield region according to the Fraunhofer distance. The far-field distance is the distance from the transmitting antenna to the beginning of the Fraunhofer region (far field), which was calculated as 4.16 cm for the 2.4 GHz MFPEMA. Since all of the antennas have a diameter not greater than 0.051 m as was used for the above calculation, each will also be situated within the farfield. Figure 57 illustrates the rhinoceros flank phantom model and antenna locations.

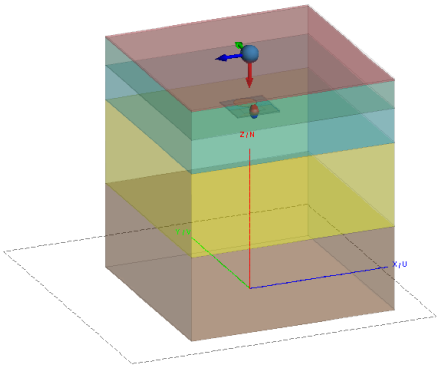

Figure 57: Configuration of the rhinoceros flank phantom model.

The results of the CPFLPPA transmitting and receiving pair simulation were much less favourable in terms of their electric field and power efficiency than those of the MFPEMA and PIFA and can be viewed in the external media (Appendix I, page 133). The results of additional simulations pertaining to the rhinoceros flank model such as those of the MFPEMA, PIFA and CPFLPPA transmitters paired with the CCFA receiver, as well as the 403 MHz CCFA transmitter and MFPEMA receiver simulation, can also be viewed in the external media.

6.1.1 MFPEMA Transmitting and Receiving Pair

It is clear from both dermis configurations that the rhinoceros tissue has a significant influence on the shape and performance of the antenna propagation, with severe attenuation in the lower layers of the model. Detailed illustrations of the total realised gain of the MFPEMA implanted in the flank model, can be viewed in Appendix G (page 127). The influence of each phantom medium on the antenna properties are better described by the specific absorption rate (SAR) of the various layers, which is a measure of the rate at which energy is absorbed by a medium when exposed to a radiofrequency electromagnetic field. Figure 58 illustrates the SAR [W/kg] through the slab in the z-direction (from the bottom of the model to the top) with x and y positions close to the centre of the model.

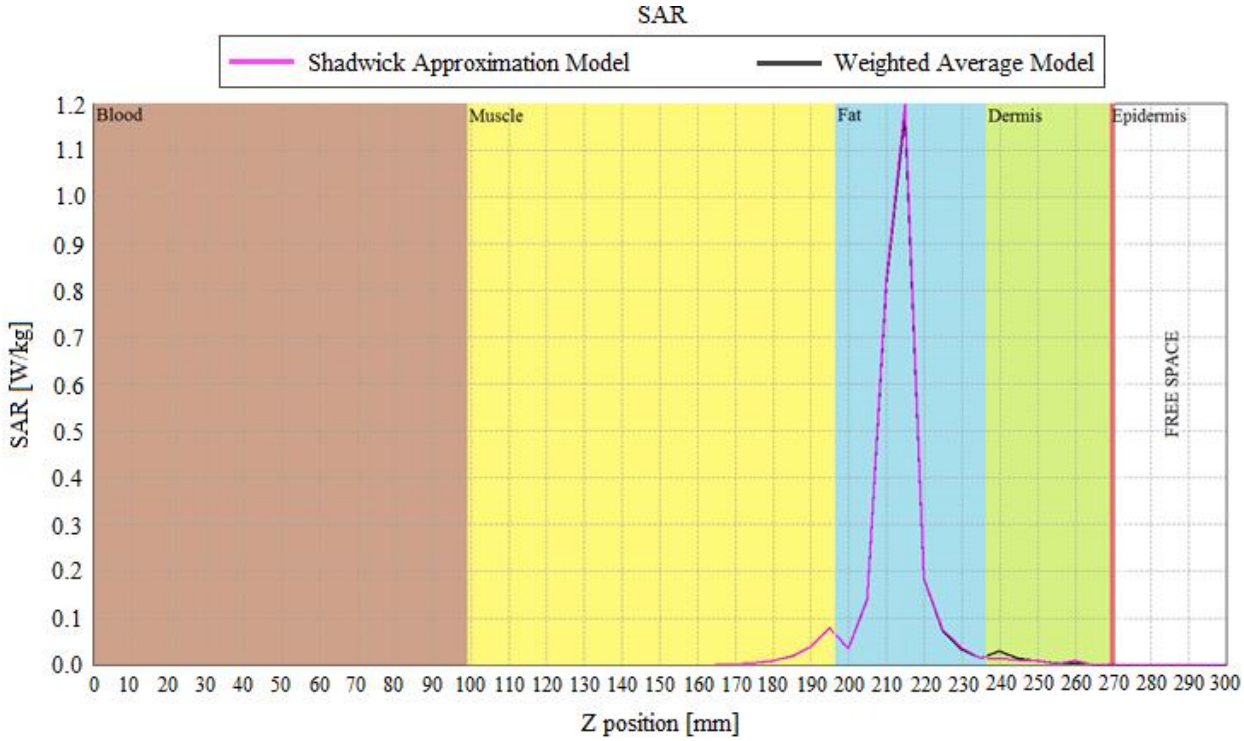

Figure 58: SAR values of the MFPEMA Shadwick and weighted average flank models.

The simulated SAR illustrated in Figure 58 indicates a peak value of approximately 1.2 W/kg at the point of implantation. It is clear from this illustration that the energy moving through the model dissipates quite quickly moving away from the source. This suggests that signal strength would also be greatly decreased compared to a free space model. All configurations of the flank model display similar trends, with most of the energy being absorbed by the fat layer. Table 29 indicates the dielectric medium average SAR values for the individual layers. Although the SAR values between the weighted average and Shadwick models differ per medium, the average SAR of both models are quite similar. The input power was approximately 15.15 mW for both models.

Table 29: Specific absorption rate of the individual phantom layers (Flank - MFPEMA).

Biological Tissue	Specific Absorption Rate [W/kg]		Power Loss [W]	
	Shadwick Model	Weighted Average Model	Shadwick Model	Weighted Average Model
Epidermis	0.3584E-03	0.0789E-03	0.0381E-03	8.3848E-06
Dermis	0.8126E-03	1.0949E-03	1.5211E-03	2.0497E-03
Fat	4.8837E-03	4.6057E-03	11.2384E-03	10.5987E-03
Muscle	0.3536E-03	0.3531E-04	1.9992E-03	1.9961E-03
Blood	4.3979E-08	2.0775E-08	2.4864E-07	1.1746E-07
Average SAR for entire domain/Sum of all losses	0.9493E-03	0.9401E-03	15.1050E-03	14.9760E-03

The SAR of the signals emitted by cellular phones are regularly measured to ensure the safety of their users. In the United States of America, the SAR of mobile phones is restricted to 1.6 W/kg averaged over 1 gram of human tissue, while in the European Union the limit is 2.0 W/kg over 10g of human tissue. Table 30 indicates the SAR values specified by the Institute of Electrical and Electronic Engineers (IEEE) and the International Commission on Non-Ionizing Radiation Protection (ICNIRP) for human tissue.

Table 30: The IEEE and ICNIRP SAR limitations for human tissue exposure **[40]**.

Localisation	Source	SAR [W/kg]
Whole-body average	ICNIRP/IEEE	0.4
10 g in head and trunk	ICNIRP	10
10 g in limbs	ICNIRP	20
1 g in body[a]	IEEE	8

[a] The IEEE states that the 1 g limit is applicable to the entire body, except the hands, wrists, feet and ankles, which should not exceed a 10 g psSAR of 20 W/kg (same value as the one from ICNIRP for the limbs).

Based on the dense cross-linking of collagen in rhinoceros tissue, it is assumed that rhinoceros tissue could withstand higher levels of SAR than human tissue. Thus, the comparison between Table 29 and Table 30 suggests that the implantable antenna is within safe operating conditions with regards to its SAR exposure. The SAR level in the x and y directions dissipates towards the edges of the model, with each layer's maximum SAR in the centre of the flank (aligned with the implanted antenna).

Since the same type of antenna is used for transmission and reception, their free space characteristics are identical. The Friis equation describes the ratio of power available at the input of the receiving antenna to the output power of the transmitting antenna, and is given by (for farfield only):

$$\frac{P_r}{P_t} = G_t G_r \left(\frac{\lambda}{4\pi R}\right)^2 \qquad (5.0)$$

with

P_r = Power of receiving antenna.
P_t = Power of transmitting antenna.
G_r = Gain of receiving antenna with respect to an isotropic radiator.
G_t = Gain of transmitting antenna with respect to an isotropic radiator.
λ = Wavelength.
R = Distance between the antennas.

Using the Friis equation for the MFPEMA pair in free space with a wavelength of 0.1249 m (corresponding to 2.4 GHz in free space) and gains of 2.12 dBi for the two identical antennas a distance of 0.062692 m apart, the ratio of power transmitted to power received is calculated to be 6.67%. This translates to 1.012 mW of received power when the source transmits 15.157 mW. After embedding the transmitting antenna within the fat layer of the Shadwick model, its simulated gain was reduced to -21.91 dBi (theta = 0°), which reduced the power ratio to less than 0.01%. This relates to a received power of 3.999 uW for the Shadwick model and 0.3507 uW for the weighted average model, with all other parameters kept constant. However, these values are unreliable since the Friis equation is valid only for antennas in free space, which is not necessarily the case with regards to this configuration even after the phantom is assumed to represent an entirely new antenna.

Thus, even by examining the implanted antenna's properties and applying its altered characteristics to the power equation, the calculation may still be somewhat inaccurate due to assumptions and unseen changes such as the alteration of the wavelength of the signal as it passes through the medium. The wavelength, which is assumed to be constant in the Friis equation due to the nature of free space, changes as it moves through the various layers of the simulation model. Thus, the simulations do not make Friis' assumptions. The received power calculated by the simulation software was 25.852 uW for the Shadwick model and 4.525 uW for the weighted average model. It is clear that these values differ from the Friis equation calculations and thus confirms that the Friis equation is not applicable for this configuration. Assuming the software calculations are correct, the power efficiency of the MFPEMA flank model is 0.17% for the Shadwick model and 0.03% for the weighted average model.

6.1.2 PIFA Transmitting and Receiving Pair

Similar to the MFPEMA, it would appear that the PIFA achieves better propagation through the Shadwick model than the weighted average model, with regards to its realised gain. This can also be deduced from Figure 59, which illustrates the SAR [W/kg] through the slab in the z-direction and illustrates slightly more energy being absorbed by the weighted average model, particularly in the dermis layer. Illustrations of the total realised gain of the PIFA implanted in the flank model, can be viewed in Appendix G (page 127).

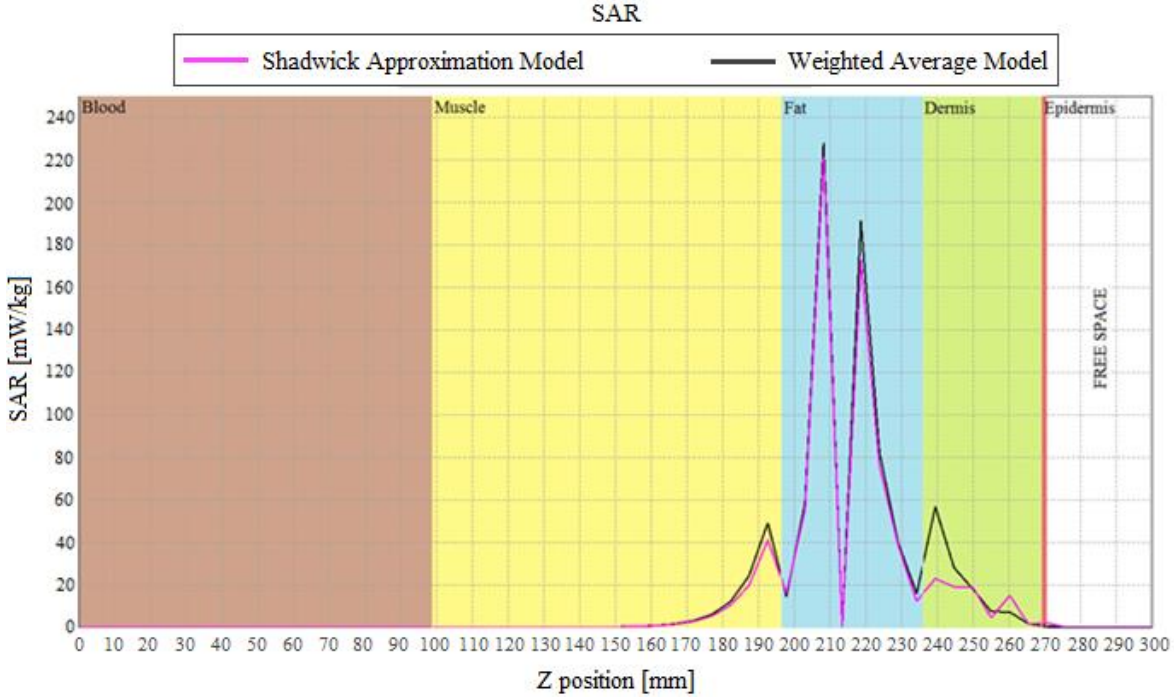

Figure 59: SAR values of the PIFA Shadwick and weighted average flank models.

The SAR illustrated by Figure 59 indicates a peak value of approximately 230 mW/kg close to the point of implantation, whereas the rest of the model absorbs much lower quantities of energy in the order of tens of milli-Watts or less. Once again, the energy dissipates quite quickly moving away from the source and most of the energy is absorbed by the fat layer, which has a very low electrical conductivity of 0.175 at 2.4 GHz. Table 31 indicates the dielectric medium average SAR values for each of the individual layers. The input power was approximately 12.5 mW for both models.

Table 31: Specific absorption rate of the individual phantom layers (Flank - PIFA).

Biological Tissue	Specific Absorption Rate [W/kg]		Power Loss [W]	
	Shadwick Model	Weighted Average Model	Shadwick Model	Weighted Average Model
Epidermis	0.2289E-03	-	0.0243E-03	4.9379E-06
Dermis	0.4567E-03	-	0.8550E-03	1.3057E-03
Fat	4.1932E-03	-	9.6468E-03	9.5217E-03
Muscle	0.1609E-03	-	0.9099E-03	0.9635E-03
Blood	1.1785E-08	-	6.6626E-08	9.9396E-09
Average SAR for entire domain/Sum of all losses	0.7337E-03	0.7568E-03	12.2410E-03	12.4990E-03

Comparing Tables 31 and 30 and the SAR exposure limits regulated in the United States of America and Europe, the PIFA's energy exposure is also within safe operating conditions. Once again, the same type of antenna is used for transmission and reception. Thus all of their free space characteristics are identical. Using the Friis free space equation for the PIFA pair with a wavelength of 0.1249 m (corresponding to 2.4 GHz) and gains of 1.73 dBi for the two identical antennas 0.062692 m apart, the power ratio was calculated as 5.58%. This translates to 0.6976 mW of received power with a source transmitting at 12.51 mW. Simulations using FEKO calculated the received power to be 21.65 uW for the Shadwick model and 7.11 uW for the weighted average model, when the receiving antenna is embedded in the fat layer. These values are much lower than those calculated using the Friis equation, which is to be expected since the Friis equation assumes that both antennas are in free space. Assuming that the FEKO power values are accurate, this would suggest a power efficiency of 0.18 % for the Shadwick model and 0.06 % for the weighted average model.

6.1.3 Summary and Conclusion

The flank phantom model simulations have confirmed that penetrating the thick skin of a rhinoceros by means of an in-vivo antenna is difficult, but not impossible. It is clear from the SAR values that most of the energy is absorbed by the fat layer in which the antenna is implanted and that the propagated energy quickly dissipates moving away from the antenna's position. The peak values of the simulated specific absorption rates of all the models also seem to be within the ranges as regulated by the United States of America, Europe and the IEEE. Considering all the configurations, the MFPEMA and PIFA remain the preferred choices for implantation antennas, because they deliver greater power efficiency. The 2.4 GHz CCFA model used in the additional computer simulations is impractical due to the delicate and thin rails of copper that need to be milled to form the antenna. These railings would have a width of less than one millimetre and thus, this antenna is not deemed viable for empirical experimentation. It was not necessary to simulate the PTMA model, due to its similarities with the CPFLPPA, which resembles the worst case scenario antenna.

Thus, henceforth only the MFPEMA and PIFA models will be used in simulations. Seeing as the PIFA is a well-known model that is regularly used as an implantation antenna, it will be used as

the baseline model to which the MFPEMA will be compared. The results suggest that the weighted average dermis configuration is more difficult to penetrate, since it had a higher specific absorption rate than the alternative dermis model. Thus, the weighted average model would henceforth be used as a worst case scenario, while the alternative dermis approximation model will represent an ideal case scenario. The flank model delivered insight into the characteristics of the phantom materials and it is an early indication that communication through the body of the rhinoceros is difficult, which suggests that successful transmission from an in-vivo antenna in the back, neck or chest to an ex-vivo antenna located at the hind leg will be very challenging. These results also indicate that wireless charging to in-vivo devices would be difficult due to the loss of energy through the tissue layers. Practical measurements of the rhinoceros flank phantom model are discussed in Chapter 7 (page 92).

6.2 Rhinoceros Cylindrical Phantom Model

This model serves as a simplified full-scale rhinoceros approximation by avoiding complex geometrical surfaces, therefore delivering a more practically achievable model. Many cylindrical phantoms have been proposed for observing the propagation and attenuation effects of mobile phones through human tissue, specifically in the torso and head region. Similar to the rhinoceros flank model, this model was configured for both the weighted average and alternative dermis approximations (all other layers kept constant). Two types of implantation antennas were used in this model, namely the MFPEMA and the PIFA. These were simulated as transmitting and receiving pairs. Simulations were also performed using the CCFA as a receiving antenna. The transmitting antenna was placed in the fat layer of the model at the two locations specified in Section 3.2.2 (page 34), namely in the back and neck regions. The receiving antenna was placed outside of the slab model at the location of the left hind leg of the rhinoceros, which is itself not part of this simplified model. Figures 60 and 61 illustrate the two configurations for this model.

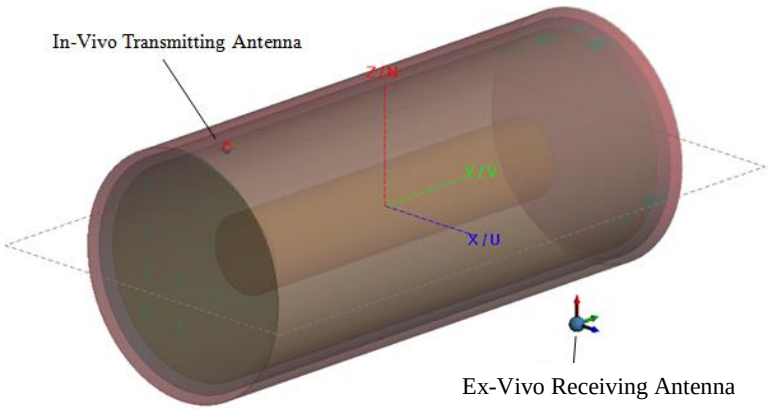

Figure 60: Configuration of the cylindrical phantom back implantation model.

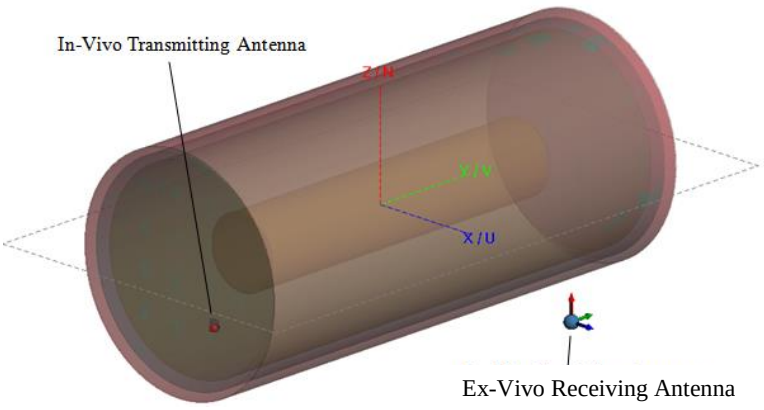

Figure 61: Configuration of the cylindrical phantom neck implantation model.

The direct distance between the in-vivo back antenna and the ex-vivo receiving antenna is approximately 2.18 m, which places the receiving antenna within the far-field region according to the Fraunhofer distance. The receiving antenna was also in the far-field region relative to the neck implantation antenna at a direct distance of approximately 2.07 m. The receiving antenna was positioned in the forward facing direction relative to the rhinoceros for all simulation models. The results of additional simulations pertaining to the cylindrical phantom model such as those of the MFPEMA and PIFA transmitters paired with the CCFA receiver, can be viewed in the external media (Appendix I, page 133).

6.2.1 MFPEMA Transmitting and Receiving Pair

Once again, the results seem to indicate that the alternative dermis model is easier to penetrate and allows slightly greater propagation through the cylindrical model. This is confirmed by Table 32, which indicates the dielectric medium average SAR values for each of the individual layers with a slightly higher absorption rate observed in the weighted average model. Illustrations of the total realised gain of the MFPEMA implanted in the back and neck positions of the cylindrical model, can be viewed in Appendix G (page 127).

Table 32: Specific absorption rate of the individual phantom layers (Cylinder - MFPEMA).

Back Implantation Model				
Biological Tissue	**Specific Absorption Rate [W/kg]**		**Power Loss [W]**	
	Shadwick Model	**Weighted Average Model**	**Shadwick Model**	**Weighted Average Model**
Epidermis	2.1716E-06	0.4716E-06	0.0407E-03	8.8447E-06
Dermis	4.7791E-06	6.8695E-06	1.5023E-03	2.1595E-03
Fat	29.9733E-06	30.3849E-06	10.4088E-03	10.5517E-03
Muscle	1.3012E-06	1.3363E-06	1.8738E-03	1.9243E-03
Blood	4.0578E-19	3.8878E-19	6.4945E-17	6.2225E-17
Average SAR for entire domain/Sum of all losses	6.0626E-06	6.4216E-06	14.2040E-03	14.9970E-03
Neck Implantation Model				
Biological Tissue	**Specific Absorption Rate [W/kg]**		**Power Loss [W]**	
	Shadwick Model	**Weighted Average Model**	**Shadwick Model**	**Weighted Average Model**
Epidermis	2.7781E-06	0.5249E-06	0.0521E-03	9.8437E-06
Dermis	4.7860E-06	6.2783E-06	1.5045E-03	1.9736E-03
Fat	30.9324E-06	29.7615E-06	10.7418E-03	10.3352E-03
Muscle	1.4194E-06	1.3506E-06	2.0440E-03	1.9450E-03
Blood	8.5935E-19	1.1204E-18	1.3754E-16	1.7932E-16
Average SAR for entire domain/Sum of all losses	6.2893E-06	6.2547E-06	14.6150E-03	14.5200E-03

As was the case in Table 31, the SAR values are within safe operating ranges. Using the Friis equation for the MFPEMA pair in free space with a wavelength of 0.1249 m (corresponding to 2.4 GHz) and gains of 2.12 dBi for the two identical antennas at a distance of 2.18 m (back model) and 2.07 m (neck model) apart, the power ratio was calculated to be approximately 0.006% or less for both models. This translates to 0.7849 uW (back model) and 0.8705 uW (neck model) of received power with a source transmitting at approximately 14.62 mW. FEKO calculated the received power as 35.47 pW for the Shadwick model and 13.33 pW for the weighted average model, after the antennas have been embedded in the fat layer. Assuming that the FEKO estimations are correct, this suggests a power efficiency of less than 0.01% for both

back implantation models. Similar results were observed with both neck implantation models, which delivered received power values of 19.432 pW for the Shadwick dermis approximation model and 37.616 pW for the weighted average model.

6.2.2 PIFA Transmitting and Receiving Pair

Illustrations of the total realised gain of the PIFA implanted in the back and neck positions of the cylindrical model, can be viewed in Appendix G (page 127). Here the difference between the alternative and weighted average model is quite apparent in terms of realised gain, as it is clear that the weighted average model absorbs much more energy. The general shape of propagation of the two models seem to be similar, although the weighted average model seems to distort or attenuate the signal much more than the alternative dermis model. Table 33 indicates the dielectric medium average SAR values for each of the individual layers. Once again, the average SAR for the entire domain of both models are quite similar and within safe operating ranges.

Table 33: Specific absorption rate of the individual phantom layers (Cylinder - PIFA).

Back Implantation Model				
Biological Tissue	**Specific Absorption Rate [W/kg]**		**Power Loss [W]**	
	Shadwick Model	**Weighted Average Model**	**Shadwick Model**	**Weighted Average Model**
Epidermis	1.4752E-06	0.2195E-06	0.0277E-03	4.1166E-06
Dermis	3.3103E-06	4.6079E-06	1.0406E-03	1.4414E-03
Fat	28.5294E-06	27.5731E-06	9.9074E-03	9.5752E-03
Muscle	0.6269E-06	0.6372E-06	0.9028E-03	0.9176E-03
Blood	1.0397E-18	1.5565E-18	1.6641E-16	2.4911E-16
Average SAR for entire domain/Sum of all losses	5.2088E-06	5.2351E-06	12.6180E-03	12.8600E-03
Neck Implantation Model				
Biological Tissue	**Specific Absorption Rate [W/kg]**		**Power Loss [W]**	
	Shadwick Model	**Weighted Average Model**	**Shadwick Model**	**Weighted Average Model**
Epidermis	1.6553E-06	0.2902E-06	0.0310E-03	5.4432E-06
Dermis	3.5936E-06	4.7720E-06	1.1297E-03	1.5001E-03
Fat	29.1948E-06	28.3915E-06	10.1384E-03	9.8594E-03
Muscle	0.7120E-06	0.6730E-06	1.0254E-03	0.9692E-03
Blood	6.7987E-18	4.9318E-18	1.0881E-15	7.8933E-16
Average SAR for entire domain/Sum of all losses	5.4044E-06	5.4086E-06	13.0450E-03	13.0770E-03

Using Friis equation for the PIFA pair in free space with a wavelength of 0.1249 m (corresponding to 2.4 GHz) and gains of 1.73 dBi for the two identical antennas at a distance of 2.18 m (back model) and 2.07 m (neck model) apart, the power ratio was calculated as approximately 0.005% for both models. This translates to 0.5903 uW (back model) and 0.6547 uW (neck model) of received power with a source transmitting at approximately 12.8 mW. FEKO calculated the received power as 15.89 pW for the Shadwick model and 190.78 pW for the weighted average model, after the antennas have been embedded in the fat layer. Here the received power of the weighted average model was higher due to the directional gain towards the receiving antenna being slightly better, although as a whole, the realised gain is less than the gain observed in the Shadwick dermis model. Assuming that the FEKO estimations are correct, this suggests a power efficiency of approximately 0.01% for both back implantation models. Similar results were observed with both neck implantation models, which delivered received

power values of 587.89 pW for the Shadwick configuration and 72.64 pW for the weighted average configuration with approximate power ratios of less than 0.01%.

6.2.3 Summary and Conclusion

Based on the low power efficiency of 0.01% or less for all model configurations, the findings of the cylindrical phantom model have confirmed the predictions made from the analysis of the rhinoceros flank model - successful transmission from an in-vivo antenna in the back, neck or chest to an ex-vivo antenna located at the hind leg, will be very challenging. Once again, most of the energy is absorbed by the fat layer in which the antenna is implanted and the simulated specific absorption rates of all the models also seem to be within the ranges as regulated by the United States of America, Europe and the IEEE.

6.3 Anatomical Rhinoceros Phantom Model

This model serves as full-scale anatomical representation of rhinoceros tissue. Three models were designed, including an anatomical layered model, an organ model and a skeletal model.

6.3.1 Anatomical Layered Model

This final model serves as a full-scale rhinoceros approximation without organs or skeletal structure. It is an anatomical approximation of the various layers of rhinoceros skin, such as the epidermis, dermis and fat, and includes the muscle and blood layers specified in previous models. As for previous models, this model was configured for both the weighted average and alternative dermis approximations (all other layers were kept constant). Two types of implantation antennas were used in this model, namely the MFPEMA and PIFA. These were simulated as transmitting and receiving pairs and were also simulated using the CCFA as a receiving antenna. The transmitting antenna was placed in the fat layer of the model at the locations specified in Section 3.2.2 (page 34), namely in the back, neck and chest regions. The receiving antenna was placed outside of the rhinoceros body against the hind left leg. Due to the negligible effect of the epidermis found in initial simulations, this layer was removed to reduce the computational requirements. Figures 62 to 64 illustrate the three antenna configurations considered for this model. Additional illustrations can be viewed in the external media (Appendix I, page 133).

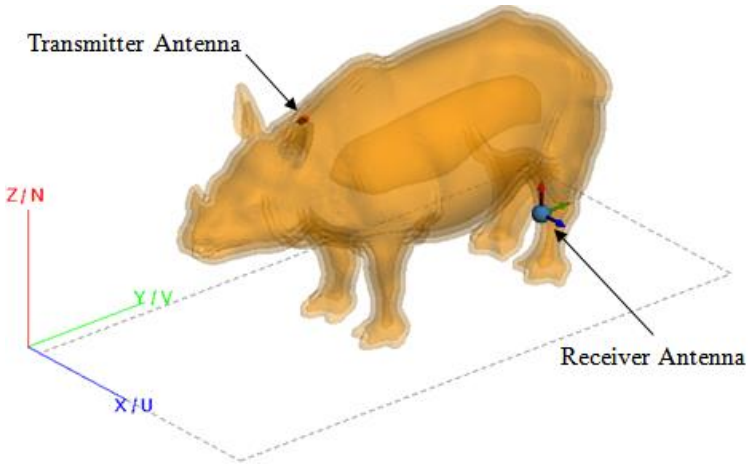

Figure 62: Configuration of the anatomical phantom back implantation model.

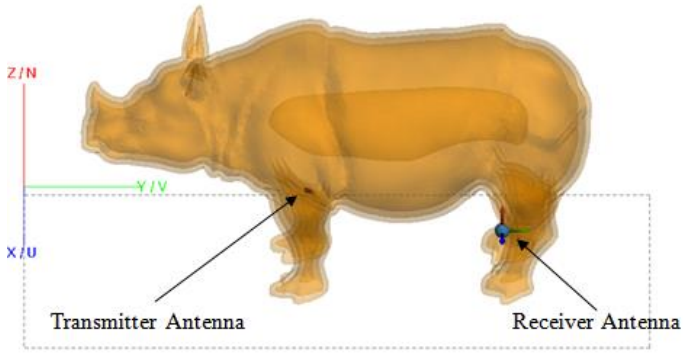

Figure 63: Configuration of the anatomical phantom chest implantation model.

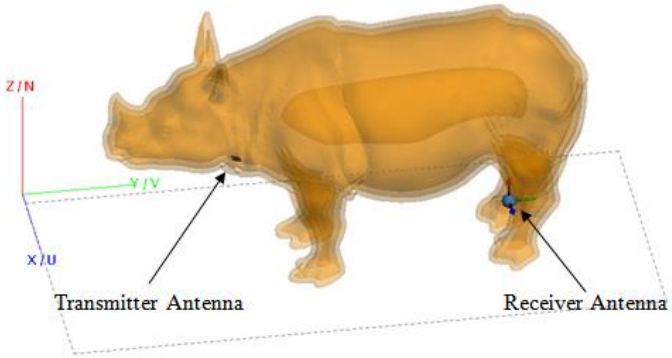

Figure 64: Configuration of the anatomical phantom neck implantation model

The direct distance between the in-vivo back antenna and the ex-vivo receiving antenna is approximately 2.181 m, which places the receiving antenna within the far-field region according to the Fraunhofer distance. The receiving antenna was also in the far-field region relative to the chest implantation antenna at a direct distance of approximately 1.335 m and 1.945 m relative to the neck implantation antenna. The receiving antenna was positioned in the forward facing direction relative to the rhinoceros for all simulation models. The same directional referencing used in Figures 62 to 64 was used for all simulations.

6.3.1.1 MFPEMA Transmitting and Receiving Pair

Six configurations were used to investigate the propagation characteristics of the MFPEMA, namely the weighted average and Shadwick dermis dielectric approximations for the back, chest and neck configurations. In all cases the organs and skeleton were excluded from the anatomically correct rhinoceros model. Specifically, the gain, SAR, electric field and received power were investigated. Figures 65 and 66 show the realised gain when using the MFPEMA located in the back and neck respectively for both the Shadwick and weighted average approximations. The realised gain is calculated by determining the total efficiency of the antenna by considering the reflection coefficient of the 50Ω connector, as well as the directivity of the antenna. Additional illustrations pertaining to the directionality of the gain, can be viewed in Appendix H (page 131).

It is clear from both models that the propagation towards the hind of the rhinoceros is severely attenuated and that most of the energy escapes in the forward facing direction relative to the rhinoceros. The maximum gain is approximately -23 dBi for the Shadwick model and -27 dBi for the weighted average model, when the implant is located in the back, and -26 dBi for the Shadwick model and -33 dBi for the weighted average model, when the implant is located in the neck. The input power to the transmitting antenna was approximately 14.6 mW for all

simulations. These results agree with previous findings which suggested that the weighted average model has a greater attenuating effect on the antenna radiation.

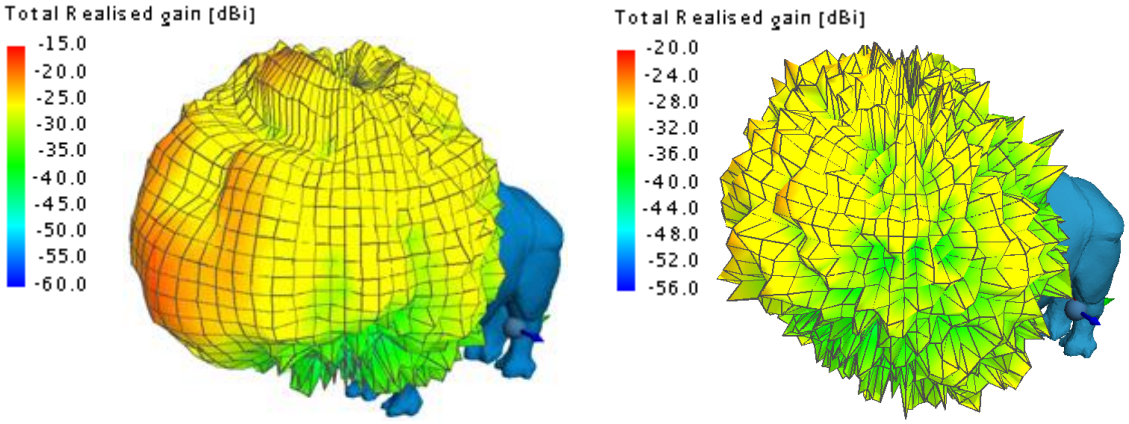

Figure 65: Realised gain of the Shadwick (left) and weighted average (right) anatomical rhinoceros back model [MFPEMA pair].

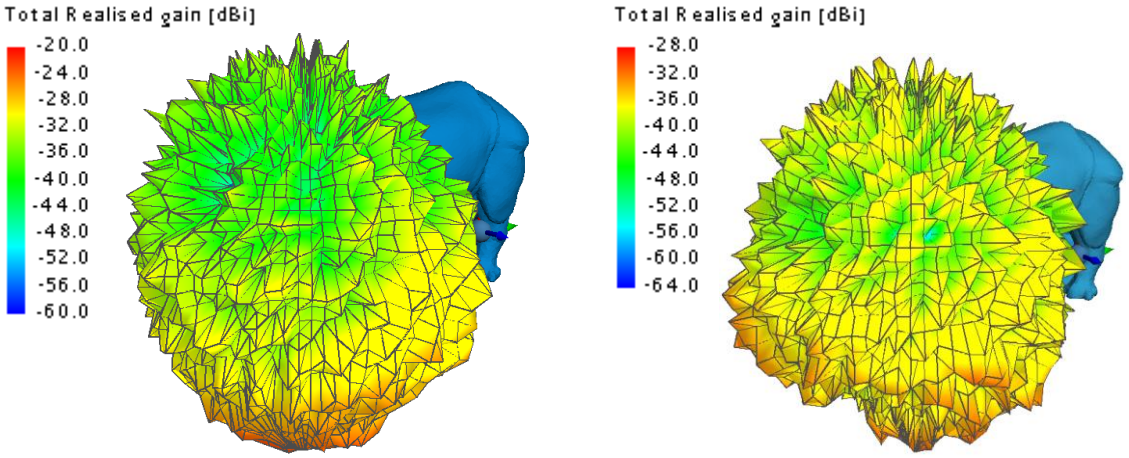

Figure 66: Realised gain of the Shadwick (left) and weighted average (right) anatomical rhinoceros neck model [MFPEMA pair].

The dispersion of the electrical field around the rhinoceros gives a visual representation of the way in which the transmitted energy dissipates. Figures 67 to 70 illustrate the electric field of the Shadwick and weighted average configurations for the back and neck antenna locations on yz- and xy-surfaces. Once again, it is clear that very little energy penetrates the thick hide of the rhinoceros. The maximum electric field values were 210 mV/m and 108 mV/m for the Shadwick and weighted average models respectively at the location of the back implant, and 87.5 mV/m and 32 mV/m for the Shadwick and weighted average models respectively, at the location of the neck implant.

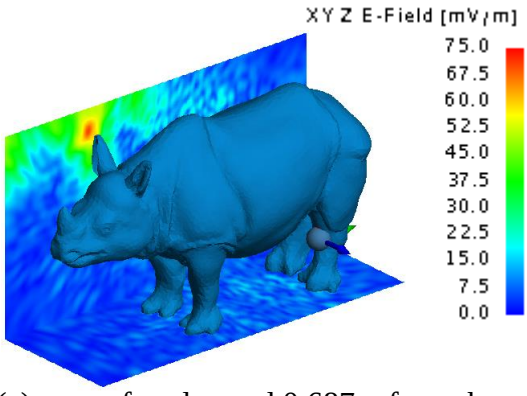

(a) xy-surface located 0.687m from the antenna and the xy-surface located 1.647m from the antenna.

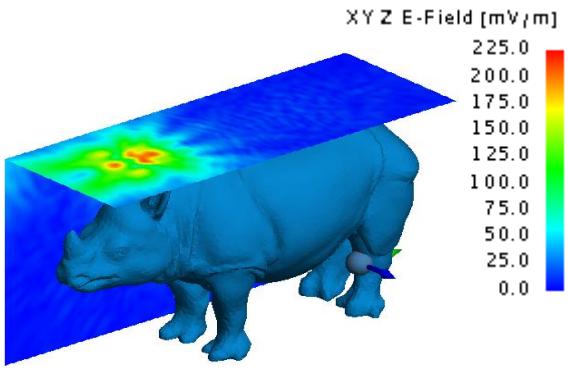

(b) yz-surface located 0.687m from the antenna and the xy-surface located 0.312m from the antenna.

Figure 67: Electric field of the MFPEMA in the back location for the Shadwick approximation.

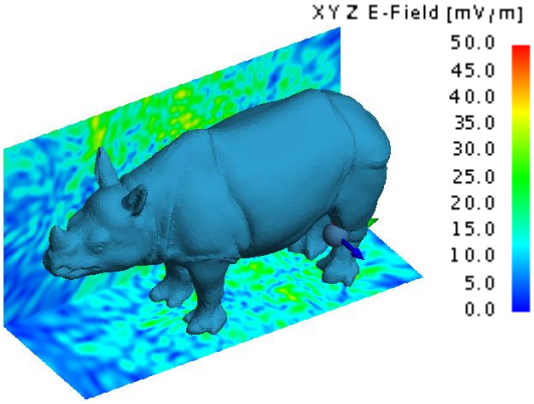

(a) yz-surface located 0.687m from the antenna and the xy-surface located 1.647m from the antenna.

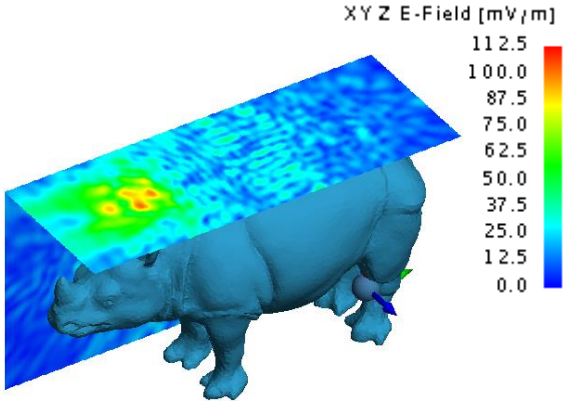

(b) yz-surface located 0.687m from the antenna and the xy-surface located 0.312m from the antenna.

Figure 68: Electric field of the MFPEMA in the back location for the weighted average approximation.

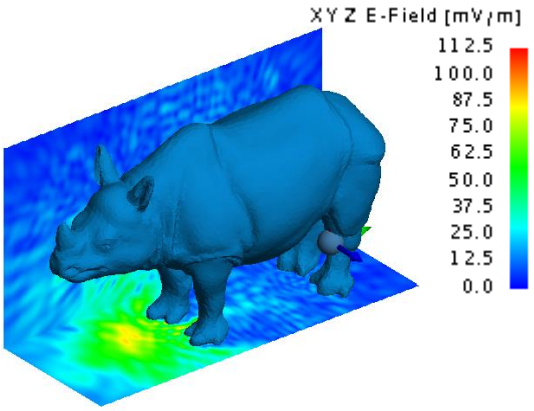

(a) yz-surface located 0.687m from the antenna and the xy-surface located 0.854m from the antenna.

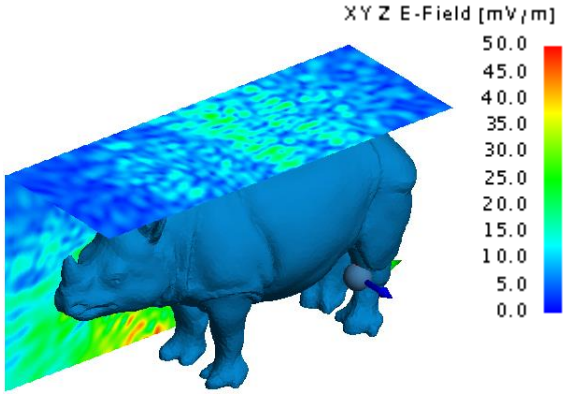

(b) yz-surface located 0.687m from the antenna and the xy-surface located 1.105m from the antenna.

Figure 69: Electric field of the MFPEMA in the neck location for the Shadwick approximation.

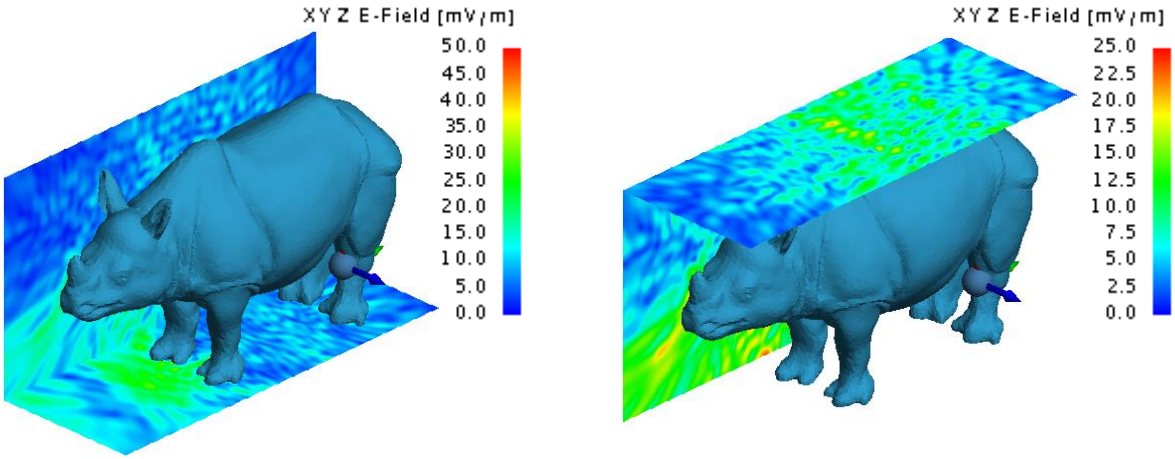

(a) yz-surface located 0.687m from the antenna and the xy-surface located 0.854m from the antenna.

(b) yz-surface located 0.687m from the antenna and the xy-surface located 1.105m from the antenna.

Figure 70: Electric field of the MFPEMA in the neck location for the weighted average approximation.

Both models indicate similar electric field strengths at the location of the receiving antenna as illustrated by Figures 71 and 72. The approximate electric field values were 30 mV/m for the Shadwick model and 27 mV/m for the weighted average model, with regards to the back implantation and 25 mV/m for the Shadwick model and 12 mV/m for the weighted average model, with regards to the neck implantation. The yz-surface is located 0.272 m from the x-position of the implantation antenna and cuts through the position of the receiving antenna.

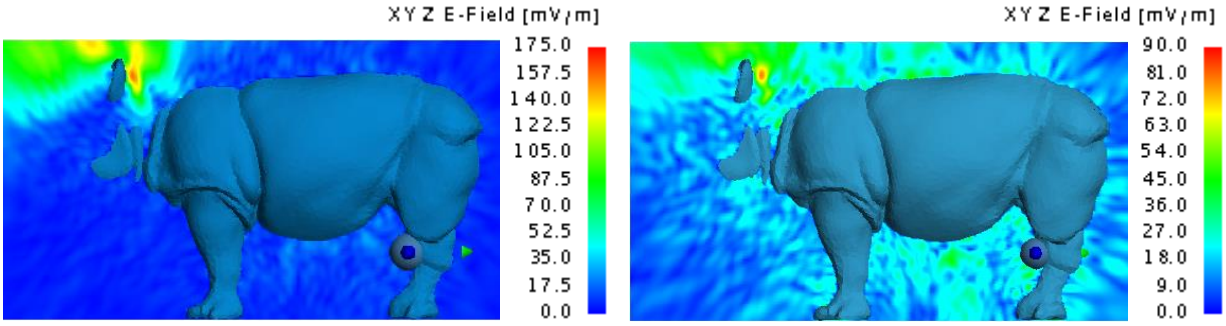

Figure 71: Electric field of the MFPEMA in the back location for the Shadwick [left] and weighted average [right] approximations.

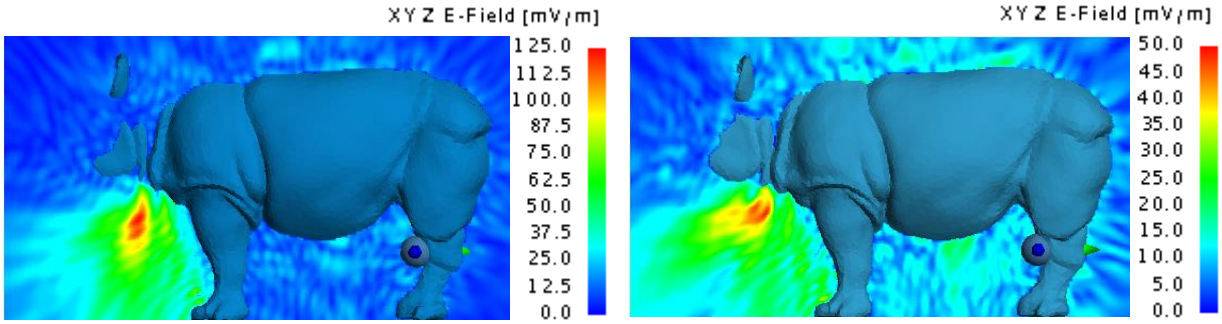

Figure 72: Electric field of the MFPEMA in the neck location for the Shadwick [left] and weighted average [right] approximations.

These analyses support the notion that, although the implanted antennas are capable of penetrating the thick hide of the rhinoceros, they are not effective at transmitting a signal from an in-vivo position at the back of the neck to an ex-vivo location at the hind leg. This is supported by the very low received power values of 149.86 pW and 214.44 pW for the Shadwick and weighted average models respectively, for the configuration in which the implant is located in the back. Similar received power values were attained when the implant was located in the neck, with 194 pW and 2.468 pW for the Shadwick and weighted average models respectively. As can be seen from Figure 73, which illustrates the SAR through the rhinoceros models in the y-direction, most of the energy is absorbed within a few centimetres of the point of implantation.

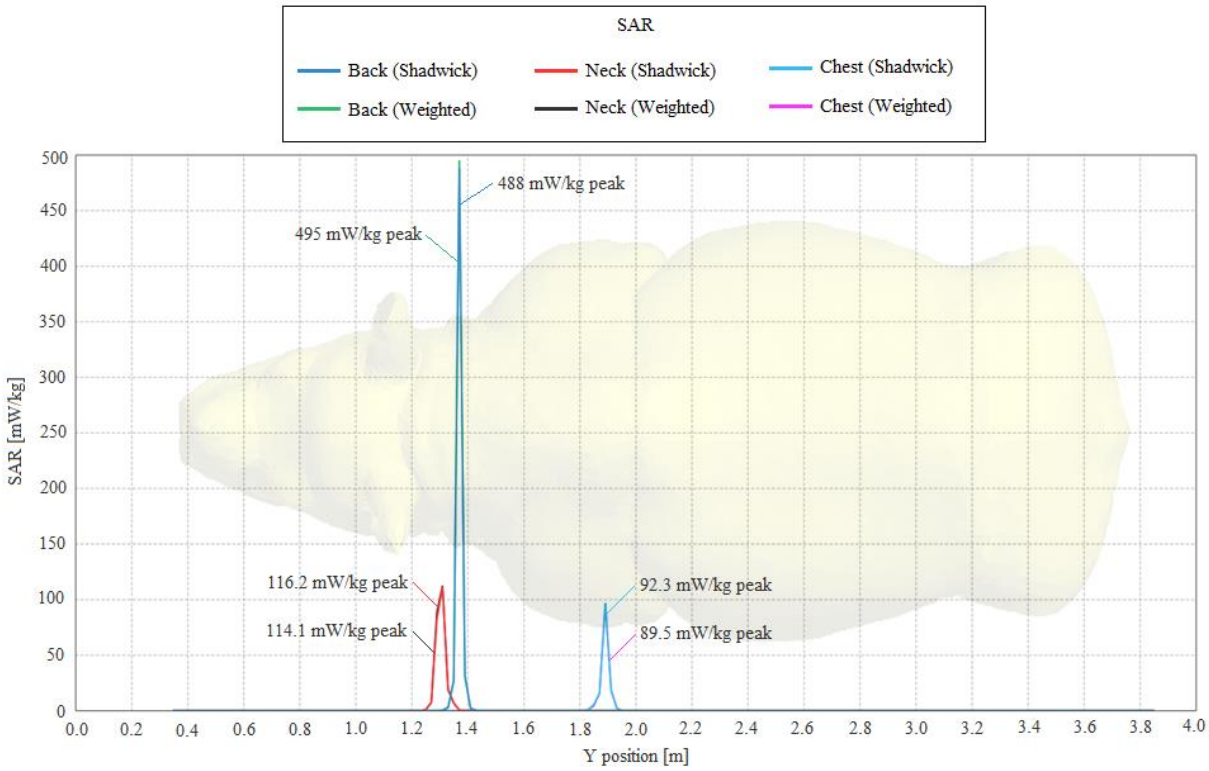

Figure 73: SAR of the MFPEMA propagating through the back, chest and neck of the Shadwick and weighted average models in the y-direction.

The positions of the SAR peaks coincide with the positions of the implanted antennas. The SAR values of 488 mW/kg and 495 mW/kg shown in Figure 73 for the Shadwick and weighted average models for the case of the implant located in the back, were the highest of all the model configurations. These values are believed to be within the acceptable range of SAR exposure as regulated by the IEEE and ICNIRP, although these restrictions are specified for human tissue only. The specific absorption rates per rhinoceros tissue presented in Table 34, are within the radiation exposure limits indicated in Table 30. However, the power loss per medium indicates that most of the propagation energy is absorbed and suggests that the implanted antenna would only be capable of transmitting a short distance. Based on the total active power of approximately 14.6 mW, the simulations indicate that the efficiency of the MFPEMA is 0.1254% or less for the Shadwick models and 0.0489% or less for the weighted average models.

Table 34: Specific absorption rate and power loss of the individual phantom layers (Rhinoceros back - MFPEMA).

Back Implantation				
Biological Tissue	**Shadwick Model**		**Weighted Average Model**	
	Specific Absorption Rate [W/kg]	**Power Loss [W]**	**Specific Absorption Rate [W/kg]**	**Power Loss [W]**
Dermis	3.8242E-06	1.8476E-03	4.0404E-06	1.9512E-03
Fat	21.0474E-06	10.4998E-03	20.8363E-06	10.3945E-03
Muscle	0.9412E-06	1.5809E-03	0.9233E-06	1.5508E-03
Blood	4.6313E-17	8.4227E-15	8.1877E-18	1.4891E-15
Average SAR for entire domain/ Sum of all losses	4.8983E-06	14.5860E-03	4.8875E-06	14.5510E-03
Chest Implantation				
Biological Tissue	**Shadwick Model**		**Weighted Average Model**	
	Specific Absorption Rate [W/kg]	**Power Loss [W]**	**Specific Absorption Rate [W/kg]**	**Power Loss [W]**
Dermis	2.5520E-06	1.2020E-03	2.8846E-06	1.3583E-03
Fat	23.4933E-06	11.4297E-03	22.7535E-06	11.0675E-03
Muscle	0.6057E-06	0.9920E-03	0.5779E-06	0.9463E-03
Blood	1.1628E-15	2.0623E-13	1.7178E-17	3.0462E-15
Average SAR for entire domain/ Sum of all losses	4.9132E-06	14.6574E-03	4.8235E-06	14.3952E-03
Neck Implantation				
Biological Tissue	**Shadwick Model**		**Weighted Average Model**	
	Specific Absorption Rate [W/kg]	**Power Loss [W]**	**Specific Absorption Rate [W/kg]**	**Power Loss [W]**
Dermis	3.3955E-06	1.6397E-03	3.5934E-06	1.7353E-03
Fat	20.3610E-06	10.1574E-03	20.3369E-06	10.1453E-03
Muscle	1.2090E-06	2.0307E-03	1.2012E-06	2.0175E-03
Blood	4.4469E-16	8.0873E-14	6.5232E-15	1.1863E-12
Average SAR for entire domain/ Sum of all losses	4.8634E-06	14.4860E-03	4.8881E-06	14.5530E-03

It is apparent from Table 34 that most of the power is absorbed by the fat layer (> 10 mW), followed by the dermis and the muscle layers. Almost no energy is absorbed by the blood layer. The power loss experienced in these layers is corroborated by the specific absorption rates, which indicate similar trends with the highest power loss mediums indicated in Table 34 also having the highest absorption rates due to lower permittivity and conductivity values.

6.3.1.2 PIFA Transmitting and Receiving Pair

Six configurations were used to investigate the propagation characteristics of the PIFA, namely our Shadwick and weighted average approximations for each of the back, chest and neck configurations respectively. In all cases the organs and skeleton were excluded from the anatomically correct rhinoceros model. Specifically, the gain, SAR, electric field and received power were investigated. Figures 74 to 76 show the realised gain when using the PIFA located in the back, chest and neck respectively for both the Shadwick and weighted average tissue approximations. Additional illustrations pertaining to the directionality of the gain, can be viewed in Appendix H (page 131).

It is clear that the propagation towards the hind of the rhinoceros is severely attenuated and that most of the energy escapes in the forward facing direction relative to the rhinoceros. The maximum gain is approximately -26 dBi, -24 dBi and -25 dBi when implant is located in the back, chest and neck for the Shadwick configuration and -28 dBi, -26 dBi and - 27 dBi when the implant is located in the back, chest and neck for the weighted average configuration. The input power to the transmitting antenna was approximately 12.6 mW for all simulations. These results agree with previous findings which suggested that the weighted average model has a greater attenuating effect on the antenna radiation.

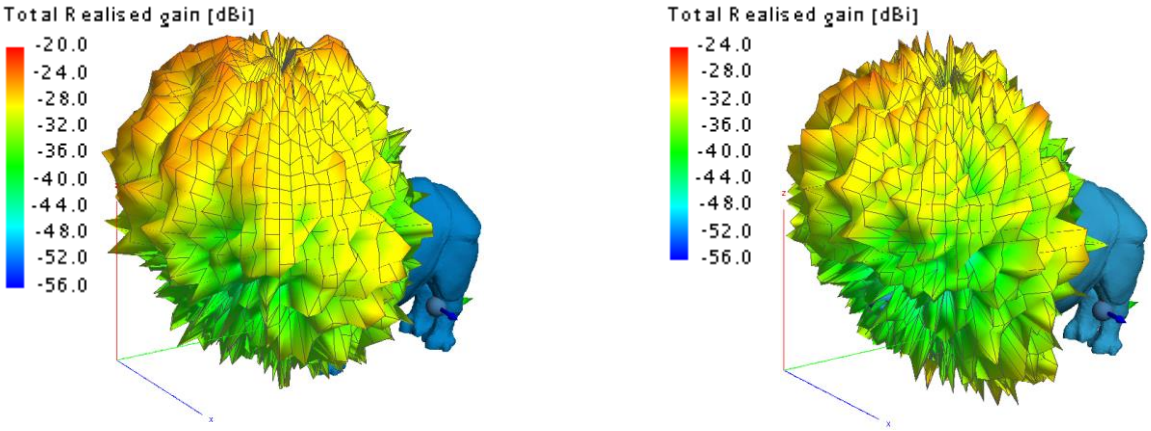

Figure 74: Realised gain of the Shadwick (left) and weighted average (right) anatomical rhinoceros back model [PIFA pair].

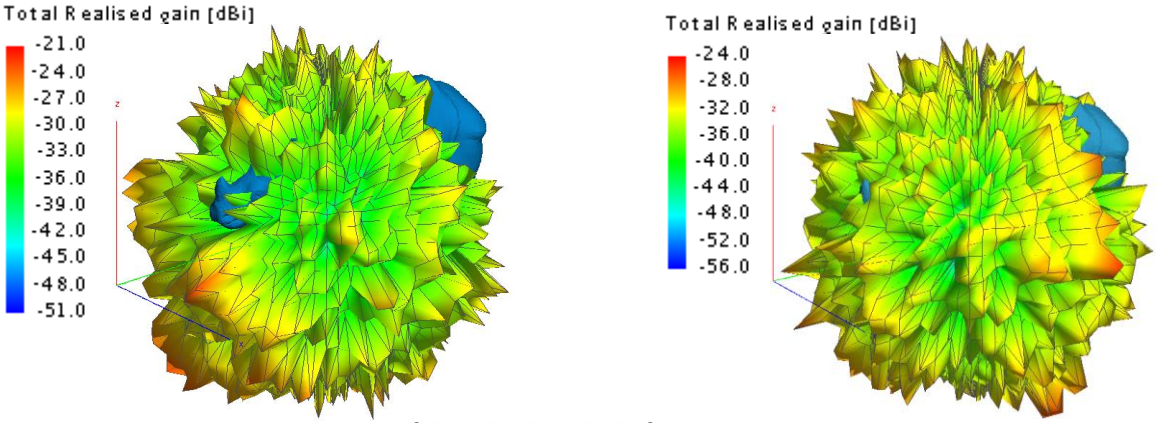

Figure 75: Realised gain of the Shadwick (left) and weighted average (right) anatomical rhinoceros chest model [PIFA pair].

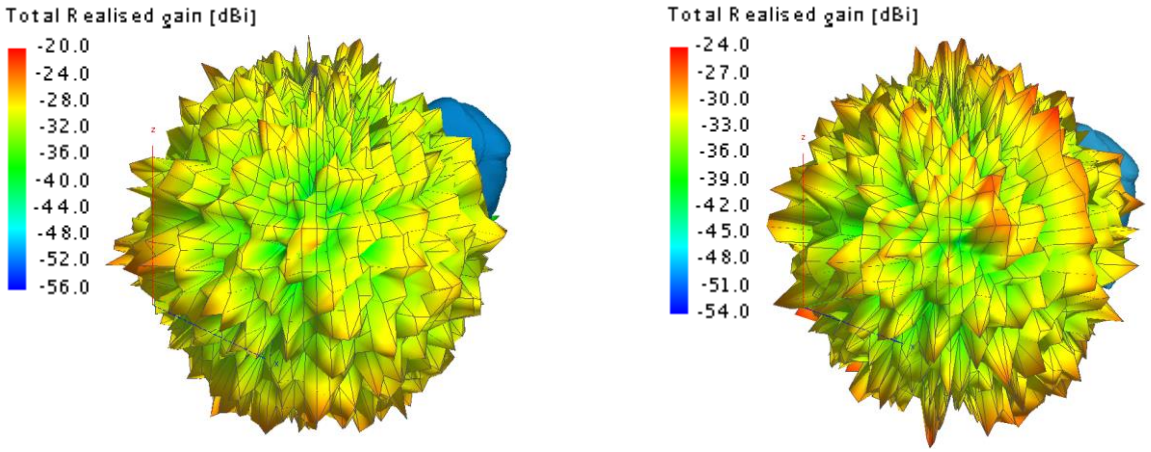

Figure 76: Realised gain of the Shadwick (left) and weighted average (right) anatomical rhinoceros neck model [PIFA pair].

The dispersion of the electrical field around the rhinoceros gives a visual representation of the way in which the energy dissipates. Figures 77 to 82 illustrate the electric field of the Shadwick and weighted average models on yz- and xy-surfaces. Once again, it is clear that very little energy penetrates the thick hide of the rhinoceros. The maximum electric field values at the point of implantation were 235 mV/m, 140 mV/m and 85 mV/m when the implant was located in the back, chest and neck of the Shadwick configuration respectively and 135 mV/m, 75 mV/m and 80 mV/m when the implant was located in the back, chest and neck of the weighted average configuration respectively.

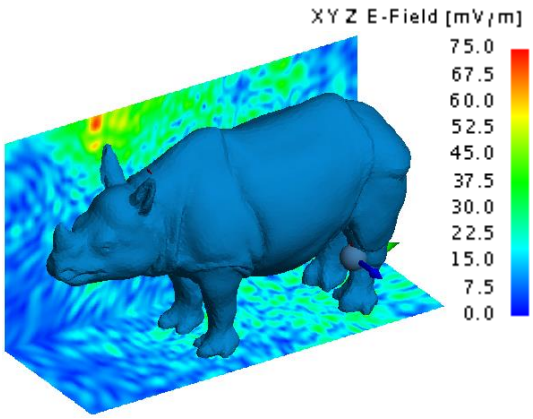

(a) yz-surface located 0.687m from the antenna and the xy-surface located 1.647m from the antenna.

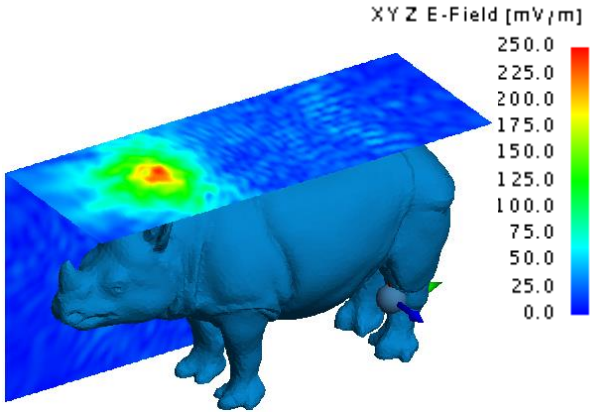

(b) yz-surface located 0.687m from the antenna and the xy-surface located 0.312m from the antenna.

Figure 77: Electric field of the PIFA located in the back location for the Shadwick approximation.

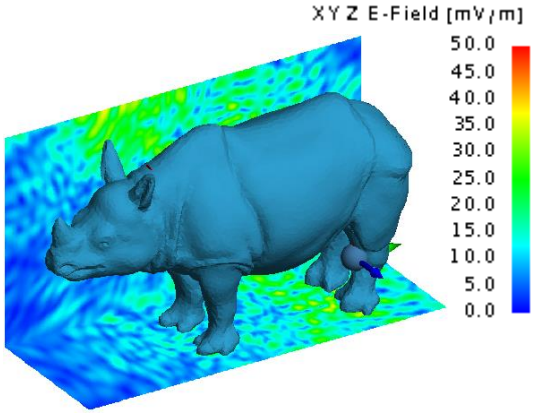

(a) yz-surface located 0.687m from the antenna and the xy-surface located 1.647m from the antenna.

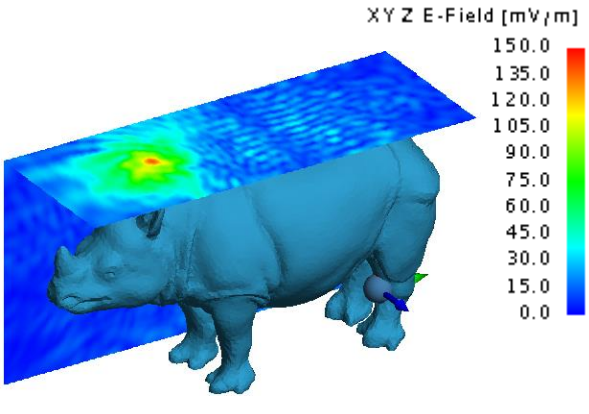

(b) yz-surface located 0.687m from the antenna and the xy-surface located 0.312m from the antenna.

Figure 78: Electric field of the PIFA located in the back location for the weighted average approximation.

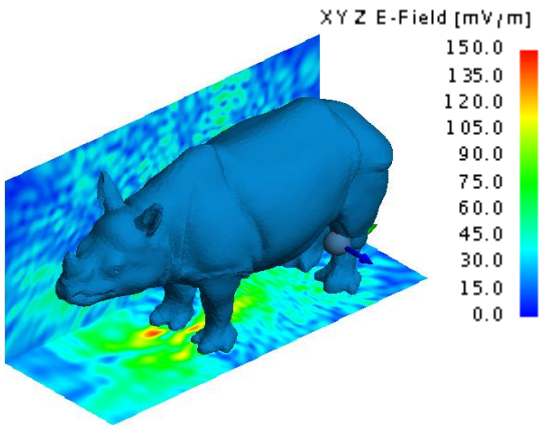

(a) yz-surface located 0.687m from the antenna and the xy-surface located 0.619m from the antenna.

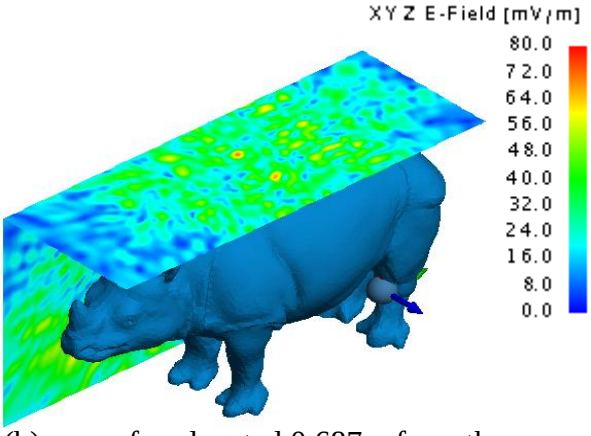

(b) yz-surface located 0.687m from the antenna and the xy-surface located 1.338m from the antenna.

Figure 79: Electric field of the PIFA in the chest location for the Shadwick approximation.

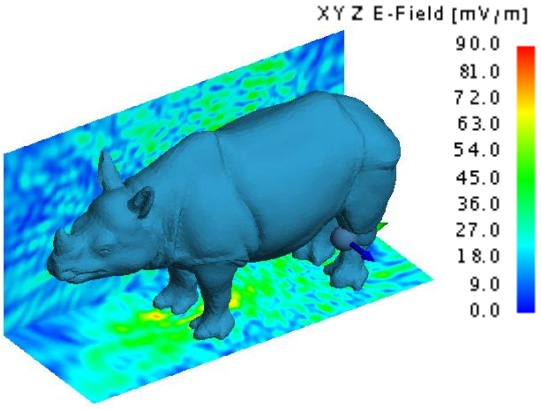

(a) yz-surface located 0.687m from the antenna and the xy-surface located 0.619m from the antenna.

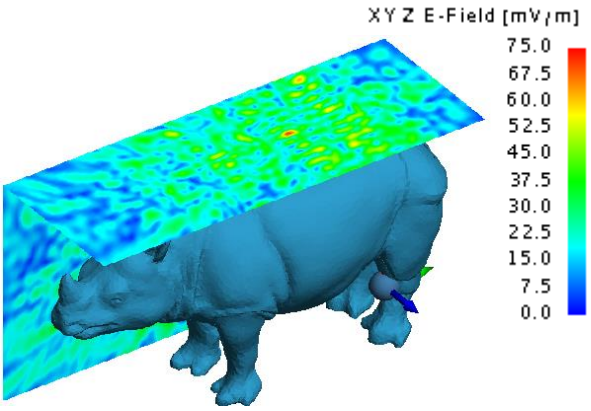

(b) yz-surface located 0.687m from the antenna and the xy-surface located 1.338m from the antenna.

Figure 80: Electric field of the PIFA in the chest location for the weighted average approximation.

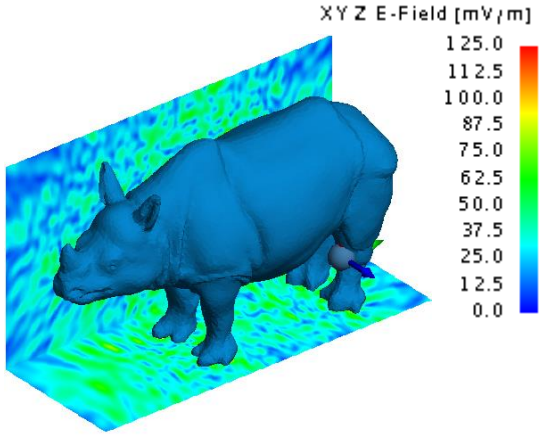

(a) yz-surface located 0.687m from the antenna and the xy-surface located 0.854m from the antenna.

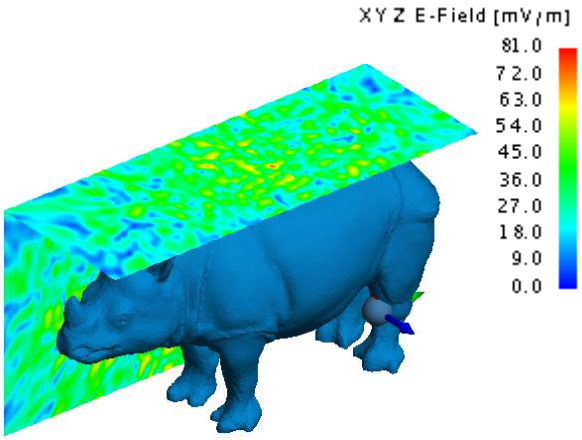

(b) yz-surface located 0.687m from the antenna and the xy-surface located 1.105m from the antenna.

Figure 81: Electric field of the PIFA in the neck location for the Shadwick approximation.

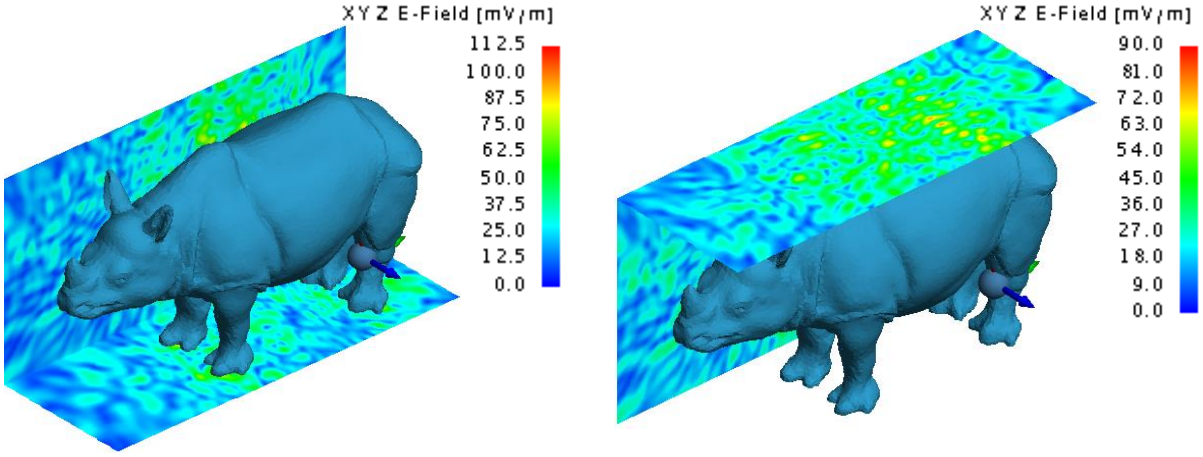

(a) yz-surface located 0.687m from the antenna and the xy-surface located 0.854m from the antenna.

(b) yz-surface located 0.687m from the antenna and the xy-surface located 1.105m from the antenna.

Figure 82: Electric field of the PIFA in the neck location for the weighted average approximation.

The electric field close to the location of the implant tends to be lower for the weighted average tissue approximation model compared to the electric field for the Shadwick tissue approximation, when the implant is in the back and chest locations. However, all models indicate similar electric field results at the location of the receiving antenna as illustrated by Figures 83 to 85. The approximate values are 55 mV/m, 55 mV/m and 70 mV/m when the implant is located in the back, chest and neck for the Shadwick model and 32 mV/m, 45 mV/m and 50 mV/m when the implant is located in the back, chest and neck for the weighted average model. The yz-surface is located 0.272 m from the x-position of the implantation antenna and cuts through the position of the receiving antenna.

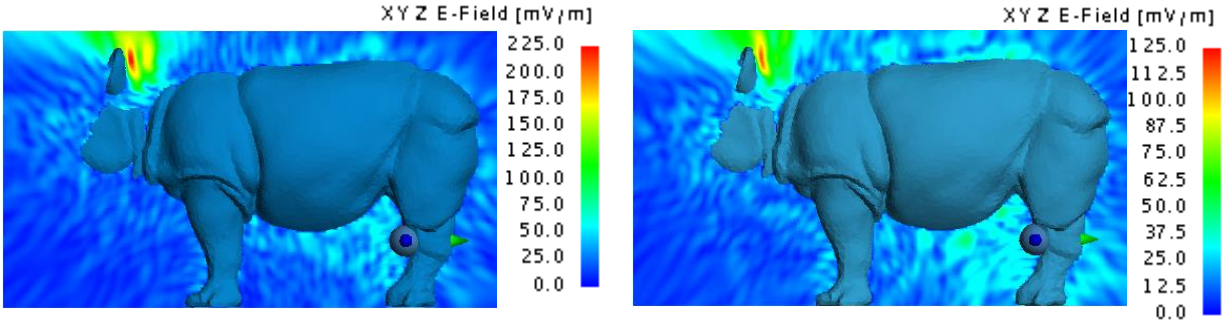

Figure 83: Electric field of the PIFA pair through the back of the Shadwick [left] and weighted average [right] approximation models.

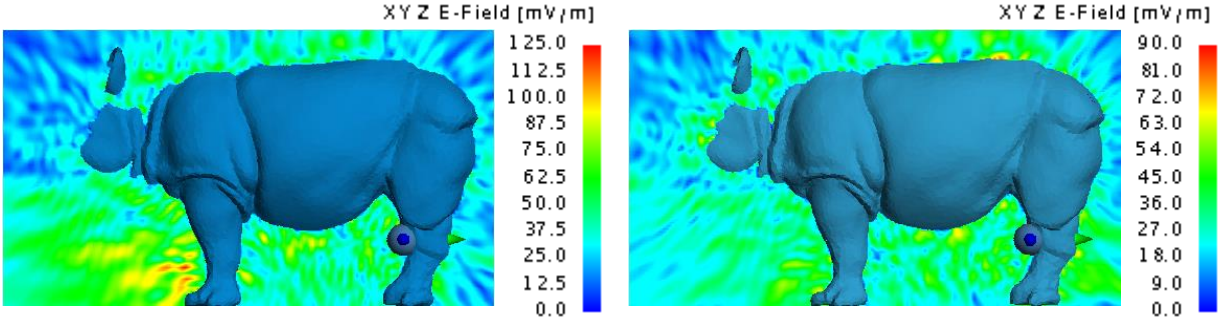

Figure 84: Electric field of the PIFA pair through the chest of the Shadwick [left] and weighted average [right] approximation models.

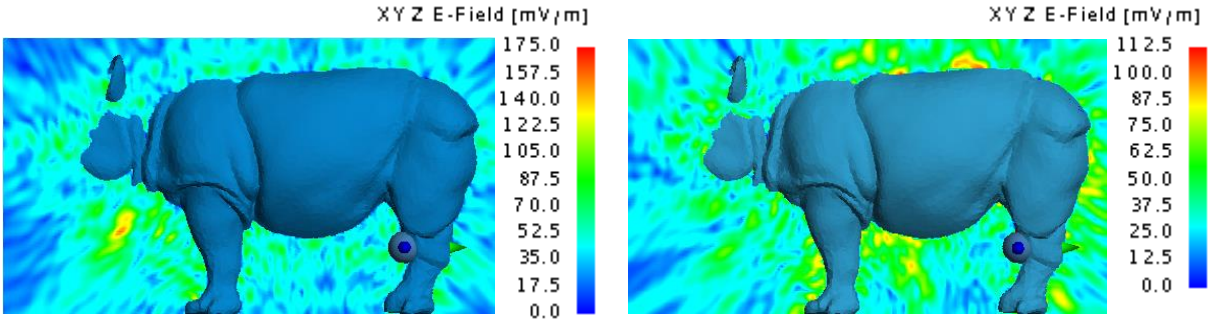

Figure 85: Electric field of the PIFA pair through the neck of the Shadwick [left] and weighted average [right] approximation models.

These analyses support the notion that, although the implanted antennas are capable of penetrating the thick hide of the rhinoceros, they are not effective at transmitting a signal from an in-vivo position at the back, chest or neck to an ex-vivo location at the hind leg. This is supported by the very low received power values of 512.81 pW, 1.62 nW and 850.7 pW when the implant is located in the back, chest and neck locations for the Shadwick model and 564.19 pW, 1.8 nW and 1.738 nW when the implant is located in the back, chest and neck locations for the weighted average model. As can be seen from Figure 86, which illustrates the SAR through the rhinoceros models in the y-direction, most of the energy is absorbed within a few centimetres of the point of implantation.

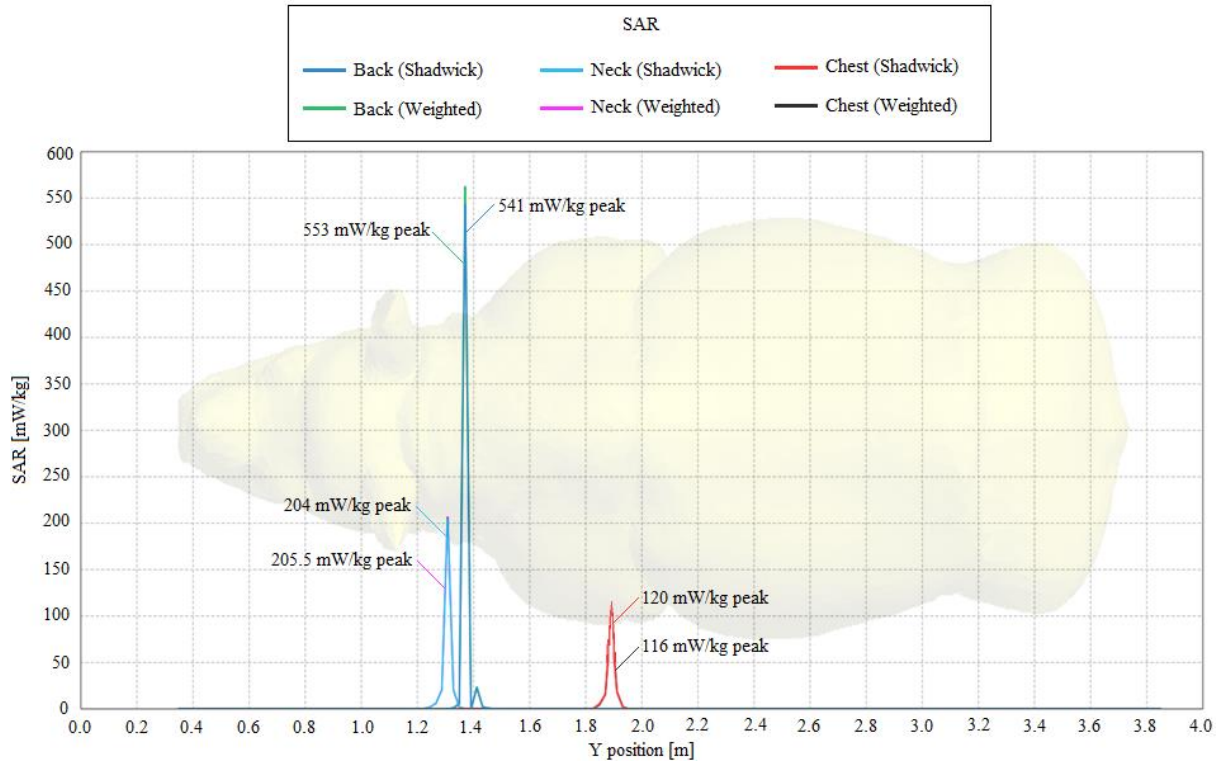

Figure 86: SAR of the PIFA propagating through the back, chest and neck of the Shadwick and weighted average models in the y-direction.

The positions of the SAR peaks coincide with the positions of the implanted antennas. The maximum SAR values of 541 mW/kg and 553 mW/kg shown in Figure 86, were attained in the Shadwick and weighted average models when the implant was in the back location. These are believed to be within the acceptable range of SAR exposure as regulated by the IEEE and ICNIRP, although these restrictions are specified for human tissue only. The specific absorption rates per rhinoceros tissue presented in Table 35, are within the radiation exposure limits indicated in Table 30. However, the power loss per medium indicates that most of the

propagation energy is absorbed and suggests that the implanted antenna would only be capable of transmitting a short distance. Based on the total active power of approximately 12.6 mW, the simulations indicate that the efficiency of the PIFA is 0.2296% or less for the Shadwick model and 0.1517% or less for the weighted average model.

Table 35: Specific absorption rate and power loss of the individual phantom layers (Rhinoceros back - PIFA).

Back Implantation				
Biological Tissue	**Shadwick Model**		**Weighted Average Model**	
	Specific Absorption Rate [W/kg]	**Power Loss [W]**	**Specific Absorption Rate [W/kg]**	**Power Loss [W]**
Dermis	2.4321E-06	1.1745E-03	2.8235E-06	1.3635E-03
Fat	19.4576E-06	9.7067E-03	19.7723E-06	9.8637E-03
Muscle	0.4272E-06	0.7175E-03	0.4606E-06	0.7736E-03
Blood	4.5788E-17	8.3272E-15	9.5966E-18	1.7453E-15
Average SAR for entire domain/ Sum of all losses	4.0794E-06	12.5050E-03	4.2208E-06	12.9450E-03
Chest Implantation				
Biological Tissue	**Shadwick Model**		**Weighted Average Model**	
	Specific Absorption Rate [W/kg]	**Power Loss [W]**	**Specific Absorption Rate [W/kg]**	**Power Loss [W]**
Dermis	2.1456E-06	1.0362E-03	2.4765E-06	1.1960E-03
Fat	19.7517E-06	9.8534E-03	19.5345E-06	9.7450E-03
Muscle	0.5092E-06	0.8552E-03	0.4961E-06	0.8332E-03
Blood	9.7760E-16	1.7779E-13	1.4748E-17	2.6821E-15
Average SAR for entire domain/ Sum of all losses	4.1307E-06	12.6360E-03	4.1411E-06	12.6750E-03
Neck Implantation				
Biological Tissue	**Shadwick Model**		**Weighted Average Model**	
	Specific Absorption Rate [W/kg]	**Power Loss [W]**	**Specific Absorption Rate [W/kg]**	**Power Loss [W]**
Dermis	2.5446E-06	1.2288E-03	2.7335E-06	1.3201E-03
Fat	19.1536E-06	9.5550E-03	19.2035E-06	9.5799E-03
Muscle	0.5675E-06	0.9532E-03	0.5729E-06	0.9622E-03
Blood	5.9628E-15	1.0844E-12	1.6932E-15	3.0793E-13
Average SAR for entire domain/ Sum of all losses	4.1281E-06	12.5580E-03	4.1721E-06	12.6840E-03

It is apparent from Table 35 that most of the power is absorbed by the fat layer (> 9.5 mW), followed by the dermis and the muscle layers. Once again, almost no energy is absorbed by the blood layer. The power loss experienced in these layers is corroborated by the specific absorption rates, which indicate similar trends with the highest power loss mediums indicated in Table 35 also having the highest absorption rates due to lower permittivity and conductivity values. The findings suggest that the PIFA has a slightly higher power efficiency than the MFPEMA.

6.3.2 Anatomical Skeleton and Organ Models

Organ and skeletal models were designed with calculated dielectric properties for each of the selected frequencies, with corresponding agar recipes to match these permittivity and conductivity values. Due to the scarcity of relevant literature, the volumes and exact locations of these organs are unknown. However, with the aid of our consulting veterinary surgeon an approximation was made by investigating the skeletal structure, organ size and organ location of cattle and horses. Figure 87 illustrates the rhinoceros skeletal model.

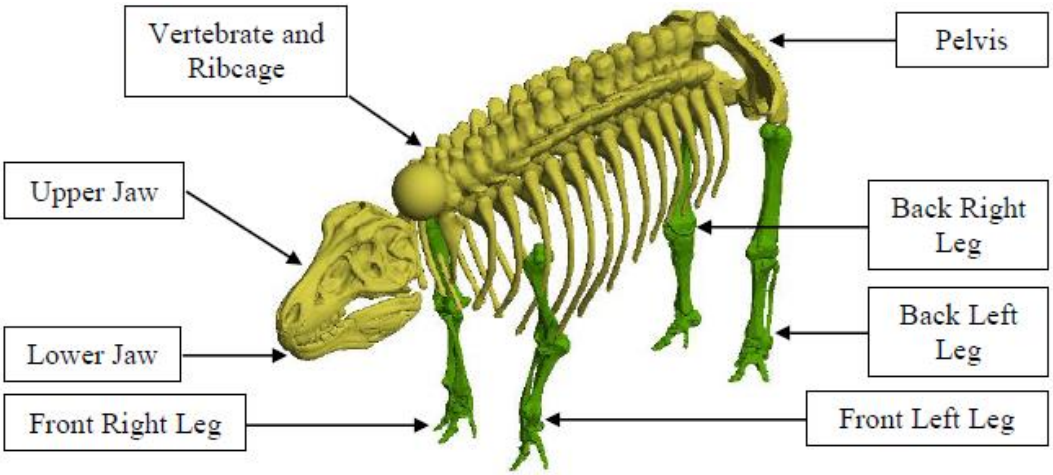

Figure 87: Rhinoceros skeletal model.

This model consists of eight sections as indicated by the corresponding labels. These different body parts are not necessarily anatomically accurate to rhinoceroses, but are approximations from various animals with estimated similar properties. The size of the model was scaled to match those of the anatomical layered rhinoceros models, although some features may need further scaling to match actual rhinoceros proportions. The two shades of green indicate the bone cancellous (light green) and bone cortical (dark green) dielectric properties, which are applied to these specific parts of the skeletal model. Figure 88 illustrates the skeletal model within the layered rhinoceros model.

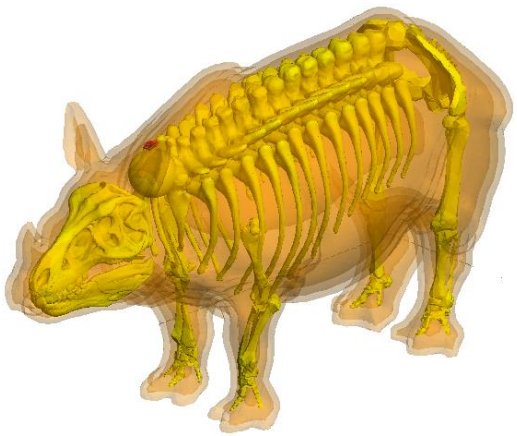

Figure 88: Combination of the skeletal and anatomical rhinoceros models.

As can be seen Figure 88, the skeletal model wraps around the "blood" layer of the rhinoceros model (which is used as an approximation of the organs) and does not obstruct the positions of the implantation antennas. Due to the previously mentioned scaling factors which are still to be established by means of the empirical investigation of actual rhinoceros organs and tissue, the skeletal model and the organ models illustrated in Figure 89 are not fully compatible. However,

individual organs can be selected and incorporated into the skeletal model as needed. Figure 90 illustrates the organ models within the layered rhinoceros model and once again, the position of the implantation antennas are unimpeded. All eleven organ models are independent and have specific dielectric properties for each of the selected frequencies.

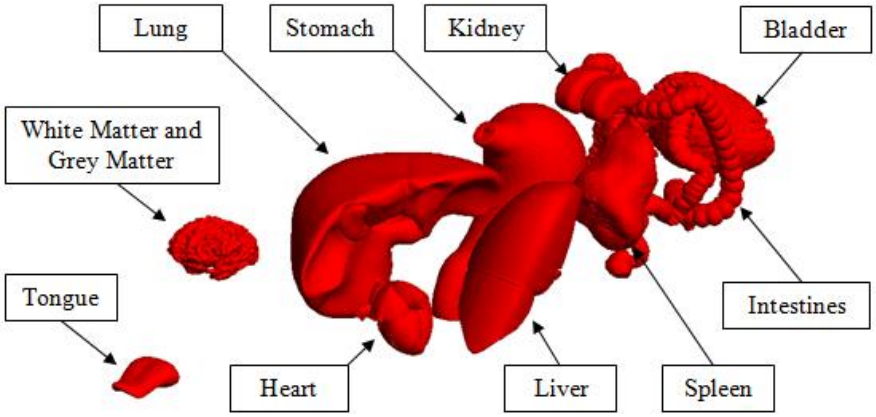

Figure 89: Rhinoceros organ models.

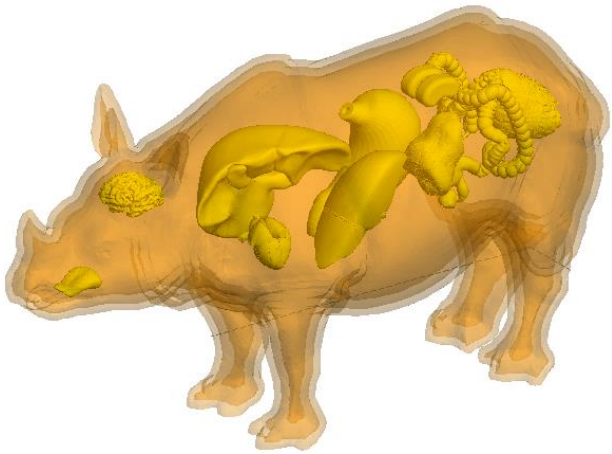

Figure 90: Combination of the organ and anatomical rhinoceros models.

The MFPEMA implanted within the back of the rhinoceros was used to simulate the effect of the skeleton and organs on the power efficiency of the antenna pair at 2.4 GHz. As expected from the theoretical permittivity and conductivity values of bone cancellous and bone cortical, the skeletal model did not have a significant influence on the propagation characteristics. The SAR peak at the point of implantation was increased slightly by approximately 10 mW/kg and the electric field at the location of the receiving antenna on the hind left leg was reduced by 7 mV/m. This reduced the power efficiency of the MFPEMA pair by a mere 0.08%.

Attempts at numerical simulation pertaining to the organs models failed due to insufficient memory on even the largest computer available to us. However, it was anticipated that these models would also have a minimal effect on the power efficiency of the antenna. This was based on the simulation results of the layered rhinoceros model, which included the blood layer that was used to approximate the organs. Thus, these models were not implemented within the layered rhinoceros model due to the complexity of their design, which significantly increased the required computational power. However, it is recommended that these models be applied for investigations strictly pertaining to in-vivo propagation to increase the accuracy of results.

6.3.3 Summary and Conclusion

This chapter has considered the simulation of the electromagnetic propagation achieved by an antenna pair located on a rhinoceros, using models of varying complexity to represent the animal itself. One antenna was located ex-vivo on the left back leg, while three locations were considered for the in-vivo implant: the back of the neck, the front of the neck and the chest. Two different antenna types (MFPEMA and PIFA) were considered, as well as two tissue approximations: the weighted average dermis approximation and the Shadwick approximation, which was calculated using the permittivity values of individual rhinoceros dermis constituents. The results indicate that the Shadwick models have a greater ability to store electrical energy in an electric field, which means that signal penetration through these materials are generally predicted to be higher. This is due to the higher permittivity of the dermis (51.06) assumed by the Shadwick model, compared to the much lower weighted average dermis permittivity of 36.36. Despite this, the observed differences in gain, electric field, power loss and specific absorption rate are quite small between these two models.

Both antennas were capable of propagating through the fat and skin of the rhinoceros configurations for a short distance. However, communication from an in-vivo antenna in the back, neck or chest to an ex-vivo receiving antenna on the hind leg is not ideal for the specified antenna characteristics. The simulations suggest that the PIFA had a slightly better penetrative capability and higher power efficiency than the MFPEMA throughout most of the configurations. Regarding the implantation positions, the ex-vivo antenna at the hind leg received 32.11% more power from the antenna located in the chest than the antenna located in the neck. It also received 217.55% more power from the antenna located in the chest than the antenna located in the back. Furthermore, the power efficiency of the PIFA was on average 14.72% higher than the MFPEMA. Based on these findings, a PIFA-based design should be used for implantation in the chest of the rhinoceros for optimum results. The power efficiency of this configuration was predicted to be 0.23%.

6.4 Conclusion

The usefulness of all the models, including the rhinoceros flank, the cylindrical and anatomical models, regarding the evaluation of an antenna design were demonstrated by means of numerical simulation. Overall, the weighted average dermis approximation absorbed 0.83% more energy and had 1.17% greater power loss than the Shadwick dermis approximation. Considering only the dermis mediums of the models, these values increased to 34.46% more energy absorbed and 38.69% more power lost in the weighted average approximation than in the alternative approximation. Thus, the weighted average dermis is much more difficult to penetrate in terms of antenna radiation. The weighted average models are believed to better represent rhinoceros tissue since their dielectric properties were calculated specifically for the respective operating frequency. The frequency of the Shadwick approximation, on the other hand, is unknown.

Chapter 7.

7. Rhinoceros Flank Agar Model Results

An agar rhinoceros flank model was made according to the size specifications and antenna positioning indicated in Section 5.4 (page 65) and Section 6.1 (page 68). This was used to compare the agar and simulation models. If these models are agreeable in terms of their results, a practical full-scale cylindrical or anatomical model would not be needed, seeing as this would mean that the simulation models could be trusted to yield accurate approximations.

7.1 The 403 MHz and 2.4 GHz Agar Rhinoceros Flank Models

Two physical models were created, namely the 403 MHz model and the 2.4 GHz model. The 403 MHz rhinoceros flank model was used to investigate the power loss and propagation through the various layers of the phantom materials by using the CCFA and was constructed by stacking 12mm x 12mm on top and next to each other. This construction method allows experimentation with individual layers and thicknesses can easily be altered by adding or removing slabs. The drawback of this method is the likelihood of air pockets between the slabs, which could affect the measurements. Figure 91 shows the deconstructed slabs used for the 403 MHz rhinoceros flank model, which represent the epidermis, dermis, fat, muscle and blood layers of the rhinoceros.

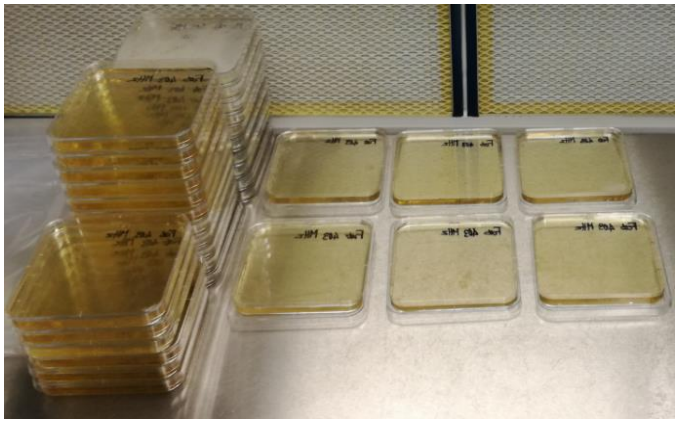

Figure 91: The deconstructed slabs of the 403 MHz rhinoceros flank model.

The 2.4 GHz rhinoceros flank model was used to investigate the power loss and propagation through the various layers of the phantom materials by using the MFPEMA and PIFA transmitting and receiving pairs respectively. Both flank models (403 MHz and 2.4 GHz) are relevant when considering communication between an in-vivo implanted sensor and an ex-vivo receiver for their respective frequencies. However, only the 2.4 GHz model was used for practical experimentation. This model was constructed by pouring the warm liquid phantom material into a mould to the specified height, letting it set and then pouring the next layer of liquid phantom material directly on top of the previous layer. To prevent the liquid agar from melting the already set layer below it, the agar was cooled to approximately 55°C which is warm enough to keep the phantom material in a liquid state, but not warm enough to melt the phantom material once it has set. This method removed most of the air gaps between the layers, but did not allow for the individual testing of the layers and required the antenna to be inserted by means of an incision.

The mould was created by fashioning five wooden plates into a box with the appropriate size. The inside of the box was lined with plastic to prevent the gelatinous material from seeping through the container or leaking from any of the edges. The container was constructed in such manner as to be easily disassembled once the phantom material had set, which would allow a free standing rhinoceros flank model. The 403 MHz and 2.4 GHz models were constructed within a laminar flow to prevent contamination of the phantom materials. Figure 92 shows the empty container used to cast the 2.4 GHz rhinoceros flank model and Figure 93 shows the container filled to various levels, with each level representing a different type of rhinoceros tissue.

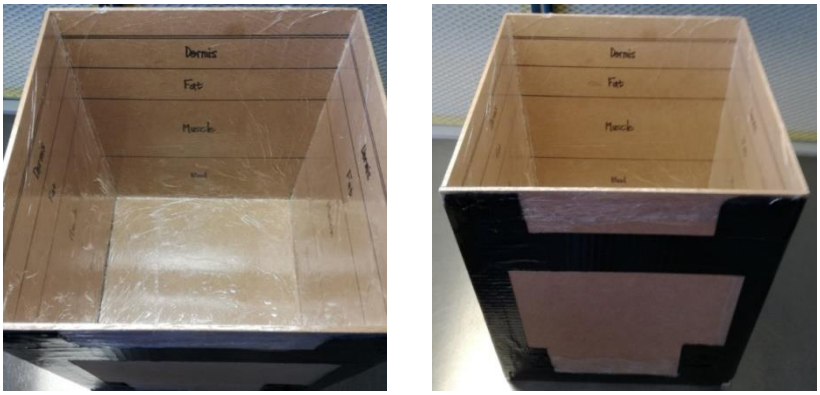

Figure 92: The mould used to cast the 2.4 GHz rhinoceros flank model.

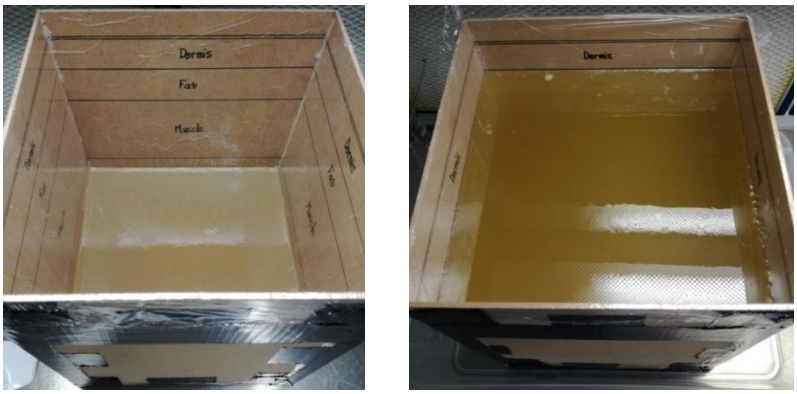

Figure 93: The partially filled container of the 2.4 GHz rhinoceros flank model.

The completed agar models were wrapped in plastic and foil and were kept in storage at 4°C until the measurements were performed. The models were removed from storage and allowed to reach room temperature (24°C) in a temperature controlled environment before commencing measurements.

7.2 The 2.4 GHz Rhinoceros Flank Power Measurements

The distance between the implanted antenna (transmitter) and the ex-vivo antenna (receiver) was 54.346 mm, which is the same distance used in the computer simulation models. Foam was used to simulate the air gap between the two antennas to measure their free space propagation characteristics. This also provided a platform to secure and align the antennas. The air gap represents the spacing between the implanted antenna and the casing of the implantation device. The cable loss at 2.4 GHz with a signal generator set to 0 dBm, was measured as -1.04 dBm using a spectrum analyzer. Keeping this in mind, the power loss through the air gap of 54.346 mm was measured to be -15.69 dBm for the MFPEMA pair and -22.50 dBm for the PIFA pair. Figure 94 shows the practical setup used to measure the cable loss at 2.4 GHz, whereas Figure

95 shows the air gap (foam) power loss measurements of the 2.4 GHz MFPEMA pair. The setup showed by Figure 94 illustrates a signal generator connected to one end of the antenna connector cable and a spectrum analyzer connected the other end of the cable.

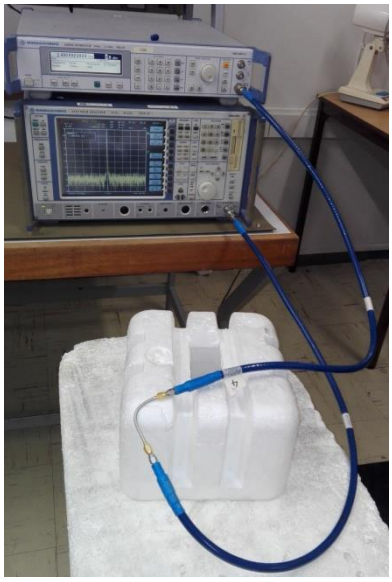

Figure 94: The practical configuration of the 2.4 GHz cable loss measurements.

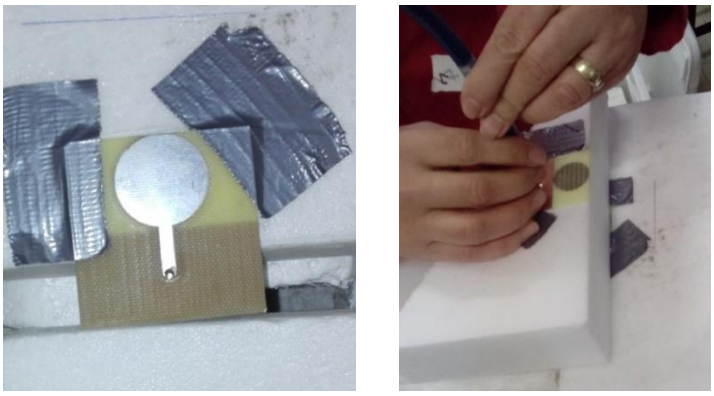

(a) (b)

Figure 95: The air gap (foam) power loss measurements of the 2.4 GHz MFPEMA pair.

Figure 95 (a) shows the receiving antenna facing upward and Figure 95 (b) shows the transmitting antenna facing downward and aligned with the receiving antenna. As previously indicated, these two antennas are identical. The air gap measurements were compared to the flank and simulation results in Section 6.1 (page 68). The same measurements were conducted using the agar rhinoceros flank model, which required the transmitting antenna to be placed within the agar phantom. This was achieved by means of a 'T' incision on the side of the flank model, as shown in Figure 96.

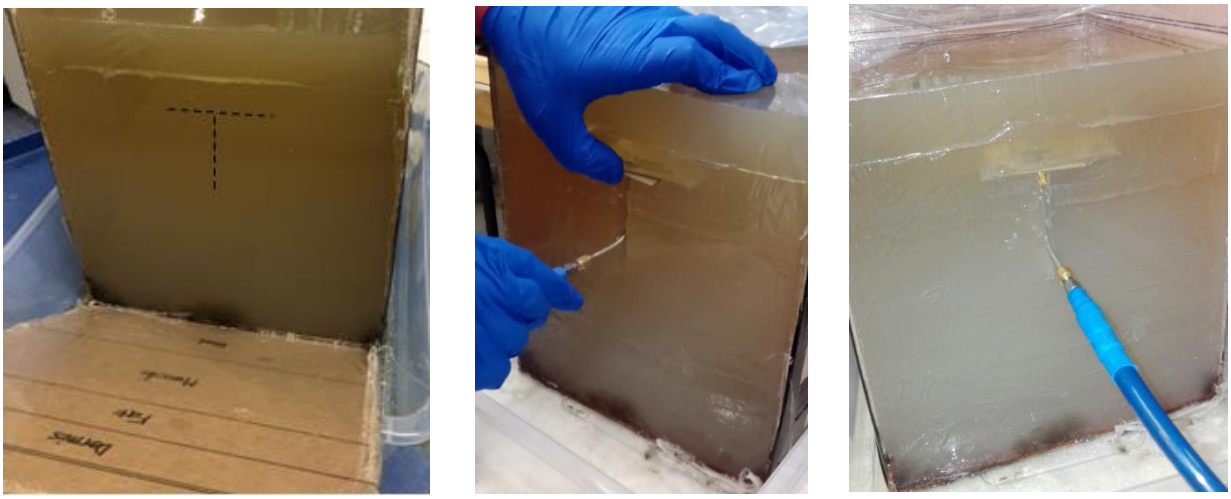

(a) (b) (c)

Figure 96: The T-incision on the side of the 2.4 GHz rhinoceros flank model with the connector cable and implanted antenna.

The upper horizontal incision of the 'T' was 54.346 mm from the top of the rhinoceros flank model, which places it exactly in the middle of the fat layer. The horizontal cut was 7 cm long and 7 cm deep to accommodate all four antenna sizes as specified in Section 2.6 (page 23). The vertical cut, which was situated in the centre of the flank model, was 6 cm long and 4 cm deep to provide an entry point for the connector cable. The loss of the cable is expected to increase with length and thus the implanted antenna was not placed deeper within the model. The vertical propagation of the antenna is not greatly affected by the horizontal positioning, but the cable loss is greatly mitigated.

To further decrease the attenuation, a thin piece of foam (10 mm thickness) was attached to the transmitting and receiving antennas, to simulate an air gap. Measurements were taken with and without the foam air gap in order to evaluate the losses introduced by direct contact with the skin. Further investigation was conducted by placing the receiving antenna at an 20 mm offset relative to the implanted MFPEMA, in order to establish whether or not the nonalignment would have a significant mitigating effect on the propagation. Table 36 depicts the results of the power loss measurement of the various antennas (cable loss excluded) and Figure 97 shows the practical configuration of the power loss measurement of the 2.4 GHz rhinoceros flank model. Dashes indicate measurements that were inconclusive or did not deliver results due to the signal transmitted by the antenna not being able to penetrate the phantom material.

Table 36: Received power through the 2.4 GHz rhinoceros flank phantom (output = 0 dBm).

Antenna	Direct Contact	10 mm Foam	20 mm nonalignment
MFPEMA	-74.92 dBm	-53.96 dBm	-58.94 dBm
PIFA	-61.95 dBm	-58.91 dBm	-
PTMA	-	-	-
CPFLPPA	-	-	-

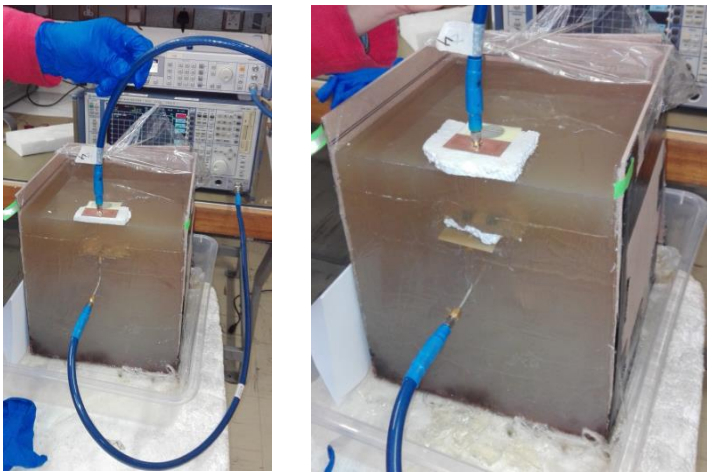

Figure 97: The configuration of the power loss measurement of the 2.4 GHz rhinoceros flank model [Left: 10 mm foam air gap above; Right: 10 mm foam air gap above and below].

Table 36 clearly illustrates an improvement of power efficiency with the introduction of an air gap between the antenna and the agar phantom. The nonalignment of the antennas also seemed to cause a slight reduction in the received power, based on the MFPEMA measurement. Furthermore, the emitted radiation of the PTMA and CPFLPPA antennas were not able to penetrate the rhinoceros flank model, which confirms the suitability of the MFPEMA and PIFA antennas for implantation. The experiment was repeated for the MFPEMA and PIFA pairs respectively, this time using the same input power as their corresponding computer simulations.

The loss of the cable that connected the transmitting antenna to the spectrum analyzer was measured as -1.15 dBm and the loss of the cable that connected the receiving antenna to the spectrum analyzer was measured as -0.8 dBm at 2.4 GHz, with an output of 11.60 dBm. The MFPEMA requires an output of 11.61 dBm, thus, taking the cable loss into account the output was adjusted to 12.75 dBm. Similarly, the output was adjusted to 12.12 dBm for the PIFA measurements in order to match the required 10.97 dBm output of the computer simulations. Table 37 depicts the power measurements of the MFPEMA and PIFA pairs through the flank model with similar parameters as the computer simulations.

Table 37: Received power through the 2.4 GHz rhinoceros flank phantom (output = +12 dBm).

Antenna	Direct Contact	10 mm Foam	Air Gap (54.346 mm)
MFPEMA	-58.6 dBm	-42.03 dBm	-3.5 dBm
PIFA	-52.7 dBm	-36.23 dBm	-8.7 dBm

Once again, the results indicate an improvement in power efficiency with the introduction of a 10 mm air gap between the antenna and the agar phantom. The rhinoceros flank model was measured to weigh approximately 20 kg, which is slightly more than the theoretical estimate of 17.16 kg. Comparing the measurements of Table 37 with the computer simulation results in Chapter 6 (Section 6.1, page 68), it is clear that the higher density of the heavier physical agar had a greater attenuating effect on the propagation pattern of the antenna. As for the computer simulations, the PIFA has a slightly higher power efficiency than the MFPEMA.

Simulations exhibit ideal circumstances and negate the effects of non-ideal contact between the antenna and the agar, as well as the cable loss, impurities within the agar and the effect of air particles. The air particles are represented by a lossless medium (free space). Thus, additional mitigation effects were added to the flank model. This included the incorporation of the measured recipe errors of the dielectric properties of each layer to the flank model and a small

attenuation factor to the air medium used in the simulations. This reduced the power received by the ex-vivo antenna and increased the comparability of the power efficiency of the theoretical and practical models to 67.38%.

Factors (such as density and the temperature of the medium) are difficult to incorporate accurately into a simulation model, because their effect on signal propagation is difficult to quantify. However, we have found their inclusion to be critical and that without them good agreement between practice and simulation can not be achieved. The correspondence between the simulation and practice could be further enhanced by identifying and applying more of these influences. Nevertheless the good correspondence already achieved allows us to conclude that our simulations are a good representation of reality, and allows us to base design decisions on simulation results with good confidence.

7.3 Conclusion

The rhinoceros flank model is an inexpensive and lightweight approximation of the anatomical rhinoceros model. The method of pouring the slightly cooled agar directly on top of the previously set layer proved to be very successful and removed most of the non-idealities within the model. The practical model weighed approximately 20 kg, which is slightly more than its theoretically estimated weight. When the measured actual densities and dielectric properties of the practical model were used, measurements on the practical model and the predictions obtained by simulation of the same model agreed to a large extent (67.38%). The remaining error is ascribed to non-idealities of the practical model not taken into account by the simulation. Nevertheless, the model is a sufficient representation of rhinoceros tissue to be used in the design of a communication system.

Chapter 8.

8. Summary and Conclusion

It was the aim of this project to deliver phantom and computational models which mimic the dielectric properties of a rhinoceros and which can be used to investigate the design of in-vivo and ex-vivo devices that are required for animal tracking and monitoring. Information regarding the mechanical properties of rhinoceros skin, tissue simulating materials and common phantom recipes was gathered. Based on the findings of the literature review and the contribution of a veterinary surgeon specialised in rhinoceros surgery, two permittivity estimates for rhinoceros skin were obtained. The first is based on the weighted average approximation and yields a permittivity of 36.36. The second, termed the Shadwick dermis approximation, yields a permittivity of 51.06. Considering only the dermis mediums of the models, 34.46% more energy was absorbed and 38.69% more power was lost in the weighted average dermis approximation. Thus, the weighted average dermis is much more difficult to penetrate with a signal transmitted from an antenna implanted in the fat layer.

Several numerical models with varying degrees of complexity were designed to investigate the propagation characteristics of antennas using both dermis approximations. These include a rhinoceros flank model, a cylindrical phantom model and an anatomically accurate rhinoceros model. Three locations were identified as the most viable for implantation in a rhinoceros, namely in the back of the neck, below the throat and in the chest. The size of the implantation was restricted to 7x5x2 cm, as specified by the veterinary surgeon. In order to verify the accuracy of our numerical model, practical measurements were necessary. Since measurements using rhinoceros flesh were not feasible, the construction of phantoms, which emulate the dielectric properties of tissue, was considered.

An investigation into various types of gelatinous material commonly used for creating phantom models identified agar as the most suitable gelling agent due to its mechanical properties such as melting and setting temperatures, its non-toxicity and its pliability. This choice was supported by additional contributing factors such as low cost and availability. Recipes using salt, sugar and agar were formulated for 13 types of rhinoceros tissue. Agar plates were made in order to compare the dielectric properties of the practical samples to their theoretical values at 2.4 GHz. The practical measurements were found to be within 4.49% of the theoretical values. This error, along with other physical parameters such as the relationship between permittivity, temperature and frequency indicated a strong agreement between the practical measurements and the theoretical estimations. This validated the choice of agar as gelling agent.

The cost of the rhinoceros phantom was greatly reduced by using household sugar rather than purified sucrose. This was shown to have an insignificant effect on the dielectric properties of the phantom. The samples were transparent and had a firm shape, yet soft consistency. The transparency was useful for the identification of spore growth on the samples and hence to establish their end-of-life. Despite the use of household sugar, the cost of creating a full-scale rhinoceros phantom model remained prohibitive. Furthermore, the weight of such a model was estimated to be 3 tons, rendering it impractical. Thus, alternatives were considered to address the weight and cost. Some designs, such as the phantom leg model, remained too heavy (estimated 283.8 kg) and expensive (R16 866.21).

The proposed flank model, which represented part of the loin of the rhinoceros, included all the layers of the full-scale rhinoceros phantom model. This model weighed approximately 20 kg and the cost of creating two flank models (403 MHz and 2.4 GHz) amounted to R3430.83. The electric field of the selected antenna designs (MFPEMA and PIFA) were measured and compared to their simulated counter-parts. A strong agreement between the simulated and practically measured antenna E-Field magnitudes was found, with almost identical patterns at most angles. Thus, we could conclude that the simulation is a good representation of a real antenna placed within the phantom flank model. The flank model simulations and practical measurements also confirmed that penetration of the thick skin of a rhinoceros by means of an in-vivo antenna is difficult. Most of the active energy will be absorbed by the fat layer in which the antenna is implanted and the propagation energy quickly dissipates from the implant position. The peak values of the simulated specific absorption rates of all the models are within the stipulated safety ranges for human tissue as regulated by the United States of America, Europe and the IEEE.

When considering the PIFA in the flank model, our results indicate an improvement in power efficiency of approximately 16 dbm with the introduction of a 10 mm air gap between the antenna and the agar phantom. In practice the air gap corresponds to the distance between the casing of the implantation device and the implanted antenna. Both practical and simulated results identified the PIFA as the best choice with regards to power efficiency. The comparability of the power efficiency of the theoretical and practical models was 67.38%. Since there are still known dissimilarities between the practical and simulation models, this comparability is good and indicates that the model is a sufficient representation of rhinoceros tissue for practical use.

Seeing as the PIFA is well-known and regularly used as an implantation antenna, it was used as baseline with which the MFPEMA was compared. Our results indicated a 14.72% higher power efficiency in favour of the PIFA. Regarding the implantation positions, the ex-vivo antenna at the hind leg received 32.11% more power from the antenna located in the chest than the antenna located in the neck. It also received 217.55% more power from the antenna located in the chest than the antenna located in the back. Based on these findings, a PIFA-based design should be implanted in the chest of the rhinoceros for optimum results. Even for the chest implant, however, communication with a receiver on the back leg is expected to be very challenging.

The weighted average models are believed to better represent rhinoceros tissue since their dielectric properties were calculated specifically for the relevant operating frequency, whereas the frequency at which the Shadwick approximation is appropriate is unknown. Very little literature regarding the dielectric properties of a rhinoceros body could be found. The approximations proposed in this project are thought to be the only documented estimations of the dielectric properties of rhinoceros tissues. Therefore, the suggested agar recipes are new and can serve as a basis for creating rhinoceros phantom tissue until such time that the dielectric values of actual rhinoceros tissue can be verified.

8.1 Achievement of Aims and Objectives

The previous section has demonstrated that all of the aims and objectives specified in the introductory chapter were achieved. The specific outcomes compliance of the project objectives can be viewed in Appendix A (page 111).

8.2 Recommendations

There are several aspects of this work that can be expanded and developed in future.

8.2.1 Internal Organs and Skeletal Structure

As described in Chapter 6 (Section 6.3.2, page 89), organ and skeletal models have been designed and dielectric properties calculated for each of the selected frequencies. Corresponding agar recipes have also been proposed to match these permittivity and conductivity values. However, these models could not be implemented fully within the numerical model due to their extreme complexity and resulting increase in computational load. Based on the numerical simulation results of less complex models, it is anticipated that the organs and skeleton would have little effect on the propagation from the in-vivo implant to the ex-vivo receiver. However, this should be verified by including all of the complex models, which will require computational resources more powerful than were available for this project.

8.2.2 Wireless Charging

Biomedical implants require incisions, which require anaesthesia, cause discomfort and require healing periods of approximately six weeks before the rhinoceros can continue its normal behaviour. During this time, the rhinoceros is vulnerable to infection and to attack from predators and should be kept in isolation for observation. According to recent developments in pacemaker technology, it is possible for implants to consume so little power that they can be charged wirelessly from another source. Thus, to minimise the need of surgery, it is recommended that the possibility of wireless charging from an external device be investigated, to minimise the need of internal batteries and to potentially prolong the life of the implantation. Transmission range and speed can also be investigated to optimize power consumption. Otherwise, the implant should be used as a “lifetime” device, which is only to be retrieved from the animal once the animal is deceased. Of course, this would include tracking tags in order to retrieve the implanted device and to identify the specific animal that the device was monitoring.

8.2.3 Measure Real Rhinoceros Tissue

The dielectric properties of actual rhinoceros tissue and organs should be measured and this information used to update the developed models. The regulations regarding such a procedure can often be time consuming (up to six months to be permitted to handle a cadaver), but the results would yield more accurate rhinoceros phantom models.

8.2.4 Develop an Implant Device

Build an implant using the knowledge provided in this project and test it using the suggested phantom and numerical models. The models could be used to improve on the design of the implant prior to field tests and also be used for comparative purposes between the results of actual rhinoceros radiation measurements and those of the numerical simulations. The findings could be used to update the developed models.

Bibliography

[1] R. Shadwick, A. Russel and R. Lauff, "The Structure and Mechanical Design of Rhinoceros Dermal Armour," in *Philosophical Transactions: Biological Sciences,* vol. 337, Royal Society Publishing, 1992, pp. 419 - 428.

[2] A. Gallagher, A. Ni Anniadh, K. Bruyere, M. Ottenio, H. Xie and M. Gilchrist, *Dynamic Tensile Properties of Human Skin,* University College Dublin, 2012.

[3] C. Lima, R. de Oliveira, S. Figueiro, C. Wehmann, J. Goes and A. Sombra, *DC conductivity and dielectric permittivity of collagen–chitosan films,* Elsevier, 2005.

[4] V. Tomaselli and M. Shamos, "Electrical properties of hydrated collagen. I. Dielectric properties," *Biopolymers,* vol. 12, no. 2, pp. 353 - 266, February 1973.

[5] C. Conran, "Antenna Designs for Wireless Medical Implants," Dublin Institute of Technology, Dublin, 2013.

[6] A. Johansson, *Wireless Communication with Medical Implants: Antennas and Propagation,* Lund, Skane County: Lund University, 2004.

[7] A. Peyman, S. Holden and C. Gabriel, "Measurement of the dielectric properties of biological tissue in vivo at microwave frequencies," *Phycs in Medicine and Biology,* vol. 54, pp. 4863-4878, 22 December 2009.

[8] A. Stogryn, "Equations for Calculating the Dielectric Constant of Saline Water," *IEEE Transactions on Microwave Theory and Techniques,* pp. 733-736, August 1971.

[9] R. Buchner, G. Hefter and P. May, "Dielectric Relaxation of Aqeous NaCl Solutions," *The Journal of Physical Chemistry A,* vol. 103, no. 1, 7 January 1999.

[10] European Telecommunications Standards Institute, "Electromagnetic Compatibility and Radio Spectrum Matters (ERM): Improvement of Radiated Methods of Measurement (Using Test Sites) and Evaluation of the Corresponding Measurement Uncertainties; Part 7: Artificial Human Beings," ETSI, 1998.

[11] P. Hall and Y. Hao, Antennas and Propagation for Body-Centric Wireless Communications, vol. ii, P. Hall and Y. Hao, Eds., Boston: Artech House, 2012.

[12] K. Olawale, R. Petrell, D. Michelson and A. Trites, *The dielectric properties of the cranial skin of five young captive Steller sea lions (Eumetopias jubatus), and a similar number of young domestic pigs (Sus scrofa) and sheep (Ovis aries) between 0.1 and 10 GHz,* IOP Publishing Ltd, 2005, pp. 627 - 637.

[13] A. Dabbagh, B. Abdullah, C. Ramasindarum and N. Kasim, "Tissue-Mimicking Gel Phantoms for Thermal Therapy Studies," *Ultrasonic Imaging,* pp. 1 - 26, 2014.

[14] Q. Duan, J. Duyn, N. Gudino, J. de Zwart, P. van Gelderen, D. Sodickson and R. Brown, "Characterization of a dielectric phantom for high-field magnetic resonance imaging applications," *Medical Physics,* no. 41, 24 September 2014.

[15] A. Hartley, "Fuel Poverty," West Midlands Public Health Observatory, Birmingham, 2006.

[16] K. Chew, R. Sudirman, N. Seman and C. Yong, "Human Brain Phantom Modeling: Concentration and Temperature Effects on Relative Permittivity," *Advanced Materials Research,* vol. 646, pp. 191 - 196, 19 January 2013.

[17] A. Singh, G. Nair, P. Liplap, Y. Gariepy, V. Orsat and V. Raghavan, "Effect of Dielectric Properties of a Solvent-Water Mixture Used in Microwave-Assisted Extraction of Antioxidants from Potato Peels," *Antioxidants,* vol. 3, pp. 99 - 113, 24 February 2014.

[18] T. Tulasidas, G. Raghavan, F. van de Voort and R. Girard, "Dielectric Properties of Grapes and Sugar Solutions at 2.45 GHz," *Journal of Microwave Power and Electromagnetic Energy,* vol. 30, no. 2, pp. 117 - 123, 28 March 1995.

[19] R. Olmi, V. Meriakri, A. Ignesti, S. Priori and C. Riminesi, "Dielectric Spectroscopy of Sugar and Ethanol Solutions in Water for Monitoring Alcoholic Fermentation Processes," *Dielectric spectroscopy of ethanol and sugar aqueous solutions,* 2007.

[20] N. Gavish and K. Promislow, "Dependence of the Dielectric Constant of Electrolyte Solutions on Ionic Concentration - a Microfield Approach," *Physical Review,* vol. 94, 1 July 2016.

[21] W. Ellison, A. Balana, G. Delbos, K. Lamkaouchi, L. Eymard, G. C. and C. Prigent, "New Permittivity Measurements of Seawater," *Radio Science,* vol. 33, no. 3, pp. 639 - 648, June 1998.

[22] R. Somaraju and J. Trumpf, *Frequency, Temperature and Salinity Variation of the Permittivity of Seawater,* vol. 54, IEEE Trans. Antennas Propagation, 2006, pp. 3441 - 3448.

[23] J. Marais, Interviewee, *Rhinoceros Anatomy and Biomedical Implantable Devices.* [Interview]. 12-17 May 2016.

[24] Altair Hyperworks, "Altair FEKO," Altair, [Online]. Available: http://www.altairhyperworks.com/product/FEKO. [Accessed 26 February 2016].

[25] Antenna Magus, "Antenna Magus," Antenna Magus, [Online]. Available: http://www.antennamagus.com/. [Accessed 26 February 2016].

[26] Autodesk, "Tinkercad," Autodesk, [Online]. Available: https://www.tinkercad.com/. [Accessed 14 March 2017].

[27] Blender, "Blender," Blender, [Online]. Available: https://www.blender.org/. [Accessed 15 March 2017].

[28] Altair Hyperworks, "Method of Moments (MoM)," 2015. [Online]. Available: https://www.feko.info/product-detail/numerical_methods/mom. [Accessed 28 July 2016].

[29] Altair Hyperworks, "Multilevel Fast Multipole Method (MLFMM)," 2015. [Online]. Available: https://www.feko.info/product-detail/numerical_methods/mlfmm. [Accessed 28 July 2016].

[30] International Rhino Foundation, "Rhino Fact Sheet," 2016. [Online]. Available: http://www.leoafrica.org/files/rhinofactsheet.pdf. [Accessed 16 April 2016].

[31] W. Bearcraft and M. Jamieson, *Epidermal Structures in a Rhinoceros (Ceratotherium Simum),* vol. 182, Yaba: Nature Publishing Group, 1958, pp. 196 - 197.

[32] J. Huang, "Rhino Anatomy Model at 1/16th Scale - Flesh and Superficial Muscle," 2016. [Online]. Available: https://www.junsanatomy.com/products/rhino-anatomy-model-at-1-20th-scale-v-1?variant=1478842497. [Accessed 1 June 2016].

[33] Save the Rhino, "Species of Rhino," 2016. [Online]. Available: https://www.savetherhino.org/rhino_info/species_of_rhino. [Accessed 15 June 2016].

[34] C. Gabriel, S. Gabriel and E. Corthout, "The Dielectric Properties of Biological Tissues: I. Literature Survey," in *Physics in Medicine and Biology*, vol. 41, London, Strand: IOP Publishing Ltd, 1996, pp. 2231 - 2249.

[35] F. Azad, *Evaluation of a New Radiofrequency Identification Tag for Subdermal Implantation,* Vancouver: The University of British Columbia , 2009.

[36] A. Rauf, "A Dielectric Study On Human Blood Plasma," *International Journal of Science, Environment and Technology,* vol. 2, no. 6, pp. 1396 - 1400, 2013.

[37] C. Malmberg and A. Maryott, "Dielectric Constant of Water from 0 to 100 C," *Journal of Research of the National Bureau of Standards,* vol. 56, no. 1, January 1956.

[38] J. Marais, "A Permittivity Measurement System for High Frequency Laboratories," 2006.

[39] P. Banerjee, G. Ghosh and S. Biswas, "A Simple Method to Determine the Dielectric Constant of Small-Sized Medium-Loss Samples at X-Band Frequencies," *International Journal of Electromagnetics and Applications,* vol. 1, no. 1, pp. 12-15, 2011.

[40] M. Gosselin, G. Vermeeren, S. Kuhn, V. Kellerman, S. Benkler, T. Uusitupa, W. Joseph, A. Gati, J. Wiart, F. Meyer, L. Martens, T. Nojima, T. Hikage, Q. Balzano, A. Christ and N. Kuster, "Estimation Formulas for the Specific Absorption Rate in Humans Exposed to Base-Station Antennas," *IEEE Transactions on Electromagnetic Compatibility,* vol. 53, no. 4, November 2011.

[41] G. Hartsgrove, A. Kraszewski and A. Surowiec, "Simulated Biological Materials for Electromagnetic Radiation Absorption Studies," *Bioelectromagnetics,* vol. 8, pp. 29 - 36, 1987.

[42] K. Yoshimura, H. Kato, M. Kuroda, A. Yoshida, K. Hanamoto, A. Tanaka, M. Tsunoda, S. Kanazawa, K. Shibuya, S. Kawasaki and Y. Hiraki, "Development of a Tissue-Equivalent MRI Phantom Using Carrageenan Gel," *Magnetic Resonance in MEdicine,* vol. 50, pp. 1011-1017, 2003.

[43] B. Huffman, *Cow Mammal,* Encyclopedia Britannica, 2016.

[44] National Geographic, "Animals," 2016. [Online]. Available: http://www.nationalgeographic.com/animals. [Accessed 3 June 2016].

[45] B. Blaxland, *Humans are Mammals,* Australian Museum, 2015.

[46] New World Encyclopedia, "Mouse," 2 April 2008. [Online]. Available: http://www.newworldencyclopedia.org/entry/Mouse. [Accessed 2 February 2017].

[47] New World Encyclopedia, "Sheep," 4 April 2008. [Online]. Available: http://www.newworldencyclopedia.org/entry/Sheep. [Accessed 2 February 2017].

[48] National Geographic, "California Sea lion," 2016. [Online]. Available: http://www.nationalgeographic.com/animals/mammals/c/california-sea-lion/. [Accessed 26 May 2016].

[49] New World Encyclopedia, "Pig," 4 April 2008. [Online]. Available: http://www.newworldencyclopedia.org/entry/Pig. [Accessed 2 February 2017].

[50] B. Huffman, *Ungulates of the World,* Ultimateungulate.com, 2014.

[51] The Open University, *Studying Mammals: Plant Predators,* Open Learn, 2016.

[52] M. Mills, *The Comparative Anatomy of Eating,* ecologos.org, 1996.

[53] K. Patry, *Carnivore Digestive System,* raising-rabbits.com, 2016.

[54] J. McArdle, "Humans are Omnivores," *Vegetarian Journal,* June 1991.

[55] New World Encyclopedia, "Seal," 28 August 2008. [Online]. Available: http://www.newworldencyclopedia.org/entry/Seal. [Accessed 2 February 2017].

[56] S. Messenger, *21 Animals Who Know Being Single Is Awesome,* The Dodo, 2015.

[57] BBC, "Territorial," October 2014. [Online]. Available: http://www.bbc.co.uk/nature/adaptations/Territory_(animal). [Accessed 27 May 2016].

[58] P. Myers, R. Espinosa, C. Parr, T. Jones, G. Hammond and T. Dewey, *Horns and Antlers,* The Animal Diversity Web (online), 2016.

[59] K. Culp, *Antelers vs. Horns,* Fossil Rim Wildlife Center, 2014.

[60] All About Eyes, *The Best Eyes In The Animal Kingdom.*

[61] Morgans Lists, *10 Examples of How Animals See - Images That Show Us The World Through Their Eyes*, 2014.

[62] Ecoist, *How Do They See? Views Through the Eyes of 7 Animals*, Web Ecoist, 2017.

[63] S. Khanwilkar, *"Eye" Wonder: 10 Things You Didn't Know About Frog Eyes*, Wordpress.com, 2014.

[64] Museum of Vision, *Animal Eyes*, The Foundation of the American Academy of Ophthalmology, 1997.

[65] M. Baker, *Neuroscience: Through the eyes of a mouse*, Nature, 2013.

[66] F. Hanke, W. Hanke, C. Scholtyssek and G. Dehnhardt, "Basic mechanisms in pinniped vision," *Experimental Brain Research*, vol. 199, pp. 299-311, December 2009.

[67] Velarde, A.; Llonch, P.; Dalmau, A., *Pig vision and management/handling*, pig333, 2009.

[68] Random Rabbit Pages, "A Rabbit's Vision," 22 January 2017. [Online]. Available: http://www.vgr1.com/vision/. [Accessed 6 February 2017].

[69] Rat Sensory World, *What Do Rats See?*, Ratbehavior.org, 2004.

[70] Ageuk, "How does an animal's hearing compare to a human's – Infographic," 2016. [Online]. Available: http://www.ageukhearingaids.co.uk/hearing-aid-news/how-does-animals-hearing-compare-humans-infographic. [Accessed 6 February 2017].

[71] Louisiana State University, "How Well Do Dogs and Other Animals Hear?," 3 June 2003. [Online]. Available: http://www.lsu.edu/deafness/HearingRange.html. [Accessed 6 February 2017].

[72] C. Reichmuth, M. Holt, J. Mulsow, J. Sills and B. Southall, "Comparative assessment of amphibious hearing in pinnipeds," *Journal of Comparative Physiology*, 14 March 2013.

[73] S. Hemila, S. Nummela, A. Berta and T. Reuter, "High-frequency hearing in phocid and otariid pinnipeds: An interpretation based on inertial and cochlear constraints (L)," *The Journal of the Acoustical Society of America*, vol. 120, no. 6, pp. 3463-3466, 2 Ocotber 2006.

[74] A. Kittawornrat and J. Zimmerman, "Toward a better understanding of pig behavior and pig welfare," *Animal Health Research Reviews*, 18 October 2010.

[75] J. Viegas, *10 Best Sniffers in the Animal Kigndom*, Seeker, 2014.

[76] B. Ache and J. Young, "Olfaction: Diverse Species, Conserved Principles," *Neuron*, vol. 48, no. 3, pp. 417-430, 3 November 2005.

[77] E. Wexler-Mitchell, *Smell - a Very Important Sense to Cats*, catcare.com, 2010.

[78] C. Dwyer, The Welfare of Sheep, Springer Science & Business Media, 2008, p. 136.

[79] B. Pitcher, R. Harcourt, B. Schaal and I. Charrier, "Social Olfaction in Marine Mammals: Wild Female Australian Sea Lions can Identify Their Pup's Scent," *Biology Letters*, vol. 7, pp. 60-62, 4 August 2010.

[80] B. Van Valkenburgh, A. Curtis, J. Samuels, D. Bird, B. Fulkerson, J. Meachen-Samuels and G. Slater, "Aquatic adaptations in the nose of carnivorans: evidence from the turbinates," *Journal of Anatomy*, vol. 218, pp. 298-310, 2011.

[81] P. Brunjes, S. Feldman and S. Osterberg, "The Pug Olfactory Brain: A Primer," *Chemical Senses*, vol. 41, pp. 415-425, 2016.

[82] W. Le Gros Clark, "Observations on the Structure and Organization of Olfactory Receptors in the Rabbit," *The Yale Journal of Biology and Medicine, Inc.*, 24 May 1956.

[83] J. Xi, X. Si, J. Kim, Y. Zhang, R. Jacob, S. Kabilan and R. Corley, "Anatomical Details of the Rabbit Nasal Passages and Their Implications in Breathing, Air Conditioning, and Olfaction," *The Anatomical Record*, vol. 299, pp. 853-868, 2016.

[84] Enchanted Learning, “Biomes - Habitats,” 2016. [Online]. Available: http://www.enchantedlearning.com/biomes/desert/desert.shtml. [Accessed 6 February 2017].

[85] C. Parrington, The British Cyclopædia of Natural History: Combining a Scientific Classification of Animals, Plants, and Minerals, vol. 3, Orr & Smith, 1837, p. 171.

[86] D. Mills and S. McDonnell, The Domestic Horse: The Origins, Development and Management of Its Behaviour, Cambridge University Press, 2005, p. 100.

[87] K. Allan, The Routledge Handbook of Linguistics, Routledge, 2015, p. 28.

[88] House Rabbit Society, “Common Illnesses,” 2003. [Online]. Available: https://www.hrss.net/aar/health/health_dental.html. [Accessed 5 February 2017].

[89] The Website of Everything, *Mammals Ordered by Weight,* thewebsiteofeverything.com, 2011.

[90] P. Warrignton, *Animal Weights and Their Food and Water Requirements,* Government of British Columbia, 2001.

[91] P. Kinser, *What is the relationship between brain and body size??,* Serendip Studio, 2012.

[92] New World Encyclopedia, “Human being,” 20 July 2009. [Online]. Available: http://www.newworldencyclopedia.org/entry/Human_being. [Accessed 2 February 2017].

[93] B. O'Rourke, R. Russel and D. UW-Madison, “Lamb Carcass Evaluation,” 2010. [Online]. Available: sheboygan.uwex.edu/files/2010/08/Lamb-Carcass-Evaluation.pdf. [Accessed 26 May 2016].

[94] A. Aganga, *Water utilization by sheep and goats in northern Nigeria,* Food and Agriculture Organization of the United Nations, 1986.

[95] Q. Smith, “Body weight, cutaneous collagen and hexosamine of cortisone-treated female rats of various ages,” vol. 42, pp. 353-357, May 1964.

[96] A. Asante-Poku, K. Aning, B. Boi-Kikimoto and D. Yeboah-Manu, “Prevalence of bovine tuberculosis in a dairy cattle farm,” *The Onderstepoort Journal of Veterinary Research,* vol. 81, no. 2, p. 6, February 2014.

[97] E. Jensen-Jarolim, Comparative Medicine: Anatomy and Physiology, Springer Science & Business Media, 2013, p. 111.

[98] J. Cline, “Skin and Coat,” [Online]. Available: https://cdn.shopify.com/s/files/1/0659/4529/files/SkinCoat_WhiteSheet6-5.pdf?6678352109863082785. [Accessed 2 February 2017].

[99] H. Evans and A. de Lahunta, Miller's Anatomy of the Dog, Elsevier Health Sciences, 2013, p. 62.

[100] M. Volkering, *Variation of skin thickness over the equine body and the correlation between skin fold measurement and actual skin thickness,* Faculty of Veterinary Medicine, 2009.

[101] M. Kaplan, P. Heimes, E. Zarza and J. McCormack, “On the morphology of Plectrohyla chryses (Anura: Hylida; Hylini), with comments on some controversial characters, phylogenetic relationships, and diagnosis of this species,” *Caldasia,* vol. 38, no. 2, pp. 257-273, 2016.

[102] M. Meyers, P. Chen, A. Lin and Y. Seki, “Biological Materials: Structure and Mechanical Properties,” *Progress in Materials Science,* vol. 53, pp. 1-206, 2008.

[103] J. Manne, M. Markova, L. Siracusa and S. Jimenez, “Collagen Content in Skin and Internal Organs of the Tight Skin Mouse: An Animal Model of Scleroderma,” *Biochemistry Research International,* vol. 2013, p. 8, 2013.

[104] Y. Tao, "Studies on the Quality of Rex Rabbit Fur," *World Rabbit Science,* vol. 2, no. 1, pp. 21-24, 1994.

[105] A. Pearson and T. Dutson, Inedible Meat by-Products, vol. 8, Oregon: Elsevier Science Publishers LTD, 2013, p. 226.

[106] Food and Agriculture Organization of the United Nations, "Definition and Classification of Commodities," 1994. [Online]. Available: http://www.fao.org/ES/faodef/fdef19e.htm#19.1. [Accessed 26 May 2016].

[107] R. Neuman and M. Logan, *The Determination of Collagen and Elastin in Tissues,* Cincinnati: University of Cincinnati, 1950.

[108] Ovinex, *Ovinex: Premium Sheep Collagen,* Holista Colltech, 2010.

[109] Institute of Laboratory Animal Resources and the American College of Laboratory Animal Medicine, Animal Models for Biomedical Research, vol. 3, Washington, D.C., 1970, p. 83.

[110] M. De Souza, M. Silva, J. de Oliveira Pinto, M. de Souza Lima, J. Crepaldi, G. Lopes, H. Dos Santos, R. de Azambujo Ribeiro and R. Thome, "Immunohistochemical Expression of Collagens in the Skin of Horses Treated with Leukocyte-Poor Platelet-Rich Plasma," *Biomed Research International,* 12 May 2015.

[111] B. Dokuzeylul, E. Altun, T. Ozdogan, H. Bozkurt, S. Arun and M. Or, "Cutaneous asthenia (Ehlers–Danlos syndrome) in a cat," *Turkish Journal of Veterinary and Animal Sciences,* vol. 37, pp. 245-249, 2013.

[112] K. Sai and M. Babu, "Studies on Rana tigerina skin collagen," *Comparative Biochemistry and Physiology Part B,* vol. 128, pp. 81-90, 2000.

[113] H. Li, B. Liu, L. Gao and H. Chen, "Studies on bullfrog skin collagen," *Food Chemistry ,* vol. 84, pp. 65-69, 2003.

[114] K. Long, C. Artlett and E. Blankenhorn, "Tight skin 2 mice exhibit a novel time line of events leading to increased extracellular matrix deposition and dermal fibrosis," *Matrix Biology,* vol. 38, pp. 91-100, 2 May 2014.

[115] W. Khamas, H. Smodlaka, J. Leach-Robinson and L. Palmer, "Skin histology and its role in heat dissipation in three pinniped species," *Acta Veterinaria Scandinavica,* vol. 54, no. 46, 2012.

[116] F. Rodrigues, V. Martins and A. Plepis, "Porcine Skin as a Source of Biodegradable Matrices: Alkaline Treatment and Glutaraldehyde Crosslinking," *Polimeros,* vol. 20, no. 2, pp. 92-97, 2010.

[117] M. Nimni, E. de Guia and L. Bavetta, "Collagen, Hexosamine and Tensile Strength pf Rabbit Skin During Aging," *The Journal of Investigative Dermatology,* vol. 47, no. 2, pp. 156-158, August 1966.

[118] E. Johnson and M. Vidyadaran, "An Evaluation of Different Sites for Measuring Fat Thickness in the Beef Carcass to Determine Carcass Fatness," *Australian Journal for Agricultural Research,* vol. 32, pp. 999-1007, 19 June 1981.

[119] Food and Agriculture Organization of the United Nations, *Meat, Fat and Other Edible Carcass Parts,* FAO, 2010.

[120] P. Superchi, I. Vecchi, V. Beretti and A. Sabbioni, "Relationship among BCS and Fat Thickness in Horses of Different Breed, Gender and Age," *Annual Research & Review in Biology,* vol. 4, no. 2, pp. 354-365, 19 October 2013.

[121] Kentucky Equine Research Staff, "Rump Fat Measurement in Horses," 31 May 2015. [Online]. Available: http://saracen.equinews.com//article/rump-fat-measurement-horses. [Accessed 26 May 2016].

[122] J. Matton and T. Nyland, Small Animal Diagnostic Ultrasound, Elsevier Health Science, 2014, pp. 470-472.

[123] D. Ho and E. Kim, "Optical Skin-fat Thickness Measurement Using Miniaturized Chip LEDs: A Preliminary Human Study," *Journal of the Optical Society of Korea*, vol. 13, no. 3, pp. 304-309, September 2009.

[124] J. Ng, "Automatic Measurement of Human Subcutaneous Fat with Ultrasound," The University of British Columbia, 2002.

[125] B. Poligone, M. Hayden, L. Chen, A. Pentland, E. Jimi and S. Ghosh, "A Role for NF-κB Activity in Skin Hyperplasia and the Development of Keratoacanthomata in Mice," *PLoS ONE*, August 2013.

[126] G. Bruwe and R. Naude, "An evaluation of the lamb and mutton carcase grading system in the Republic of South Africa. 1. A survey of carcase characteristics of the different grades," *South African Journal of Animal Science*, vol. 17, no. 2, pp. 79-84, 2 July 1987.

[127] A. Trites and R. Jonker, "Morphometric measurements and body condition of healthy and starveling Steller sea lion pups (Eumetopias jubatus)," *Aquatic Mammals*, vol. 26.2, pp. 151-157, 2000.

[128] J. Pascual, B. j., O. Piquer, F. Quevedo and C. Cervera, "Ultrasound Measurements of Perirenal Fat Thickness to Estimate the Body Condition of Reproducing Rabbit Does in Different Physiological States," *World Rabbit Science*, vol. 12, pp. 7-21, 2004.

[129] J. Berlanga-Acosta, D. Vázquez-Blomquist, D. Cibrián, Y. Mendoza, M. Ochagavia, J. Miranda, J. Suarez, Y. Gonzalez-Ferrer, J. Vila, A. Abreu, D. Ugarte-Moreno, Y. Cruz, I. Howland, R. Coro-Antich, O. Leon, R. Bringas and D. Barco, "Growth Hormone Releasing Peptide 6 (GHRP6) reduces liver fibrosis in CCl4 chronically intoxicated rats," *Biotechnologia Aplicada*, vol. 29, no. 2, pp. 60-72, 2012.

[130] S. Bene, B. Nagy, L. Nagy, B. Kiss, J. Polgar and F. Szabo, "Comparison of body measurements of beef cows of different breeds," *Archives Animal Breeding*, vol. 50, no. 4, pp. 363-373, 28 March 2007.

[131] My Pet, "How to Measure your Dog (for Coats, Hats, Jumpers & Dog Clothes)," 2008. [Online]. Available: http://www.mypet.net.au/sizeguide.htm. [Accessed 26 May 2016].

[132] Federal Highway Administration, *Equestrian Design Guidebook for Trails, Trailheads and Campgrounds*, FHWA, 2014.

[133] M. Magged, D. Berner, H. Julke, C. Hohaus, W. Brehm and K. Gerlach, "Is sheep lumbar spine a suitable alternative model for human spinal researches? Morphometrical comparison study," *Laboratory Animal Research*, vol. 29, no. 4, pp. 183-189, 20 December 2013.

[134] S. Ramesh, T. Sivakumar, T. Gnanaraj, R. Murallidharan and M. Murugan, "Comparative Performance of Landrace and Large White Yorkshire Pigs Under Tropical Maritime Monsoon Climate," *Turkish Journal of Veterinary and Animal Sciences*, vol. 40, pp. 42-46, 2009.

[135] New World Encyclopedia, "Rat," 4 April 2008. [Online]. Available: http://www.newworldencyclopedia.org/entry/Rat. [Accessed 4 April 2017].

[136] L. Alterman, G. Doyle and M. Izard, Creatures of the Dark, Springer Science and Business Media, 2013, p. 553.

[137] K. Budras and R. Habel, Bovine Anatomy: An Illustrated Text, 1 ed., Schluterse, 2003, pp. 68-69.

[138] K. Holmes, "Thermal Properties," 2009. [Online]. Available: users.ece.utexas.edu/~valvano/research/Thermal.pdf. [Accessed 25 February 2016].

[139] C. Jack and P. Watson, Veterinary Technician's Daily Reference Guide: Canine and Feline, John Wiley & Sons, 2014.

[140] R. Parker, Equine Science, 4 ed., Cengage Learning, 2012, pp. 88-97.

[141] B. Wingerd, Frog Dissection Manual, JHU Press, 1988, pp. 18-19.

[142] K. Saladin, Human Anatomy, McGraw Hill Higher Education, 2007, pp. 24-43.

[143] T. Albers and K. Pritchett-Corning, "Diagnostic Necropsy and Selected Tissue and Sample Collection in Rats and Mice," *Journal of Visualized Experiments,* August 2011.

[144] P. Iaizzo, Handbook of Cardiac Anatomy, Physiology, and Devices, Springer Science & Business Media, 2009, pp. 102-103.

[145] W. Perrin, B. Wursig and J. Thewissen, Encyclopedia of Marine Mammals, Academic Press, 2009, pp. 31-33.

[146] Oxford University Museum of Natural History, *Animal Skeletons,* Aniskel, 2005.

[147] I. Bab, C. Hajbi-Yonissi, Y. Gabet and R. Muller, Micro-Tomographic Atlas of the Mouse Skeleton, Springer Science & Business Media, 2007, pp. 149-163.

[148] Aus-Meat, *Handbook of Australian Meat,* 4 ed., 2006.

[149] M. Fraser and S. Girling, Rabbit Medicine and Surgery for Veterinary Nurses, John Wiley & Sons, 2009, pp. 106-114.

[150] D. Slatter, Textbook of Small Animal Surgery, vol. 1, Elsevier Health Sciences, 2003, pp. 1736-1768.

[151] K. Budras, W. Sack and S. Rock, Anatomy of the Horse: An Illustrated Text, Schlutersche, 2003.

[152] P. van Dijk, M. Mason, R. Schoffelen, P. Narins and S. Meenderink, "Mechanics of the frog ear," *Hearing Research,* vol. 273, no. 1-2, pp. 46-58, March 2011.

[153] T. Cox, E. Camci, D. Luquetti and E. Turner, "The genetics of auricular development and malformation: New findings in model systems driving future directions...," *European Journal of Medical Genetics,* vol. 57, pp. 394-401, May 2014.

[154] V. Seibel, L. Lavinsky and K. Irion, "CT-Scan sheep and human inner ear morphometric comparison," *Brazilian Journal of Otolaryngology,* vol. 72, no. 3, pp. 370-376, 2006.

[155] Internal Medicine, *Porcine Clinical Procedures,* Veterian Key, 2016.

[156] J. Rickel, *Rabbit Ears: A Structural Look: ...injury or disease, can send your rabbit into a spin,* House Rabbit Society.

[157] D. Duocomm, Rats: Practical, Accurate Advice from the Expert, i5 Publishing, 2011.

[158] A. Bhattacharya and R. Mahajan, "Temperature dependence of thermal conductivity of biological tissues," *Physiological Measurement,* vol. 24, no. 3, 4 July 2003.

[159] J. Choi and J. Bishof, "Review of biomaterial thermal property measurements in the cryogenic regime and their use for prediction of equilibrium and non-equilibrium freezing applications in cryobiology," *Cryobiology,* vol. 60, pp. 52-70, 3 December 2009.

[160] American Society of Heating, Refrigeration and Air-Conditioning Engineers (ASHRAE), *Thermal Properties of Foods,* ASHRAE, 2006.

[161] F. Hart and W. Dunfee, "In vivo measurement of the low-frequency dielectric spectra of frog skeletal muscle," *Physics in Medicine and Biology,* vol. 38, pp. 1099-1112, 1993.

[162] S. Lubner, J. Choi, Y. Hasegawa, A. Fong, J. Bischof and C. Dames, *Measurements of the Thermal Conductivity of Sub-Millimeter Biological Tissues,* International Mechanical Engineering Congress & Exposition (IMECE), 2012.

[163] K. Maksymowicz, K. Marycz, S. Szotek, K. Kalinski, E. Serwa, E. Lukomski and J. Czogala, "Chemical composition of human and canine fascia lata," *Acta Biochimica Polonica (ABP),* vol. 59, no. 4, pp. 531-535, 5 October 2012.

[164] D. Marshall, *Horse Health Depends on Water,* Delaware: University of Delaware, 2004.

[165] F. Syufry, “How Much Water Does an Adult Cat Need to Drink,” 29 December 2016. [Online]. Available: http://cats.about.com/od/waterforcats/f/waterneeds.htm. [Accessed 26 May 2016].

[166] J. Behler and D. Behler, Frogs: A Chorus of Colors, Sterling Publishing Company, 2008, p. 54.

[167] The USGS Water Science School, *The water in you*, USGS, 2016.

[168] J. Fox, S. Barthold, M. Davisson, C. Newcomer, F. Quimby and A. Smith, The Mouse in Biomedical Research, 2 ed., vol. 3, Elsevier, p. 76.

[169] B. Le Boeuf and R. Laws, Elephant Seals: Population Ecology, Behavior, and Physiology, Califronia: University of Califronia Press, 1994, pp. 103-105.

[170] W. Mayer, Physiological Mammalogy, vol. 2, Elsevier, 2012, p. 132.

[171] M. Bond, “Rhinoceros,” November 2008. [Online]. Available: http://a-z-animals.com/animals/rhino/. [Accessed 4 February 2016].

[172] G. Hian, N. Rusaini, S. Yusak, T. Hong and M. Hamid, “Biomaterial: Cardiac Pacemaker,” 2011/2012. [Online]. Available: https://sites.google.com/site/g10pacemaker/materials. [Accessed 9 February 2016].

[173] IEEE, *IEEE Standard for Safety Levels with Respect to Human Exposure to Radio Frequency Electromagnetic Fields, 3 kHz to 300 GHz*, New York, New York: IEEE, 2006.

[174] FCC, *Reassessment of Federal Communications Commission Radiofrequency Exposure Limits and Policies*, Washington D.C., Washington: Federal Communications Commission , 2013.

[175] A. Stogryn, *Equations for Calculating the Dielectric Constant of Saline Water*, El Monte, California: IEEE, 1971.

[176] D. Bolat, S. Bahar, S. Tipirdamaz and M. Selcuk, “Comparison of the Morphometric Features of the Left and Right Horse Kidneys: A Stereological Approach,” *Anatomia Histologia Embryologia: Journal of Veterinary Medicine*, vol. 42, pp. 448 - 452, Decemeber 2012.

[177] N. Loving, “The Equine Liver in Health and Disease,” 29 March 2016. [Online]. Available: http://www.thehorse.com/articles/37333/the-equine-liver-in-health-and-disease. [Accessed 6 June 2016].

[178] M. Durham, *What Makes The Horse Such an Amazing Athlete?*, Bay Area Equstrian Metwork, 2007.

[179] S. Davidson and M. Sherar, *Measurement of the Thermal Conductivity of Polyacrylamide Tissue-Equivalent Material*, vol. 5, 2003, pp. 551 - 562.

[180] M. Canney, V. Khoklova, O. Bessanove, M. Bailey and L. Crum, *Shock-Induced Heating and Millisecond Boiling in Gels and Tissue Due to High Intensity Focused Ultrasound*, 26 ed., vol. 2, Moscow: NIH, 2010.

[181] P. Hariharan, M. Meyers and R. Banerjee, *HIFU Procedures at Moderate Intensities - Effect of Large Blood Vessels*, vol. 52, IOP Publishing, 2007, pp. 3493 - 3513.

APPENDICES

A. Outcomes Compliance of Project Objectives

The overall aim of this project was to deliver a phantom model which replicates the dielectric properties of rhinoceroses and to provide a test environment for experimental in-vivo and ex-vivo devices. This chapter identifies where the project aims specified in the introductory chapter of this document (page 1) were accomplished.

A.1 Specific Aims Chapter Analysis

The specific aims of this project were accomplished within the following chapters:

i) Approximate the dielectric properties of rhinoceros tissue:

Chapters: 2 and 4.
Appendices: J, K, L and "External1".

ii) Identify viable and common frequency ranges of operation:

Chapters: 2.
Appendices: "External1".

iii) Identify viable antenna designs:

Chapters: 2, 6 and 7.
Appendices: B, D, G, H, M and "External1".

iv) Identify viable points of implantation within a rhinoceros:

Chapters: 2, 3, 5 and 6.
Appendices: B, D and H.

v) Identify the limitations or parameters of a rhinoceros implantation device:

Chapters: 2, 6 and 7.
Appendices: D, G, H, M and "External1".

vi) Deliver a computer simulation phantom model:

Chapters: 2, 3, 4, 5 and 6.
Appendices: B, D, J, M, O and "External1".

vii) Deliver a means of creating a phantom model for practical experimentation:

Chapters: 2, 5 and 7.
Appendices: D, E, I, M, N and "External1".

viii) Practically measure the dielectric characteristics of the phantom models:

Chapters: 5 and 7.
Appendices: E, F, J, O and "External1".

ix) Compare results of the computational and physical phantom models:

Chapters: 2, 6, 7 and 8.
Appendices: G, H, M and "External1".

x) Apply the models to the analysis of an implantable sensor.

Chapters: 5, 6, 7 and 8.
Appendices: "External1".

A.2 Additional Objective Completion

It is clear from the mentioned chapters that all the objectives listed in the introductory chapter of this document (page 1) were completed and the overall aim of this project was accomplished. Not only were all the specified goals met, but additional objectives were completed to further enhance the project value. The following list illustrates these additional objectives:

i) Additional model designs:

Although only one model was required, four models were designed to encapsulate various rhinoceros body parts and to accommodate a wider range of applications. These models include the anatomical rhinoceros model, the cylindrical phantom model, the rhinoceros leg model and the rhinoceros flank model.

ii) Multiple recipes:

Only the epidermis, dermis, fat, muscle and blood recipes were needed to fulfil the requirements of this project. However, additional recipes were calculated for various organs and body parts, including bone cancellous, bone cortical, grey matter, white matter, kidney, spleen, heart, liver and lung recipes. Not only were each of these calculated for the frequency used in this project (2.4 GHz), but also for various other frequencies including 403 MHz, 910 MHz and 4.5 GHz. Each of these recipes were created, measured and validated.

iii) Ingredient comparison:

Apart from recreating the recipes numerous times to test their repeatability, different types of ingredients were used to investigate their effect on the permittivity measurements. This was done with household sugar and purified sucrose to investigate whether or not the less expensive ingredient would cause a greater measured error, but it proved to deliver as accurate or even better results than the more expensive version. This significantly reduced the cost of the agar models.

iv) Multiple antenna designs:

Although only a few antenna designs were illustrated in this document, many more were designed and incorporated into the simulation models. Additional designs can be viewed in the external media.

v) Two permittivity approximations:

Seeing as the permittivity of actual rhinoceros skin is unknown, two logical methods were used to approximate this value. This created a set of boundaries in which the permittivity of actual rhinoceros tissue is likely to be encapsulated.

vi) Recipe trends:

Although only the permittivity trends of the agar materials were required for this project, estimations regarding various characteristics of the recipes were investigated. This included the density versus frequency, salt versus frequency, sugar versus frequency and thermal properties such as heat capacity.

vii) Detailed internal simulation models:

Although not required to accomplish the aims of this project, detailed skeleton and organ models were created. These models can be viewed in Chapter 6.3.2 (page 89) and includes the upper jaw, lower jaw front and back legs, vertebrate, ribcage, pelvis, lung, stomach, kidneys, bladder, white matter, grey matter, tongue, heart, liver, spleen and intestines of the rhinoceros.

viii) Alternative recipes:

Some recipes were calculated using more than one method of approximation, which delivered more than one recipe for the same material. Both sets of recipes are indicated due to the accuracy of the recipes varying from material to material.

ix) Additional simulations:

The frequency of 2.4 GHz was selected for this project, along with prototype antenna designs which operate at that frequency. However, a few simulations were conducted using other antenna designs and phantom models designed for lower frequencies such as 403 MHz. The results of these simulations are included in the external media (Appendix I, page 133).

B. Location and Orientation of the Antenna Designs in the Rhinoceros and Cylindrical Simulation Models

The coordinates relative to the origin of the simulation models and the angles of the implantation devices are illustrated in Figures 98 to 103.

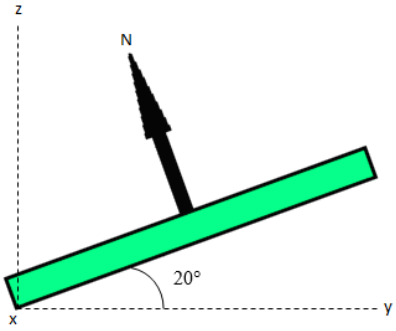

Antenna Position:

x-coordinate = 1.139 m
y-coordinate = 1.38 m
z-coordinate = 1.64 m

Rotation about the x-axis = 20°

Figure 98: Coordinates and angle of the back implantation in the anatomical phantom model.

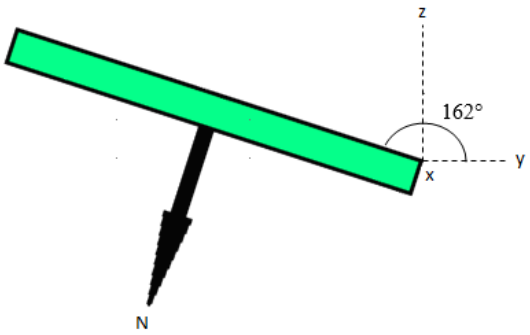

Antenna Position:

x-coordinate = 1.139 m
y-coordinate = 1.9 m
z-coordinate = 0.627 m

Rotation about the x-axis = 162°

Figure 99: Coordinates and angle of the chest implantation in the anatomical phantom model.

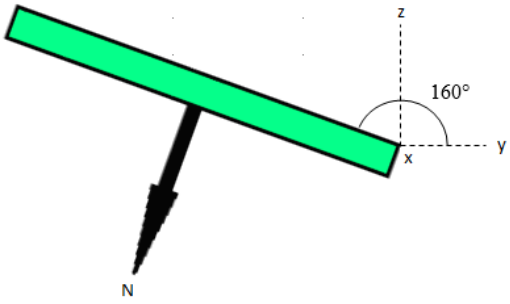

Antenna Position:

x-coordinate = 1.139 m
y-coordinate = 1.313 m
z-coordinate = 0.85 m

Rotation about the x-axis = 160°

Figure 100: Coordinates and angle of the neck implantation in the anatomical phantom model.

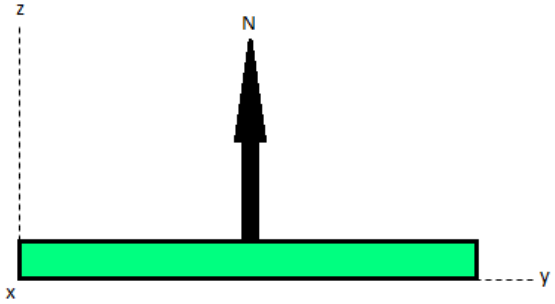

Antenna Position:

x-coordinate = 0 m
y-coordinate = -0.95 m
z-coordinate = 0.495654 m

No rotation about any axis

Figure 101: Coordinates and angle of the back implantation in the cylindrical model.

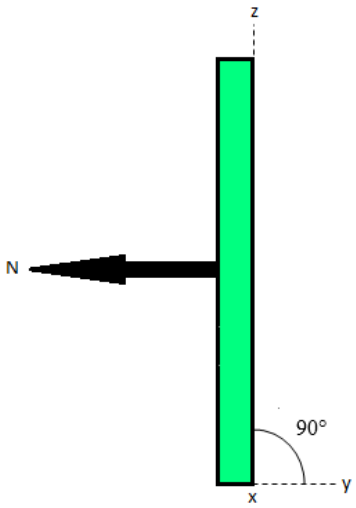

Antenna Position:

x-coordinate = 0.15 m
y-coordinate = -1.145654 m
z-coordinate = -0.2 m

Rotation about the x-axis = 90°

Figure 102: Coordinates and angle of the neck implantation in the cylindrical model.

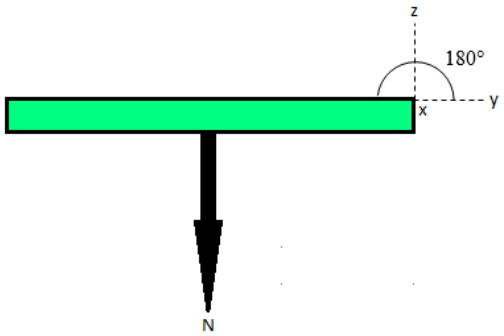

Antenna Position:

x-coordinate = 0 m
y-coordinate = -0.95 m
z-coordinate = -0.495654 m

Rotation about the x-axis = 180°

Figure 103: Coordinates and angle of the chest implantation in the cylindrical model.

C. Cylindrical Model Volume Calculations

The volumes of the cylindrical model layers and of the organs were calculated in order to estimate the amount of liquid or gelatinous substance to produce for the physical phantom model. The volumes of the gelatinous substances required, based on the cylindrical simulation models, are as follows:

Full Cylindrical Volumes: ($V = \pi r^2 h$)

Epidermis	$= \pi(0.55)^2(2.4)$	$= 2.280796267$	m^3	$= 2280.796$	litre
Dermis	$= \pi(0.548154)^2(2.396308)$	$= 2.262026485$	m^3	$= 2262.026$	litre
Fat	$= \pi(0.515654)^2(2.331308)$	$= 1.94744996$	m^3	$= 1947.450$	litre
Muscle	$= \pi(0.475654)^2(2.251308)$	$= 1.600173574$	m^3	$= 1600.174$	litre
Blood	$= \pi(0.175654)^2(1.651308)$	$= 0.16006414$	m^3	$= 160.064$	litre

Phantom Layer Volumes:

Epidermis	$= 2.28\ m^3 - 2.26\ m^3$	$= 0.18769782\ m^3$	$= 187.698$	litre
Dermis	$= 2.26\ m^3 - 1.94\ m^3$	$= 0.314576525\ m^3$	$= 314.577$	litre
Fat	$= 1.94\ m^3 - 1.60\ m^3$	$= 0.347276386\ m^3$	$= 347.276$	litre
Muscle	$= 1.60\ m^3 - 0.16\ m^3$	$= 1.440109434\ m^3$	$= 1440.109$	litre
Blood	$= 0.16\ m^3$	$= 0.16006414\ m^3$	$= 160.064$	litre

The volumes of the rhinoceros organ simulation models were based on the average sizes of equine/horse organs. The selected volumes are as follows:

Brain	= 0.532 kg	= 0.532	litre
Caecum	= 28 to 36 *l*	≈ 32	litre
Colon (Large)	= 86 kg	= 86	litre
Colon (Small)	$= 0.0255\ m^3$	≈ 25.525	litre
Heart	= 3.6 to 10 kg	≈ 6.8	litre
Intestines (Small)	= 55 to 70 *l*	≈ 62.5	litre
Kidney (left)	= 0.550 +/- 0.025 kg	≈ 0.550 +/- 0.025	litre
Kidney (Right)	= 0.585 +/- 0.023 kg	≈ 0.585 +/- 0.023	litre
Liver	= 10.35 kg	= 10.35	litre
Lung	= 42 000 m*l*	= 42	litre
Spleen	= 85.8 +/- 10.1 m*l*	= 0.0858 +/- 0.0101	litre
Stomach	= 9 to 15 *l*	≈ 12	litre

D. Interview with Dr Johan Marais

Due to the lack of published articles concerning the specific anatomy of rhinoceros skin and dielectric properties, an interview was conducted with Dr Johan Marais, a wildlife (equine) surgeon at the Faculty of Veterinary at the University of Pretoria, Onderstepoort. He has successfully operated on various large mammals including rhinoceroses, elephants, antelope and buffalo to mend fractures, abscesses and snare wounds. An initial questionnaire was delivered to Dr Johan Marais which was returned by means of written correspondence, prior to the interview conducted with Dr J Marais via Skype. The questionnaire (in question and answer format) is as follows (received 12 May 2016):

1. The selection of the materials and size of the implantation are important factors to consider when designing any implantation device. Are the standard materials and sizes used in other implantations such as pacemakers, suitable for rhinoceros implantation (i.e. are they bio-compatible)? If not, what materials would you suggest and what size would you recommend for an implant (as small as possible)?

   Yes, any biocompatible material would be okay. Smallest is always best, but the biggest should be in the region of 7x5x2 cm.

2. Could you provide a reference for rhinoceros anatomy, i.e. is there a book or article containing such information?

   Sorry, this does not exist. No anatomy other than the reproductive organs, horn and intestine of a rhino has been studied. With our research so far, the rhino is a mix between the cow and a horse, with some major differences in between.

3. Similarly, is there a standard surgical procedure that can be performed by a surgeon to insert such a device, i.e. do you have a reference for this?

   In rhinos - Nope, this has not been performed. However, it should not be difficult. I am sure other species data do exist.

4. Based on your experience, can you recommend at least three potential points within the rhinoceros that could host the implant? Why would these points be best suited for this purpose?

   Assuming they would go subcutaneous, I would basically look at points where there is (a) little movement (b) extra skin to work with and (c) not too thick skin, and my choices would be:

   1. Chest
   2. Neck
   3. Potentially the ventral abdomen, but the skin is quite thick there... (last resort).

5. Are post-surgical check-ups required after to, for example, ensure that infection does not take hold?

   Absolutely. Post-op checks for at least 4 weeks.
   Week 1 and 2: Every second day.
   Week 3 and 4: Three times per week.

6. In your experience, have you found that implants tend to migrate within the body? If so, what measures (if any) could be taken to prevent this?

   Difficult to say. I have only seen bullets and they have not migrated. One can always design the implant so that you can suture it to the s/c or dermis when you implant it, to prevent it from migrating.

7. Do you have any knowledge of any monitoring or other devices currently being used in rhinoceros monitoring or tracking?

   Nope.

8. To your knowledge, have any tests regarding the permittivity and conductivity of rhino hide ever been conducted?

   I would say definitely not.

The Skype meeting occurred on 17 May 2016 (09:00 AM) and was conducted in the following question and answer format:

1. In correspondence to the questionnaire, you mentioned that any biocompatible material would suffice and that the size of the implantation should not exceed 7x5x2 cm. Why were these specific dimensions selected?

   Any foreign material placed inside the body increased the chance of infection, especially due to the 50% of skin breakdown which occurs after surgery. The smaller incision reduces the chance of infection.

2. Considering that rhinoceroses often battle, should the implantation material be selected based on its strength or will the rhinoceros hide provide the necessary protection and thus, should the material rather be selected based on its efficiency with regards to the propagation of signals?

   Efficiency should definitely be favoured over strength.

3. Regarding the anatomy of the rhinoceros, you mentioned similarities between cows and horses - could you elaborate on this?

   The skeleton of the rhinoceros is similar to that of a cow, but when performing surgeries on rhinoceroses to remove bullets and to tend to wounds, the anatomy of the rhinoceros organs and intestines are based on those of equine/horses.

4. Do you have measurements of the thickness of the rhinoceros skin at various body positions?

   The thickness of rhinoceros skin can range from about 2 cm to 10 cm, depending on the rhino and the body part, for example, the skin in the achilles area is approximately 4 cm thick to support the weight of the rhinoceros.

5. What are the factors to look for during the post-operation check-ups?

Mostly one just looks for any type of complication, such as the breakdown of the wound, infection and swelling.

E. Phantom Material Discussion

Various types of commonly used gelling agents used to create phantom tissue materials are discussed in this chapter.

E.1 TX-150 Phantoms

The gelling agent TX-150 is material often used in hospitals for applications in radiology and has the following approximate composition [13]:

Boric Acid	: 33.5%	w/w
Guar Gum	: 35.8%	w/w
Water	: 22.9%	w/w
Polyacrylamide	: 6.7%	w/w
Ester (Triglyceride)	: 1.1%	w/w

The concentration of the gelling agent greatly influences the electrical and thermal properties of these phantoms, which allows a wide range of physical properties to be obtained by simply adjusting the ratio of the TX-150. Similar to many of the other phantom types, the electrical conductivity can be modified by altering the NaCl content and the permittivity can be adjusted by adding aluminium and polyethylene powder. These types of phantoms are good at replicating tissues with high water content such as brain or muscle tissue, but delivers poor results for lower water content tissues such as bone and fat [13]. A sealed TX-150 phantom could preserve its integrity and properties for approximately two weeks if maintained properly. Due to the variation in the gelation time, the gelation parameters such as the temperature and mixing time are difficult to standardize and the dielectric and physical properties change drastically once the gel begins to deteriorate.

E.2 Agar Phantoms

Agar, which is a gelatinous substance attained from certain species of algae and seaweed, is regularly used to fabricate thermal phantoms due to its thermal and physical properties. Agarose (the purified form of agar) phantoms are moulded from a lightly opaque gelatinous substance, which is obtained by heating the agar solution above 85°C before letting the aqueous liquid cool to room temperature. These phantoms are commonly used for replicating biological tissues for applications in the Industrial, Scientific and Medical (ISM) frequency bands such as 435 MHz, 900 MHz and 2.4 GHz [13]. The recipes mainly consist of water and agar (used as a gelling agent), although certain preservatives can be added to alter either the electrical conductivity or the dielectric constant. Once again, polyethylene powder is used as a permittivity modifier and NaCl or polyvinyl chloride (PVC) is used as a conductivity modifier, although the addition of any of the preservatives slightly effects both the permittivity and conductivity of the solution. Thus, the addition of these preservatives should be carefully modulated.

Agar phantoms are not viable models for microwave applications, since their permittivity is lower than those of biological tissue. This limitation can be overcome by adding preservatives such as corn syrup, although this increases the perishability of the model. Graphite is an additive specifically used to regulate the permittivity and electrical conductivity of agar phantoms in the microwave frequency range, which could produce more realistic ultrasound images due to the speckles it creates in the model - similar speckles can be observed in biological tissue. Agar phantoms are among the best characterized models with regards to their optical, thermal, electrical and acoustic modalities, as well as the additives that regulate the appropriate properties at various frequencies and those that provide protection from deterioration.

Heterogeneous agar-based phantoms are favourable candidates for simulating inner tissue surrounded by background tissue, which could be ideal for applications regarding phantom organs with different properties to those of their surrounding material. Agar-based gels also provide phantoms with the desired mechanical strength to construct tissue-mimicking solutions for replicating hard and soft tissues, blood and even vascular systems. Silicon and rubber tubes are often used to simulate blood vessels, which are surrounded by the phantom material. Wall-less vessels can be created due to the relatively high stiffness of the gel and are formed by placing metallic holders around the unhardened solution, which are removed once the gel has set [13].

Apart from its mechanical strength which allows the fabrication of larger models, agar-based gel has a high melting point of approximately 80°C, which is desirable for temperature sensitive applications. Although the characteristics of agar phantoms (such as the permittivity and conductivity) can easily be manipulated independently by adjusting the ingredient ratios, these phantoms remain quite fragile during handling.

E.3 Acrylamide Phantoms

Acrylamide-based polymer phantoms are the most commonly fabricated phantoms utilized in experiments ranging from applications in the radiofrequency and microwave spectrum, to those in the High Intensity Focused Ultrasound (HIFU) range. The properties of the polymers are influenced by frequency and thus different polymer phantoms, such as polyacrylamide (PAA), acrylamide monomer (AA), ammonium presulphate (AMPS) and tetramethyl-ethylene-diamine (TEMED) are used for different sections of the frequency spectrum. Similar to TX-150 phantoms, the ratio of ingredients and gel constituents have a significant influence on the dielectric properties of the phantom - a lower NaCl content can be used to simulate tissues with reduced conductivity and low permittivity or non-polar liquids (such as ethylene glycol) can be used instead of water to reduce the permittivity of the phantom. Another example is the negative correlation between the AA concentration and the permittivity and electrical conductivity of the phantom, and its positive correlation with the phantom's mechanical strength [13].

Polymer phantoms are mostly used for HIFU applications, but their dielectric properties could be modified to suit those needed for radiofrequency experiments. RF polymer phantoms require higher MBAA and AA concentrations than those used in HIFU phantoms, in order to maintain their structural integrity without cracking whilst electrodes are inserted into the model and to enable the gel to harden in the selected shape. The mechanical properties of PAA-based gels make them suitable candidates for creating heat sensitive vascular-mimicking models with thin-wall vessels, which are fabricated with silicon-based gel and thermal sensitive powder. This gel is often favoured in simulating low conductivity and permittivity tissues such as bone and fat, as well as high water content tissues such as brain matter and muscle, due to its high melting point, optical transparency, facile formability, mechanical properties and ability to replicate a wide range of acoustic, thermal and electric properties [13]. The downside of these phantoms are their limited lifespan, which ranges from a few hours to a few weeks (if maintained properly) and the toxicity of the model constituents, for instance acrylamide monomer, which is a severe neurotoxin. The polymerization of acrylamides also causes exothermic reactions which causes the temperature to rise rapidly and thus the mixing, casting and degassing time of the unpolymerized solution is limited to approximately thirty seconds.

E.4 Hydroxyethyl Cellulose Phantoms

Hydroxyethyl cellulose (HEC) is a gelling agent first used by Hartsgrove et al [41] in 1987 to develop phantoms for hyperthermia and electromagnetic dosimetry applications. The substance,

which is derived from cellulose, is often used to thicken solutions and HEC-based phantoms usually have fairly straightforward recipes. Primarily, these phantoms consist of water, HEC, NaCl and sugar (which are respectively used to increase and reduce the electrical conductivity of the phantom). Preservatives can be added to slow the deterioration of the model and if water evaporation prevention techniques are applied, the model can be preserved for approximately one year [13]. These models are easily fabricated and offer long-term stability, although their optical, acoustic and thermal stability and properties still need to be characterized.

E.5 Gelatin Phantoms

Gelatin is a biocompatible mixture of proteins and peptides, which is produced through the thermal, chemical or physical degradation process of collagen. The collagen used to create gelatin is acquired from the bone, cartilage, skin, intestines and tendons of animals, which gives gelatin its non-immunogenic and biodegradable properties. It is also commercially available at low cost and has a biological origin, which makes it ideal for pharmaceutical and medical applications. Gelation occurs at temperatures below 40°C due to the conformational disorder-order transition of the gelatin chains, which is why these phantoms are often used to simulate human tissue at lower temperatures and frequencies. Gelatin-based phantoms can suitably replicate both low- and high-water content tissues at various frequencies, due to its desirable physical, thermal and dielectric properties [13].

Similar to agar, gelatin is able to fabricate heterogeneous phantom materials which offers long-term stability of mechanical and physical properties. Various human tissues have been simulated with gelatin phantoms, including the breast, prostate, hepatic tissue, rectum, fat, urethra, cancerous lesions, tumors and muscle. NaCl can be used to alter the electrical conductivity of gelatin-based heterogeneous phantom materials at frequencies lower than 1 GHz, whereas the oil ratio has an effect on both the electrical conductivity and permittivity at higher frequencies, due to the higher conductivity of water at these frequencies. Similar to HEC-phantoms, gelatin-based phantoms are easily fabricated and offer long-term stability at low cost. Dielectric properties can be modified by the addition of ethane-diol and polyethylene powder, whereas honey syrup acts as preservative to slow deterioration and graphite powder can be used to alter the mechanical and physical properties of the model [13]. Gelatin phantoms are limited by their low melting temperatures and low mechanical strength, especially at temperatures above 50°C. Although constituents such as formaldehyde may be added to improve the mechanical and thermal properties of the solution, the properties of the resulting material may still be less desirable than those of agar or acrylamide phantom models.

E.6 Gellan Gum Phantoms

Gellan gum is a linearly structured extracellular polysaccharide with repeating units of tetra-saccharide, which is secreted by microorganisms (Sphingomonas Elodea). The gum was first used to produce phantom materials for electromagnetic investigations in 1995 and has since been altered for fabricating phantoms for HIFU experimentation, where gel strength is increased by the addition of calcium chloride dehydrate and potassium sorbate is used as preservative. A gelatinous substance can be acquired from low concentrations of gellan gum (approximately 0.01% w/w) and it provides a moderately transparent homogeneous material, which is stable at high temperatures (approximately 95°C). If needed, alumina powder can be added to reduce the homogeneity of the material. The thermal and acoustic properties of these phantoms are greatly dependent on the construction protocol and thus it is difficult to reproduce results, which in turn complicates the process of characterizing these phantoms [13].

E.7 Carrageenan Phantoms

Carrageenan is a natural polymeric substance which is extracted from red algae and refined to a gelling agent, as was done for the first time in 2003 by Yoshimura et al [42] for MRI applications. Various salt formulations (KCl, CaCl and NaCl) can be used as additives to modify the gel strength, elastic modulus and melting temperature – NaCl also prompts a linear increase in permittivity and conductivity, whilst GdCl and agarose also have a slight effect on these parameters. A positive correlation between the applied frequency and the dielectric properties of the phantom material exists between 5 to 130 MHz [13]. Carrageenan is sometimes preferred over agar, due to its resistance to cracking and superior elasticity, which removes the need for reinforcing materials and simplifies the sculpting process of the model. If water loss prevention techniques are applied, these phantoms could retain their properties for a few weeks. However, liquefaction can occur at low temperatures (approximately 60°C) and the electrical properties of these phantoms are difficult to manipulate.

E.8 Alginate Phantoms

Alginate is a copolymer that forms a gelatinous substance when introduced to chemicals such as barium, strontium or calcium. It is extracted from brown seaweed as a polysaccharide with D-mannuronic acid (M) and L-guluronic acid (G), which prompts gelation when the G-blocks start binding to each other. Thus, the length of the G-blocks, their molecular weight and the overall G content regulates the mechanical properties of alginate phantom materials. This material has been used for applications in LIT experiments and to simulate breast tumor tissue. Alginate phantoms have desirable optical and mechanical properties with thermal stability for high-temperature experimentation, although they tend to produce heterogeneous models. However, more uniform substances can be obtained by adding constituents such as CaCl, which decreases the gelation rate. The molar ratio of $CaCO_3$:$CaSO_4$, the polymer concentration, calcium content and temperature can also be used to adjust the gelation rate [13].

F. Additional Phantom Material Characteristics and Trends

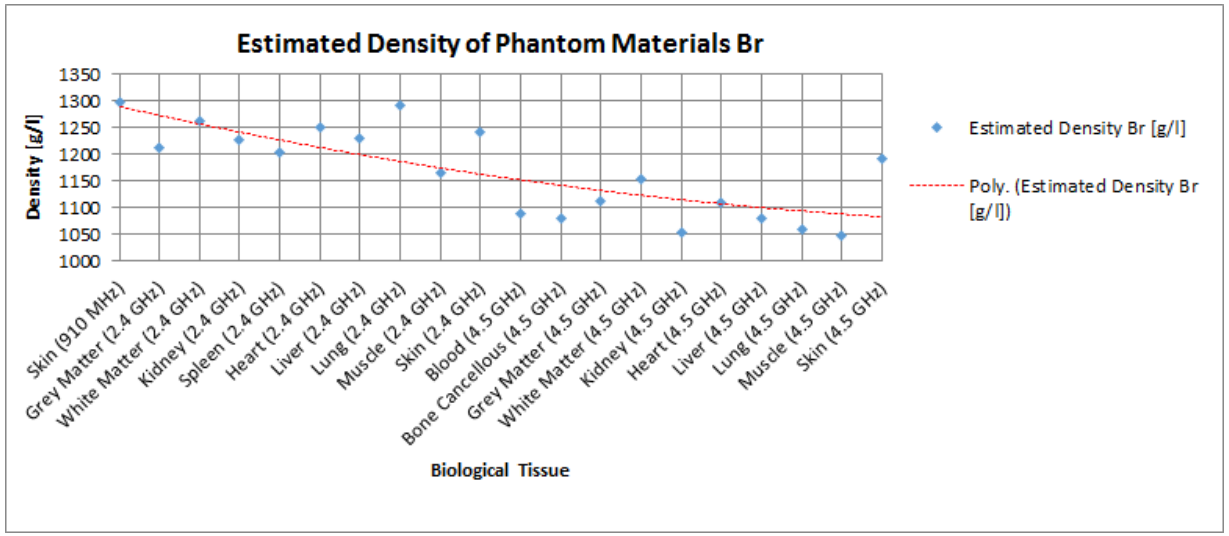

Figure 104: The estimated density of the rhinoceros phantom materials at the specified frequencies.

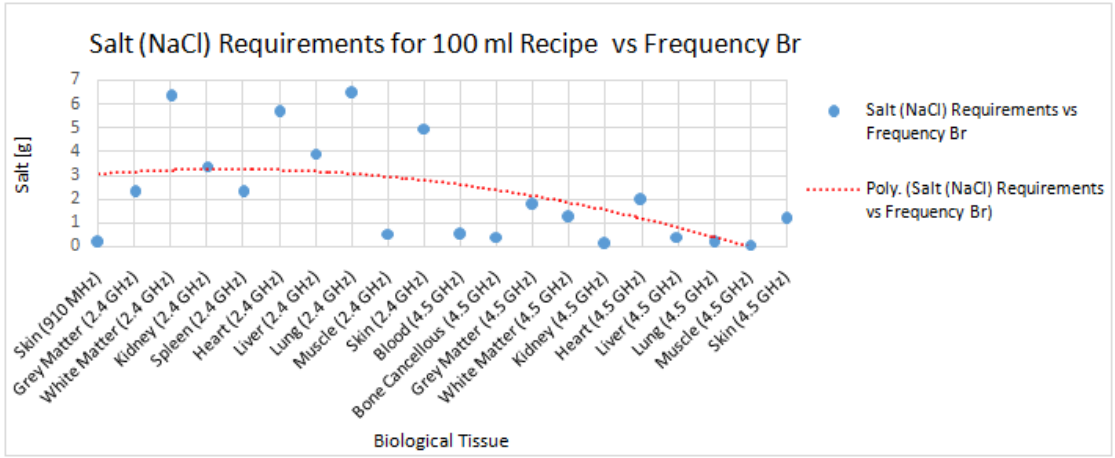

Figure 105: Salt requirements for the 100 ml alternative recipes for the specified frequencies.

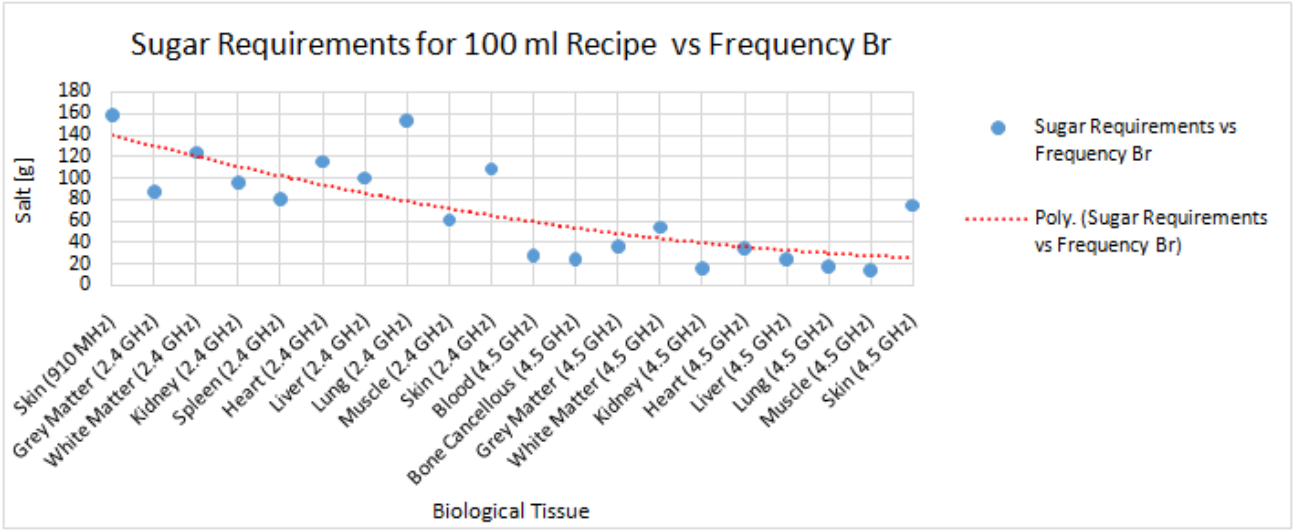

Figure 106: Sugar requirements for the 100 ml alternative recipes for the specified frequencies.

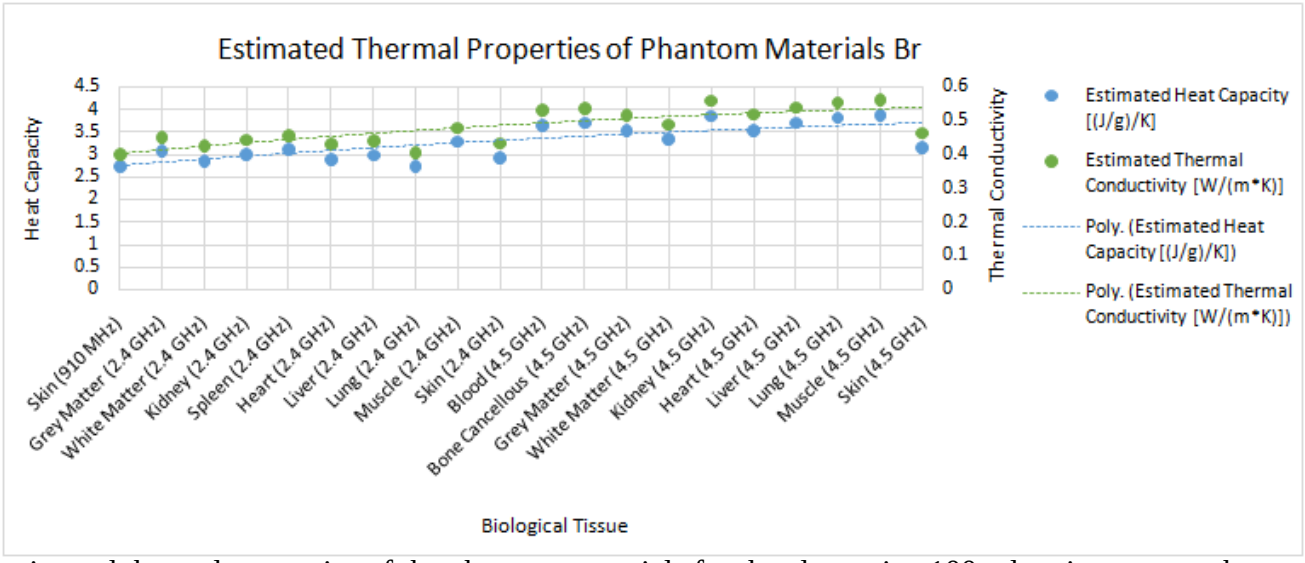

Figure 107: The estimated thermal properties of the phantom materials for the alternative 100 ml recipes across the specified frequencies.

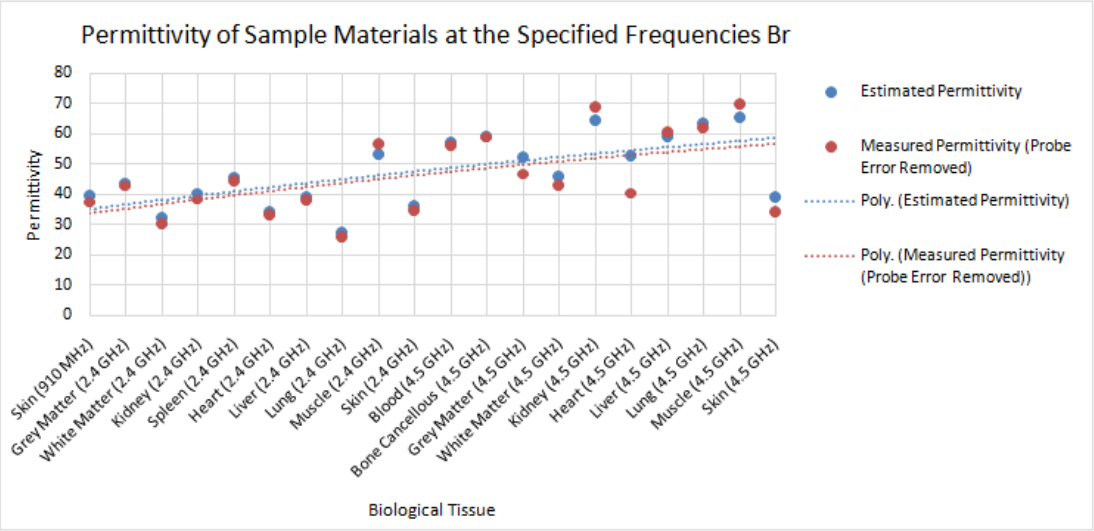

Figure 108: The permittivity of the sample materials for the alternative 100 ml recipes across the specified frequencies.

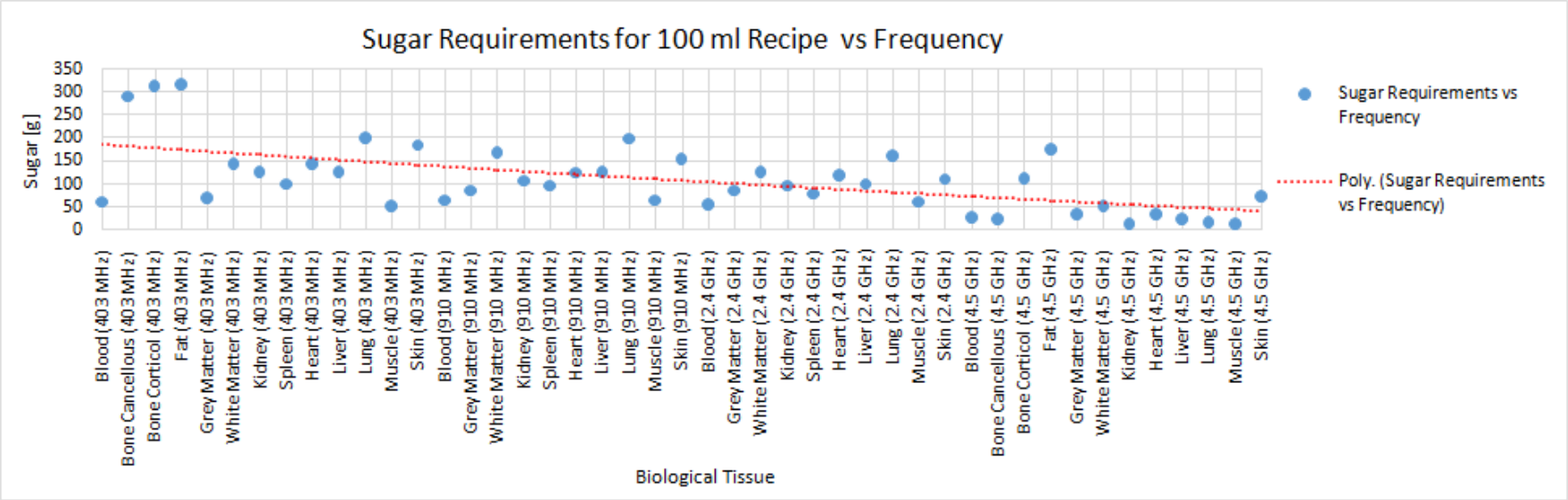

Figure 109: Sugar requirements for the 100 ml recipes for the specified frequencies.

G. Simulation Model Radiation Patterns

This chapter illustrates the radiation patterns of the antennas embedded within the rhinoceros flank and cylindrical models.

G.1 Rhinoceros Flank Model Radiation Patterns

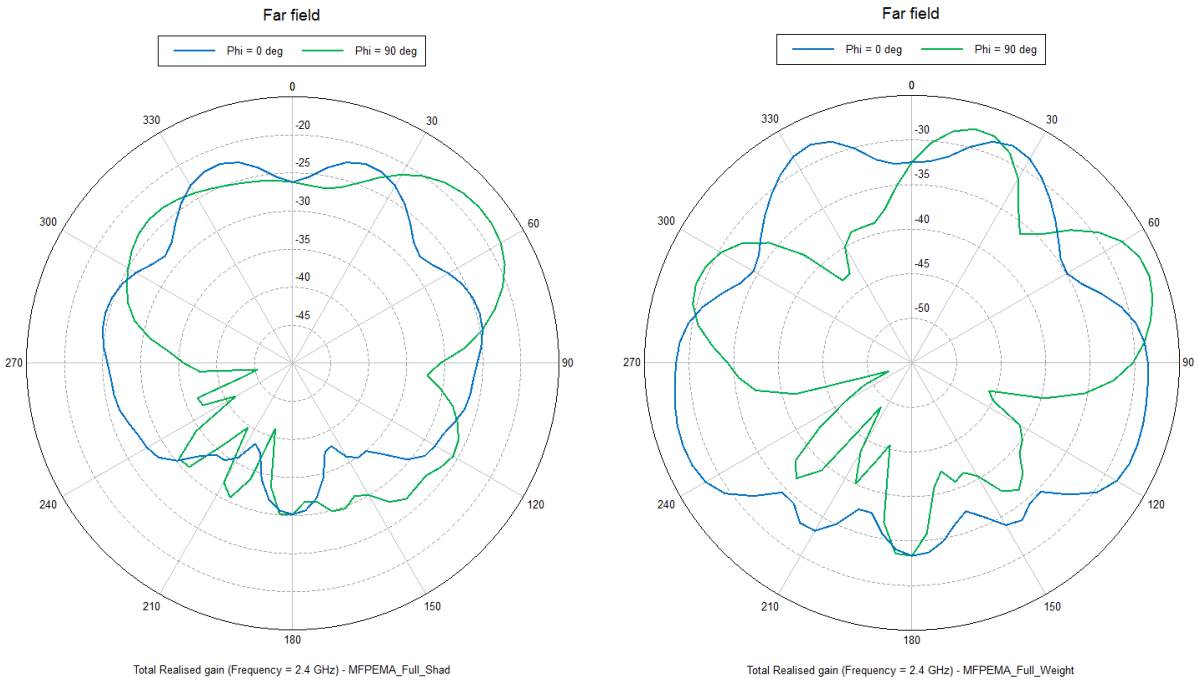

Figure 110: Realised gain of the embedded MFPEMA: Shadwick model (left) and weighted average model (right).

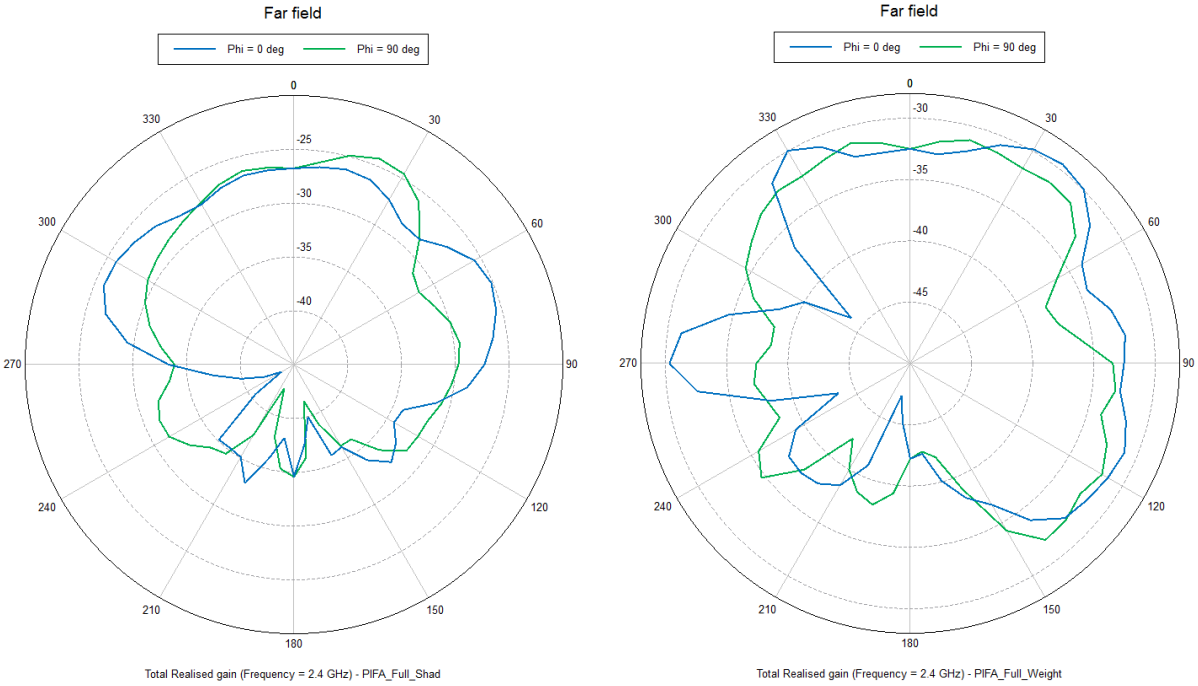

Figure 111: Realised gain of the embedded PIFA: Shadwick model (left) and weighted average model (right).

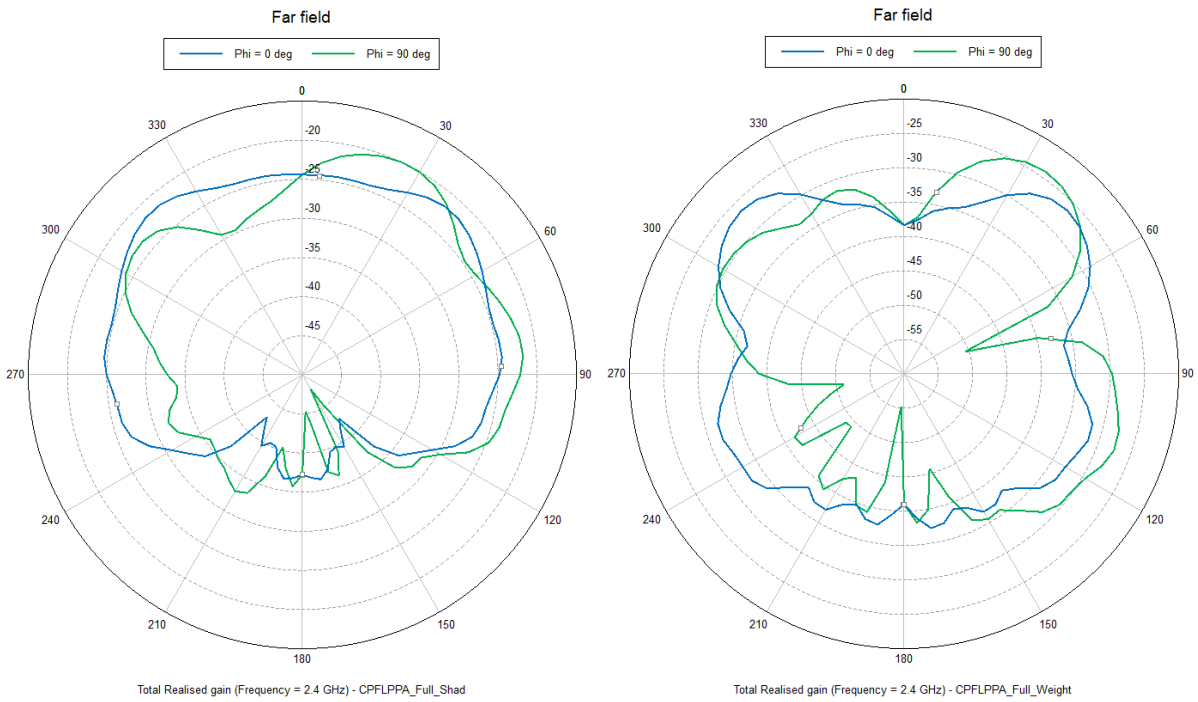

Figure 112: Realised gain of the embedded CPFLPPA: Shadwick model (left) and weighted average model (right).

G.2 Cylindrical Phantom Model Radiation Patterns

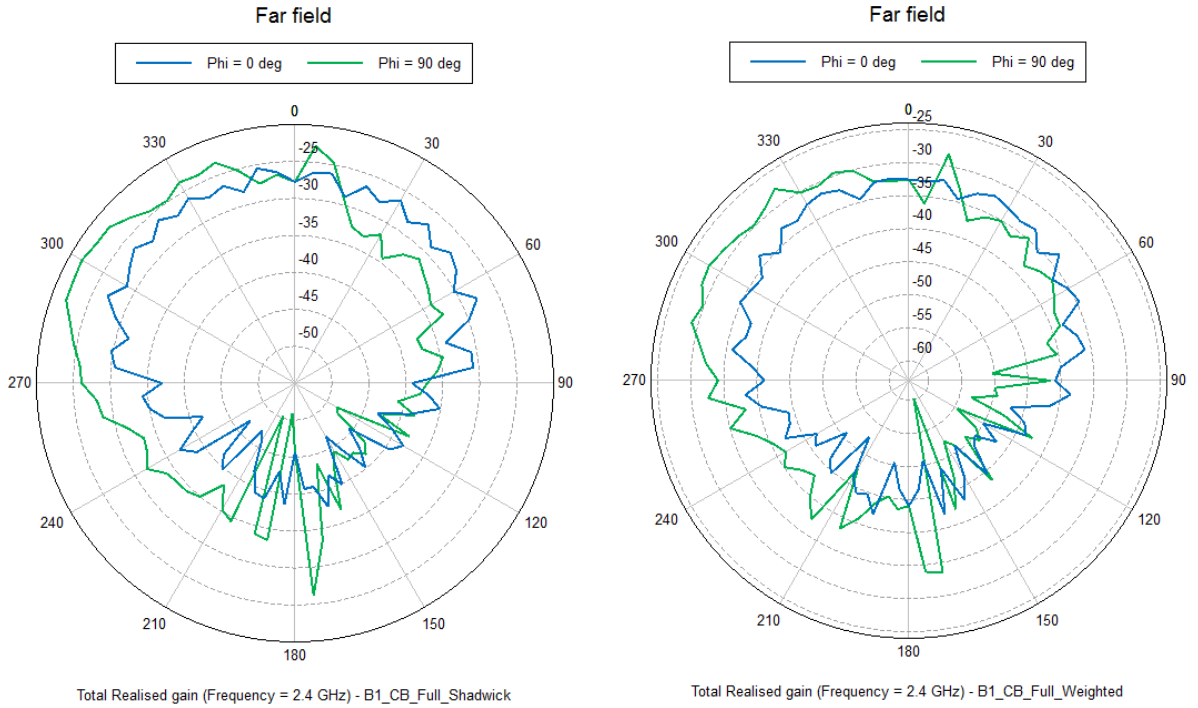

Figure 113: Realised gain of the embedded MFPEMA [Back]: Shadwick model (left) and weighted average model (right).

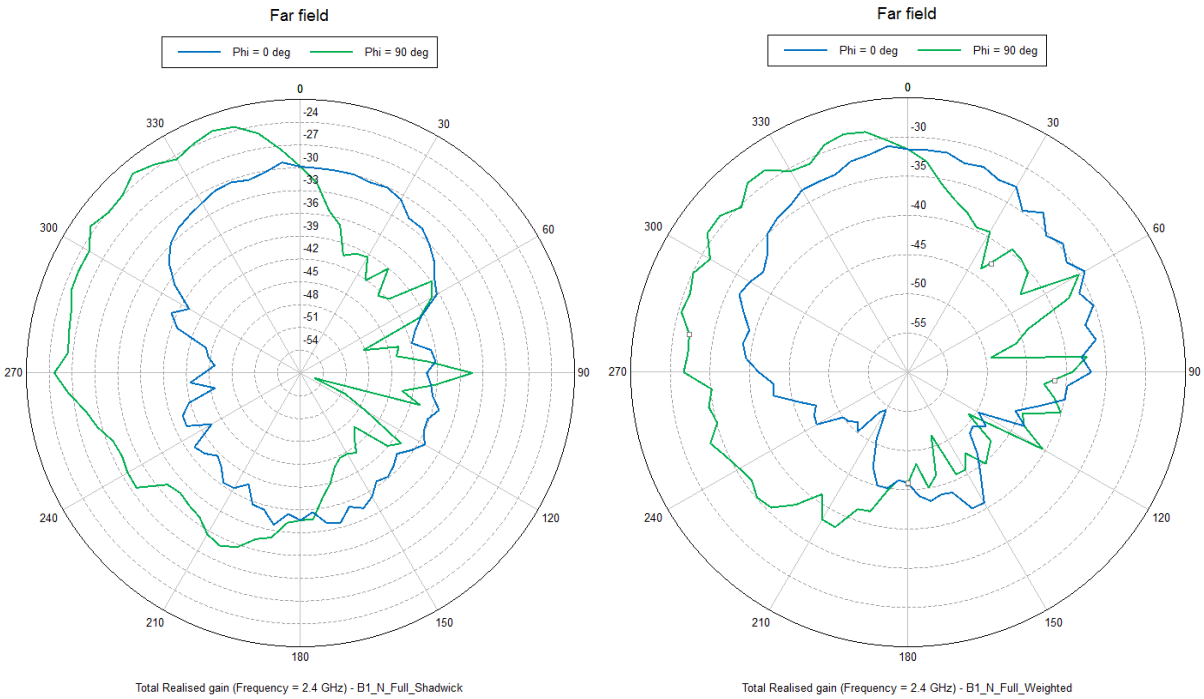

Figure 114: Realised gain of the embedded MFPEMA [Neck]: Shadwick model (left) and weighted average model (right).

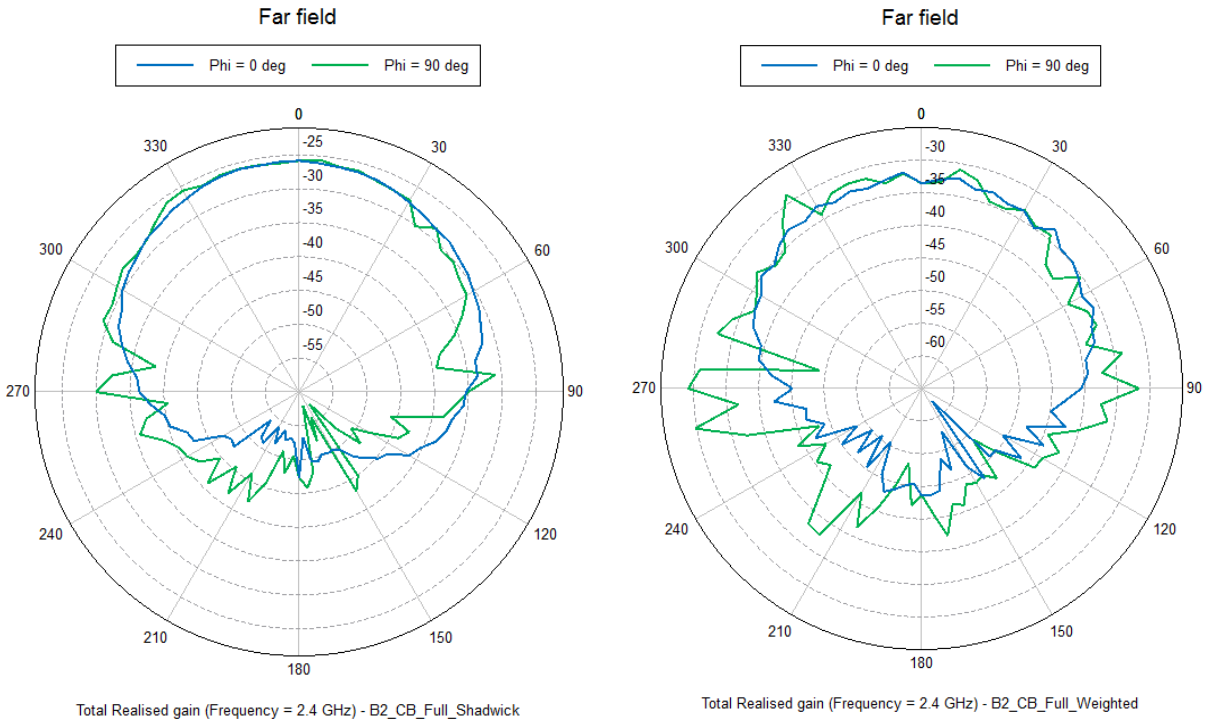

Figure 115: Realised gain of the embedded PIFA [Back]: Shadwick model (left) and weighted average model (right).

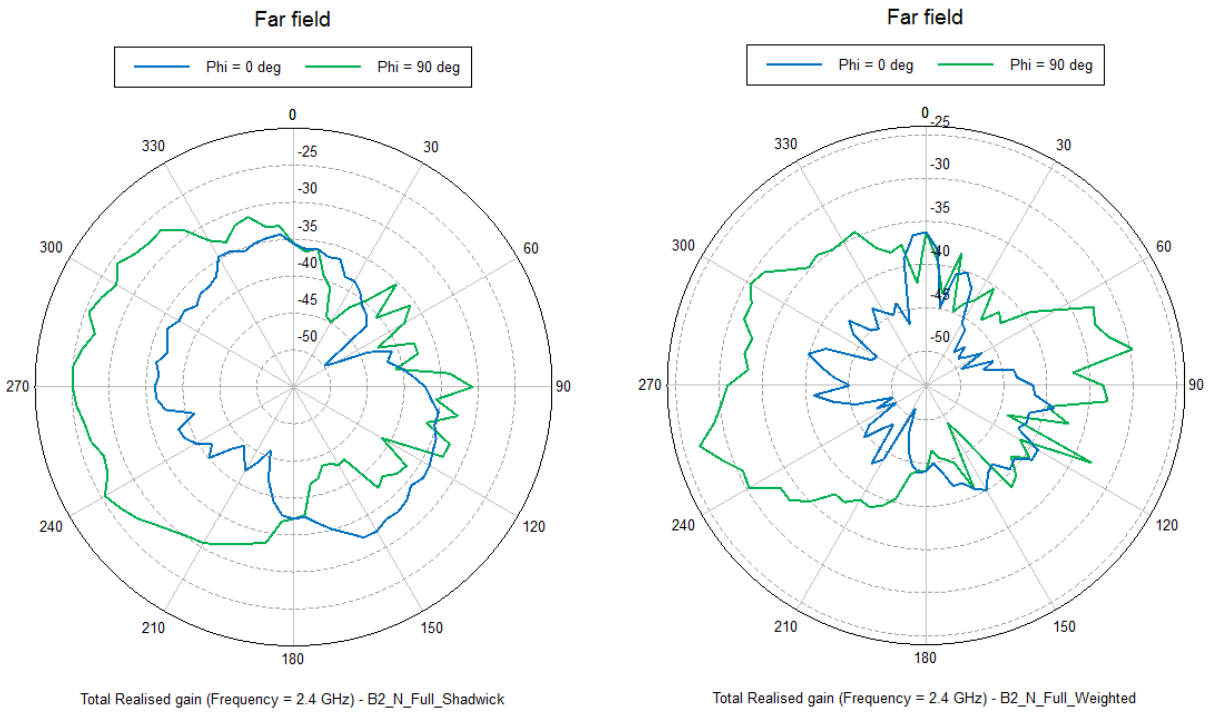

Figure 116: Realised gain of the embedded PIFA [Neck]: Shadwick model (left) and weighted average model (right).

H. Directional Realised Gain of the Rhinoceros Model

This chapter illustrates the directional gain of the MFPEMA and PIFA as they propagate through the anatomical rhinoceros phantom model.

H.1 Back Implantation

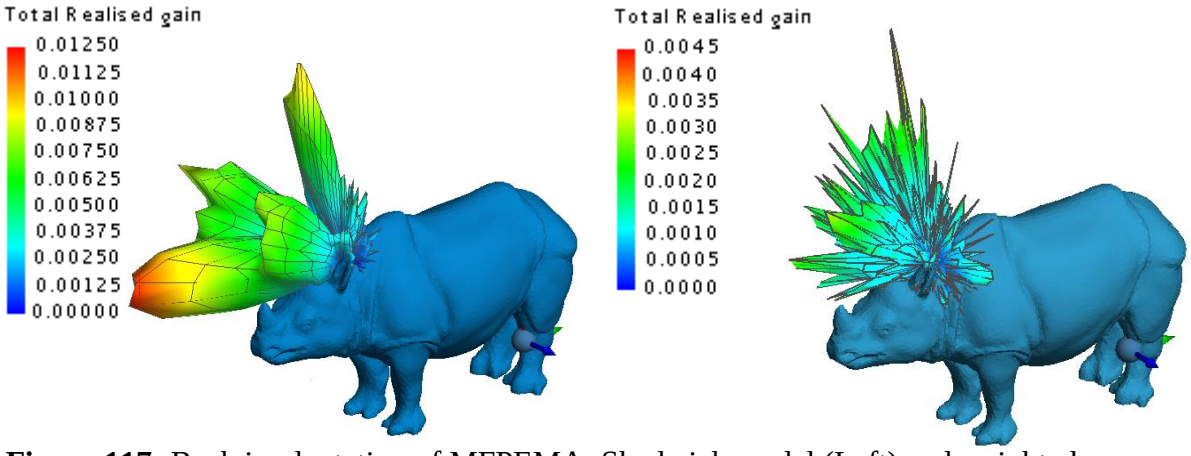

Figure 117: Back implantation of MFPEMA: Shadwick model (Left) and weighted average model (Right).

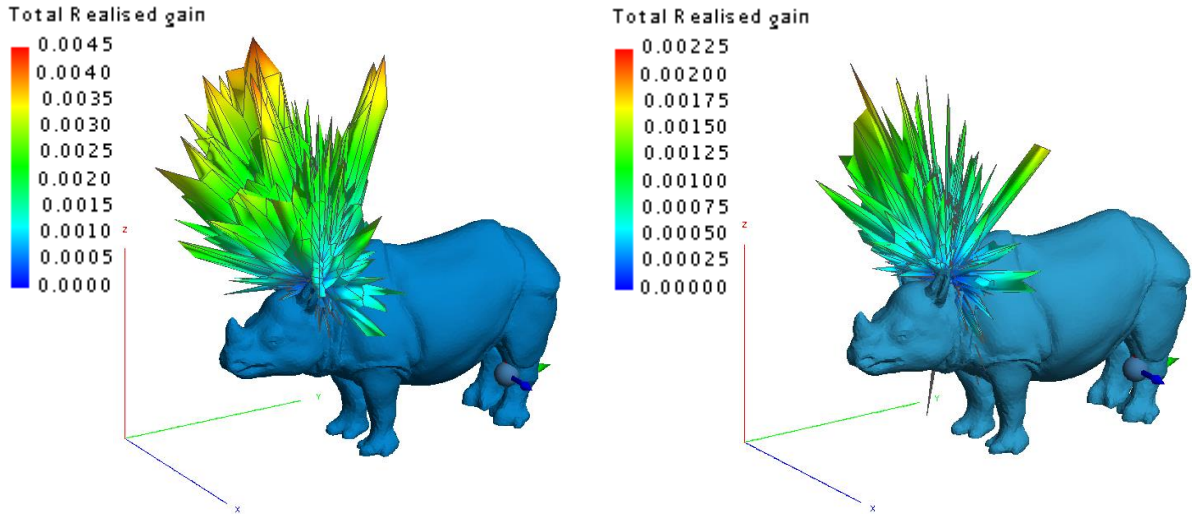

Figure 118: Back implantation of PIFA: Shadwick model (Left) and weighted average model (Right).

H.2 Chest Implantation

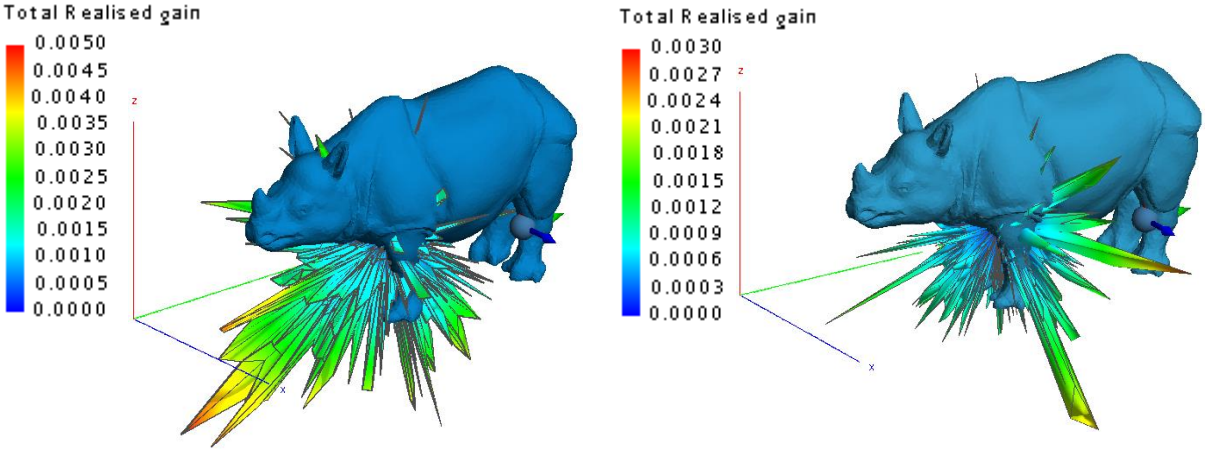

Figure 119: Chest implantation of PIFA: Shadwick model (Left) and weighted average model (Right).

H.3 Neck Implantation

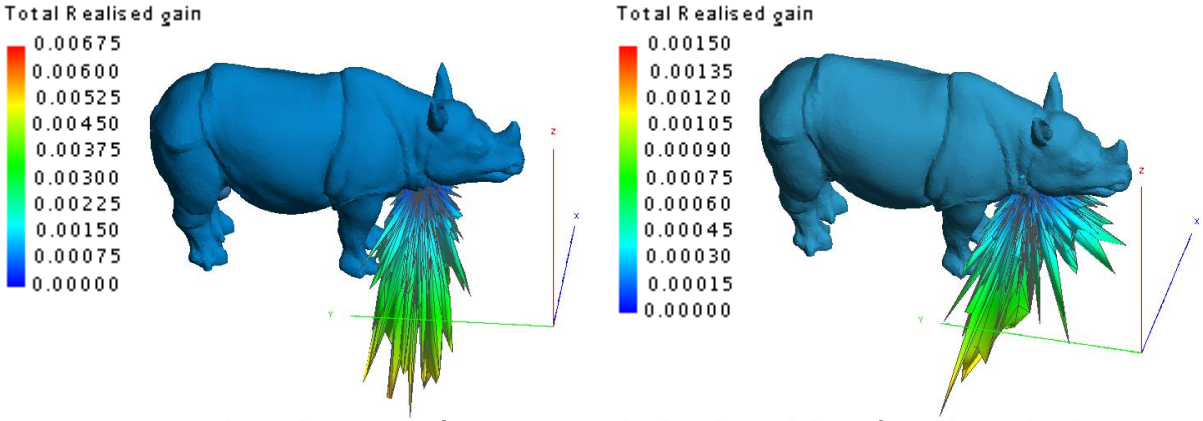

Figure 120: Neck implantation of MFPEMA: Shadwick model (Left) and weighted average model (Right).

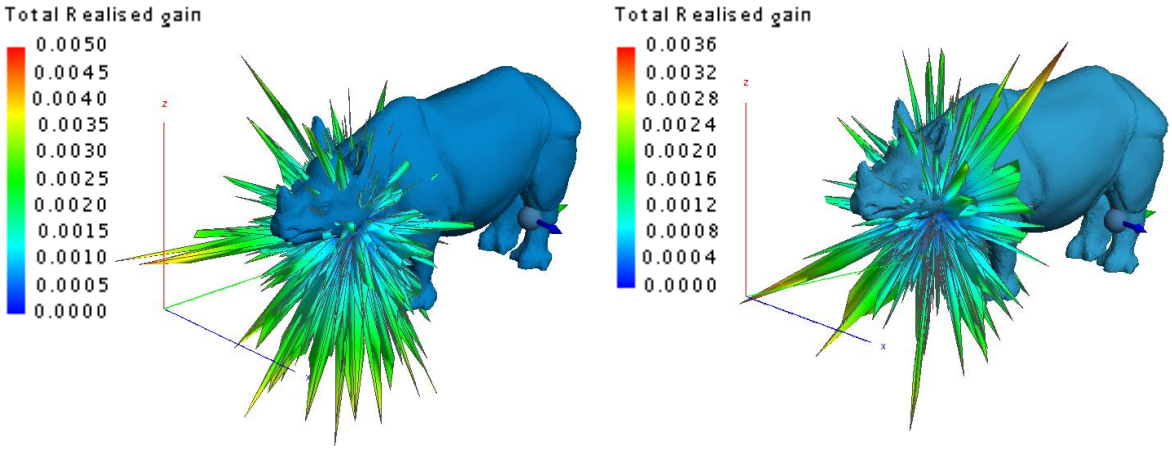

Figure 121: Neck implantation of PIFA: Shadwick model (Left) and weighted average model (Right).

I. List of External Media

This chapter lists the external media submitted with this document. The list is as follows:

1. MATLAB scripts for dielectric property conversion.

2. "External1":
    - 2.1 Characteristics of animals similar to rhinoceroses.
    - 2.2 Characteristics of the selected antennas.
    - 2.3 Popular and suggested phantom material gelling agent recipes.
    - 2.4 Recipe ratio parameters.
    - 2.5 Additional simulation results: Rhinoceros flank model.
    - 2.6 Challenges and risk factors.
    - 2.7 Decision matrix criteria.
    - 2.8 Frequency Bands Available in Europe and the United States.
    - 2.9 IEEE Standards for Maximum Permissible Exposure (MPE).
    - 2.10 FCC Standards for Maximum Permissible Exposure (MPE).
    - 2.11 Mechanical and Dielectric Properties of Porcine, Ovine and Sea Lions.

3. Additional Illustrations of the computer simulation models.
4. Permittivity graphs of the agar samples.

J. Permittivity Measurements of the 403 MHz, 910 MHz and 4.5 GHz Recipes

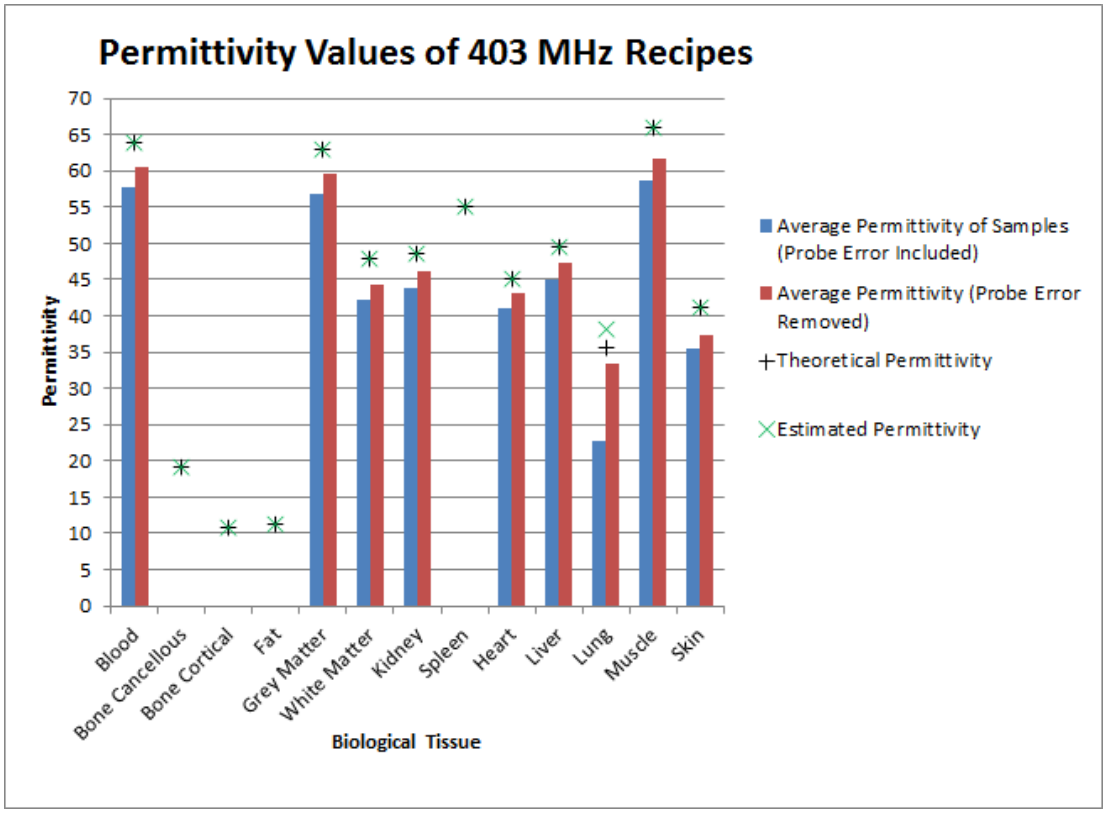

Figure 122: Measured permittivity values of the 403 MHz recipes.

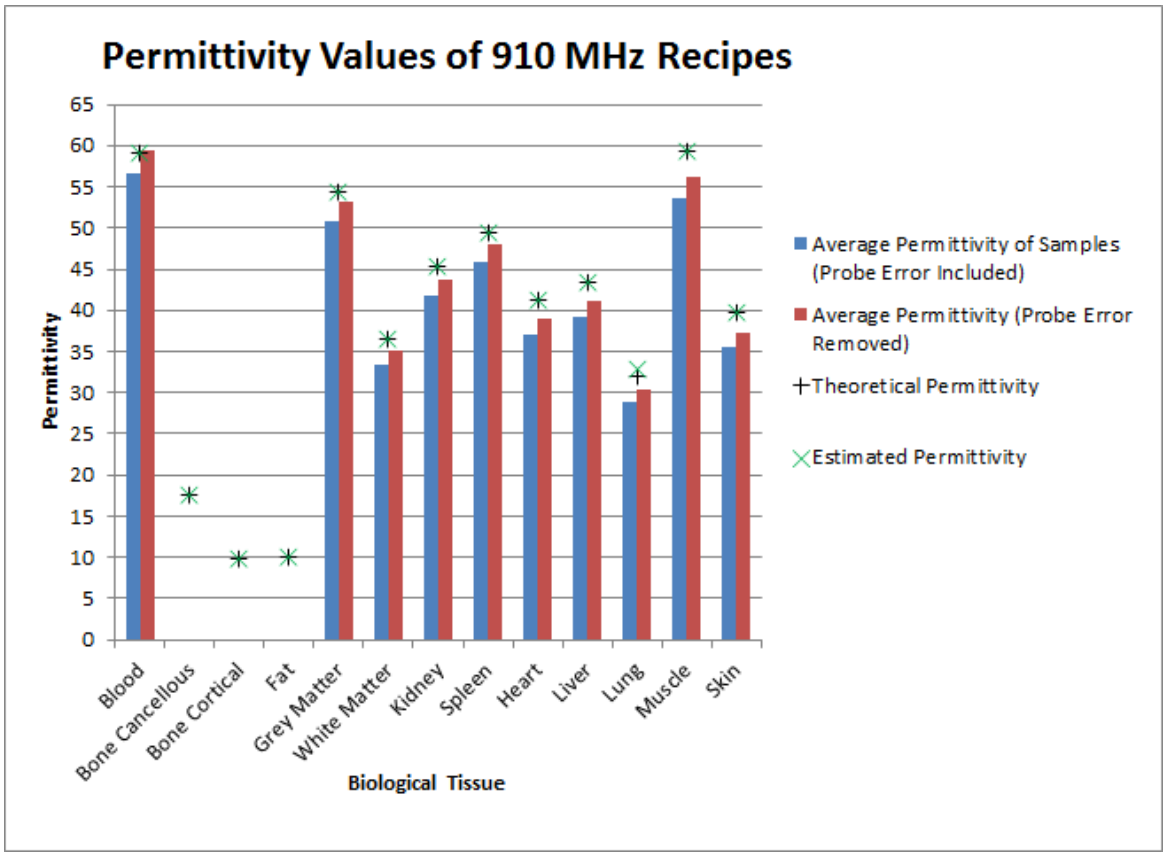

Figure 123: Measured permittivity values of the 910 MHz recipes.

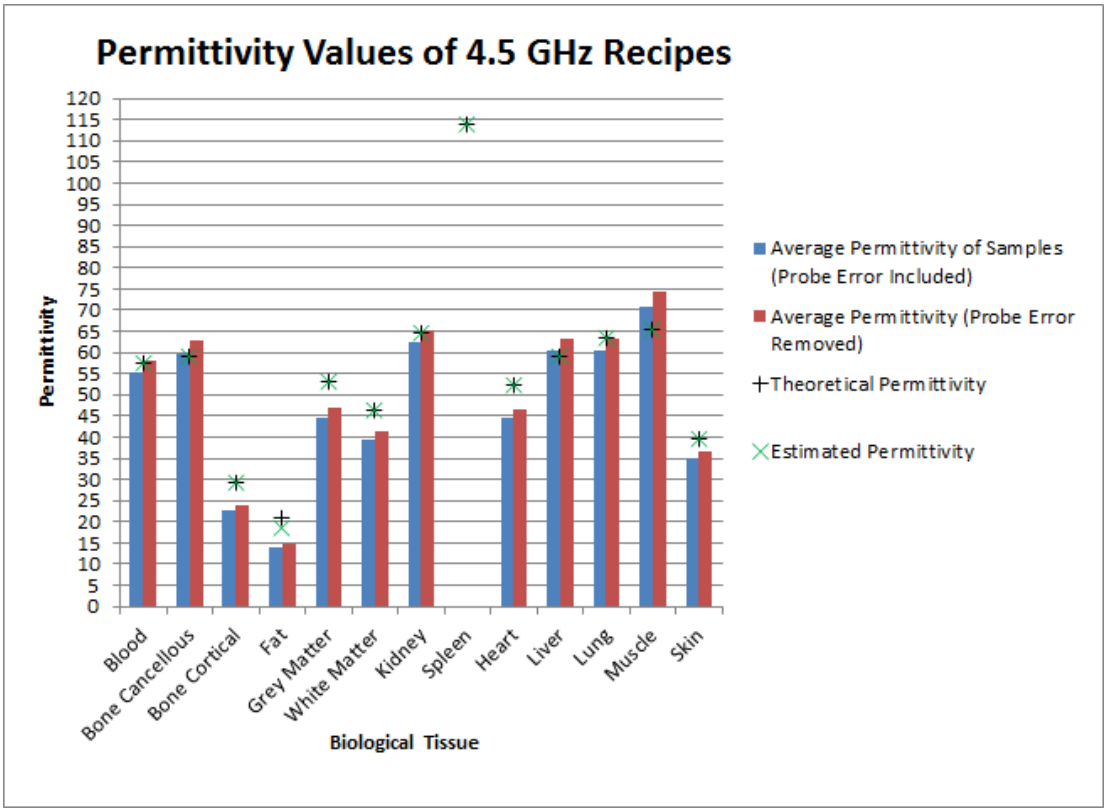

Figure 124: Permittivity values of the 4.5 GHz recipes.

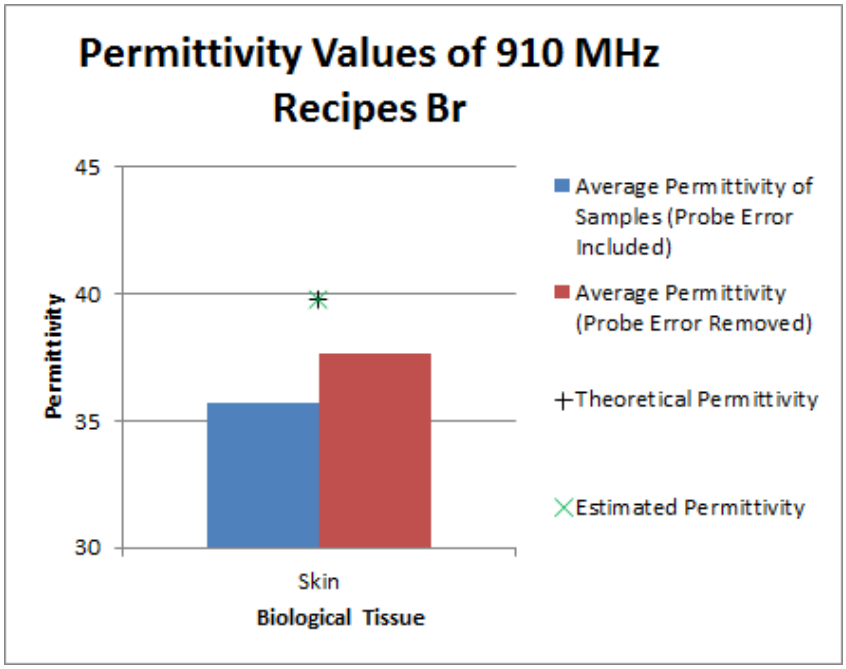

Figure 125: Permittivity values of the 910 MHz closest point polynomial regression recipes.

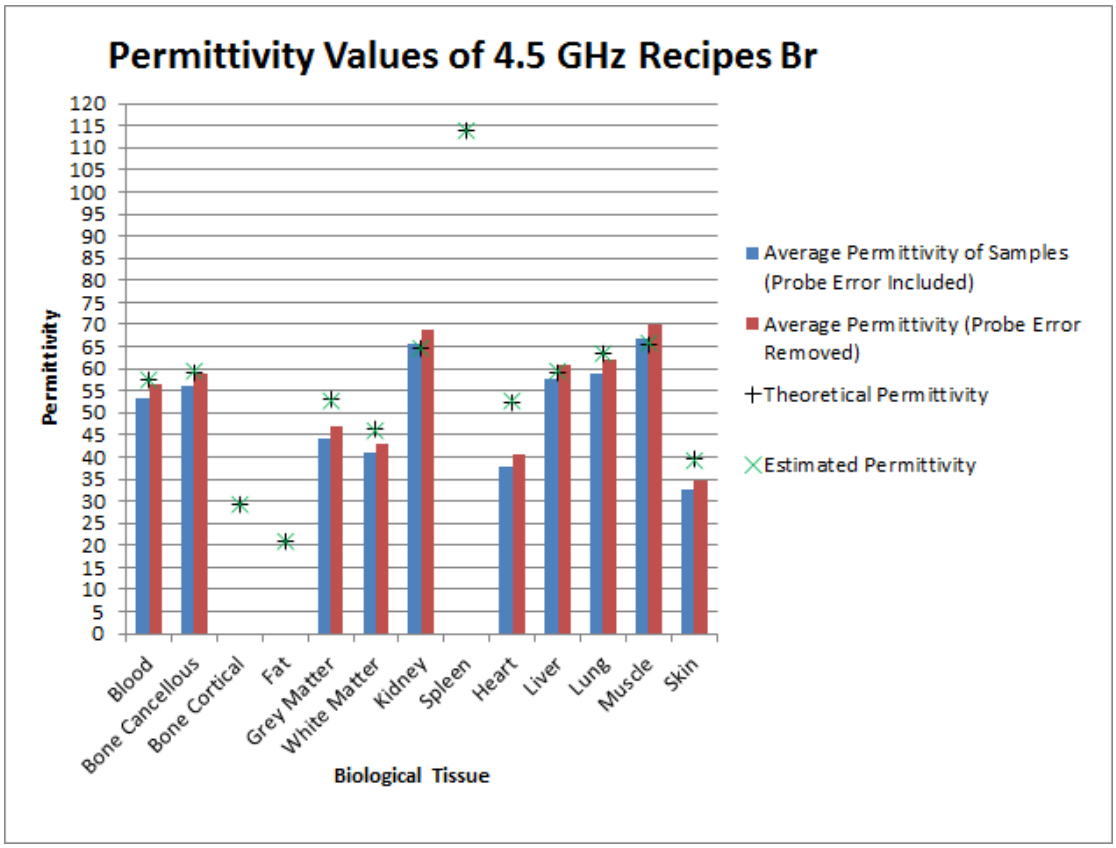

Figure 126: Permittivity values of the 4.5 GHz closest point polynomial regression recipes.

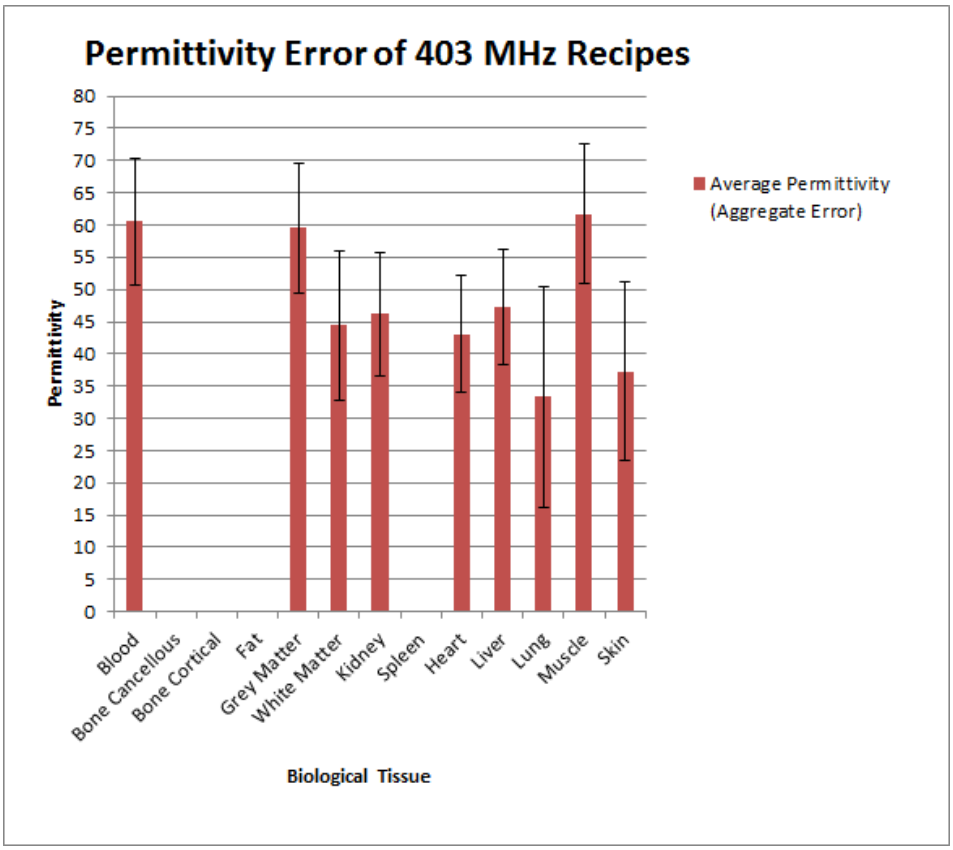

Figure 127: Permittivity error of the 403 MHz recipes with aggregate error margins.

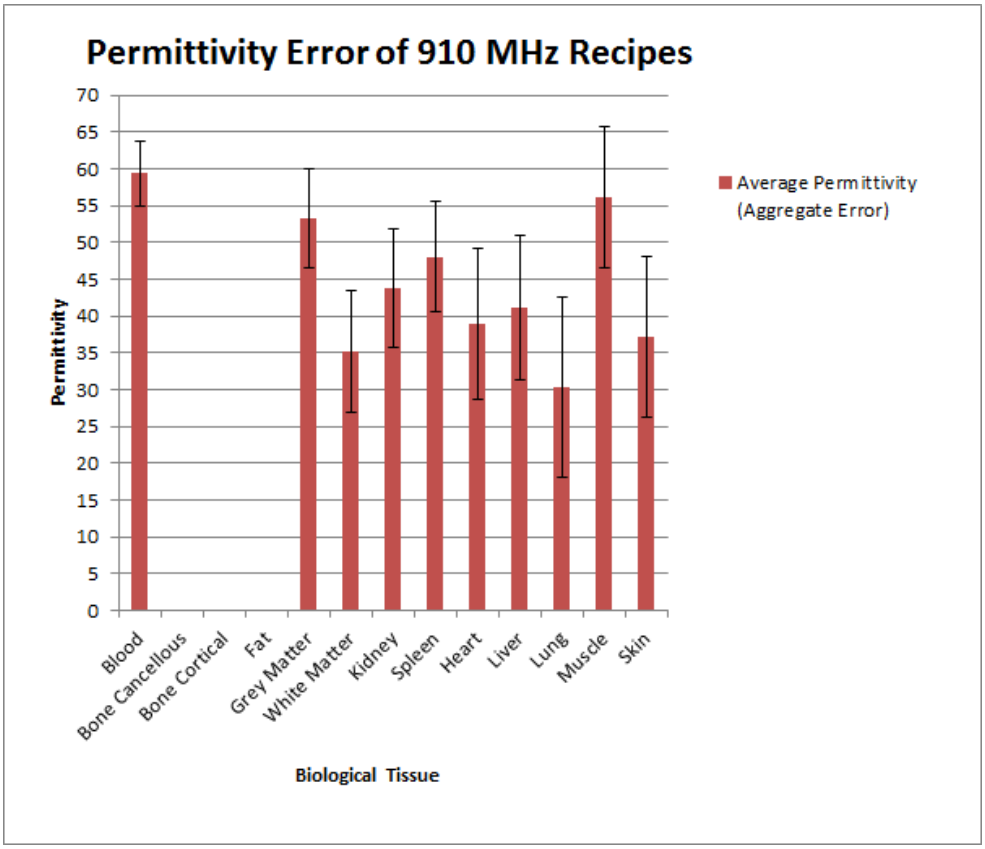

Figure 128: Permittivity error of the 910 MHz recipes with aggregate error margins.

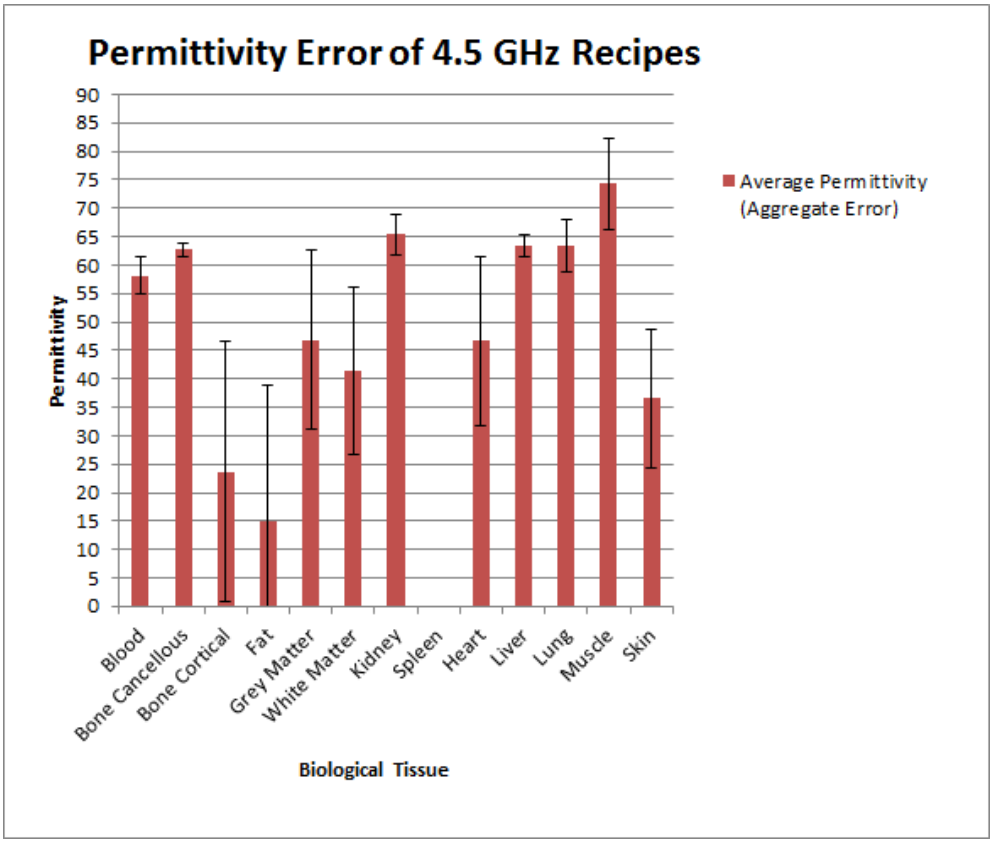

Figure 129: Permittivity error of the 4.5 GHz recipes with aggregate error margins.

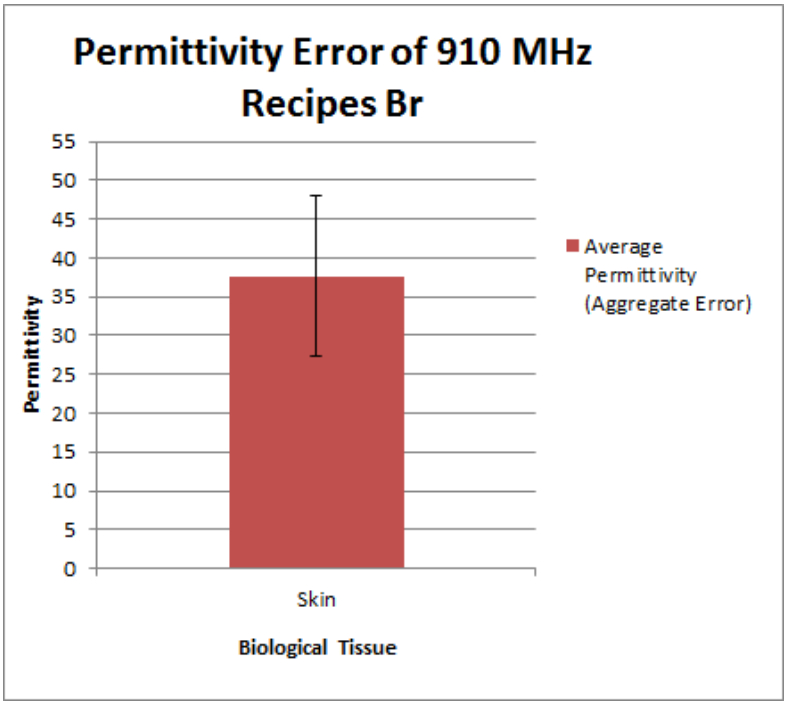

Figure 130: Permittivity error of the 910 MHz closest point polynomial regression recipes with aggregate error margins.

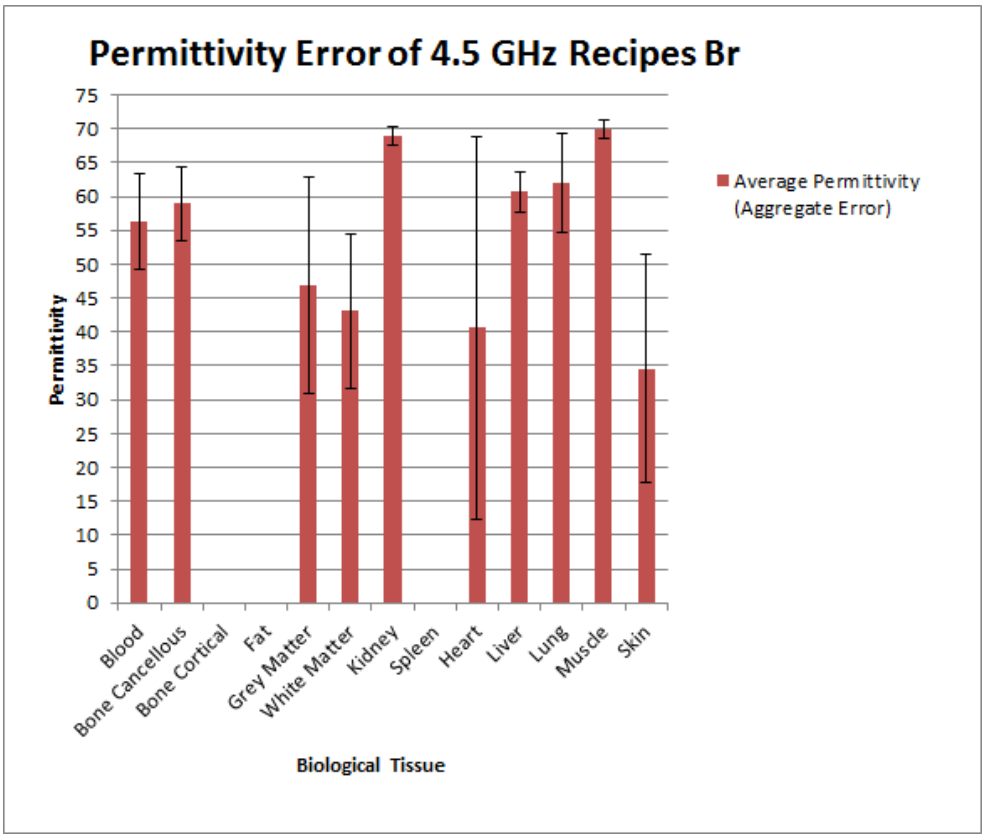

Figure 131: Permittivity values of the 4.5 GHz closest point polynomial regression recipes with aggregate error margins.

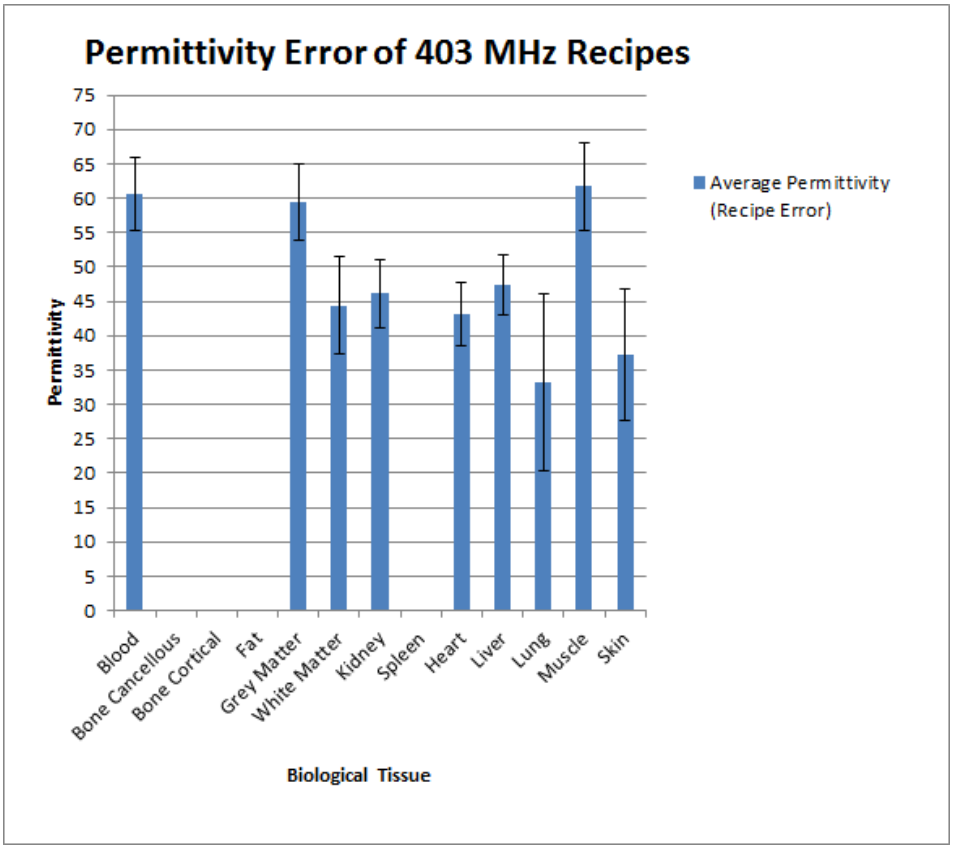

Figure 132: Permittivity error of the 403 MHz recipes with recipe error margins.

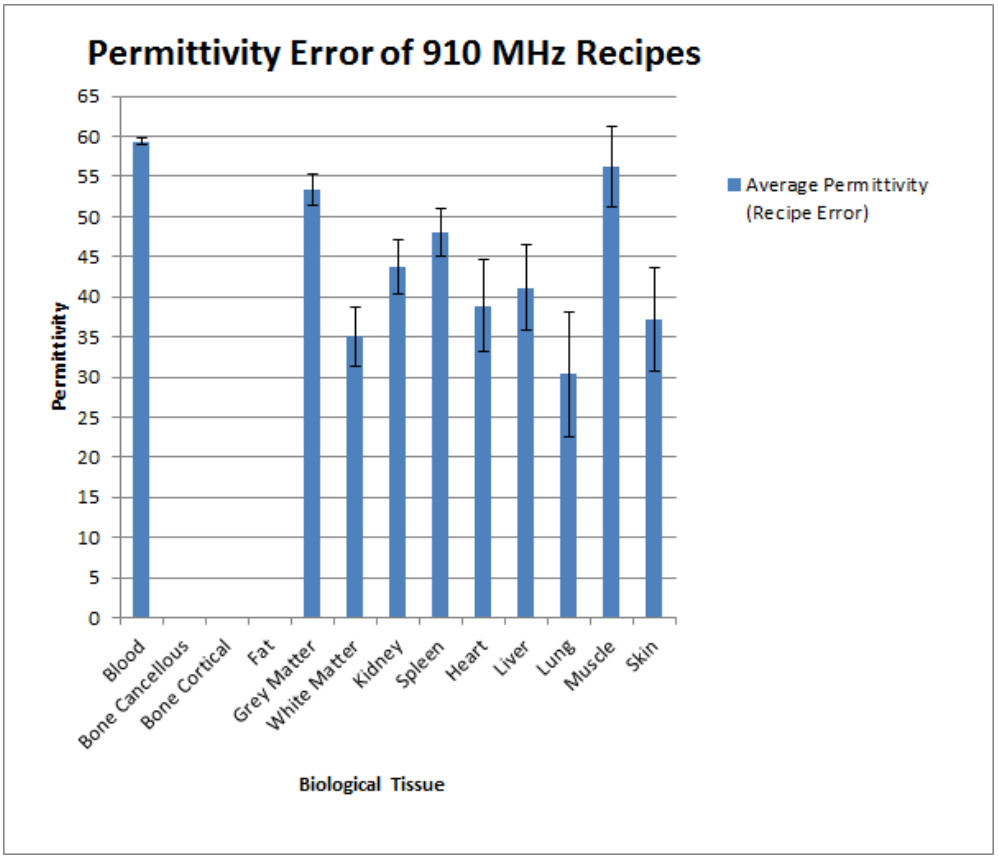

Figure 133: Permittivity error of the 910 MHz recipes with recipe error margins.

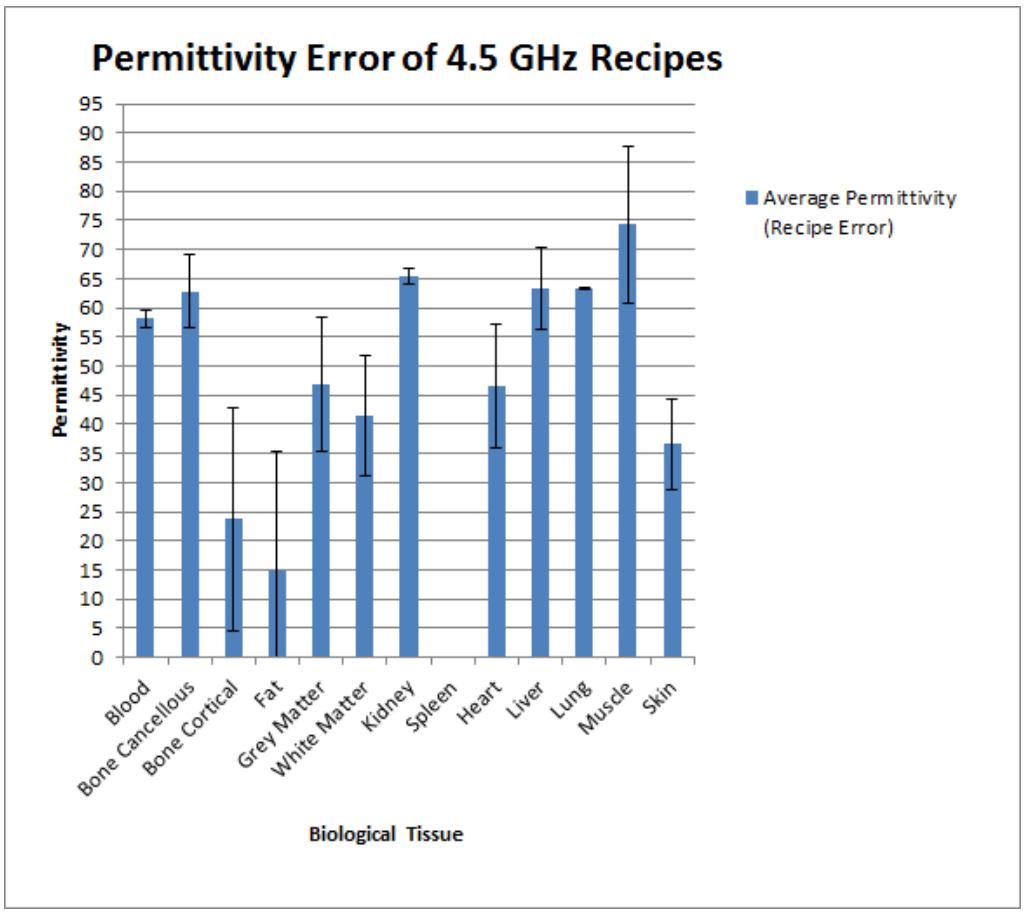

Figure 134: Permittivity error of the 4.5 GHz recipes with recipe error margins.

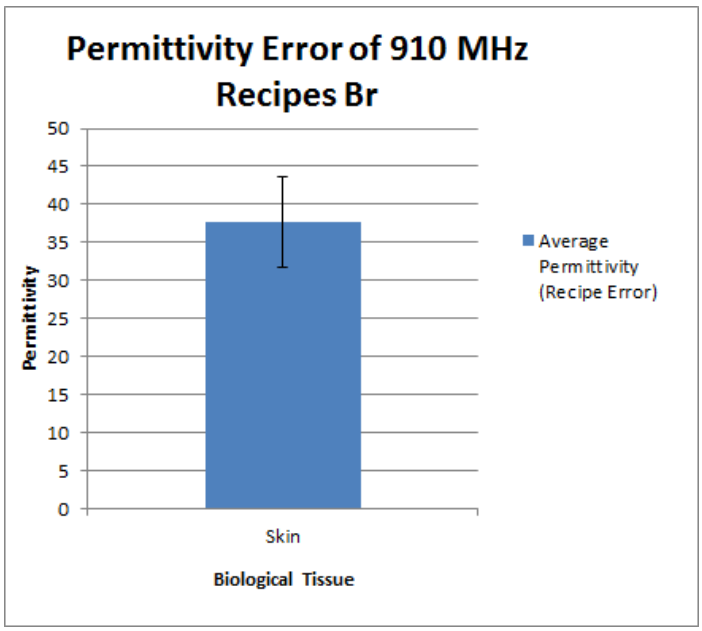

Figure 135: Permittivity values of the 910 MHz closest point polynomial regression recipes with recipe error margins.

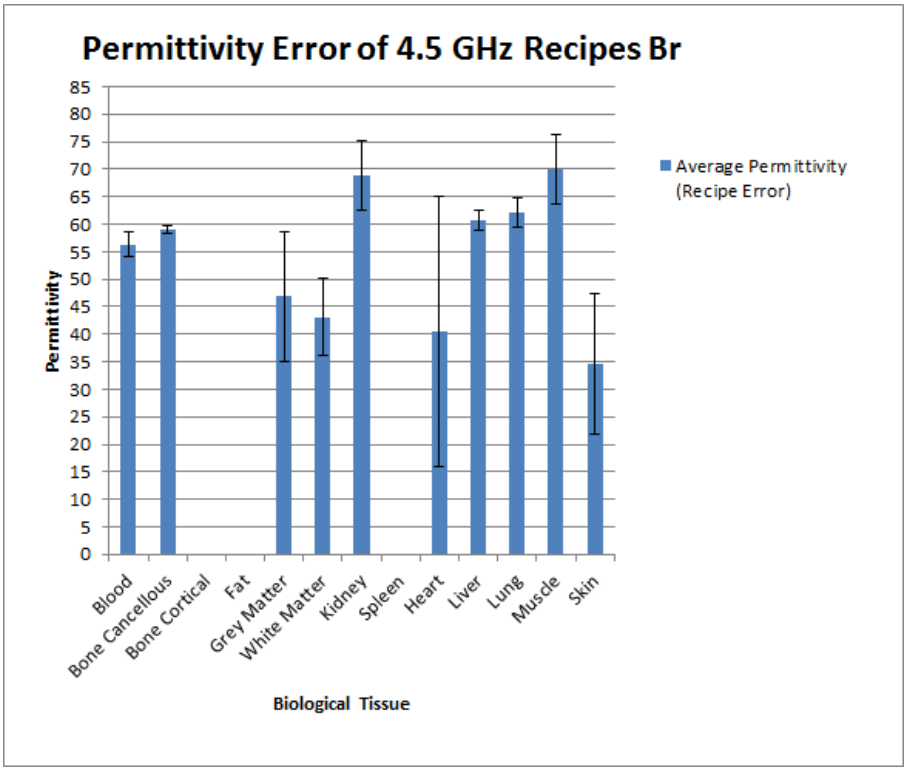

Figure 136: Permittivity values of the 4.5 GHz closest point polynomial regression recipes with recipe error margins.

K. Decision Matrix and Similarity Criteria

Table 38 was used to formulate the respective contributions of each animal's relevance to a specific property of rhinoceroses. These influences were used to calculate a weighted average in conjunction with the permittivity and conductivity values of the identified animals to approximate the dielectric properties of various rhinoceros tissues. As illustrated in Appendix L (page 144), some tissues did not have contributions from all of the animals listed in Table 38, due to the permittivity and conductivity values not being available for those specific tissues or at a specific frequency for those animals. Figure 26 (page 37) indicates the calculated contribution of each animal towards the rhinoceros approximation model and Appendix L (page 144) indicates the contribuions of each animal towards a specific tissue approximation.

Due to the limited publications pertaining to rhinoceros anatomy and dielectric properties [23], some of the values (indicated by *) in Table 38 were deduced intuitively by means of a process of elimination and insight provided by Dr J. Marais. These properties were mostly low ranking contributing factors or simple true or false statements. The point system used to distinguish between essential and low consequentiality identifiers for the rhinoceros model, utilizes four colours pertaining to a specific points multiplier. Thus, properties considered to bare greater weight on the outcome of the rhinoceros model have greater influence in determining the animal and rhinoceros similarities.

Table 38: Decision matrix for dielectric property weighting factors.

Decision Matrix for Permittivity and Conductivity Weighting Factors													
Criteria: Similarity to Rhinoceros	**Available Points**	**Animals**											
		Bovine	Canine	Equine	Feline	Frog	Human	Mouse	Ovine	Pinniped	Porcine	Rabbit	Rat
Mammal	0 – 1	1 [43]	1 [44]	1 [44]	1 [44]	0 [44]	1 [45]	1 [46]	1 [47]	1 [48]	1 [49]	1 [44]	1 [44]
Ungulate (Odd-Toed)	0 – 2	1 [50]	0*	2 [50]	0*	0*	0*	0*	1 [50]	0*	1 [50]	0*	0*
Hindgut Fermenter	0 – 1	0*	0*	1 [51]	0*	0*	0*	1 [51]	0*	0*	0*	1 [51]	1 [51]
Herbivorous	0 – 2	2 [51] [52]	1 [53] [44]	2 [51] [52]	0 [44]	1 [44]	1 [52] [54]	2 [51] [52]	2 [51] [52] [47]	1 [55]	1 [49]	2 [51] [44]	1 [44]
Primarily Solitary	0 – 1	0*	0*	0*	0*	1 [56]	0*	0*	0 [47]	0*	0 [49]	0*	0*
Territorial (Males Battle)	0 – 1	0*	1 [57]	0*	1 [57]	1 [57]	1 [57]	1 [57]	1 [47]	1 [57]	0 [49]	1 [57]	1 [57]
Horn (True Horn or Boneless)	0 – 2	1 [58] [59]	0*	0*	0*	0*	0*	0*	1 [58] [59]	0*	0*	0*	0*
Vision	0 – 2	1 [60]	1 [61] [62]	1 [60] [62]	2 [61] [62]	1 [63]	0 [60] [64]	1 [65]	1 [60]	0 [66]	1 [67]	0 [68]	1 [69]
Audition	0 – 2	1 [70] [71]	1 [70] [71]	2 [70] [71]	1 [70] [71]	0 [71]	1 [70] [71]	0 [70] [71]	1 [70] [71]	1 [72] [73]	1 [74]	0 [70] [71]	0 [71]
Olfaction	0 – 2	2 [75]	2 [76] [75]	2 [75]	1 [77]	0 [76]	1 [76]	2 [76] [75]	2 [78]	2 [79] [80]	2 [81]	1 [82] [83]	1 [76] [75]
Habitat	0 – 2	2 [84]	1 [84]	2 [84]	1 [84]	1 [84]	1*	1 [84]	1 [84]	0 [84]	1 [84]	1 [84]	1 [84]
Prehensile Lip	0 – 1	1 [85]	0*	1 [86]	0*	0*	1 [87]	0*	1 [85]	0*	0*	1 [88]	0*
Weight	0 – 2	1 [89] [90]	0 [89] [90]	1 [89] [90]	0 [91] [89] [90]	0 [91] [44]	0 [92]	0 [91] [89] [90]	0 [93] [94] [89] [90]	1 [48] [89] [89] [90]	0 [89] [90]	0 [91] [89] [90]	0 [95] [89] [90]
Skin Thickness	0 – 3	3 [96] [97]	1 [98] [99] [97]	1 [100] [97]	1 [98] [97]	0 [101]	1 [102] [6]	0 [103]	1 [12] [35]	2 [12] [35]	1 [12] [35] [97]	1 [104]	0 [102]
Collagen Content of Skin	0 – 3	3 [105] [106] [107] [108]	1 [109] [107]	3 [110] [106]	1 [111]	0 [112] [113]	2 [107] [108] [102]	1 [114]	2 [106] [108]	3 [115]	3 [105] [106] [107] [108] [116]	1 [117]	1 [107] [95]
Fat Layer	0 – 3	2 [118] [119]	0 [99]	2 [120] [121]	0 [122]	0*	1 [123] [124]	0 [125]	1 [93] [126] [94] [119]	2 [127] [12] [35]	2 [119] [35]	0 [128]	0 [129]
Body Length	0 – 2	2 [130] [23]	0 [131]	3 [132] [23]	0 [91]	0 [91]	1 [91]	0 [46]	1 [133]	2 [48]	1 [134]	0 [91]	0 [135]
Body Height	0 – 2	2 [130] [23]	1 [131] [44]	2 [44] [23]	0 [44]	0 [44]	2 [92]	0 [136]	1 [47]	2 [48]	1 [49]	0 [44]	0 [44]
Intestines/Organs	0 – 3	2 [137] [23]	0 [138] [139]	3 [140] [23]	0 [138] [139]	0 [141]	1 [138] [142]	0 [143]	1 [138] [144]	1 [145]	1 [138] [144]	0 [138]	0 [138] [143]
Skeletal Structure	0 – 3	3 [146] [102] [23]	1 [99] [139]	2 [140] [23]	1 [146] [139]	0 [146] [141]	1 [138] [142]	1 [147]	1 [138] [148]	1 [145]	2 [146]	1 [149]	1 [138]
Straight Legs	0 – 1	1 [137] [23]	1 [99] [139]	1 [140] [23]	1 [146] [139]	0 [141]	1 [142]	0 [147]	1 [148]	0 [145]	1 [146]	0 [149]	0 [149]
Swiveling Ears	0 – 1	1 [137]	1 [150]	1 [151]	1 [150]	0 [152]	0 [142]	1 [153]	1 [154]	0 [145]	0 [155]	1 [156]	1 [157]
Thermal Properties of Organs	0 – 3	3 [138] [158] [159]	1 [138] [159]	3 [160]	1 [138]	0 [161]	2 [138] [159]	0 [162]	2 [138] [158] [159]	2 [138] [159] [160]	2 [138] [158] [159]	1 [138] [159]	1 [138]
Water Content of Organs	0 – 3	2 [119] [160]	1 [163]	3 [164] [160]	2 [165]	0 [166]	3 [167] [163]	1 [168]	2 [94] [119] [160]	2 [169] [160]	2 [119] [160]	1 [170]	1 [170]
Points Total	**Max [48]**	37	16	39	15	5	22	13	26	24	24	14	12
Multiplier Total	**Max [327]**	262	85	264	84	11	151	67	164	174	171	89	69

Legend: Decision Matrix Criteria			
Colour Representation	Level of Importance	Relevance to Rhinoceros Model	Points Multiplier
230	High	This aspect is an essential identifier for approximating the model	10
63	Moderate	This aspect is a significant identifier for approximating the model	7
24	Low	This aspect is an auxiliary identifier for approximating the model	4
10	Very Low	This aspect has low consequentiality for model approximations	1

Sum of Multiplier Total = 262 + 85 + 264 + 84 + 11 + 151 + 67 + 164 + 174 + 171 + 89 + 69
= 1591

L. Constituents of the Dielectric Properties of Specific Tissues

L.1 Constituents of 403 MHz Permittivity and Conductivity Approximations

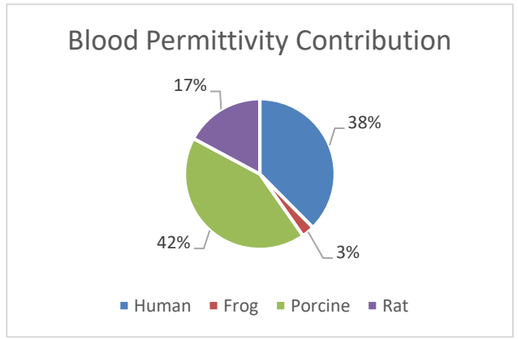

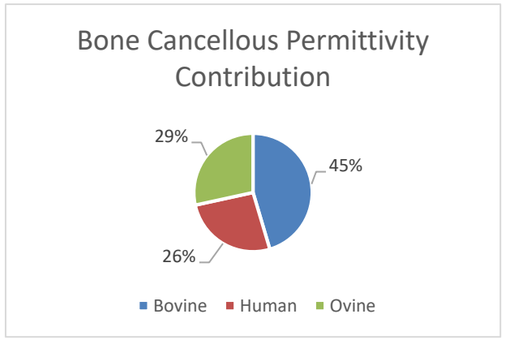

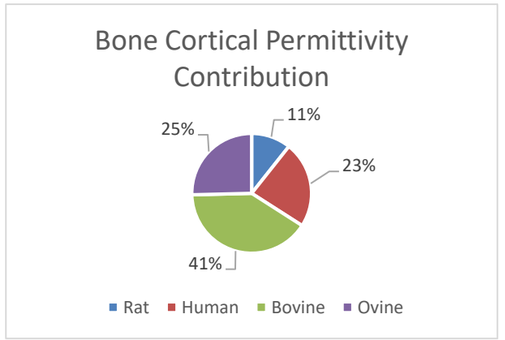

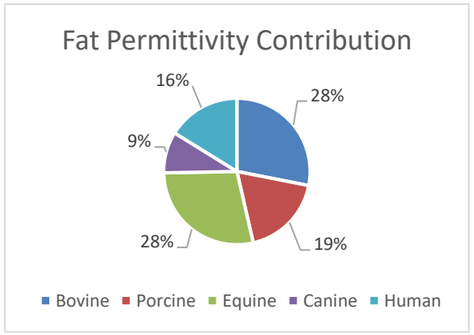

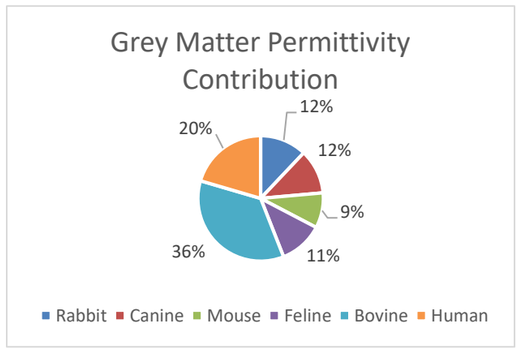

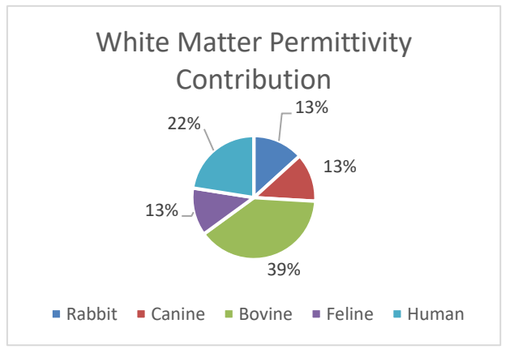

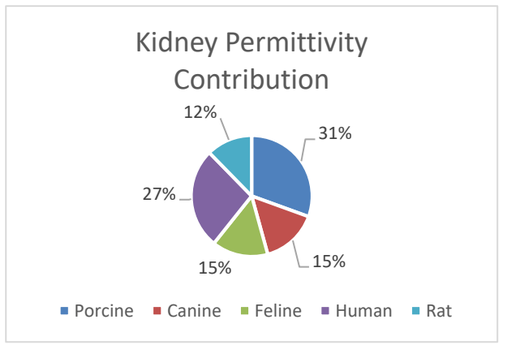

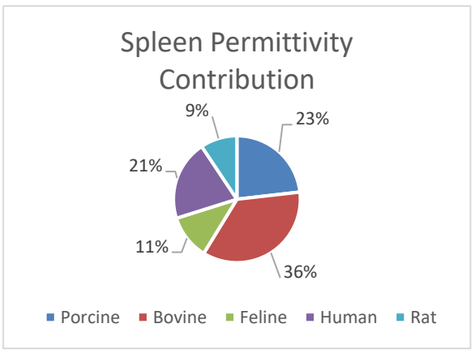

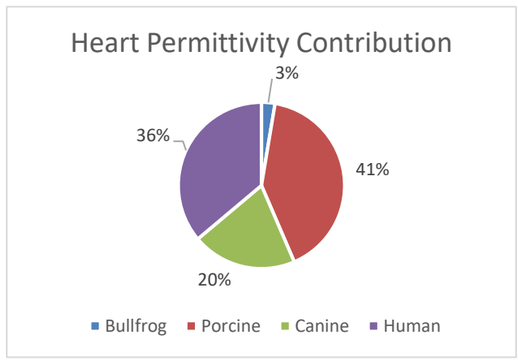

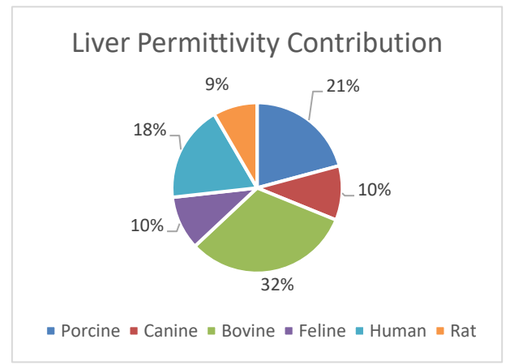

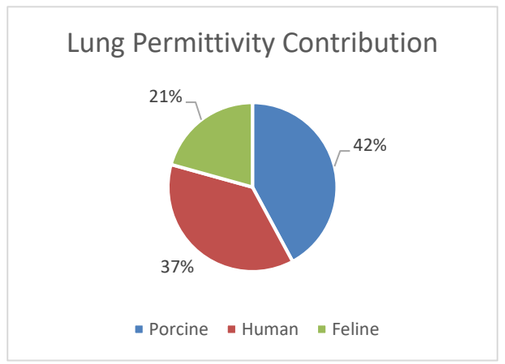

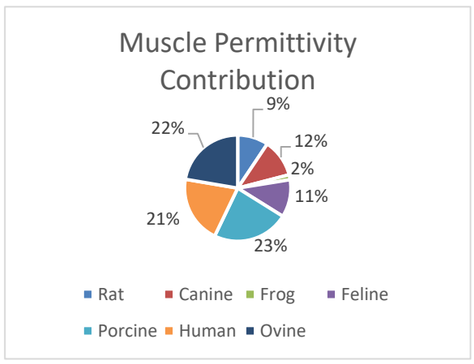

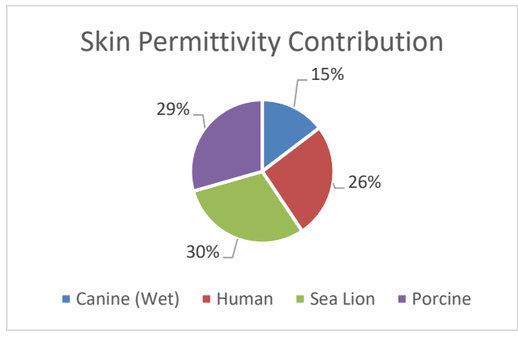

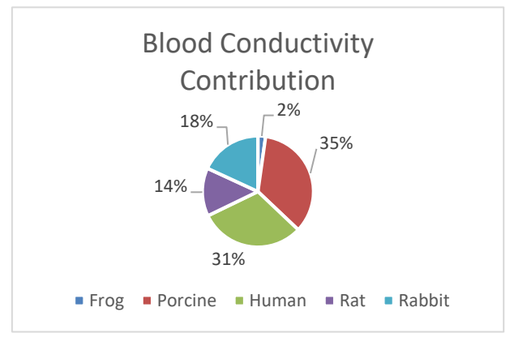

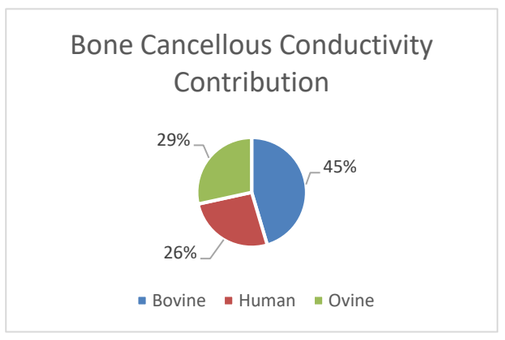

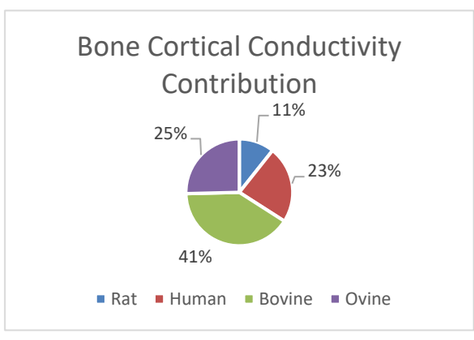

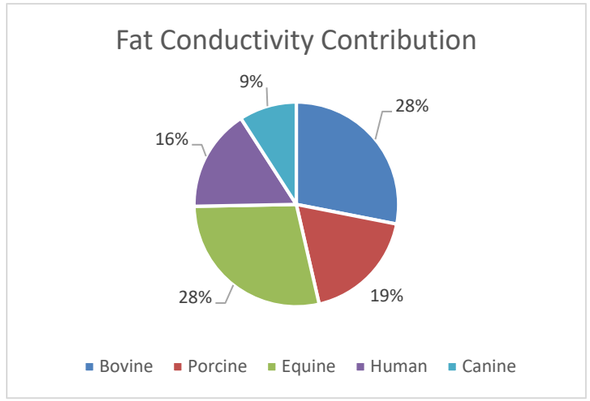

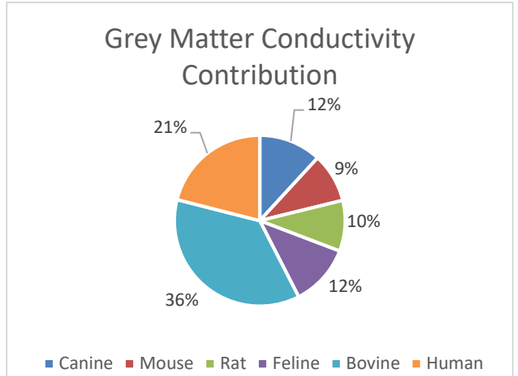

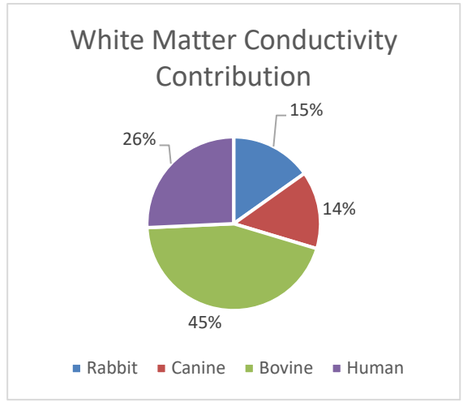

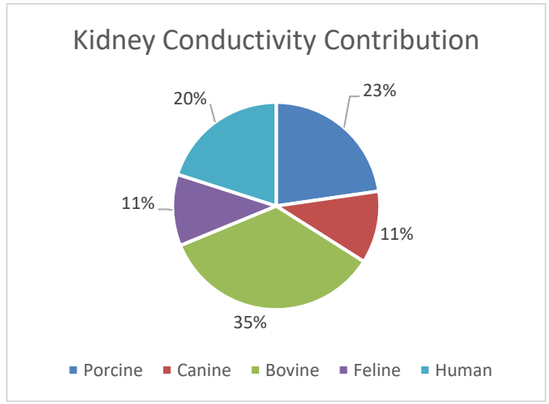

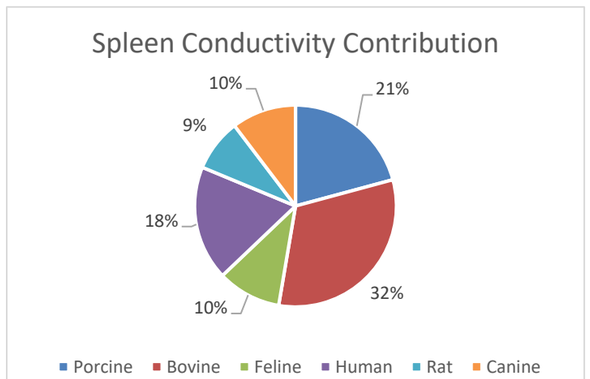

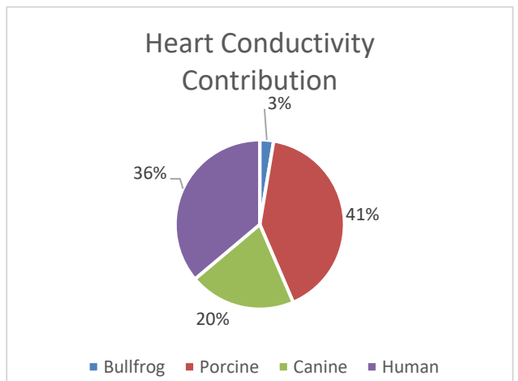

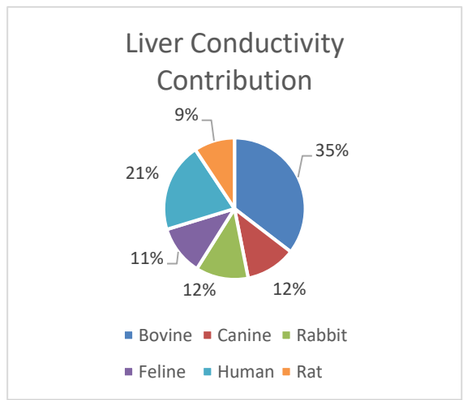

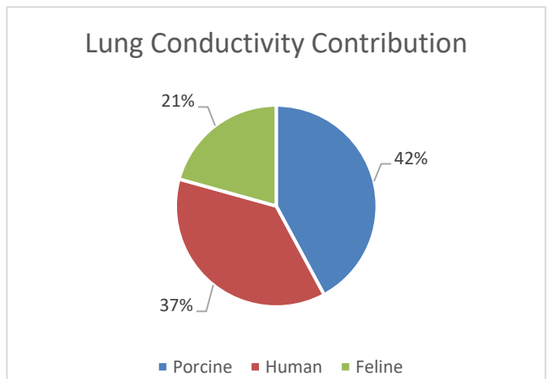

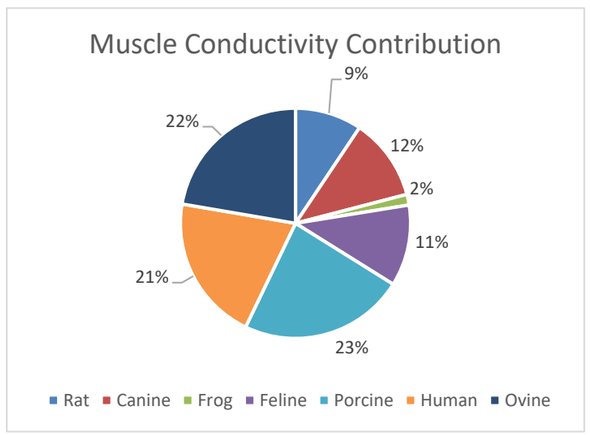

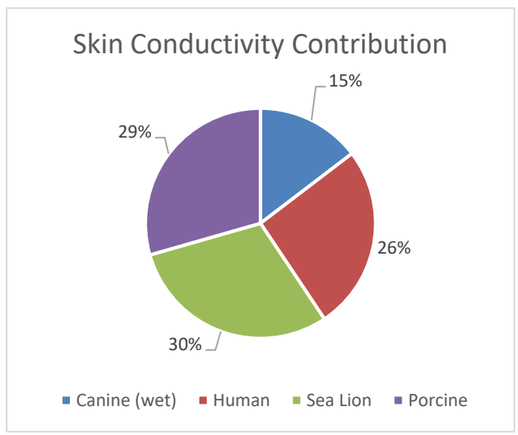

L.2 Constituents of 910 MHz Permittivity and Conductivity Approximations

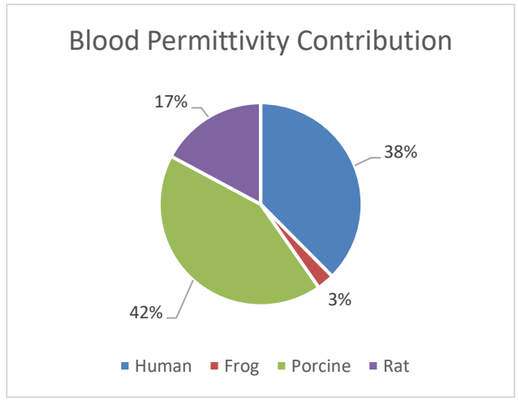

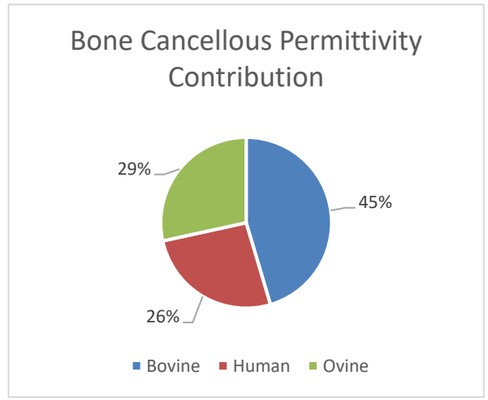

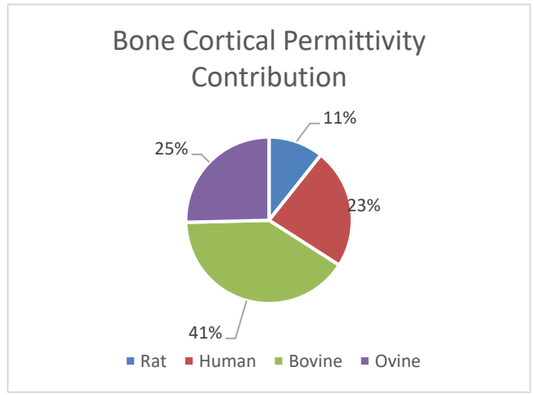

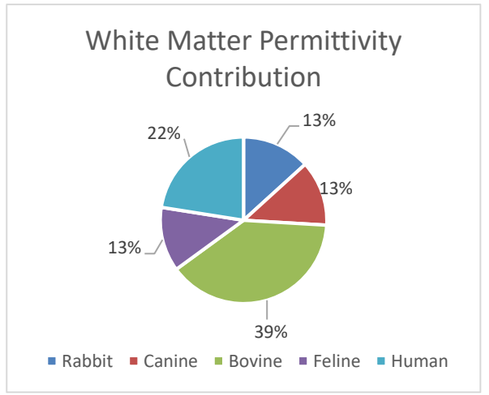

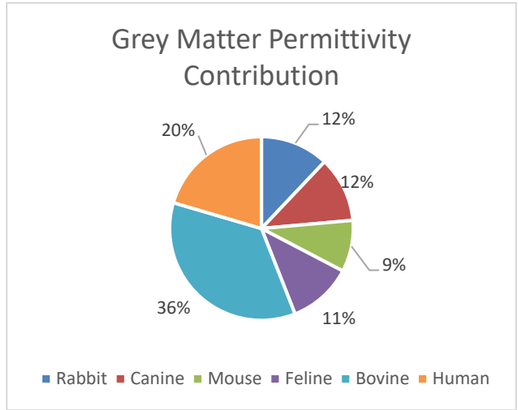

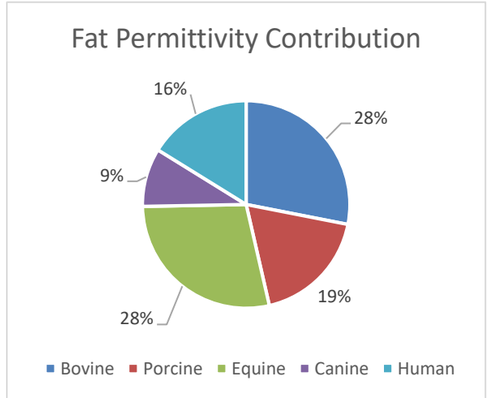

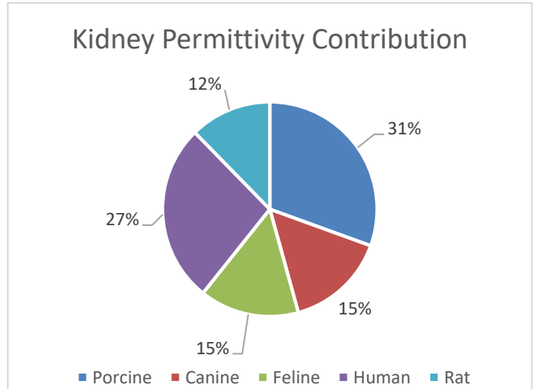

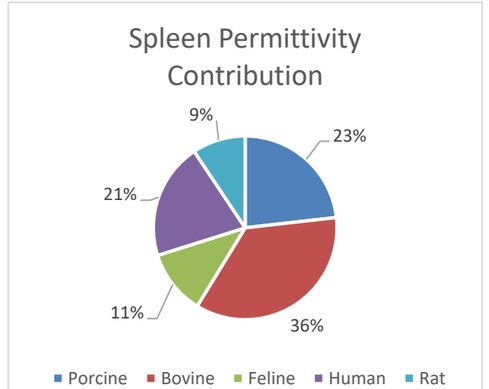

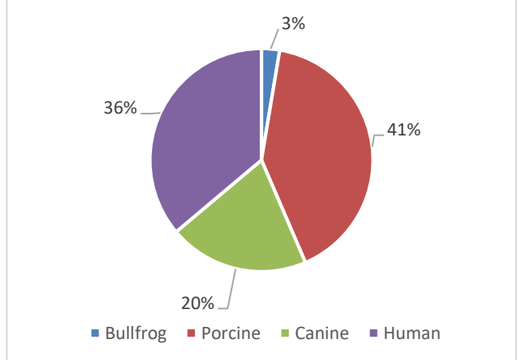

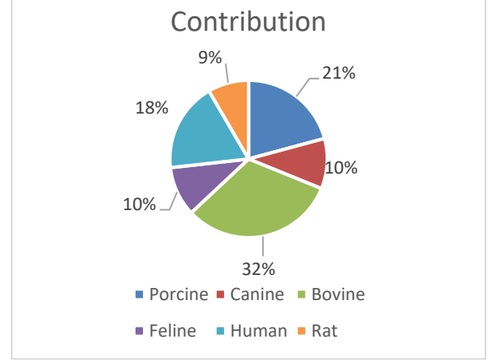

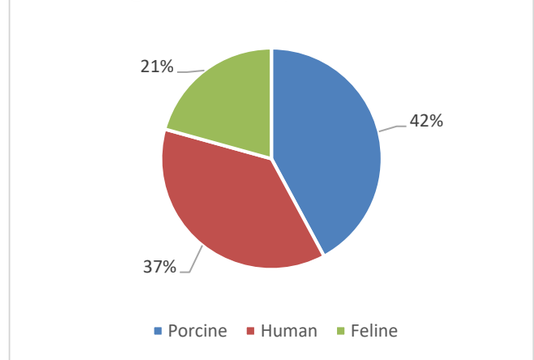

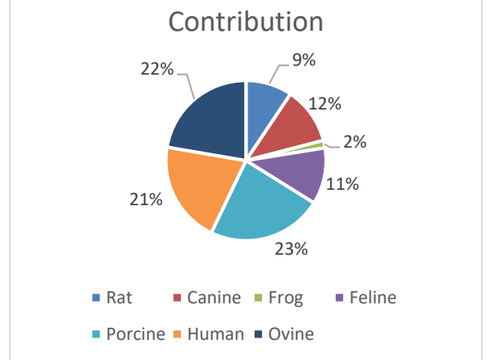

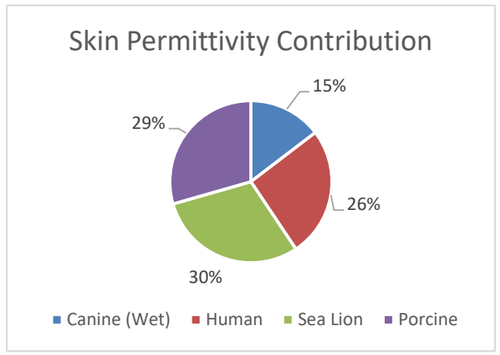

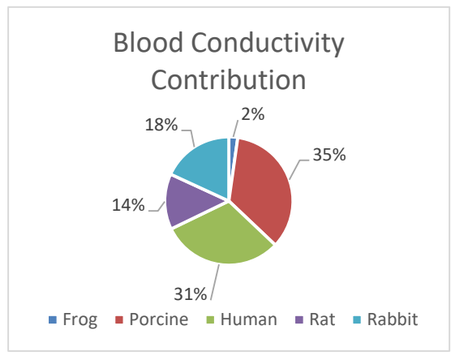

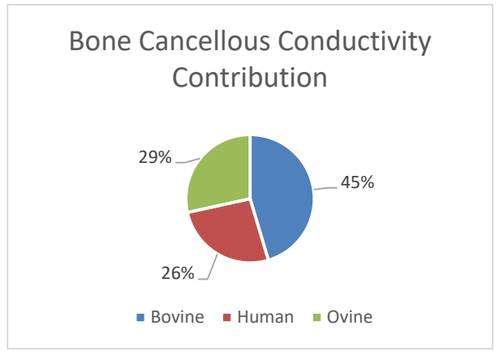

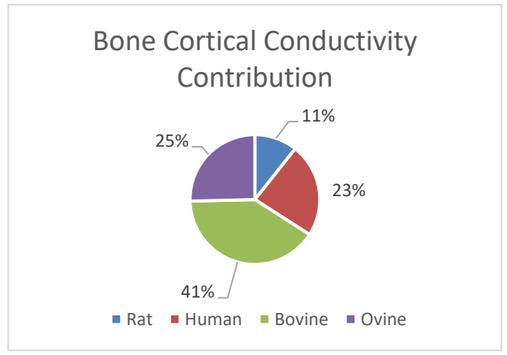

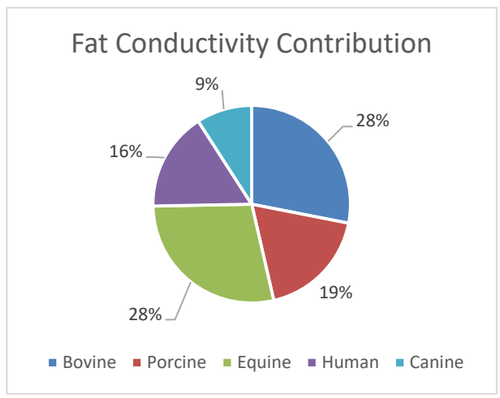

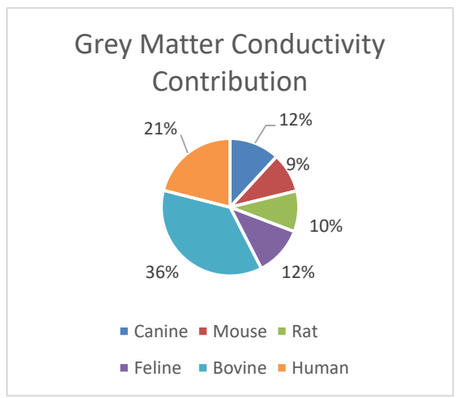

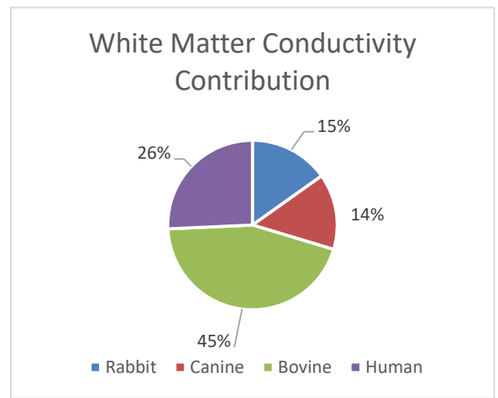

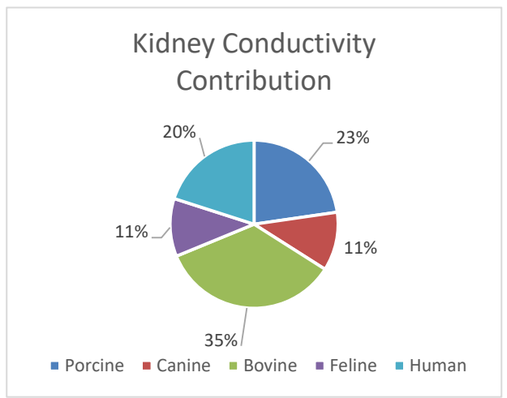

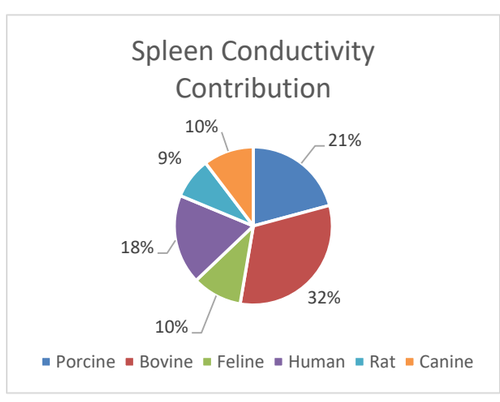

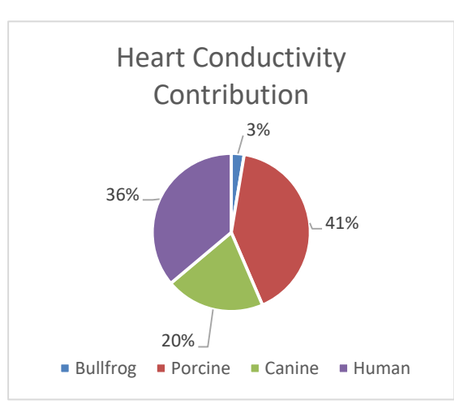

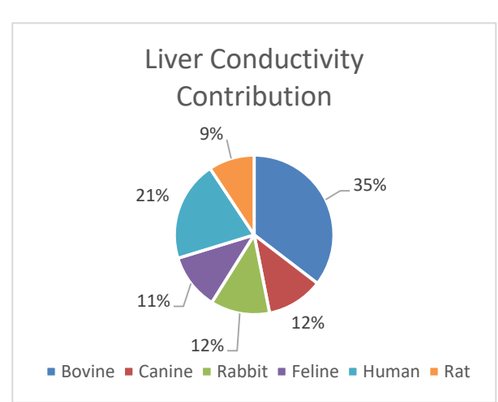

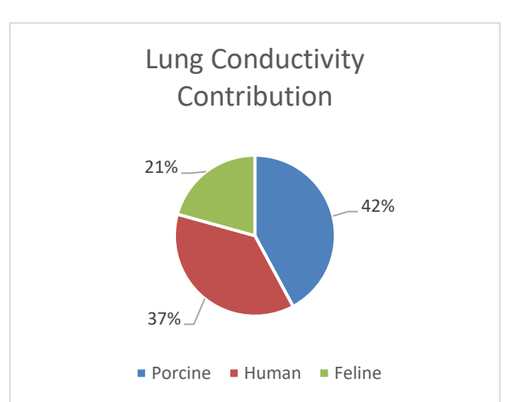

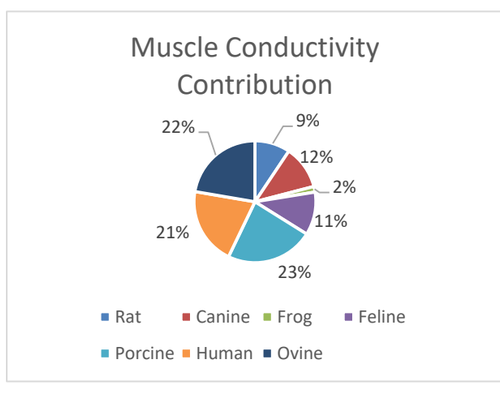

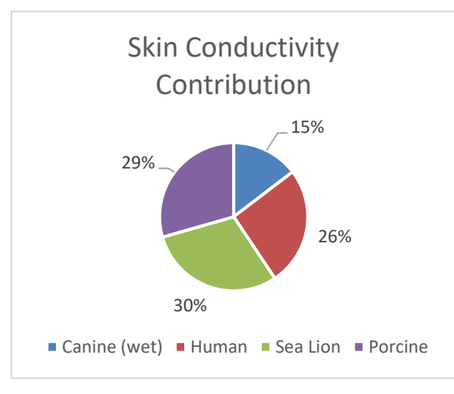

L.3 Constituents of 2.4 GHz Permittivity and Conductivity Approximations

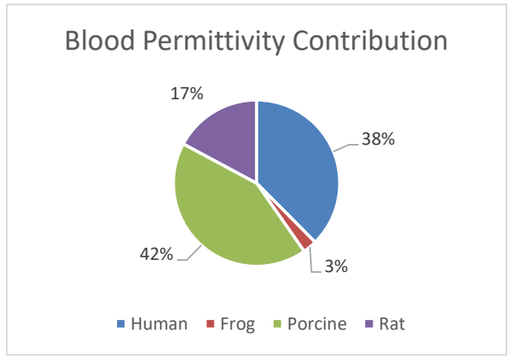

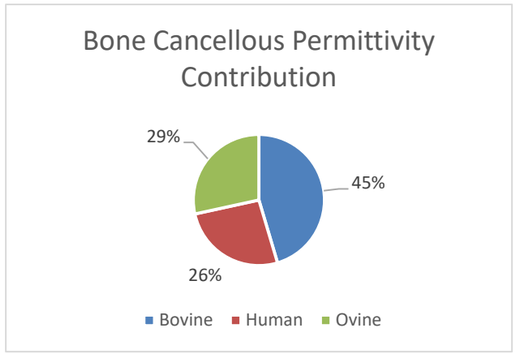

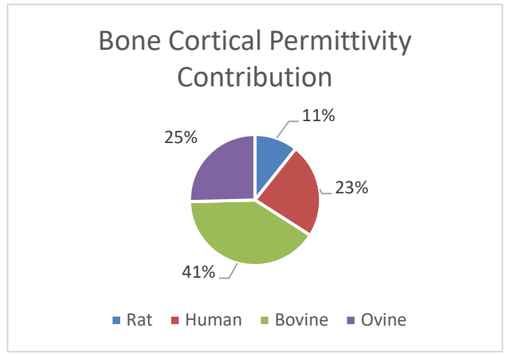

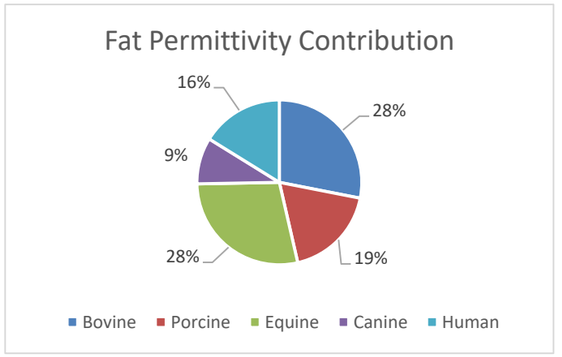

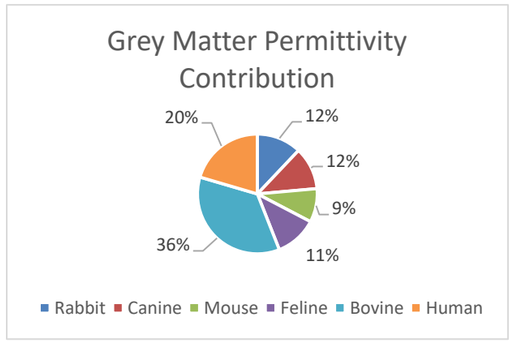

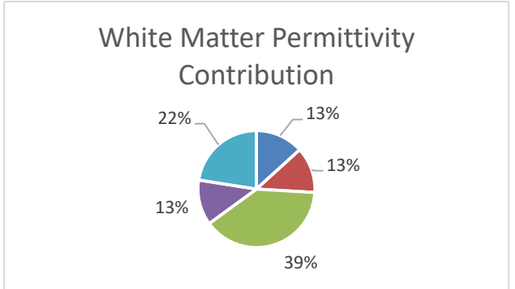

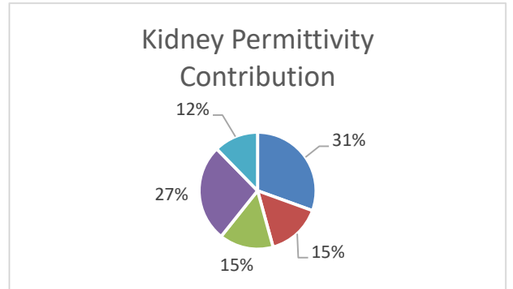

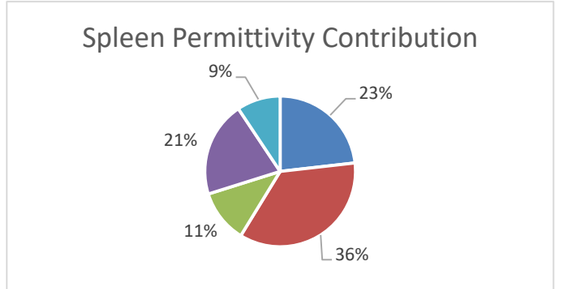

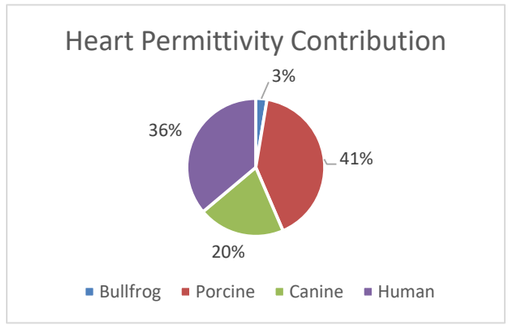

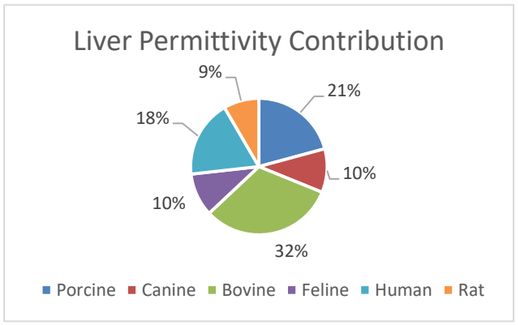

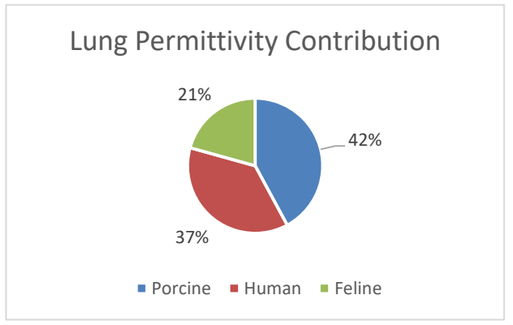

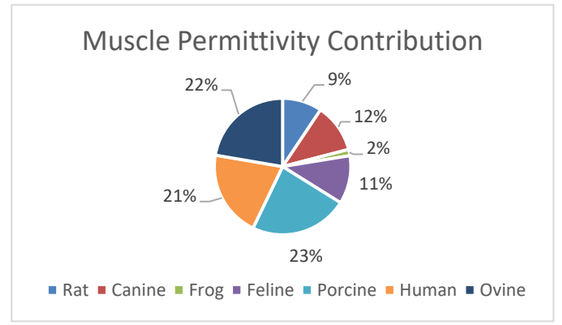

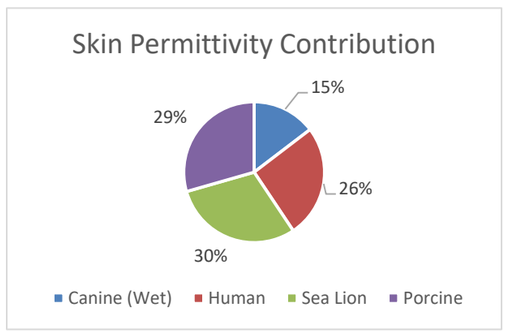

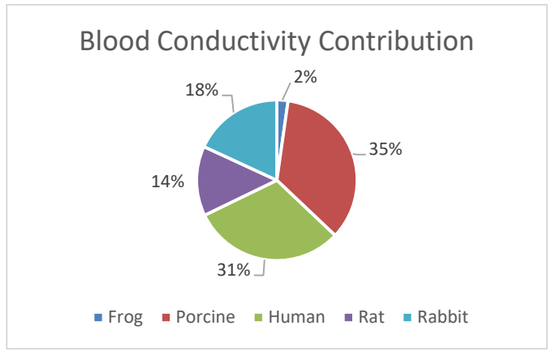

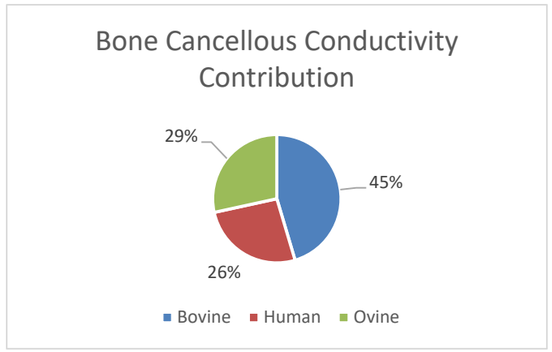

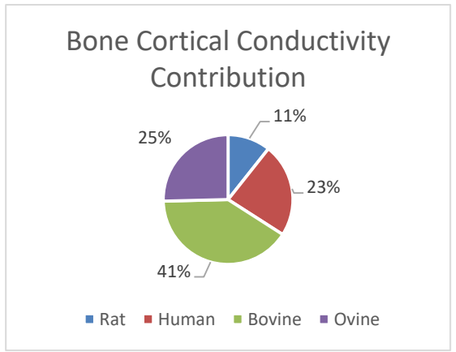

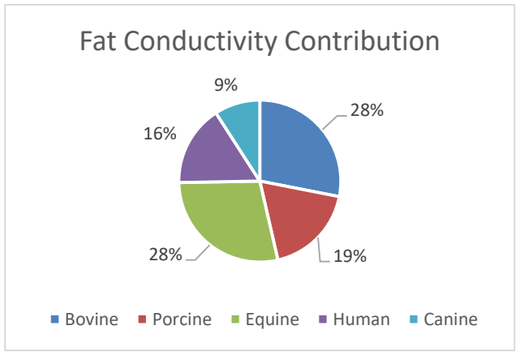

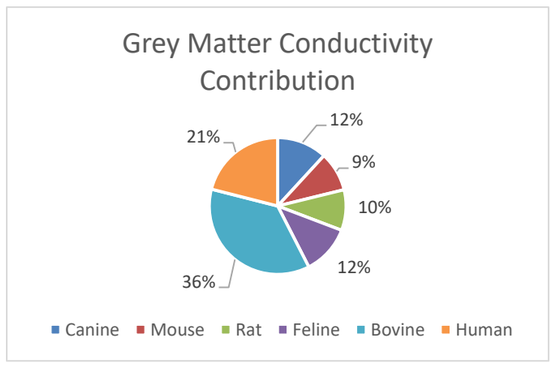

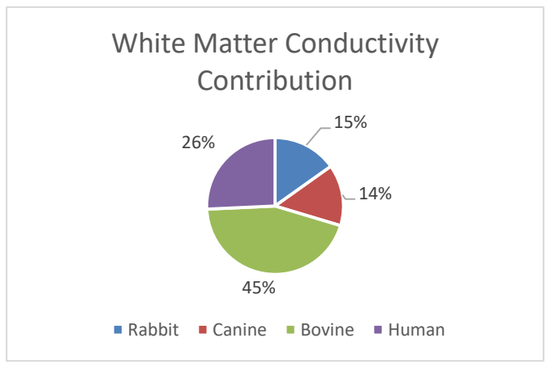

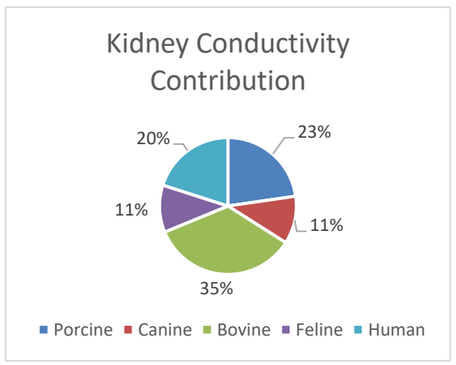

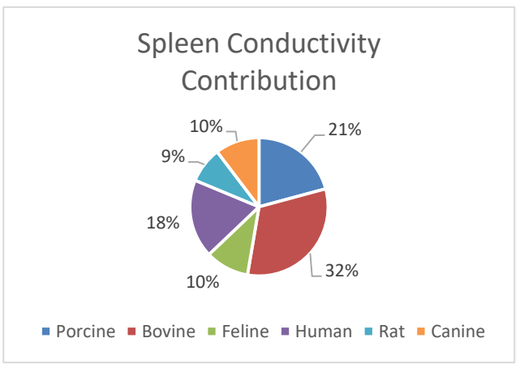

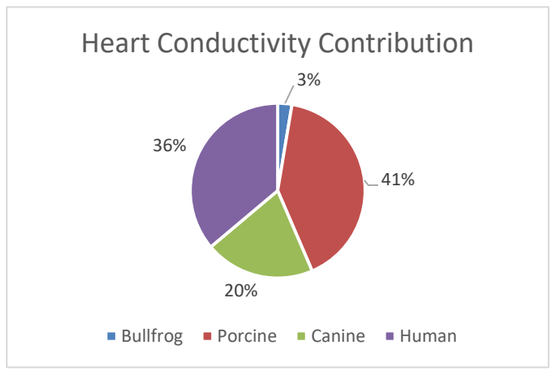

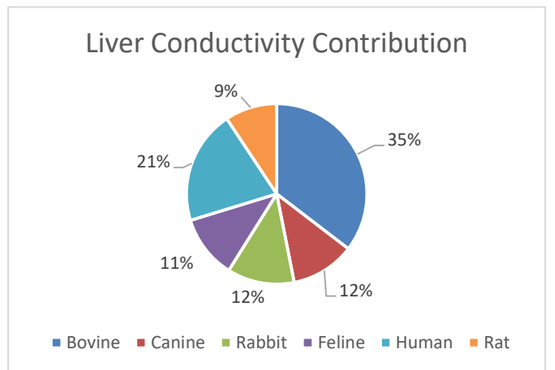

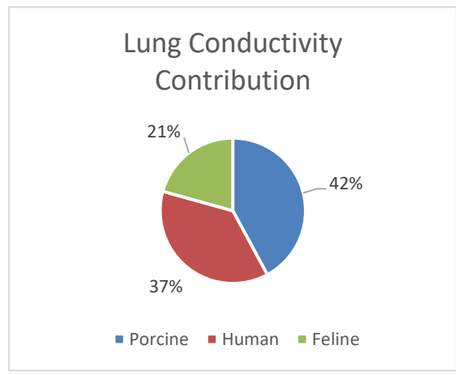

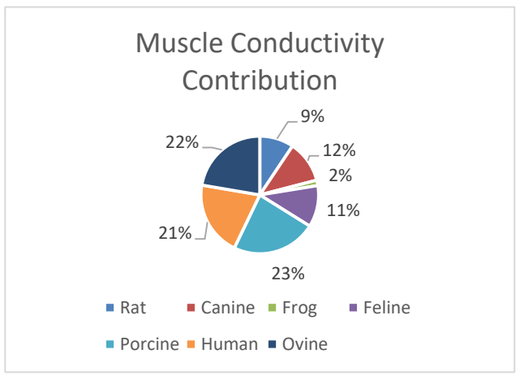

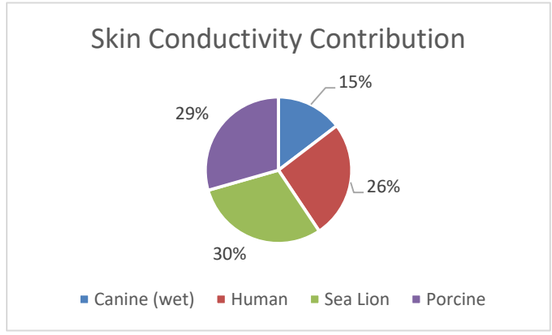

L.4 Constituents of 4.5 GHz Permittivity and Conductivity Approximations

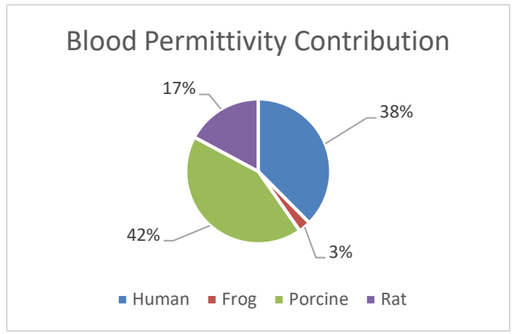

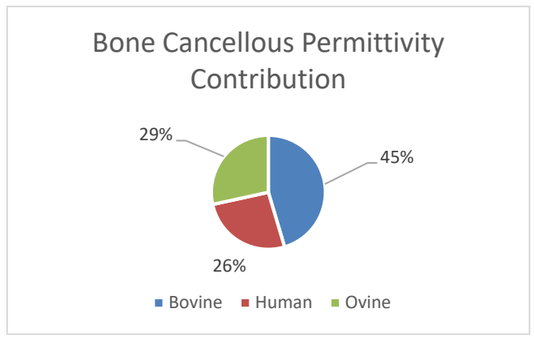

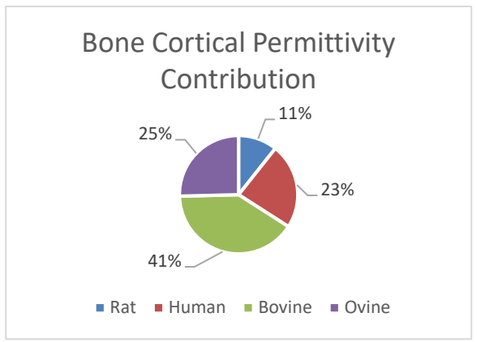

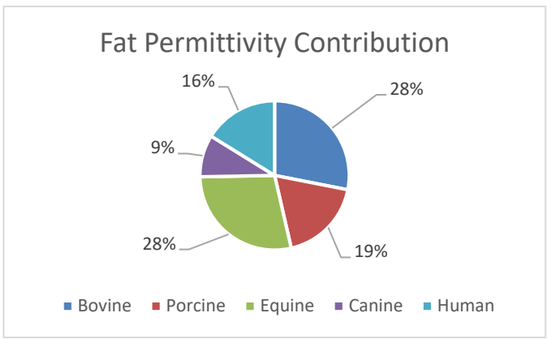

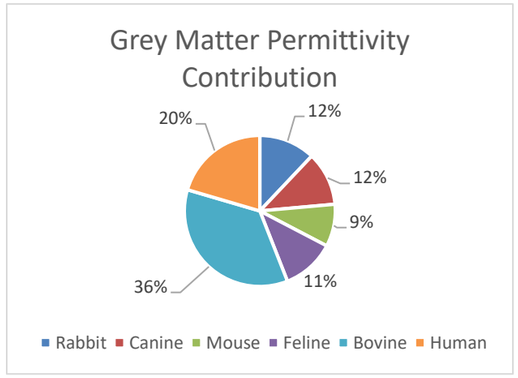

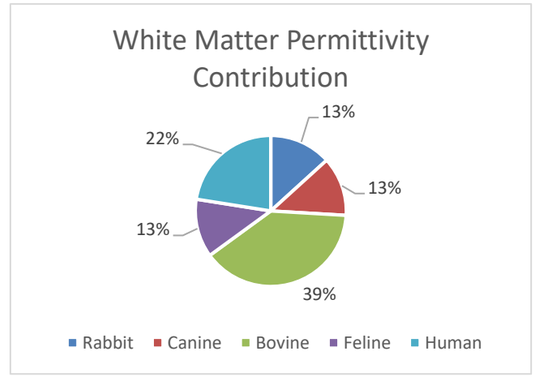

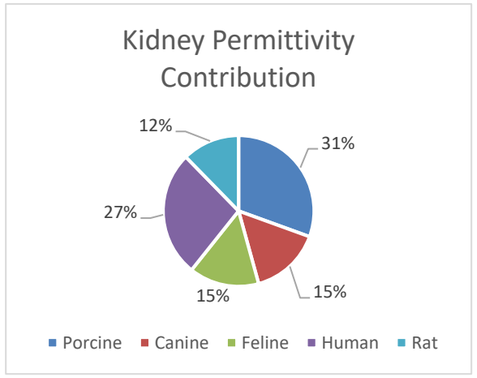

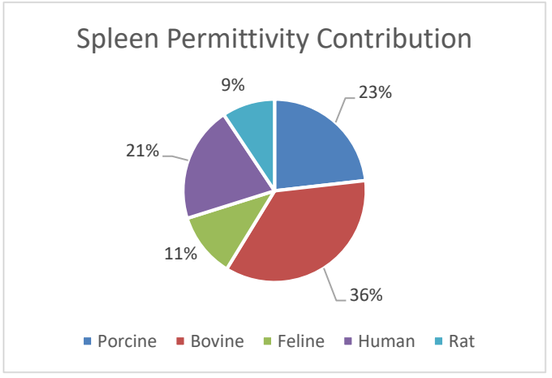

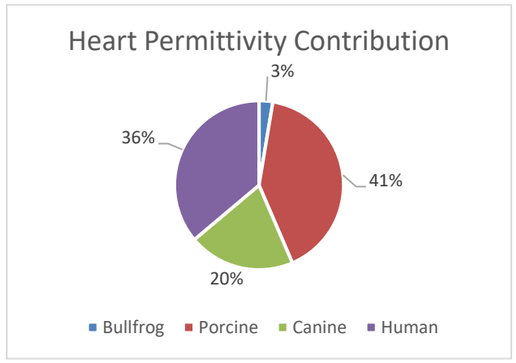

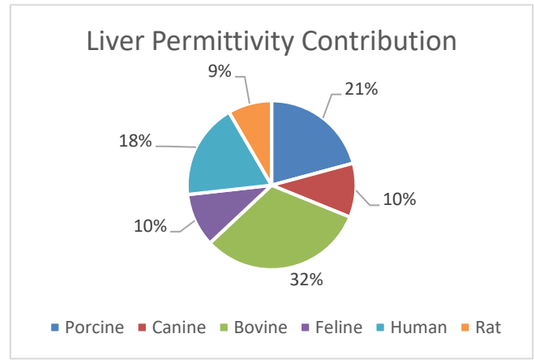

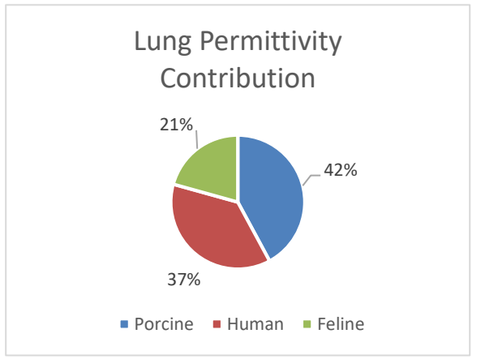

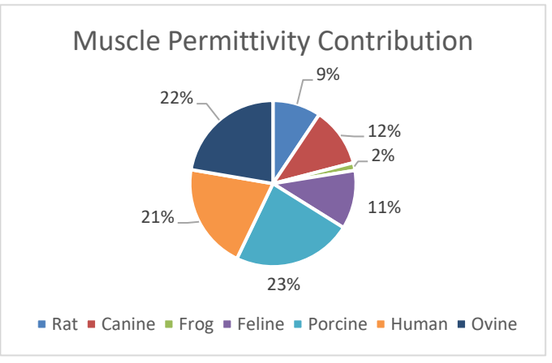

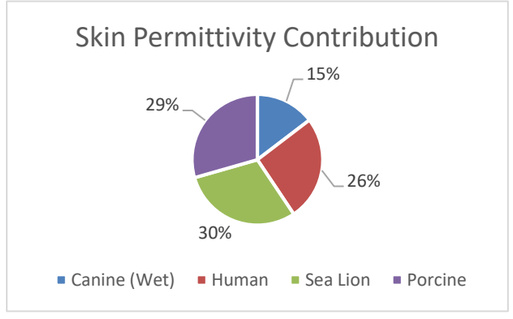

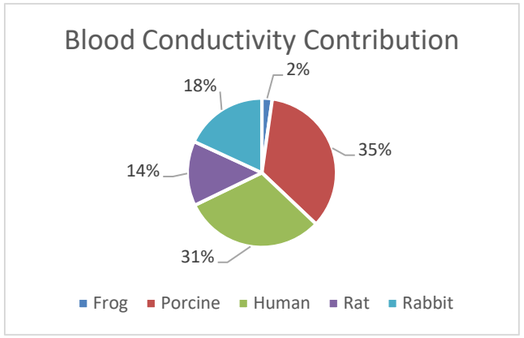

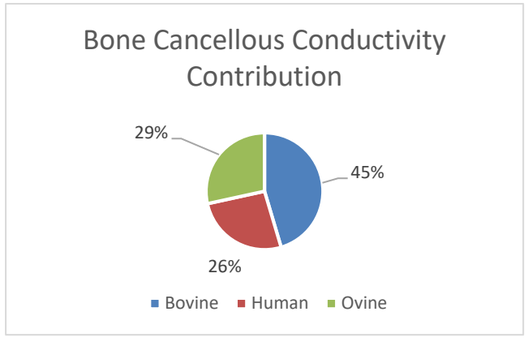

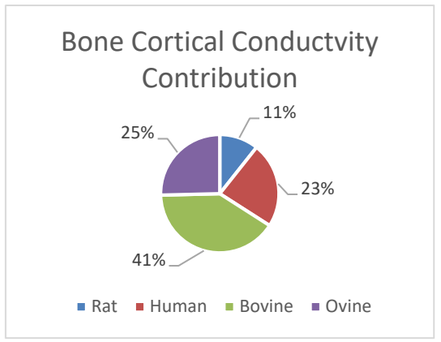

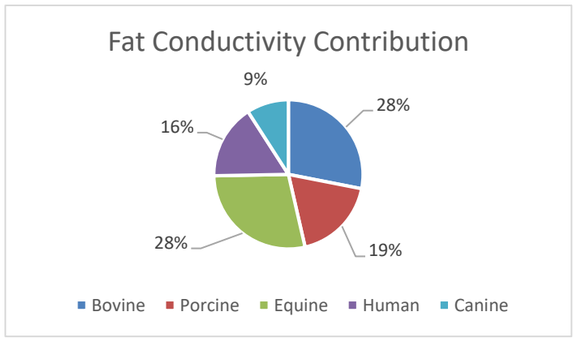

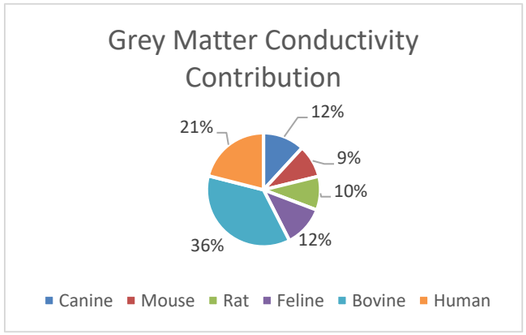

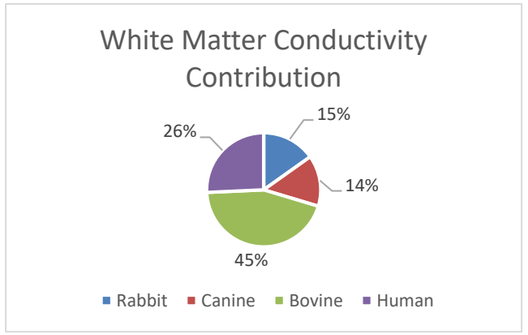

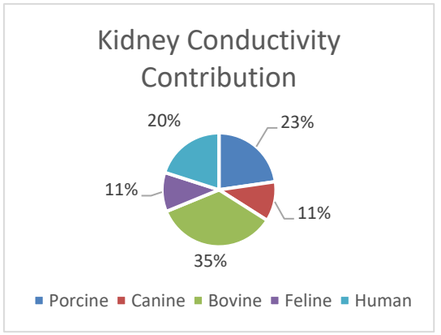

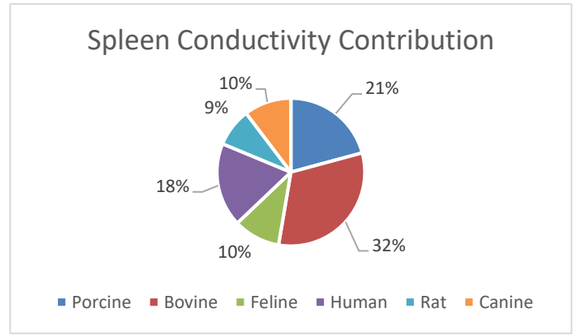

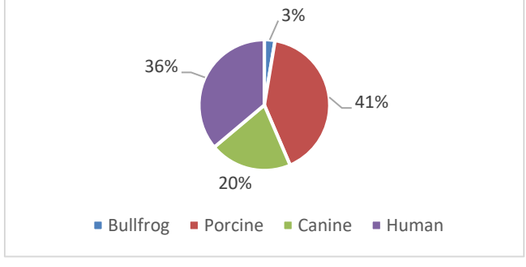

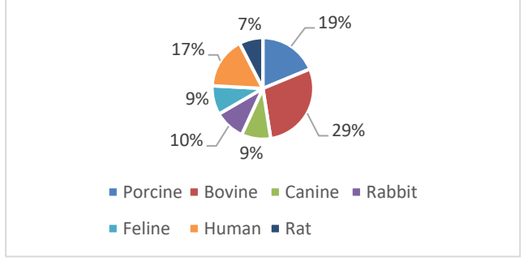

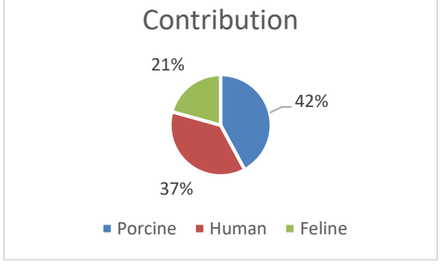

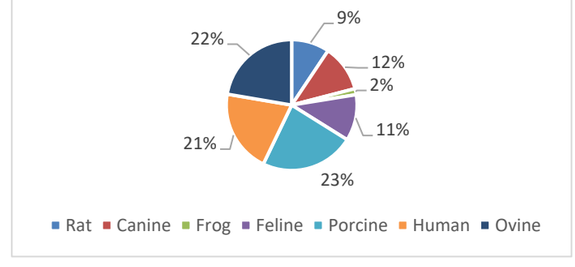

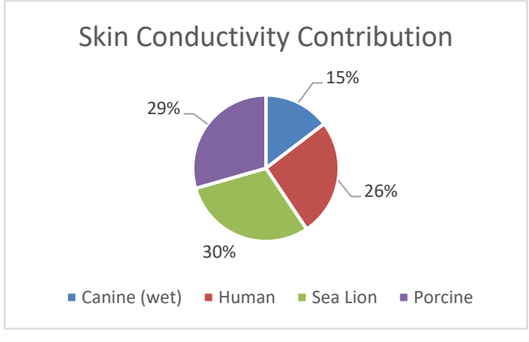

M. Characteristics of the Considered Generic Antenna Designs

Table 39: Prototype antenna considerations.

Antenna	Design Frequency	Approximate Gain [dBi]	Radiation Pattern	Reflection Coefficient (At Design Frequency)	S11 [dB] (Return Loss for Refl. Coef. At Design Frequency)	Minimum Reflection Coefficient	S11 [dB] (Return Loss for Minimum Refl. Coef.)	Frequency At Minimum Reflection Coefficient	Approximate Bandwidth Range (Refl. Coef. < 0.316)	Approximate Bandwidth (Refl. Coef. < 0.316)	Physical Size [Length x Width x Height] (Millimetre)
2-by-2 Rectangular Microstrip Patch Array	2.4 GHz	14.2	Five Lobes Directional	0.653	-3.702	0.0889	-21.022	2.34 GHz	2.313 GHz - 2.361 GHz	47.5686 MHz	150.9 x 193.2 x 2.65
2-by-2 Rectangular Microstrip Patch Array	403 MHz	14.2	Five Lobes Directional	0.654	-3.688	0.0833	-21.587	392.8 MHz	388.5 MHz - 396.4 MHz	7.98368 MHz	898.8 x 1151 x 15.78
2-by-2 Rectangular Patch Array with Corporate Feed	2.4 GHz	13	Five Lobes Directional	0.141	-17.016	0.0136	-37.329	2.393 GHz	2.376 GHz - 2.41 GHz	33.7479 MHz	135.7 x 175.6 x 1.684
2-by-2 Rectangular Patch Array with Corporate Feed	403 MHz	13	Five Lobes Directional	0.150	-16.478	0.00546	-45.256	401.8 MHz	399 MHz - 404.6 MHz	5.64625 MHz	808.3 x 1046 x 10.03
8-by-1 Rectangular Patch Array with Corporate Feed	2.4 GHz	15.4	Parabolic Directional	0.226	-12.918	0.172	-15.289	2.407 GHz	2.392 GHz - 2.424 GHz	31.9554 MHz	572.8 x 101.2 x 1.684
8-by-1 Rectangular Patch Array with Corporate Feed	403 MHz	15.4	Parabolic Directional	0.213	-13.432	0.166	-15.598	404.3 MHz	401.6 MHz - 407 MHz	5.48285 MHz	3411 x 602.4 x 10.03
Antipodal Vivaldi Antenna	2.4 GHz	2.588	Semi-Toroidal	0.531	-5.505	0.2026	-13.867	1.9207 GHz	-	-	51.06 x 61.81 x 2.188
Antipodal Vivaldi Antenna	403 MHz	2.597	Semi-Toroidal	0.535	-5.438	0.2037	-13.820	322.4 MHz	-	-	304.1 x 368.1 x 13.03
Circular Edge-Fed Linearly Polarised Patch Antenna	2.4 GHz	7.36	Semi-Toroidal	0.506	-5.917	0.02	-33.979	2.359 GHz	2.335 GHz - 2.382 MHz	47.1115 MHz	98.19 x 49.75 x 2.65
Circular Edge-Fed Linearly Polarised Patch Antenna	403 MHz	7.36	Semi-Toroidal	0.506	-5.917	0.0181	-34.846	396.1 MHz	392 MHz - 400 MHz	7.91051 MHz	584.8 x 296.3 x 15.78
Circular Inset-Fed Linearly Polarised Patch Antenna	2.4 GHz	5.96	Semi-Toroidal	0.688	-3.248	0.0858	-21.330	2.47 GHz	2.448 GHz - 2.492 GHz	44.4602 MHz	78.44 x 50.31 x 2.65
Circular Inset-Fed Linearly Polarised Patch Antenna	403 MHz	5.96	Semi-Toroidal	0.687	-3.261	0.0855	-21.361	414.8 MHz	411 MHz - 418.5 MHz	7.47009 MHz	467.2 x 299.6 x 15.78
Circular Pin-Fed Linearly Polarised Patch Antenna	2.4 GHz	7.49	Semi-Toroidal	0.557	-5.083	0.221	-13.112	2.358 GHz	2.341 GHz - 2.373 GHz	32.7124 MHz	49.75 x 49.75 x 2.65
Circular Pin-Fed Linearly Polarised Patch Antenna	403 MHz	7.49	Semi-Toroidal	0.554	-5.130	0.22	-13.152	396.1 MHz	393.1 MHz - 398.6 MHz	5.48377 MHz	296.3 x 296.3 x 15.78
Edge-Fed Microstrip Franklin Array	2.4 GHz	11.3	Parabolic Directional	0.676	-3.397	0.5563	-5.094	2.595 GHz	-	-	262.8 x 56.45 x 2.765
Edge-Fed Microstrip Franklin Array	910 MHz	11.3	Parabolic Directional	0.679	-3.369	0.5571	-5.081	983.8 MHz	-	-	693 x 148.9 x 7.293
Elliptical-Ring Pin-Fed Patch Antenna	2.4 GHz	8.55	Directional	0.564	-4.974	0.14	-17.077	2.606 GHz	2.602 GHz - 2.614 GHz	12.6438 MHz	164.4 x 164.4 x 2.65
Elliptical-Ring Pin-Fed Patch Antenna	910 MHz	8.29	Directional	0.533	-5.465	0.137	-17.266	989.9 MHz	987.3 MHz - 992.1 MHz	4.78386 MHz	433.5 x 433.5 x 6.989
Inset-Fed 4-by-1 Patch Array with Corporate Feed	2.4 GHz	12.8	Parabolic Directional	0.201	-13.936	0.019	-34.425	2.383 GHz	2.355 GHz - 2.411 GHz	56.839 MHz	350.8 x 111.6 x 2.65
Inset-Fed 4-by-1 Patch Array with Corporate Feed	910 MHz	12.9	Parabolic Directional	0.196	-14.155	0.018	-34.895	903.7 MHz	892.7 MHz - 914.3 MHz	21.5233 MHz	925.2 x 294.4 x 6.989
Logarithmic Spiral Antenna	2.4 GHz	5.74	Directional	0.593	-4.539	0.5906	-4.574	2.937 GHz	-	-	207.8 x 207.8 x z
Logarithmic Spiral Antenna	403 MHz	5.74	Directional	0.593	-4.533	0.5912	-4.565	493.1 MHz	-	-	1237 x 1237 x z
Microstrip-Fed Linear Tapered Slot Antenna	2.4 GHz	-2.12	Directional	0.289	-10.782	0.00992	-40.070	2.74 GHz	1.7 GHz - 7.68 GHz	5.98 GHz	194.8 x 120.2 x 0.9915
Microstrip-Fed Linear Tapered Slot Antenna	910 MHz	-2.11	Directional	0.286	-10.873	0.0157	-36.082	1.04 GHz	806 MHz - 2.908 GHz	2.102 GHz	513.7 x 317.1 x 2.615
Microstrip-Fed Planar Elliptical Monopole Antenna	2.4 GHz	2.11	Toroidal	0.123	-18.230	0.1057	-19.519	2.512 GHz	2.072 GHz - 3.894 GHz	1.82603 GHz	49.97 x 50.7 x 1.104
Microstrip-Fed Vivaldi Antenna	2.4 GHz	-2.7	Directional	0.202	-13.893	0.0136	-37.329	1.68 GHz	2.14 GHz - 7.68 GHz	5.54 GHz	189.9 x 109.3 x 0.9915
Microstrip-Fed Vivaldi Antenna	910 MHz	-2.73	Directional	0.199	-14.023	0.0392	-28.134	642 MHz	812 MHz - 2.91 GHz	2.098 GHz	500.8 x 288.3 x 2.615
Pin-Fed 4-by-1 Patch Array with Underside Corporate Feed	910 MHz	13.1	Parabolic Directional	0.617	-4.194	0.0455	-26.840	879.7 MHz	867.2 MHz - 892.5 MHz	25.4519 MHz	925.2 x 112.2 x 13.98
Pin-Fed Rectangular Patch Antenna	2.4 GHz	7.67	Semi-Toroidal	0.428	-7.371	0.138	-17.202	2.365 GHz	2.341 GHz - 2.388 GHz	46.7591 MHz	102 x 84.17 x 2.65
Pin-Fed Rectangular Patch Antenna	403 MHz	7.67	Semi-Toroidal	0.428	-7.371	0.1362	-17.316	396.9 MHz	393.2 MHz - 401 MHz	7.83656 MHz	607.4 x 501.3 x 15.78
Planar Four-Arm Sinuous Antenna	2.4 GHz	5.286	Directional	0.776	-2.206	0.242	-12.324	1.749 GHz	1.745 GHz - 1.753 GHz	7.18582 MHz	79.52 x 79.52 x z
Planar Four-Arm Sinuous Antenna	403 MHz	5.272	Directional	0.725	-2.793	0.433	-7.270	293.5 MHz	-	-	473.6 x 473.6 x z
Planar Log-Periodic Dipole Array (LPDA)	2.4 GHz	8.59	Directional	0.416	-7.612	-	-	-	-	-	223.1 x 96.3 x 2.65
Planar Log-Periodic Dipole Array (LPDA)	403 MHz	8.6	Directional	0.411	-7.728	-	-	-	-	-	1329 x 573.5 x 15

Antenna	Design Frequency	Approximate Gain [dBi]	Radiation Pattern	Reflection Coefficient (At Design Frequency)	S11 [dB] (Return Loss for Refl. Coef. At Design Frequency)	Minimum Reflection Coefficient	S11 [dB] (Return Loss for Minimum Refl. Coef.)	Frequency At Minimum Reflection Coefficient	Approximate Bandwidth Range (Refl. Coef. < 0.316)	Approximate Bandwidth (Refl. Coef. < 0.316)	Physical Size [Length x Width x Height] (Millimetre)
Planar Sleeve Monopole Antenna	2.4 GHz	2.907	Toroidal	0.370	-8.636	0.0667	-23.517	2.05 GHz	1.88 GHz - 2.31 GHz	435.683 MHz	50.71 x 101.4 x 2.208
Planar Sleeve Monopole Antenna	910 MHz	2.911	Toroidal	0.371	-8.613	0.0667	-23.517	775 MHz	711 MHz - 877 MHz	165.334 MHz	133.7 x 267.5 x 5.824
Planar Trapezoidal Monopole Antenna	2.4 GHz	1.37	Toroidal	0.139	-17.140	0.1265	-17.958	2.305 GHz	1.918 GHz - 2.862 GHz	944.871 MHz	52.32 x 69.7 x 2.208
Planar Trapezoidal Monopole Antenna	403 MHz	1.36	Toroidal	0.140	-17.109	0.1267	-17.944	386.6 MHz	322 MHz - 480.4 MHz	158.665 MHz	311.6 x 415.1 x 13.15
Printed Collinear Dipole Array	2.45 GHz	3.7	Toroidal	0.261	-11.667	0.0326	-29.736	2.316 GHz	2.224 GHz - 2.421 GHz	197.807 MHz	13.1 x 139.2 x 1
Printed Dual-Band Double-T Monopole Antenna	910 MHz/2.4 GHz	0.436	Semi-Spherical	0.646	-3.795	0.0521	-25.663	2.282 GHz	2.241 GHz - 2.319 GHz	77.3635 MHz	199 x 265.4 x 2.891
Printed Folded Dipole	2.4 GHz	1.68	Toroidal	0.515	-5.764	0.283	-10.964	1.874 GHz	1.839 GHz - 1.915 GHz	75.1908 MHz	57.23 x 100.8 x 2.65
Printed Folded Dipole	403 MHz	1.68	Toroidal	0.515	-5.764	0.283	-10.964	314.6 MHz	309 MHz - 321.6 MHz	12.6402 MHz	340.8 x 600.6 x 15.78
Printed Inverted-F Antenna (PIFA)	2.4 GHz	2.461	Toroidal Directional	0.128	-17.856	0.0517	-25.730	2.3565 GHz	2.2318 GHz - 2.4818 GHz	250.008 MHz	53.66 x 35.77 x 1.767
Printed Inverted-F Antenna (PIFA)	910 MHz	2.461	Toroidal Directional	0.130	-17.721	0.0519	-25.697	893.5 MHz	846.1 MHz - 940.8 MHz	94.7036 MHz	141.5 x 94.34 x 4.659
Printed Yagi-Uda Dipole Array with Balun	2.4 GHz	6.81	Directional	0.834	-1.577	0.281	-11.026	2.365 GHz	2.3533 GHz - 2.3673 GHz	14.0414 MHz	153.5 x 55.6 x 0.7212
Printed Yagi-Uda Dipole Array with Balun	403 MHz	4.59	Directional	0.889	-1.022	0.291	-10.722	394 MHz	393.6 MHz - 395.7 MHz	2.16254 MHz	914.4 x 331.1 x 4.295
Rectangular Inset-Fed Microstrip Patch Antenna	2.4 GHz	7	Semi-Toroidal	0.282	-10.995	0.162	-15.810	2.422 GHz	2.396 GHz - 2.446 GHz	51.0734 MHz	102 x 85.1 x 2.65
Rectangular Inset-Fed Microstrip Patch Antenna	403 MHz	7	Semi-Toroidal	0.280	-11.057	0.162	-15.810	406.8 MHz	402.3 MHz - 411 MHz	8.57598 MHz	607.4 x 506.8 x 15.78
Resonant Series-Fed Rectangular Microstrip Patch Array	2.4 GHz	15.69	Parabolic Directional	0.890	-1.012	0.166	-15.598	2.446 GHz	2.442 GHz - 2.454 GHz	11.6627 MHz	771.6 x 41.03 x 1.684
Resonant Series-Fed Rectangular Microstrip Patch Array	910 MHz	15.7	Parabolic Directional	0.889	-1.022	0.164	-15.703	927.4 MHz	925.9 MHz - 930.2 MHz	4.38662 MHz	2035 x 108.2 x 4.442
Self-Complimentary 4-Arm Archimedes Spiral Antenna	2.4 GHz	5.185	Directional	0.998	-0.022	0.9969	-0.027	2.879 GHz	-	-	111.8 x 111.8 x z
Self-Complimentary 4-Arm Archimedes Spiral Antenna	403 MHz	5.184	Directional	0.998	-0.021	0.996941	-0.027	483.4 MHz	-	-	666 x 666 x z
Self-Complimentary Archimedes Spiral Antenna	2.4 GHz	5.015	Directional	0.602	-4.405	0.60014	-4.435	1.9204 GHz	-	-	111.8 x 111.8 x z
Self-Complimentary Archimedes Spiral Antenna	403 MHz	5.015	Directional	0.602	-4.406	0.60013	-4.435	322.4 MHz	-	-	666 x 666 x z
Sequentially Rotated 2-by-2 Array Notched Circular Patches	2.4 GHz	12.81	Directional	0.197	-14.111	0.0442	-27.092	2.431 GHz	2.343 GHz - 2.464 GHz	120.209 MHz	122.5 x 122.5 x 2.65
Sequentially Rotated 2-by-2 Array Notched Circular Patches	910 MHz	12.8	Directional	0.199	-14.023	0.0493	-26.143	921.8 MHz	888.2 MHz - 933.8 MHz	45.6212 MHz	323.2 x 323.2 x 6.989
Sierpinksi Bow-Tie Antenna	2.4 GHz	5.67	Directional	0.451	-6.916	0.312	-10.117	2.29 GHz	9.15 GHz - 9.76 GHz	612.151 MHz	77.29 x 133.8 x 0.2995
Sierpinksi Bow-Tie Antenna	403 MHz	5.67	Directional	0.452	-6.897	0.314	-10.061	384 MHz	1.536 GHz - 1.639 GHz	102.45 MHz	460.3 x 796.7 x 1.783
Sierpinksi Bow-Tie Antenna	910 MHz	5.67	Directional	0.452	-6.897	0.312	-10.117	867 MHz	3.47 GHz - 3.7 GHz	230.995 MHz	203.9 x 352.8 x 0.7898
Square-Ring Pin-Fed Patch Antenna	2.4 GHz	7.38	Semi-Toroidal	0.902	-0.898	0.8614	-1.296	2.59 GHz	-	-	33.53 x 33.53 x 2.65
Square-Ring Pin-Fed Patch Antenna	910 MHz	7.38	Semi-Toroidal	0.902	-0.900	0.8614	-1.296	983.5 MHz	-	-	88.43 x 88.43 x 6.989
Traveling-Wave Series-Fed Rectangular Microstrip Patch Array	2.4 GHz	14.4	Parabolic Directional	0.549	-5.209	0.113	-18.938	2.535 GHz	2.435 GHz - 2.612 GHz	177.587 MHz	712.9 x 59.87 x 1.684
Traveling-Wave Series-Fed Rectangular Microstrip Patch Array	910 MHz	14.4	Parabolic Directional	0.549	-5.209	0.111	-19.094	960.5 MHz	923 MHz - 991.2 MHz	68.2244 MHz	1880 x 157.9 x 4.442
Triangular Edge-Fed Patch Antenna	2.4 GHz	7.18	Semi-Toroidal	0.859	-1.320	0.53	-5.514	2.3082 GHz	-	-	62.44 x 31.22 x 1.767
Triangular Edge-Fed Patch Antenna	403 MHz	7.18	Semi-Toroidal	0.856	-1.351	0.536	-5.417	387.9 MHz	-	-	371.9 x 185.9 x 10.52
Triangular Pin-Fed Patch Antenna	2.4 GHz	7.32	Directional	0.506	-5.917	0.153	-16.306	2.373 GHz	2.357 GHz - 2.386 GHz	29.5984 MHz	48.5 x 56.01 x 2.65
Triangular Pin-Fed Patch Antenna	403 MHz	7.32	Directional	0.520	-5.680	0.226	-12.918	398.6 MHz	396.7 MHz - 400.4 MHz	3.69915 MHz	288.9 x 333.5 x 15.78

N. Rhinoceros Phantom Material Recipes

Table 40: Phantom recipes for biological tissue A.

Biological Tissue	Desired Gel Characteristics					Ingredients			Estimations					
	Conductivity [S/m]	Permittivity	Resonance Frequency	Water Volume [ml]	Temperature [degC]	NaCl [g]	Sugar [g]	Agar [g]	Estimated Conductivity [S/m]	Estimated Permittivity	Estimated Final Volume [ml]	Estimated Density [g/l]	Estimated Heat Capacity [(J/g)/K]	Estimated Thermal Conductivity [W/(m*K)]
Blood	1.269	63.980	403 MHz	100	24	3.107	62.394	2.500	1.269	63.980	1387.408	1170.487	3.233	0.478
Bone Cancellous	0.190	19.215	403 MHz	100	24	35.442	291.797	2.500	0.190	19.215	-	-	-	-
Bone Cortical	0.102	10.890	403 MHz	100	24	67.126	314.510	2.500	0.102	10.890	-	-	-	-
Fat	0.091	11.358	403 MHz	100	24	62.678	318.342	2.500	0.091	11.358	-	-	-	-
Grey Matter	0.870	63.029	403 MHz	100	24	2.295	70.216	2.500	0.870	63.029	1436.424	1184.997	3.180	0.468
White Matter	0.508	47.802	403 MHz	100	24	3.631	145.304	2.500	0.508	47.802	1910.111	1284.237	2.775	0.408
Kidney	1.122	48.580	403 MHz	100	24	10.106	128.429	2.500	1.122	48.580	1803.263	1266.751	2.802	0.423
Spleen	1.081	55.014	403 MHz	100	24	5.808	101.066	2.500	1.081	55.014	1630.458	1233.188	2.955	0.440
Heart	1.137	45.167	403 MHz	100	24	13.505	144.866	2.500	1.137	45.167	1907.337	1283.810	2.724	0.416
Liver	0.903	49.491	403 MHz	100	24	7.361	128.217	2.500	0.903	49.491	1801.927	1266.518	2.819	0.421
Lung	0.552	35.645	403 MHz	100	24	14.195	201.452	2.500	0.586	38.225	2266.812	1329.848	2.567	0.389
Muscle	1.122	65.941	403 MHz	100	24	2.245	54.110	2.500	1.122	65.941	1335.589	1153.870	3.315	0.488
Skin	0.477	41.240	403 MHz	100	24	4.912	185.169	2.500	0.477	41.240	2163.211	1318.267	2.643	0.389
Blood	1.486	59.142	910 MHz	100	24	2.750	65.396	2.500	1.486	59.142	1406.208	1176.183	3.213	0.474
Bone Cancellous	0.339	17.499	910 MHz	100	24	-	-	2.500	-	-	-	-	-	-
Bone Cortical	0.146	9.783	910 MHz	100	24	-	-	2.500	-	-	-	-	-	-
Fat	0.114	10.071	910 MHz	100	24	-	-	2.500	-	-	-	-	-	-
Grey Matter	1.166	54.350	910 MHz	100	24	2.405	86.741	2.500	1.166	54.350	1540.241	1212.417	3.064	0.450
White Matter	0.819	36.437	910 MHz	100	24	1.708	169.528	2.500	0.819	36.437	2063.808	1305.975	2.703	0.394
Kidney	1.692	45.316	910 MHz	100	24	8.460	108.248	2.500	1.692	45.316	1675.755	1242.710	2.900	0.436
Spleen	1.504	49.486	910 MHz	100	24	5.326	97.602	2.500	1.504	49.486	1608.627	1228.392	2.977	0.443
Heart	1.606	41.263	910 MHz	100	24	10.493	125.583	2.500	1.606	41.263	1785.264	1263.582	2.811	0.425
Liver	1.144	43.459	910 MHz	100	24	4.737	126.249	2.500	1.144	43.459	1789.477	1264.330	2.843	0.421
Lung	0.753	31.909	910 MHz	100	24	0.413	199.593	2.500	0.759	32.942	2254.983	1328.584	2.624	0.380
Muscle	1.362	59.233	910 MHz	100	24	2.394	66.312	2.500	1.362	59.233	1411.946	1177.889	3.209	0.473
Skin	0.736	39.792	910 MHz	100	24	0.561	156.671	2.500	0.736	39.792	-	-	-	-
Blood	2.558	54.142	2.4 GHz	100	24	0.810	57.288	2.500	2.558	54.142	1355.455	1160.406	3.303	0.483
Bone Cancellous	0.685	15.783	2.4 GHz	100	24	-	-	2.500	-	-	-	-	-	-
Bone Cortical	0.288	8.783	2.4 GHz	100	24	-	-	2.500	-	-	-	-	-	-
Fat	0.175	8.293	2.4 GHz	100	24	-	-	2.500	-	-	-	-	-	-
Grey Matter	2.286	43.852	2.4 GHz	100	24	2.214	87.343	2.500	2.765	43.852	1544.024	1213.341	3.062	0.450
White Matter	1.435	32.531	2.4 GHz	100	24	3.715	128.002	2.500	2.435	32.531	1800.563	1266.280	2.842	0.419
Kidney	2.681	40.557	2.4 GHz	100	24	2.642	97.822	2.500	2.711	40.557	1610.008	1228.700	2.996	0.440
Spleen	2.117	45.829	2.4 GHz	100	24	2.279	80.407	2.500	2.844	45.829	1500.410	1202.384	3.107	0.457
Heart	2.467	34.469	2.4 GHz	100	24	3.563	119.492	2.500	2.527	34.469	1746.759	1256.565	2.880	0.424
Liver	1.750	39.139	2.4 GHz	100	24	3.279	101.395	2.500	2.732	39.139	1632.533	1233.637	2.972	0.438
Lung	1.050	27.567	2.4 GHz	100	24	0.100	162.855	2.500	2.045	27.567	2021.436	1300.339	2.732	0.396
Muscle	2.055	53.396	2.4 GHz	100	24	0.001	61.909	2.500	2.260	53.396	1384.370	1169.550	3.272	0.476
Skin	1.426	36.405	2.4 GHz	100	24	3.643	111.154	2.500	2.636	36.405	1694.100	1246.410	2.919	0.430
Blood	1.297	57.264	4.5 GHz	100	24	0.618	27.799	2.500	5.545	57.264	1171.698	1090.713	3.633	0.532
Bone Cancellous	0.175	59.012	4.5 GHz	100	24	0.001	25.763	2.500	5.100	59.012	1159.055	1085.050	3.672	0.536

Biological Tissue	Conductivity [S/m]	Permittivity	Resonance Frequency	Water Volume [ml]	Temperature [degC]	NaCl [g]	Sugar [g]	Agar [g]	Estimated Conductivity [S/m]	Estimated Permittivity	Estimated Final Volume [ml]	Estimated Density [g/l]	Estimated Heat Capacity [(J/g)/K]	Estimated Thermal Conductivity [W/(m*K)]
Bone Cortical	0.114	29.285	4.5 GHz	100	24	0.014	114.407	2.500	4.388	29.285	1714.640	1250.451	2.929	0.425
Fat	0.068	20.706	4.5 GHz	100	24	12.834	176.698	2.500	3.074	18.638	2109.362	1311.763	2.632	0.399
Grey Matter	0.986	52.914	4.5 GHz	100	24	1.862	34.601	2.500	6.185	52.914	1213.987	1108.751	3.525	0.520
White Matter	0.582	46.213	4.5 GHz	100	24	0.951	53.790	2.500	5.518	46.213	1333.591	1153.200	3.334	0.488
Kidney	1.056	64.455	4.5 GHz	100	24	0.000	15.794	2.500	4.964	64.455	1097.298	1055.261	3.825	0.559
Spleen	0.863	113.928	4.5 GHz	100	24	-	-	2.500	-	-	-	-	-	-
Heart	0.775	52.213	4.5 GHz	100	24	1.592	36.928	2.500	6.012	52.213	1228.465	1114.626	3.502	0.515
Liver	0.456	59.197	4.5 GHz	100	24	0.001	25.403	2.500	5.096	59.197	1156.821	1084.035	3.677	0.537
Lung	0.665	63.264	4.5 GHz	100	24	0.000	17.876	2.500	4.998	63.264	1110.164	1061.793	3.791	0.554
Muscle	1.155	65.469	4.5 GHz	100	24	0.001	14.060	2.500	4.934	65.469	1086.609	1049.684	3.855	0.563
Skin	0.801	39.647	4.5 GHz	100	24	0.001	75.162	2.500	5.043	39.647	1467.462	1193.637	3.166	0.460

Table 41: Phantom recipes for biological tissue B.

Biological Tissue	Desired Gel Characteristics					Ingredients			Estimations					
	Conductivity [S/m]	Permittivity	Resonance Frequency	Water Volume [ml]	Temperature [degC]	NaCl [g]	Sugar [g]	Agar [g]	Estimated Conductivity [S/m]	Estimated Permittivity	Estimated Final Volume [ml]	Estimated Density [g/l]	Estimated Heat Capacity [(J/g)/K]	Estimated Thermal Conductivity [W/(m*K)]
Skin	0.736	39.792	910 MHz	100	24	0.181	158.811	2.500	0.803	39.791	1995.769	1296.799	2.745	0.398
Grey Matter	2.286	43.852	2.4 GHz	100	24	2.298	87.079	2.500	2.781	43.861	1542.365	1212.936	3.063	0.450
White Matter	1.435	32.531	2.4 GHz	100	24	6.314	123.489	2.500	2.635	32.470	1772.025	1261.207	2.845	0.424
Kidney	2.681	40.557	2.4 GHz	100	24	3.387	95.878	2.500	2.817	40.558	1597.761	1225.953	3.002	0.443
Spleen	2.117	45.829	2.4 GHz	100	24	2.279	80.352	2.500	2.845	45.845	1500.063	1202.294	3.107	0.457
Heart	2.467	34.469	2.4 GHz	100	24	5.684	115.102	2.500	2.722	34.460	1719.027	1251.301	2.886	0.429
Liver	1.750	39.139	2.4 GHz	100	24	3.915	99.844	2.500	2.815	39.133	1622.756	1231.512	2.975	0.440
Lung	1.050	27.567	2.4 GHz	100	24	6.464	153.565	2.500	2.271	27.450	1962.486	1292.059	2.731	0.406
Muscle	2.055	53.396	2.4 GHz	100	24	0.537	60.369	2.500	2.457	53.414	1374.733	1166.550	3.279	0.479
Skin	1.426	36.405	2.4 GHz	100	24	4.975	108.281	2.500	2.777	36.375	1675.963	1242.752	2.924	0.434
Blood	1.297	57.264	4.5 GHz	100	24	0.522	27.652	2.500	5.480	57.447	1170.786	1090.309	3.636	0.532
Bone Cancellous	0.175	59.012	4.5 GHz	100	24	0.409	24.223	2.500	5.392	59.282	1149.491	1080.676	3.686	0.539
Bone Cortical	0.114	29.285	4.5 GHz	100	24	-	-	2.500	-	-	-	-	-	-
Fat	0.068	20.706	4.5 GHz	100	24	-	-	2.500	-	-	-	-	-	-
Grey Matter	0.986	52.914	4.5 GHz	100	24	1.777	35.539	2.500	6.125	52.610	1219.821	1111.136	3.515	0.518
White Matter	0.582	46.213	4.5 GHz	100	24	1.242	53.620	2.500	5.613	46.080	1332.531	1152.844	3.332	0.488
Kidney	1.056	64.455	4.5 GHz	100	24	0.112	14.980	2.500	5.057	64.735	1092.279	1052.660	3.837	0.561
Spleen	0.863	113.928	4.5 GHz	100	24	-	-	2.500	-	-	-	-	-	-
Heart	0.775	52.213	4.5 GHz	100	24	1.974	34.629	2.500	6.239	52.793	1214.164	1108.823	3.523	0.520
Liver	0.456	59.197	4.5 GHz	100	24	0.398	23.908	2.500	5.383	59.456	1147.537	1079.773	3.691	0.540
Lung	0.665	63.264	4.5 GHz	100	24	0.171	16.863	2.500	5.137	63.562	1103.901	1058.637	3.804	0.556
Muscle	1.155	65.469	4.5 GHz	100	24	0.065	13.396	2.500	4.985	65.747	1082.522	1047.514	3.865	0.565
Skin	0.801	39.647	4.5 GHz	100	24	1.148	74.287	2.500	5.238	39.267	1461.968	1192.137	3.161	0.462

White: Approximated with Dielectric Phantom Recipe Generator

Blue: Constant permittivity, increment conductivity until closest point is reached (3 decimal point)

Purple: Approximated by inserting conductivity and permittivity into polynomial regression function

Brown: Closest point in estimated polynomial regression curve

O. Full List of Sample Measurements

Table 42: Measured dielectric properties of rhinoceros phantom recipes (24 degC, 100 ml) A.

Biological Tissue	Desired Gel Characteristics			Properties of Measurements															
	Conductivity [S/m]	Permittivity	Resonance Frequency	Calculated Avg Permittivity	Estimated Conductivity [S/m]	Estimated Permittivity	Sample A: Measured Epsilon	Sample B: Measured Epsilon	Sample C: Measured Epsilon	Sample D: Measured Epsilon	Sample E: Measured Epsilon	Measurement Frequency	Date Created	Date Measured	Error (From Avg)	Error [%] (From Avg)	Error [%] (Per Frequency)	Avg Permittivity (Probe Error of 4.986% Removed)	Error [%] (Probe Error of 4.986% Removed)	Error [%] (Per Frequency: Probe Error of 4.986% Removed)
Blood	1.269	63.980	403 MHz	57.713	1.269	63.980	57.615	57.755	57.194	58.290	-	0.400285 GHz	22/11/2016	2/12/2016	6.267	9.795	11.181	60.591	5.297	6.752
Bone Cancellous	0.190	19.215	403 MHz	-	0.190	19.215	#	#	#	#	-	-	-	-	-	-		-	-	
Bone Cortical	0.102	10.890	403 MHz	-	0.102	10.890	#	#	#	#	-	-	-	-	-	-		-	-	
Fat	0.091	11.358	403 MHz	-	0.091	11.358	#	#	#	#	-	-	-	-	-	-		-	-	
Grey Matter	0.870	63.029	403 MHz	56.705	0.870	63.029	57.146	57.241	56.983	55.452	-	0.400285 GHz	22/11/2016	2/12/2016	6.324	10.033		59.533	5.547	
White Matter	0.508	47.802	403 MHz	42.297	0.508	47.802	42.597	42.954	42.666	40.970	-	0.400285 GHz	22/11/2016	2/12/2016	5.505	11.516		44.406	7.104	
Kidney	1.122	48.580	403 MHz	43.946	1.122	48.580	44.591	44.327	44.383	42.485	-	0.400285 GHz	22/11/2016	2/12/2016	4.634	9.539		46.138	5.028	
Spleen	1.081	55.014	403 MHz	-	1.081	55.014	#	#	#	#	-	-	-	-	-	-		-	-	
Heart	1.137	45.167	403 MHz	41.062	1.137	45.167	40.931	41.011	40.936	40.847	41.585	0.400285 GHz	17/01/2017	18/01/2017	4.106	9.090		43.109	4.557	
Liver	0.903	49.491	403 MHz	45.079	0.903	49.491	45.286	45.057	44.986	44.988	-	0.400285 GHz	22/11/2016	2/12/2016	4.412	8.915		47.327	4.374	
Lung	0.552	35.645	403 MHz	31.719	0.586	38.225	33.304	32.038	30.841	30.661	31.749	0.400285 GHz	17/01/2017	18/01/2017	6.507	17.022		33.300	12.884	
Muscle	1.122	65.941	403 MHz	58.761	1.122	65.941	58.876	57.912	58.659	59.600	-	0.400285 GHz	22/11/2016	2/12/2016	7.180	10.888		61.691	6.445	
Skin	0.477	41.240	403 MHz	35.536	0.477	41.240	34.402	34.617	36.724	36.403	-	0.400285 GHz	22/11/2016	2/12/2016	5.703	13.829		37.308	9.533	
Blood	1.486	59.142	910 MHz	56.531	1.486	59.142	55.787	55.277	56.759	58.299	-	0.920265 GHz	23/09/2016	14/11/2016	2.611	4.415	8.762	59.349	0.351	4.283
Bone Cancellous	0.339	17.499	910 MHz	-	0.339	17.499	-	-	-	-	-	-	-	-	-	-		-	-	
Bone Cortical	0.146	9.783	910 MHz	-	0.146	9.783	-	-	-	-	-	-	-	-	-	-		-	-	
Fat	0.114	10.071	910 MHz	-	0.114	10.071	-	-	-	-	-	-	-	-	-	-		-	-	
Grey Matter	1.166	54.350	910 MHz	50.748	1.166	54.350	52.146	49.156	49.885	51.805	-	0.920265 GHz	23/09/2016	14/11/2016	3.602	6.628		53.278	1.972	
White Matter	0.819	36.437	910 MHz	33.430	0.819	36.437	33.700	33.381	33.347	33.290	-	0.912266 GHz	22/11/2016	2/12/2016	3.007	8.253		35.096	3.678	
Kidney	1.692	45.316	910 MHz	41.695	1.692	45.316	41.165	41.571	40.965	43.078	-	0.920265 GHz	23/09/2016	14/11/2016	3.621	7.991		43.774	3.403	
Spleen	1.504	49.486	910 MHz	45.759	1.504	49.486	46.236	45.467	45.537	45.795	-	0.920265 GHz	23/09/2016	14/11/2016	3.727	7.531		48.040	2.921	
Heart	1.606	41.263	910 MHz	37.033	1.606	41.263	36.968	37.158	36.894	37.114	-	0.912266 GHz	22/11/2016	2/12/2016	4.230	10.251		38.880	5.776	
Liver	1.144	43.459	910 MHz	39.180	1.144	43.459	40.200	35.858	41.555	39.108	-	0.920265 GHz	23/09/2016	14/11/2016	4.278	9.844		41.134	5.349	
Lung	0.753	31.909	910 MHz	28.933	0.759	32.942	29.747	29.524	28.643	27.821	-	0.912266 GHz	22/11/2016	2/12/2016	4.009	12.170		30.376	7.790	
Muscle	1.362	59.233	910 MHz	53.557	1.362	59.233	53.646	53.322	53.771	53.488	-	0.912266 GHz	22/11/2016	2/12/2016	5.676	9.582		56.227	5.074	
Skin	0.736	39.792	910 MHz	35.434	0.736	39.792	35.095	35.102	35.666	35.873	-	0.912266 GHz	22/11/2016	2/12/2016	4.358	10.952		37.201	6.512	

Biological Tissue	Desired Gel Characteristics			Properties of Measurements															
	Conductivity [S/m]	Permittivity	Resonance Frequency	Calculated Avg Permittivity	Estimated Conductivity [S/m]	Estimated Permittivity	Sample A: Measured Epsilon	Sample B: Measured Epsilon	Sample C: Measured Epsilon	Sample D: Measured Epsilon	Sample E: Measured Epsilon	Measurement Frequency	Date Created	Date Measured	Error (From Avg)	Error [%] (From Avg)	Error [%] (Per Frequency)	Avg Permittivity (Probe Error of 4.986% Removed)	Error [%] (Probe Error of 4.986% Removed)	Error [%] (Per Frequency: Probe Error of 4.986% Removed)
Blood	2.558	54.142	2.4 GHz	53.950	2.558	54.142	53.425	53.322	55.737	53.315	-	2.400210 GHz	24/09/2016	11/11/2016	0.192	0.355	7.194	56.639	4.613	4.487
Bone Cancellous	0.685	15.783	2.4 GHz	-	0.685	15.783	-	-	-	-	-	-	-	-	-	-		-	-	
Bone Cortical	0.288	8.783	2.4 GHz	-	0.288	8.783	-	-	-	-	-	-	-	-	-	-		-	-	
Fat	0.175	8.293	2.4 GHz	-	0.175	8.293	-	-	-	-	-	-	-	-	-	-		-	-	
Grey Matter	2.286	43.852	2.4 GHz	40.257	2.765	43.852	40.320	39.225	41.563	39.920	-	2.400210 GHz	24/09/2016	11/11/2016	3.595	8.198		42.264	3.621	
White Matter	1.435	32.531	2.4 GHz	29.695	2.435	32.531	28.820	30.190	29.791	29.979	-	2.400210 GHz	22/11/2016	2/12/2016	2.836	8.717		31.176	4.166	
Kidney	2.681	40.557	2.4 GHz	37.743	2.711	40.557	37.804	37.847	37.575	37.745	-	2.400210 GHz	22/11/2016	2/12/2016	2.814	6.939		39.625	2.299	
Spleen	2.117	45.829	2.4 GHz	42.354	2.844	45.829	42.119	42.786	42.173	42.337	-	2.400210 GHz	24/09/2016	11/11/2016	3.475	7.583		44.466	2.975	
Heart	2.467	34.469	2.4 GHz	31.104	2.527	34.469	31.298	30.384	31.463	31.268	-	2.400210 GHz	24/09/2016	13/11/2016	3.365	9.763		32.654	5.264	
Liver	1.750	39.139	2.4 GHz	35.396	2.732	39.139	35.272	35.777	34.768	35.768	-	2.400210 GHz	24/09/2016	14/11/2016	3.742	9.562		37.161	5.052	
Lung	1.050	27.567	2.4 GHz	24.720	2.045	27.567	24.771	25.024	24.346	24.739	-	2.400210 GHz	22/11/2016	2/12/2016	2.847	10.326		25.952	5.855	
Muscle	2.055	53.396	2.4 GHz	53.700	2.260	53.396	53.077	53.067	54.146	54.510	-	2.400210 GHz	24/09/2016	11/11/2016	-0.304	0.569		56.377	5.584	
Skin	1.426	36.405	2.4 GHz	32.791	2.636	36.405	32.392	32.411	33.123	33.236	-	2.400210 GHz	22/11/2016	2/12/2016	3.614	9.928		34.426	5.437	
Blood	1.297	57.264	4.5 GHz	55.362	5.545	57.264	53.509	57.351	52.999	57.589	-	4.496131 GHz	22/11/2016	2/12/2016	1.902	3.321	10.591	58.122	1.500	9.127
Bone Cancellous	0.175	59.012	4.5 GHz	59.745	5.100	59.012	61.523	58.573	58.560	60.326	-	4.496131 GHz	22/11/2016	2/12/2016	-0.733	1.243		62.724	6.291	
Bone Cortical	0.114	29.285	4.5 GHz	22.563	4.388	29.285	22.026	22.074	23.780	22.372	-	4.496131 GHz	22/11/2016	2/12/2016	6.722	22.954		23.688	19.112	
Fat	0.068	20.706	4.5 GHz	14.139	3.074	18.638	14.131	13.639	14.508	14.280	-	4.496131 GHz	22/11/2016	2/12/2016	4.498	24.136		14.844	20.353	
Grey Matter	0.986	52.914	4.5 GHz	44.608	6.185	52.914	46.234	43.795	42.836	45.567	-	4.496131 GHz	22/11/2016	2/12/2016	8.306	15.697		46.832	11.494	
White Matter	0.582	46.213	4.5 GHz	39.442	5.518	46.213	40.386	39.279	37.826	40.275	-	4.496131 GHz	22/11/2016	2/12/2016	6.772	14.653		41.408	10.398	
Kidney	1.056	64.455	4.5 GHz	62.241	4.964	64.455	62.876	64.796	58.714	62.575	-	4.496131 GHz	22/11/2016	2/12/2016	2.215	3.436		65.344	1.378	
Spleen	0.863	113.928	4.5 GHz	-	0.863	113.928	-	-	-	-	-	-	-	-	-	-		-	-	
Heart	0.775	52.213	4.5 GHz	44.458	6.012	52.213	45.487	43.649	45.309	43.388	-	4.496131 GHz	22/11/2016	2/12/2016	7.755	14.852		46.675	10.607	
Liver	0.456	59.197	4.5 GHz	60.353	5.096	59.197	60.206	60.963	60.085	60.156	-	4.496131 GHz	22/11/2016	2/12/2016	-1.156	1.952		63.362	7.035	
Lung	0.665	63.264	4.5 GHz	60.334	4.998	63.264	55.096	62.631	61.164	62.445	-	4.480132 GHz	24/09/2016	14/11/2016	2.930	4.631		63.342	0.124	
Muscle	1.155	65.469	4.5 GHz	70.724	4.934	65.469	72.146	72.385	70.026	68.338	-	4.496131 GHz	22/11/2016	2/12/2016	-5.254	8.025		74.250	13.412	
Skin	0.801	39.647	4.5 GHz	34.811	5.043	39.647	34.817	34.663	35.032	34.734	-	4.496131 GHz	22/11/2016	2/12/2016	4.836	12.197		36.547	7.820	

Table 43: Measured dielectric properties of rhinoceros phantom recipes (24 degC, 100 ml) B.

Biological Tissue	Desired Gel Characteristics																			
	Conductivity [S/m]	Permittivity	Resonance Frequency	Water Volume [ml]	Calculated Avg Permittivity	Estimated Conductivity [S/m]	Estimated Permittivity	Sample A: Measured Epsilon	Sample B: Measured Epsilon	Sample C: Measured Epsilon	Sample D: Measured Epsilon	Sample E: Measured Epsilon	Measurement Frequency	Date Created	Date Measured	Error (From Avg)	Error [%] (From Avg)	Error [%] (Per Frequency)	Avg Permittivity (Probe Error of 4.986% Removed)	Error [%] (Probe Error of 4.986% Removed)	Error [%] (Per Frequency: Probe Error of 4.986% Removed)
Skin	0.736	39.792	910 MHz	100	35.680	0.803	39.791	35.956	36.369	36.272	34.600	35.202	0.912266 GHz	23/11/2016	1/12/2016	4.111	10.333	10.333	37.453	5.878	5.878
Grey Matter	2.286	43.852	2.4 GHz	100	40.775	2.781	43.861	40.557	40.457	40.696	41.389	-	2.400210 GHz	25/09/2016	12/11/2016	3.087	7.037		42.808	2.402	
White Matter	1.435	32.531	2.4 GHz	100	28.794	2.635	32.470	29.086	28.096	28.373	29.140	29.276	2.400210 GHz	23/11/2016	1/12/2016	3.675	11.319		30.225	6.913	
Kidney	2.681	40.557	2.4 GHz	100	36.613	2.817	40.558	36.708	36.616	36.698	36.432	-	2.400210 GHz	25/09/2016	12/11/2016	3.944	9.725		38.439	5.224	
Spleen	2.117	45.829	2.4 GHz	100	42.448	2.845	45.845	41.923	42.686	42.787	42.396	-	2.400210 GHz	25/09/2016	12/11/2016	3.397	7.410		44.565	2.793	
Heart	2.467	34.469	2.4 GHz	100	31.757	2.722	34.460	31.675	32.118	31.580	31.787	31.623	2.400210 GHz	23/11/2016	1/12/2016	2.703	7.844	7.796	33.334	3.266	4.314
Liver	1.750	39.139	2.4 GHz	100	36.246	2.815	39.133	37.033	36.844	36.638	35.089	35.625	2.400210 GHz	23/11/2016	1/12/2016	2.887	7.378		38.047	2.776	
Lung	1.050	27.567	2.4 GHz	100	24.772	2.271	27.450	24.500	24.933	24.694	24.935	24.798	2.400210 GHz	23/11/2016	1/12/2016	2.678	9.756		26.003	5.273	
Muscle	2.055	53.396	2.4 GHz	100	53.982	2.457	53.414	53.883	53.762	54.248	54.036	-	2.400210 GHz	25/09/2016	12/11/2016	-0.569	1.065		56.674	6.104	
Skin	1.426	36.405	2.4 GHz	100	33.234	2.777	36.375	32.740	33.100	34.111	32.986	-	2.400210 GHz	25/09/2016	12/11/2016	3.141	8.634		34.891	4.078	
Blood	1.297	57.264	4.5 GHz	100	53.448	5.480	57.447	50.411	48.444	58.563	56.375	-	4.480132 GHz	25/09/2016	15/11/2016	3.999	6.961		56.113	2.322	
Bone Cancellous	0.175	59.012	4.5 GHz	100	56.035	5.392	59.282	54.560	56.904	54.641	56.526	57.546	4.496131 GHz	23/11/2016	1/12/2016	3.247	5.477		58.819	0.782	
Bone Cortical	0.114	29.285	4.5 GHz	100	-	0.114	29.285	-	-	-	-	-	-	-	-	-	-		-	-	
Fat	0.068	20.706	4.5 GHz	100	-	0.068	20.706	-	-	-	-	-	-	-	-	-	-		-	-	
Grey Matter	0.986	52.914	4.5 GHz	100	44.200	6.125	52.610	43.485	43.913	44.762	44.024	44.816	4.496131 GHz	23/11/2016	1/12/2016	8.410	15.986		46.396	11.812	
White Matter	0.582	46.213	4.5 GHz	100	40.804	5.613	46.080	39.649	39.363	40.093	42.339	42.576	4.496131 GHz	23/11/2016	2/12/2016	5.276	11.450		42.831	7.051	
Kidney	1.056	64.455	4.5 GHz	100	65.632	5.057	64.735	64.136	63.393	67.227	66.615	66.788	4.496131 GHz	23/11/2016	1/12/2016	-0.897	1.385	9.789	68.892	6.422	7.666
Spleen	0.863	113.928	4.5 GHz	100	-	0.863	113.928	-	-	-	-	-	-	-	-	-	-		-	-	
Heart	0.775	52.213	4.5 GHz	100	37.942	6.239	52.793	36.077	34.131	40.429	36.599	42.473	4.496131 GHz	23/11/2016	1/12/2016	14.851	28.131		39.826	24.562	
Liver	0.456	59.197	4.5 GHz	100	57.696	5.383	59.456	51.867	59.044	62.033	57.838	-	4.480132 GHz	25/09/2016	15/11/2016	1.760	2.960		60.572	1.878	
Lung	0.665	63.264	4.5 GHz	100	58.901	5.137	63.562	58.491	58.896	63.044	56.575	57.496	4.496131 GHz	23/11/2016	1/12/2016	4.662	7.334		61.827	2.730	
Muscle	1.155	65.469	4.5 GHz	100	66.630	4.985	65.747	65.459	67.348	66.744	66.710	66.890	4.496131 GHz	23/11/2016	1/12/2016	-0.883	1.344		69.940	6.378	
Skin	0.801	39.647	4.5 GHz	100	32.647	5.238	39.267	32.404	33.401	31.573	33.158	32.698	4.496131 GHz	23/11/2016	1/12/2016	6.620	16.858		34.269	12.728	